Universidade de Aveiro Departamento de Química
2009

Penka Ilieva Girginova

Novos materiais magnéticos: de compostos de coordenação aos nanomateriais

Novel magnetic materials: from coordination compounds to nanomaterials

Universidade de Aveiro Departamento de Química
2009

Penka Ilieva Girginova

Novos materiais magnéticos: de compostos de coordenação aos nanomateriais

Novel magnetic materials: from coordination compounds to nanomaterials

Tese apresentada à Universidade de Aveiro para cumprimento dos requisitos necessários à obtenção do grau de Doutor em Química, realizada sob a orientação científica do Doutor Tito da Silva Trindade, Professor Associado com Agregação do Departamento de Química da Universidade de Aveiro e do Doutor Vítor Sequeira Amaral, Professor Associado com Agregação do Departamento de Física da Universidade de Aveiro

Apoio financeiro do POCTI no âmbito do III Quadro Comunitário de Apoio.

Apoio financeiro da FCT e do FSE no âmbito do III Quadro Comunitário de Apoio.

To my family

In memory of my father

o júri

presidente

Doutor José Rodrigues Ferreira da Rocha
Professor catedrático da Universidade de Aveiro

Doutor Ricardo Ibarra Garcia
Professor catedrático do Instituto de Nanosciência de Aragão de Universidade de Saragoça (Espanha)

Doutora Ana Cristina Moreira Freire
Professor associado com agregação da Faculdade de Ciências da Universidade do Porto

Doutor Vítor Sequeira Amaral
Professor associado com agregação do Departamento de Física da Universidade de Aveiro

Doutor Tito da Silva Trindade
Professor associado com agregação do Departamento de Química da Universidade de Aveiro

Doutor Manuel Leite de Almeida
Investigador coordenador do Instituto Tecnológico e Nuclear de Sacavém

Doutor Filipe Alexandre Almeida Paz
Investigador auxiliar do Laboratório Associado do CICECO da Universidade de Aveiro

agradecimentos

My acknowledgments are to several people whose presence and work directly or indirectly became a part in the elaboration of this thesis.

At first I want to express gratitude to my supervisor, Prof. Tito Trindade, for the trust in my abilities. He gave me the chance to work in his research group and to grow scientifically. I thank him for the patience, the help and the motivation especially in the moments of doubts and hesitations. I have learned a lot from him as a teacher and as a leader.

Then, I acknowledge my co-supervisor, Prof. Vítor Amaral, for his guidance and help in the study of magnetism. The discussions with him about this matter were very useful and important for the realization of this work.

I am thankful to the University of Aveiro and to Fundação para a Ciência e Tecnologia (Portugal) for the award of the PhD grant.

I am grateful to Prof. Helena Nogueira for the collaboration in the work related to Chapter 2 and also for being always ready to help or advice me in the work on the coordination chemistry.

I also acknowledge the collaboration to the following people, whose contribution was very important for the characterization of the materials:

Dr. Filipe Paz for the enormous work on crystallography and to Dr. Luís Cunha for crystallographic measurements and solving of some structures; to Prof. Jacek Klinowski from University of Cambridge;
Dr. Fa-Nian Shi, who allowed me to study the magnetic properties of some of the crystals synthesized by him in Chapter 4;
Dr. Cláudia Lopes, Dr. Marta Otero and Prof. Eduarda Pereira from Analytical chemistry, and to Dr. Ana Luísa Silva, who collaborated with us in the work on Chapter 5. To Paula Figueira, for letting me compare the results from the Cd^{2+} and Pb^{2+} uptake of her materials to those, from the Hg^{2+} uptake of my materials in the same chapter;
Celeste Azevedo, MSc, for the TGA measurements and for being very helpful in solving of the laboratory problems;
Dr. Paula Santos and Prof. Luís Carlos for the luminescent measurements of the compounds in Chapter 3;
Marta Ferro, MSc, Eng. Augusto Lopes, Dr. Protima Singh-Rauwel and Dr. Marc Willinger for the microscopy;

agradecimentos (cont.)

Dr. Rosário Soares and Dr. Ângela Pereira for the powder XRD analysis;
Dr. João Pedro Araújo for the given possibility to use the SQUID in IFIMUP, University of Porto;
Prof. Margarida Godinho for the chance to perform the magnetic measurements of some compounds reported in Chapter 2 at the Faculty of Sciences, University of Lisbon;
Prof. Benilde Costa from FCT of University of Coimbra for the Mössbauer spectroscopy measurements of the nanomaterials in Chapter 5;
Dr. Soma Das for some magnetic measurements in Aveiro.

Dr. Nuno Silva for the fruitful discussions about magnetism.

My thanks are also to all the team of Aragon Institute of Nanoscience (University of Saragossa, Spain) and especially to Prof. Ricardo Ibarra, then, to Prof. Clara Marquina and Prof. Gerardo Goya, who, on first place, gave me the opportunity to work with them and also for not saving time and energy to teach me. I also want to thank to Teo, Ana, Henrique, Sara and Prof. Pedro Algarabel who also turned my stay in Saragossa very useful and productive for the study of the magnetic properties of my compounds.

I am very grateful to my mother Varvara, my father Ilia and my sister Dessislava for the support I know they give me in every step of my way even far from them. They have always given me the freedom and the right to choose, and have been teaching me to fight and not to give up. I was very lucky to have with them all the interesting and fruitful discussions we had at home about scientific, political and philosophical matters which formed my views and will for knowledge and improvement. The tenacity and love to science and foreign languages are due to my family. To them and to my niece Elena, grandparents and aunt Venera (great help with the chemistry): for the criticism and the advices; for all cares and concerns.

I also thank to Luciano for being beside me most of the time in the personal and professional life, for the encouragement, the constructive criticism and advices; for the help with LaTeX; without him I would never go back to Portugal and fight to make this PhD happen there.

I want to thank infinitely to my friends and colleagues Sandra and Iva, who give me incredible support and keep on being my friends during the best and worst moments! I am grateful to my colleagues who I first met in Minho University in Guimarães and who became my friends: to Ricardo Pires, Sofia and Domingos;

agradecimentos (cont.)

also to Salete, Luís, Dora Gago and Nuno Correia: for the sympathies. To all of them I owe a big part of my priceless knowledge on Portuguese language, literature and culture. I thank to my best friends from all over the world for the friendship and the professional discussions.

The everyday life and work in the laboratory become easier when a kind word is received, when a problem, a success, a thought or even a glassware are shared; when somebody makes you feel you are not alone…For this, I want to thank to my colleagues from the laboratory on Inorganic Chemistry, to the professors, colleagues and employees from Chemistry Department, LCA, Physics Department and CICECO who I crossed my way with the last years, especially to Catarina, Fátima, Paula Santos, Ângela, Sofia, Sergio, Patrícia Neves, Diana Fernandes, Mariela, Stanislav, Soma, Mir, Susana Quintal, João Madureira, Paula Brandão, Zé, Mariana, Isabel Vieira, Ana Estrada and Carlos.

благодарности

Бих искала да благодаря на всички, които пряко или косвено допринесоха за изработването на тази теза. Най-напред искам да кажа, че посвещавам този труд на семейството ми и е в памет на баща ми.

Благодарна съм на ръководителя ми, проф. Тито Триндаде за това, че се довери в моите умения и ми даде възможност да работя и да се развивам професионално в неговия екип; че ме мотивираше и ми помагаше в моментите на колебания и съмнения. Научих много от него като учител и лидер на научна група. Признателна съм на втория ми ръководител, проф. Витор Амарал, под чието ръководство изучавах магнитизъм. Беседите на тази тема с него, бяха от голямо значение за обучението и работата ми.

Благодарна съм на Университета в Авейро и на Португалската фондация за наука и технология, която отпусна докторантската ми стипендия.

Благодарности за отзивчивостта и съдействието при характеризирането на материалите на:

проф. Елена Ногейра за съдействието в работата, описана в глава 2 и изобщо в работата, свързана с координационна химия;
д-р Филип Паш за огромния обем работа по разрешаването на кристалните структури и на д-р Луиш Куня за някои кристалографски измервания и анализи; на проф. Ясек Клиновски от университета в Кембридж.
д-р Фа-Ниан Ши за предоставянето на кристали, синтетизирани от него, чиито магнитни свойства изучавах в Глава 4.
д-р Клаудия Лопеш, д-р Марта Отеро, проф. Едуарда Перейра и д-р Ана Луиза Силва, с които работихме съвместно върху аналитичните измервания в Глава 5. На бакалавър Паула Фигейра за предоставените резултати за адсорбционните свойства на нейните материали спрямо Cd^{2+} и Pb^{2+} йони, за сравнение с моите материали спрямо Hg^{2+} йони в същата глава;
магистър Селеще Азеведо за термо-гравиметричните измервания и за отзивчивостта при разрешаването на всеки един проблем в лабараторията;
д-р Паула Сантош и проф. Луиш Карлош за измерванията на луминесцентните свойства на съединенията в глава 3;
магистър Марта Феро, инж. Аугущо Лопеш, д-р Протима Син-Роуел и д-р Марк Вилингер за съдействието с микроскопските методи;

благодарности (продълж.)

д-р Розарио Соареш и д-р Анжела Перейра за ретгеновите анализи;
д-р Жоао Педро Араужо за предоставеното време за измервания с магнетометъра в Университета в Порто;
проф. Маргарида Годиньо за предоставената възможност за магнитни измервания в Лисабонския Университет на някои съединения описани в глава 2;
проф. Бенилде Коста от Университета в Коимбра за спектроскопските Мьосбауер измервания на наноматериалите в глава 5;
д-р Сома Даш за някои магнитни измервания.

Благодарня на д-р Нуно Силва за ползотворните дискусии и помощ върху магнетизъм.

Специално искам да изразя благодарност към екипа на Арагонския институт за нано-науки (Университет на Сарагоса, Испания) и преди всичко на проф. Рикардо Ибара, проф. Клара Маркина и проф. Херардо Гоша, които не само че ме приеха в екипа си, но не пощадиха време и усилия да ме обучават. Благодаря също на Тео, Ана, Енрике, Сара и проф. Педро Алгарабел, които също допринесоха много за моя ползотворен престой в Сарагоса и за осъществените успешни измервания на магнитните свойства на материалите ми.

Благодарна съм на майка ми, Варвара, баща ми Илия и сестра ми Десислава за подкрепата, дадените възможностите и поощрението; за това, че ме възпитаха в отговорност и упоритост; за градивната критика и съветите; за насърчаването към самостоятелност и приемане на предизвикателства; за ползотворните дискусии у дома, които ми помогнаха да формирам моите виждания и позиции. На родителите си далжа любовта към точните науки и чуждите езици. Освен това благодаря на бабите ми и дядо ми, на леля Венера (голяма помощ по химия), на племенницата ми Елена за обичта, подкрепата и грижите.

Благодаря на Лусиано за това, че ме придружаваше и подкрепяше през повечето моменти по този дълъг път, за съветите и насърчаването в трудните мигове. Без него нямаше да се върна в Португалия и да се боря за осъществяването на дисертацията в тази държава.

Безкрайни благодарности на моите приятелки и колежки Сандра и Ива, които ме подкрепяха през много хубави и лоши моменти и ми дадоха невероятно голяма помощ в много битки.

благодарности (продълж.)

Благодаря на моите колеги, които най-напред срещнах в университета Миньо в Гимараеш, а след това станаха мои приятели: на Рикардо Пиреш, на София и Домингуш за отзивчивостта и приятелството. Признателна съм също и на на Салете, Луиш, Дора Гаго и на Нуно Корея за помощта и търпението. На всички тях дължа голяма част от безценните си познания по португалски език, литература и култура. Благодаря за приятелството и професионалните дискусии на най-добрите ми приятели, които се намират в различни точки на света.

Ежедневието ни изправя пред най-различни предизвикатилства. А работата е по-спорна и приятна, когато имаме с кого да споделим проблем или успех, идея или дори лабораторен материал. За това съм признателна на колегите от лаборатарията по неорганична химия, а и на колегите, преподавателите и служителите изобщо от целия Химически факултет, от Физика, от секретариата и ръководството на Асоциираната лаборатория по материалознание СИСЕКО, с които преплетохме професионалните си пътища и най-вече на Катарина, Фатима, Паула Сантош, Анжела, София, Сержо, Патрисия Невиш, Станислав, Диана Фернандес, Мариела, Сома, Мир, Сузана Кинтал, Жоао Мадурейра, Паула Брандао, Жозе, Изабел Виейра, Ана Страда и Карлош.

palavras-chave

Sistemas magnéticos, Polímeros de coordenação, Nanomateriais, Materiais Híbridos, Propriedades magnéticas.

resumo

A presente tese aborda a síntese de unidades finitas de complexos do tipo metal-ligando e polímeros de coordenação infinitos, a síntese e modificação superficial de nanopartículas de magnetite, bem como o fenómeno de magnetismo observado nestes materiais. São também investigadas as várias possibilidades de coordenação de ligandos, com determinados tamanhos e formas, a metais de estrutura electrónica única, obtendo-se assim novas estruturas de tamanhos e dimensionalidades diferentes, e como as propriedades magnéticas são alteradas. Os resultados de magnetismo neste trabalho são interpretados do ponto de vista da magnetoquímica.

O Capítulo 1 é uma breve introdução à química dos metais de transição e mostra a correlação entre a estrutura e as propriedades magnéticas. Neste capítulo foi feita também uma revisão de compostos de coordenação magnéticos importantes e a descrição dos fenómenos fundamentais de magnetismo. No Capítulo 2 é explorada a química de coordenação dos ligandos ambidentados derivados dos ácidos piridina-carboxílicos para síntese de novos complexos de metais de transição. As estruturas e propriedades magnéticas duma série de novos compostos foram investigadas. O Capítulo 3 consiste na descrição de polímeros de coordenação com lantanídeos (Eu^{3+}, Tb^{3+}, Sm^{3+}) com a presença simultânea na estrutura dum ligando aromático quelato (ácido picolínico) e um ligando de ponte flexível (acido glutárico). Foram estudadas as propriedades estruturais, luminescentes e magnéticas. O Capítulo 4 descreve o comportamento magnético de híbridos orgânico-inorgânicos com ácido N-(fosfonometil)iminodiacético e metais da 1ª série de transição. A investigação abordada no Capítulo 5 relaciona-se com a modificação superficial e a funcionalização das nanopartículas ferrimagnéticas de magnetite (Fe_3O_4). Foi feito o estudo das possibilidades de aplicar estes últimos materiais na remoção de iões de metais pesados em águas poluídas. No Capítulo 6 são generalizadas as conclusões deste trabalho. Detalhes da parte experimental e das técnicas de caracterização podem ser consultadas no Capítulo 7.

keywords

Magnetic systems, Coordination polymers, Nanomaterials, Hybrid materials, Magnetic properties.

abstract

The research in this thesis is focused on the synthesis of bulk finite units of metal-ligand complexes and infinite coordination polymers as well as the synthesis and surface modification of Iron oxide nanoparticles. Subject of study is the magnetic phenomena raised in those materials. This is a research of the possibilities of the ligands with such size and shape that makes them able to trap a metal with unique electronic structure and build the new molecular assemblies with different structures, dimensionalities and sizes and of the study if / how the magnetic phenomena changes. The magnetic results in this work are interpreted in the frame of magnetochemistry.

Chapter 1 is an introduction to transition metals chemistry and correlation between structure and magnetic properties. It contains a short review of the existing magnetic coordination compounds and a description of some fundamentals in magnetism. Also some basic magnetic properties and correlations are explained. In Chapter 2 the coordination chemistry of derivatives of pyridine-carboxylic acids as ambidentate ligands is exploited to synthesize a series of transition metal complexes. Novel coordination compounds were synthesized and in particular their structures and magnetic properties are described. In Chapter 3 is discussed the simultaneous presence of a chelating aromatic ligand (picolinic acid) and a highly flexible bridging ligand (glutaric acid) in lanthanide-organic coordination polymers with Eu^{3+}, Tb^{3+}, Sm^{3+}. The structural, luminescent and magnetic properties are studied. In Chapter 4 the magnetic behaviour of organic-inorganic hybrids with the multidentate chelating ligand N-(phosphonomethyl)iminodiacetic acid and 1st row transition metals were investigated. In Chapter 5 is described the surface modification and functionalization of ferrimagnetic magnetite (Fe_3O_4) nanoparticles and their application for removal of heavy meals in waste waters. Conclusions from this work are generalized in Chapter 6. In Chapter 7 can be seen details about the experimental part and the characterization techniques.

ключови думи

Магнитни системи, Координационни полимери, Наноматериали, Хибридни материали, Магнитни свойства.

резюме

Работата, описана в настоящата теза, е фокусирана върху синтеза на обемни метал-лиганд комплекси и координационни полимери, а също и върху синтез и повърхностно модифициране на наночастици железен оксид. Предмет на изучаване е феноменът магнетизъм, който се появява в тези материали. Изучават се кординационните свойства на лигандите, чиито размери и форми позволяват да координират с метали с точно определена електронна конфигурация и да изградят нови молекулни структури, а също и дали / как се променят магнитните свойства. Резултатите от изследването на магнитните свойства се интерпретират в рамките на магнетохимията.

Глава 1 съдържа кратко въведение в химията на преходните метали. Обсъжда се връзката между структура и магнитни свойства и се описват някои съществуващи магнитни координационни съединения; въвеждат се основни понятия и зависимости в магнетизма. В глава 2 се дискутира координационната химия лиганди, производни на пиридин-карбоксилни киселини. Редица нови координационни съединения на преходни метали са синтезирани и в частност се обсъждат техните стуктурни и магнитни свойства. Глава 3 описва лантанид-органично координационни полимери на Eu^{3+}, Tb^{3+}, Sm^{3+} с хелатен ароматен лиганд (пиколинова киселина) и втори лиганд (глутарова киселина). Изучават се структурните, оптични и магнитни свойства на тези нови комплекси. В глава 4 се описват магнитните свойства на органично-неорганични хибриди с Н-(фосфонометил)иминдиоцетна киселина и преходни метали. Глава 5 описва синез, повърхностно модифициране и функциализиране на феримагнитни наночастици магнетит (Fe_3O_4), а също и приложението им за отстранявяне на тежки метали от отпадни води. Заключения от работата са представени в глава 6. В глава 7 могат да се намерят детайли по експерименталната част и техниките за характеризиране.

True knowledge exists in knowing that you know nothing…True wisdom comes to each of us when we realize how little we understand about life, ourselves, and the world around us... Wisdom begins in wonder…

Socrates (c. 469 BC–399 BC), in Socratic dialogues of Plato and in the Socratic Works of Xenophon

Contents

List of Figures

List of Tables

Introduction **1**

Coordination compounds of 1st row transition metals and ambidentate aromatic ligands **53**

Coordination compounds of lanthanides with picolinic acid and glutaric acid **91**

Magnetic behaviour of organic-inorganic hybrids of N–(phosphonomethyl) iminodiace tic acid and 1st row transition metals **115**

Magnetic nanoparticles for removal of heavy metals from water **139**

Experimental and characterisation techniques **161**

Appendices **179**

Abbreviations and symbols

A	area
ac	acetate
APTES	3–aminopropyltriethoxysilane
ATR	attenuated total reflection
B	magnetic induction
B_{hf}	hyperfine field
B_J	Brillouin function
BPE	1,2–bis (4–pyridyl) ethane
bpy	bipyridine
Bu_4N	tetra(n-butyl) ammonium
C	Curie constant; concentration
CCD	charge coupled device
CSD	Cambridge structural database
CN	coordination number
D, Δ	crystal field splitting
DMSA	dimercaptosuccinic acid
DTC	dithiocarbamate
g_J	g-factor (Landé factor)
g, g_e	isotropic g-factor for free electron
H_2glu	glutaric acid
E, ΔE	energy, energy barrier
EDS	energy dispersive analysis of X-rays spectroscopy
en	ethylenediamine
EPR	electron paramagnetic resonance
F	quantum yield
FC	field-cooled
FT–IR	Fourier transform infrared
H	field
H_C	coercivity
H_{ext}	external applied field
HnicOH	2–hydroxynicotinic acid
HnicSH	2–mercaptonicotinic acid
$H_2nic_2S_2$	2,2′–dithiobisnicotinic acid
HP	high pressure
Hpic	picolinic acid

HpicOH	3–hydroxypicolinic acid
HS	high-spin
LS	low-spin
I	fluorescence intensity
i	current
IC	internal conversion
ICP	inducted coupled plasma
ISC	intersystem crossing
J	total angular moment, exchange energy coupling constant, interaction parameter
k_B or k	Boltzman constant
K_{eff}	anisotropy constant
k_f	rate of spontaneous emission of radiation
k_i	rate of excited state decay
k_r or τ	fluorescence lifetime
k_{nrad}	probability of non-radiative transition
k_{rad}	probability of radiative transition
L	ligand; orbital quantum number
LCAO–MO	linear combination of atomic orbitals — molecular orbital
Ln	lanthanide
M	magnetization, molar magnetization
	molecular weight
	metal
M_S	saturation magnetization
MACS	magnetically assisted chemical separation
MD	multidomain
MO	molecular orbital
MOF	metal-organic frameworks
M_R	remanent magnetization
MRI	magnetic resonance imaging
M_S	saturation magnetization
N	Avogadro number
ox	oxalate
P	mean spin pairing energy
phen	1,10–phenanthroline
PMIDA, H$_4$pmida	N-(phosphonomethyl)iminodiacetic acid
pK$_a$	dissociation constant

ppm	parts per million
PPMS	quantum design physical properties measurement system
PSD	pseudosingle domain
py	pyridine
pyr	pyrazine
q	quantum efficiency
r	radius
S	spin, electronic singlet states
SC–XRD	single-crystal X-ray diffraction
SD	single domain
SEM	scanning electron microscopy
SP	superparamagnetic
SQUID	superconducting quantum interference device
T	temperature
t	time
tacn	1,4,7–triazacyclononane
T_B	blocking temperature
T_C	Curie temperature, critical temperature
T_M	temperature of Morin transition
TEM	transmission electron microscopy
TEOS	tetraethylorthosilicate
T_{fN}	ferrimagnetic Néel temperature
TGA	thermogravimetric analyses
THF	tetrahydrofuran
TIP	temperature-independent paramagnetism
T_M	temperature of Morin transition
T_N	Néel temperature
UV	ultraviolet
V	volume
VR	vibrational energy relaxation
VSM	vibrating sample magnetometer
W	weight
W_a, W_f	field coefficients for antiferro- and ferromagnetic contributions
XRD	X-ray diffraction
Z	nuclear charge
z	number of nearest neighbours around magnetic molecule in the lattice
ZFC	zero-field cooled

n_{eff} or μ_{eff}	effective Bohr magneton number
β (μ_B)	electronic Bohr magneton
χ (χ')	magnetic susceptibility (in-phase magnetic susceptibility)
χ^D	susceptibility of a diamagnet
χ_M, χ_{mol}	molar magnetic susceptibility
χ^P	susceptibility of a paramagnet
$\chi_{x(\perp)}$ and $\chi_{z(\mathrm{II})}$	perpendicular and parallel magnetic susceptibilities
δ	bending vibration
ΔE_Q	quadrupole splitting
Δ_t, Δ_o	crystal field splitting energy in tetrahedral and octahedral geometry
γ	out-of-plane deformation
λ	spin-orbit coupling constant
μ_0	magnetic permeability
μ_B (β)	electronic Bohr magneton
ν	stretching vibration
ν_{asym}	asymmetric stretching vibration
ν_{sym}	symmetric stretching vibration
Θ	Weiss temperature, Weiss constant
ρ	density
τ	relaxation time

INTRODUCTION

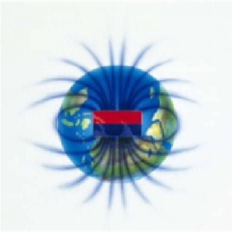

23	24	25	26	27	28	29
V	Cr	Mn	Fe	Co	Ni	Cu
$3d^34s^2$	$3d^54s^1$	$3d^54s^2$	$3d^64s^2$	$3d^74s^2$	$3d^84s^2$	$3d^{10}4s^1$

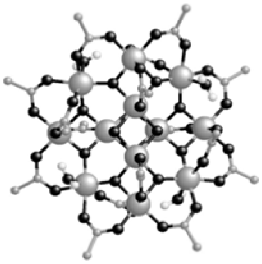

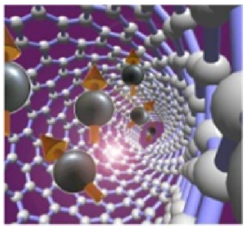

CHAPTER I

Chapter 1.

Introduction

1.1. Fundamentals of coordination chemistry of transition metal compounds

1.1.1. Coordination compounds of 1st row transition metals

The transition metals are elements located between groups 3 and 12 (including) in the periodic table (Fig. 1.1). Their properties are transitional between the *s*- and *p*-block elements. Nowadays, the transition metals are defined as those elements which have partially filled *d*- or *f*-orbitals, either as the elements or in one of the ionic forms.[1] In this work we will refer in most of the cases to the *d*-block elements as transition elements, except in Chapter 3 where lanthanide compounds have been also investigated. These elements are widely distributed throughout the Earth's crust and the oceans. Iron in the crust is one of the most abundant elements. Most of them are biologically necessary trace elements and they are basic constituents of minerals. For instance, the haemoglobin is a molecule, which contains Iron(III), bound inside a haem group and further attached to a complex protein chain. Another example is Vitamin B_{12} (cyanocobalamin), a complex of Co(III).

The main characteristic of the *d*-transition elements is the partly filled *d*-orbitals (3*d*, 4*d*, 5*d* and 6*d*). The metals are ductile, malleable, lustrous, good heat and electricity conductors, exhibiting high boiling and melting points. They are hard, have high density and form compounds with high catalytic activity. These elements have electropositive metallic nature and form stable complex compounds with neutral molecules (e.g. water). They can form alloys between them and with other metals. Many of the compounds of transition metals are coloured (Fig. 1.2) and paramagnetic, due to allowed electronic transitions involving *d*-orbitals in the former and partially filled *d*-orbitals, in the latter case. The first row of the transition elements (with partially filled 3*d* orbitals) formally begins with Scandium (Sc; electronic configuration $1s^22s^23s^23p^63d^14s^2$) and ends with Zinc (Zn; $1s^22s^23s^23p^63d^{10}4s^2$ — filled 3*d* shell).[3] The elements of the second and the third rows exhibit partly filled 4*d* and 5*d* orbitals, while the elements of the fourth row — partly filled 6*d* orbitals. This work is mainly focused on coordination compounds mainly of V, Cr, Mn, Fe, Co, Ni and Cu.

Multiple oxidation states (Table 1.1) are possible for transition metals, which is one of their main characteristic. From Ti to Mn the highest oxidation state (usually found only in oxo compounds and fluorides or chlorides) corresponds to the total number of *d* and *s* electrons in the atom, i.e. is related to the loss of all the 3*d* and 4*s* electrons.[3–5] The stability of the highest oxidation state is reduced from Ti(IV) towards Mn(VII). For Fe, Co and Ni the higher oxidation states are difficult to obtain and not very common.[3,5] This acts to decrease of the energies of the *d*-orbitals and draw them into the core of electrons not readily available for bonding. The oxides of a given element become more acidic with increasing the oxidation

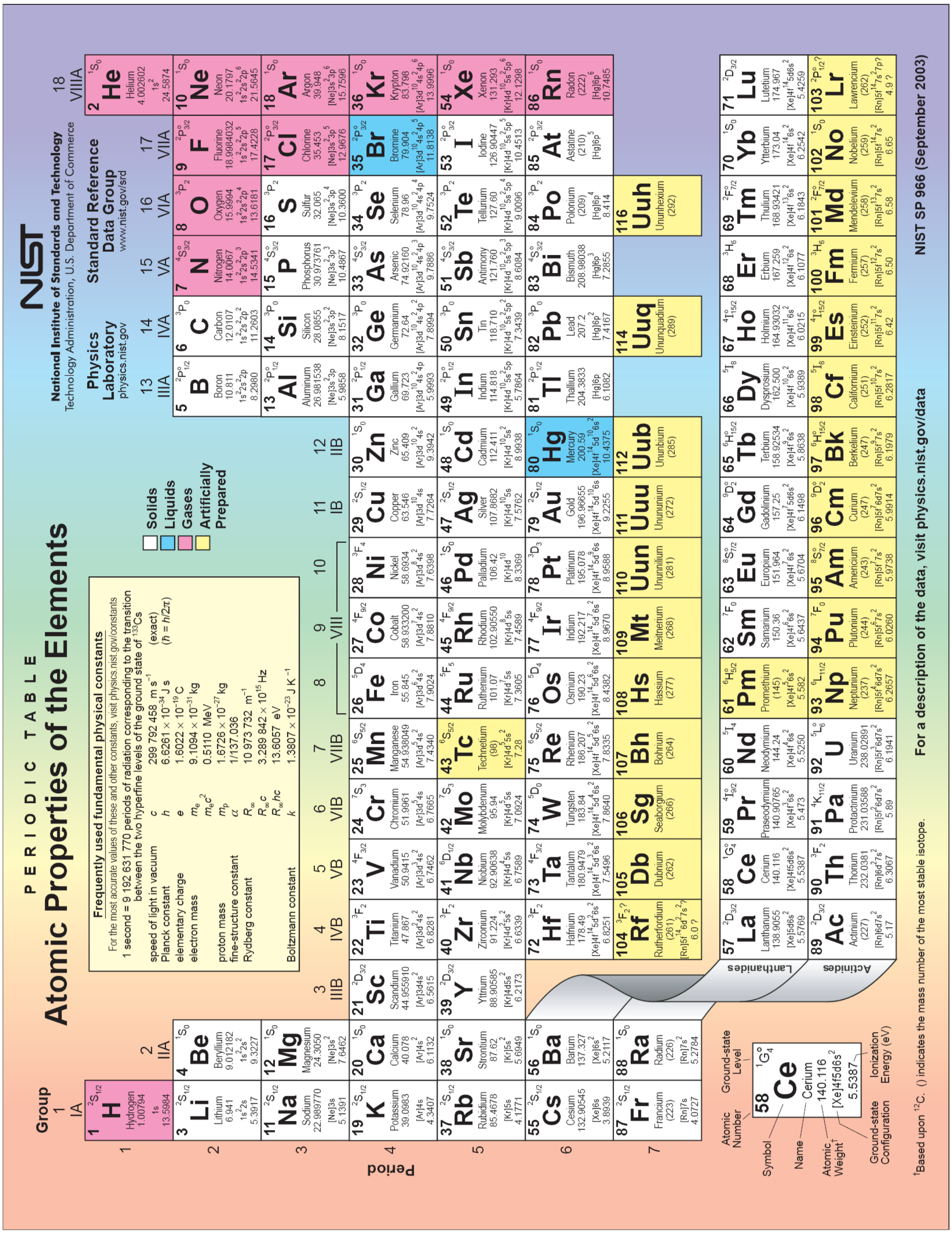

Figure 1.1.: Periodic table of the elements.[2]

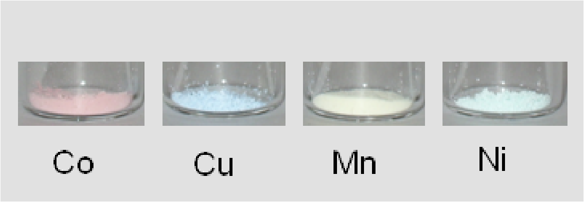

Figure 1.2.: Coordination compounds of transition metals with 2–hydroxypicolinic acid.

Table 1.1.: Oxidation states displayed by 1st row transition elements.[3,5] (The most common are in bold.)

	Oxidation states	Properties of the metal oxides
Ti	**+4**,**+3**,**+2**,0,–1	amphoteric oxides
V	**+5**,**+4**,**+3**,**+2**,+1,0,–1,–3	amphoteric oxides
Cr	**+6**,+5,+4,**+3**,**+2**,+1,0,–1,–2,–3,–4	acidic oxides
Mn	**+7**,**+6**,**+5**,**+4**,**+3**,**+2**,+1,0,–1,–2,–3	amphoteric, acidic or basic oxides
Fe	+6,**+5**,+4,**+3**,**+2**,+1,0,–1	amphoteric oxides
Co	+5,+4,**+3**,**+2**,+1,0,–1	amphoteric oxides
Ni	+4,**+3**,**+2**,+1,0,–1	basic oxides
Cu	+4,+3,**+2**,**+1**	basic oxides

state. In the II and III state complexes in aqueous solution or in crystals the metals are either in four or six coordination and across the 1st row exhibit similar chemical properties. The oxidation states less than II (except of Cu^{1+}) usually are formed only with $\pi-$ acid type ligands or in organometallic compounds. The transition metals are denser than the *s*-block elements and show an increase in density from V to Cu. There is also small decrease in the metallic radii with the increasing of the atomic number. Since it depends on the oxidation state of the metals, as the value of the oxidation state increases, the ionic radii decreases. The charge/radius ratios of the metal ions are large and the ionisation energies from Cr to Fe increase with the increase of the atomic number, after a slight decrease is observed and again increase from Ni to Cu (Fig. 1.3).

The most common coordination numbers for 1st row transition metal complexes are four and six. Coordination number (CN) 4 is one of the very common CNs for transition metal coordination compounds. The most important geometries for four coordinate species are tetrahedral and square planar, although there are many examples of intermediate or distorted geometries. For CN 5 two interconverting geometries are very common: trigonal bipyramidal and square pyramidal. There are many structures with intermediate geometry between these geometries (since the energy difference between the trigonal bipyramidal and square pyramidal structures is small). The most common CN for *d*-elements complexes is 6, the geometry being most often octahedral (rarely trigonal prismatic). There are many examples where such structures are distorted, due to the metals' electronic configurations. Compounds with CN higher than 6 are less common. The higher the CN, the more important are the ligand-ligand interactions, so that only smaller ligands can allow those high

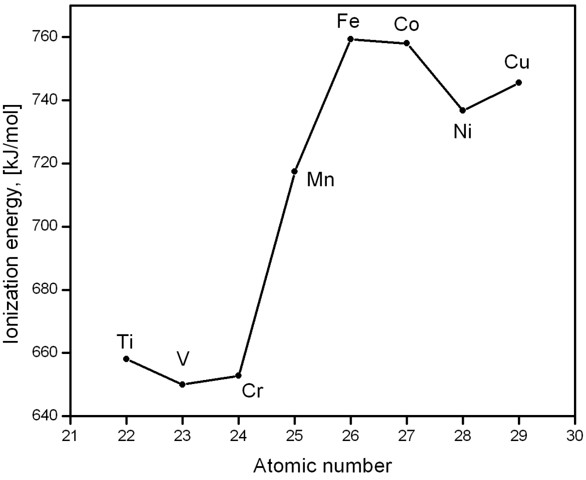

Figure 1.3.: Ionization energies of the first row metals.[6]

CNs. CN 7 is common for heavier *d*-elements. The geometry can be pentagonal bipyramidal, capped octahedral and trigonal bipyramidal with the seventh ligand on one face. There are many intermediate structures.[7] Compounds with 8 coordinated geometry are square antiprismatic or dodecahedral, and are common for *f*-elements.

The chemistry of the transition metals allows the formation of a variety of coordination compounds. When combining the metal with appropriate ligand(s) in suitable solvents and under optimized conditions, coordination compounds or polymeric assemblies of complexes can be formed. The variety of their interesting properties (e.g. magnetic and luminescent) is a big challenge to design coordination compounds of transition metals with precise composition and specific coordination environments. The coordination chemistry as a part of the molecular science (since Kahn[8]) allows such design of molecules and crystals, and the predicting of their properties. The building of structure-property relationship of complexes and the results' treatment is facilitated by the fact that the metal coordination environment might be well defined. A very important characteristic feature of the transition metals is their paramagnetism. However, magnetic ordering and superexchange interactions along the coordination complexes can be propagated through diamagnetic aromatic ligands too. These magnetic properties must be entirely studied and understood. They have been investigated using experimental and theoretical approaches of magnetochemistry and molecular magnetism which are giving solution of chemical problems by application of magnetic susceptibility and related physical quantities. They comprise many experimental techniques and give interpretation of the magnetic properties of the compounds as well as provide the optimisation of the useful properties and potential applications in different areas, such as molecular electronics, nanotechnology, biotechnology, catalysis, molecular biology, medicine, diagnostic, bioinorganic chemistry, in environmental sciences as well as in magnetic recording and magnetic fluids. But while the more restricted magnetochemistry studies the magnetic properties of the materials,[8,9] and in some cases clarify the structures of paramagnetic species, molecular magnetism concerns more the design, synthesis and study of new molecular systems with new, but predicted magnetic properties by use of quantum models. Then it makes possible the synthesis of new compounds and study of their properties. The contemporary research trends include the investigation of molecular clusters, high-spin molecules, molecular magnets, spin-crossover systems and nano-scale magnetism. The accumulation of large amount of experimental data makes their theoretical interpretation and systematisation possible. In the next section, some paradigmatic examples of magnetism associated to the chemical nature and structure of compounds will be given.

1.1.2. Magnetism of inorganic compounds with varying dimensionality and size

Although an exhaustive presentation of compounds with interesting magnetic properties is out of the scope of this introduction, it is possible to show selected examples highlighting the interplay between structure/size and magnetic behaviour.

Prussian blue $Fe_4[Fe(CN)_6]_3$, ferric ferrocyanide, known as Prussian blue, was accidentally discovered by the German artist Diebach in 1703. Initially it was used only as a blue pigment for textiles. It is one of the classical examples of a mixed-valence compound whose physical properties have been largely investigated. At low temperatures the iron(III) spins order ferroniagnetically.[10] The chemistry of Prussian blue and its transition metal analogues has been explored since it was found that cyanide materials behave as high-temperature molecular magnets[11–13] and also can be applied as hydrogen storage materials,[14,15] molecular sieves,[16] photoswitchable magnetic solids,[17] etc. The novel cyanide-bridged complexes of general composition $C_mM_x[M'(CN)_6]_y \cdot nH_2O$ manifest, at the molecular level, interesting structural, electronic and magnetic properties and are a line in the investigation of the new molecular-based magnets. The synthesis of such molecular compounds involves the use of multidentate organic ligands, capable of blocking a specific number of coordination sites on the transition metal ions, thus preventing the formation of infinite structures. All the compounds from this family display spontaneous magnetization and some long-range magnetic ordering with Curie temperature (T_c) above room temperature: ferrimagnetic;[18,19] ferromagnetic (Mn_9^{II} and Mo_6^{V} clusters below 44 K;[20] infinite stair-like layered structure;[21] bimetallic magnetic material with extended 2D network, becoming metamagnet on dehydratation;[22] two-dimensional Cu–Cr cyano-bridged ferromagnet [23] and microcrystals of $[Cu(dien)]_3[Fe(CN)_6]_2 \cdot 6\,H_2O$[24] (dien = diethylenetriamine)); an antiferromagnetic nanomolecule ($[Fe^{II}(CNFe^{III}(salmeten))_6]\ Cl_2 \cdot 17.25CH_3OH$).[25] Shatruk *et al.*[26] have reported a series of trigonal bipyramidal cyanobridged pentanuclear clusters $[M(tmphen)_2]_3[M'(CN)_6]_2$ (M/M′ = Zn/Cr, Zn/Fe, Fe/Fe, Fe/Co and Fe/Cr; tmphen = 3,4,7,8-tetramethyl-1,10-phenanthroline), some of which contain Fe(II) ions in the equatorial positions (see Fig. 1.4). The complexes exhibit a variety of magnetic properties: the cluster with M/M′ = Fe/Co shows a charge transfer induced spin transition, the Fe(II) sites in the

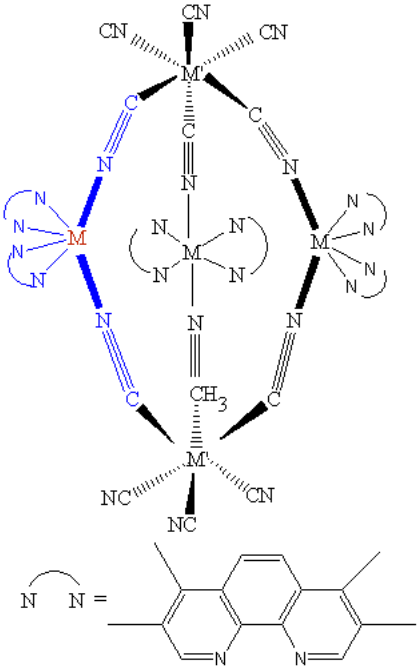

Figure 1.4.: Trigonal bipyramidal cluster with coordination environment of one equatorial metal ion (Fe(II) in most cases; in colour) in the pentanuclear, cyanide-bridged clusters $[M(tmphen)_2]_3[M'(CN)_6]_2$ (M/M′ = Zn/Cr, Zn/Fe, Fe/Fe, Fe/Co and Fe/Cr; tmphen = 3,4,7,8-tetramethyl-1,10-phenanthroline).[26]

clusters with M/M′ = Fe/Fe or Co undergo thermally induced transition from the high spin to the low spin state.[26]

The magnetism of two new weak ferromagnetic six-coordinated octahedral Cu(II) complexes (CuL_2 and $CuL_2(H_2O)_2$) were compared with strong antiferromagnetic chlorine bridged dimer ($[Cu(HL)Cl_2]_2$); HL = $C_4H_3N_2COOH$, pyrazinecarboxylic acid).[27] Although the compounds display similar structures, the ferromagnetic interactions propagate through different exchange paths, i.e. the mechanism of magnetic coupling is different. The magnetic exchange in CuL_2 is propagated along a single atom bridge, in $CuL_2(H_2O)_2$ — along three atom bridging involving hydrogen bonding. The dimer has a perpendicular plane single-atom bridge, resulting in the antiferromagnetic coupling.

Coordination polymers Chemistry methodologies provide paths in which simple mononuclear units can be extended to crystalline solids through van der Waals forces, hydrogen bonding, electrostatic interactions and metal-ligand coordination. An approach for building multi-nuclear complexes with magnetic interactions is the activation of spin polarization mechanism. This can be achieved if the paramagnetic metal ions are linked with aromatic bridging ligands and then the structural units are bridged with linear organic ligands.

Magnetic properties of these extended structures such as inorganic-organic hybrid frameworks have been the subject of study for many researchers.[8,28,29] Ismaylov *et al.*[30] report how the magnetic properties of one, two and three dimensional polymeric complexes of Cu(II) with pyrazine-ring containing ligands, change in compounds with same composition but different dimensionality. The magnetic interactions in those compounds change with the dimensionality from chains with weak antiferromagnetic exchanges (1D complexes), through ferromagnetic (2D) to weak antiferromagnetic (3D complexes) Heisenberg magnetic interactions.

Azide (N_3^-) and oxalate ($C_2O_4^{2-}$) containing coordination polymers have been used for building new molecular-based magnets.[8,31,32] These ionic compounds have allowed the construction of extended two and three dimensional transition metal networks which show that the increase of the dimensionality can enhance bulk magnetic properties. The synthetic strategy consists of polymerizing the metal-oxalate or metal-azide chiral mononuclear precursor into two or three crystallographic directions.[33,34] These coordination polymers behave as ferro-,[33,35] ferri-[36] or canted antiferromagnets[34] with critical temperatures T_C ranging from 5 to 45 K. Tamaki *et al.*[33] make an approach to establish the principle of controlling the intermolecular interaction so as to achieve a three dimensional ferromagnetic ordering. They synthesized a series of ferromagnetic mixed-metal three dimensional assemblies of the type $[Bu_4N][MCr(ox)_3]_x$, where M is a divalent 1st row transition metal coordinated to oxalate bridging ligands, leading to a 3D ferromagnetic structures of alternating arrays of Cr(III) and M(II) ions. Hernández-Molina *et al.*[35] discussed the ferromagnetism in the compound $[Co^{III}(bpy)_3][Co_2^{II}(ox)_3]ClO_4$ (see Fig. 1.5). In this compound, two different counterions ($[Co(bpy)_3]^{3+}$ and ClO_4^-) induce the crystallization of the chiral 3D $[Co_2(ox)_3]^{2-}$ anionic 3D network. Novel metal-organic frameworks (MOF's) of Mn with multidentate flexible tripodal organic ligands and anionic oxalate and azide bridging ligands as efficient magnetic couplers were reported for the first time by Zhao *et al.*[32] These authors have reported the synthesis and the properties of the non-interpenetrating three dimensional framework in which the azide ligand bridges the metal centres forming $[Mn{-}N{-}N{-}N]_n$ infinite one dimensional chains, and the properties of another new complex with two-dimensional network structure in which independent one-dimensional chains are linked by the oxalate ligand (see Figs. 1.6 and 1.7). Antiferromagnetic interactions between the Mn(II) ions were detected in those extended molecules. The same type of interactions were detected in other new 2D metal(II) coordination frameworks[29] ${}^2_\infty[M(ox)(bpy)]$, where M = Fe, Co, Ni, Zn and bpy = 4,4'–bipyridine, ox = $C_2O_4^{2-}$. The canted antiferromagnetic interactions with ordering temperatures at 12, 13 and 26 K are propagated between the metal ions octahedrally coordinated through the bridging oxalate ligand.

Nanosized materials Nanosized materials possess unique properties, which are intermediate between the molecular ones and those of the corresponding bulk materials (see Fig. 1.8). Nanochemistry allows to reduce the size of the bulk materials and to synthesize nanostructured particles with different macroscopic properties of interest for example in bio-applications such as drug release and hyperthermia; in diagnostics using contrast agents and bio-markers; in quantum computing. Size effects dominate the magnetic behaviour of individual particles increasing their importance as the particle size decreases, due to the structural and morphological modifications of the compounds. The enhanced or anoma-

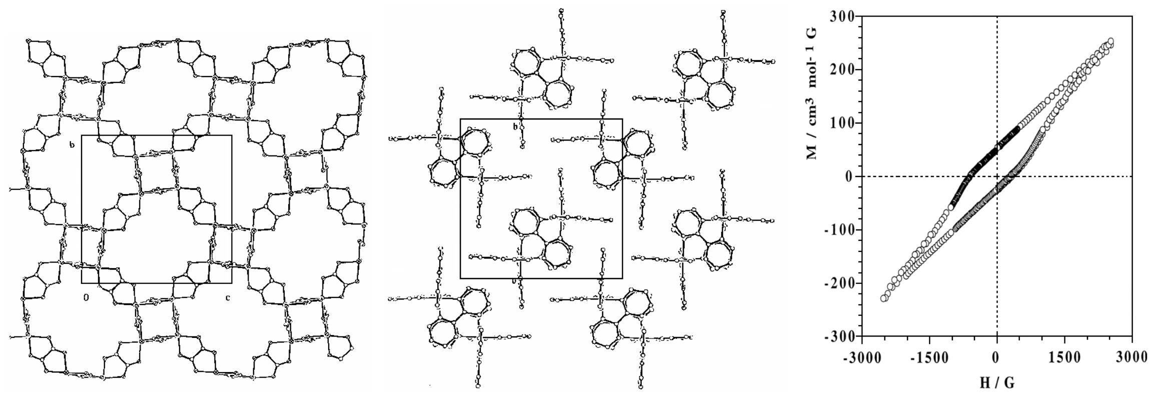

(a) (b) (c)

Figure 1.5.: Crystal structure of [Co^{III}(bpy)$_3$][Co$_2^{II}$(ox)$_3$]ClO$_4$.[35] (a) [100] projection of [Co$_2$(ox)$_3$]$^{2-}$; (b) [100] projection of [Co(bipy$_3$)]$^{3+}$; (c) Magnetic hysteresis loop at 2 K.

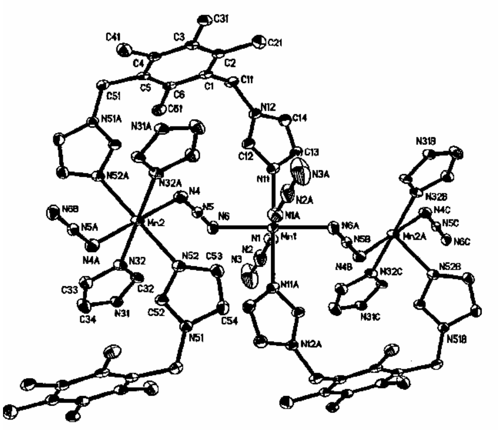

Figure 1.6.: Coordination environment around the Mn(II) atom in compound [Mn(titmb)(N$_3$)$_2$] $\cdot$ $\frac{1}{2}$H$_2$O.[32]

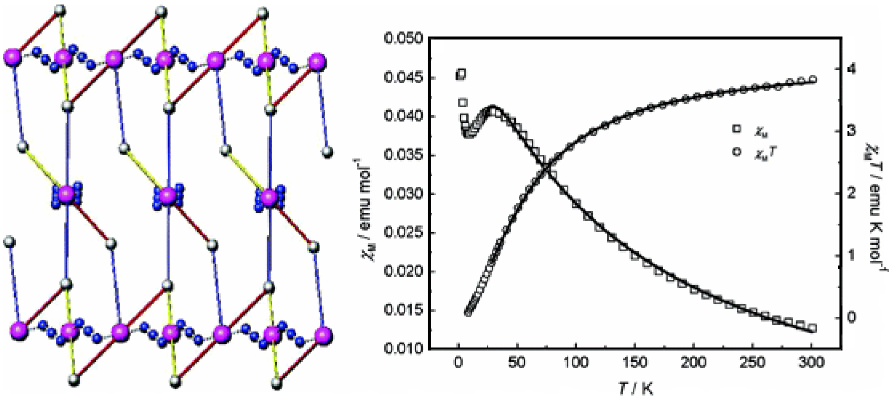

Figure 1.7.: Compound [Mn(titmb)(N$_3$)$_2$] $\cdot$ $\frac{1}{2}$H$_2$O and plots of $\chi_M T$ *vs.* T and χ_M *vs.* T under applied magnetic field of 2 kG.[32]

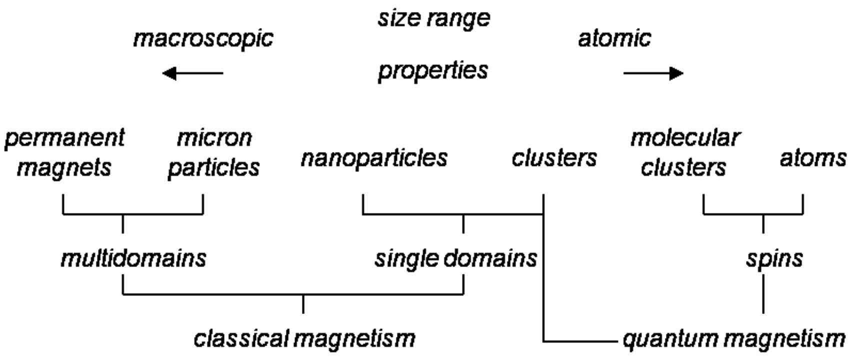

Figure 1.8.: Relationship between size–magnetic properties.[37,38]

lous properties (giant magnetoresistance, large tunnelling magnetoresistance in insulating materials, enhancement of coercivity and magnetocaloric effect, magnetization with glassy and quantum tunnelling behaviour) are result of the interaction of size distribution, finite-size effects, intrinsic properties and interparticles interactions. The most studied finite-size effect in small particles systems is superparamagnetism. It arises as a result of magnetic anisotropy. Reduction of magnetization with size is observed in nanoparticles of some ferrimagnetic and antiferromagnetic oxides.[39] In contrast, the magnetization of other metallic nanoparticles is enhanced by comparison with the bulk values (e.g. Co, Fe, iron oxide clusters, etc.)[39–52] Properties like saturation magnetization, anisotropy and Curie temperature (T_C) can be affected by the particles size[53–56] and besides, new phenomena or characteristics can appear.[57–59] For example, the influence of the size of metal clusters on magnetism was studied by Billas *et al.*[60] Magnetic moments per atom can be enhanced comparing to those of the corresponding bulk materials for nanoparticles of Co, Ni and Fe, due to changes of their band structure. Ahn *et al.*[61] reported that for cobalt ferrite nanoparticles superparamagnetism depend on the particles size. It was found that T_C increases with increasing the size of particles. The same tendency was observed by Christodoulides *et al.*[62] for FePt nanoparticles. According to Iida *et al.*,[63] the saturation magnetization and coercivity increase with the size of magnetite particles with diameters in range of 15–45 nm.

Iron oxides are good examples to investigate the magnetic behaviour of materials with varying dimensions (from bulk molecules to nanostuctures). The magnetic properties of bulk iron oxides can be seen in Table 1.2. The particle size of these materials is usually in the range of several nm to μm. Bulk magnetite (Fe_3O_4) and maghemite ($\gamma-Fe_2O_3$) are ferrimagnetic at room temperature with T_C = 850 and 820 K, respectively.[64] The two different cation sites of magnetite — tetrahedral, occupied by Fe^{3+} and octahedral, occupied by Fe^{3+} and Fe^{2+}, form the basis of two interpenetrating magnetic sublattices (see Fig. 1.9). Below T_C, the spins in the different sites are antiparallel and with unequal spin magnitude, so the spin arrangement become $Fe^{3+}[Fe^{3+}Fe^{2+}]O_4$. The coercivity of magnetite and maghemite can range from 2.4 to 20 kAm^{-1} depending on the particle size and morphology.[64] Above 956 K, hematite ($\alpha-Fe_2O_3$) is paramagnetic, being weak ferromagnetic at room temperature

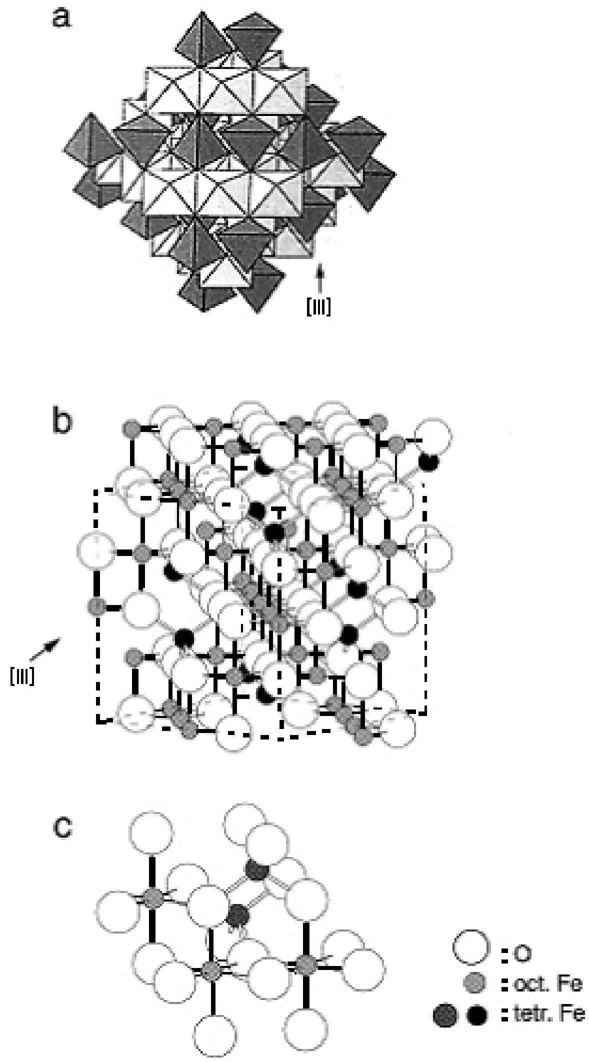

Figure 1.9.: Structure of magnetite.[64] (a) Polyhedral model with alternating octahedra and tetrahedra-octahedra layers; (b) Ball-and-stick model. Unit cell outlined; (c) Ball-and stick model of the arrangement of octahedra and tetrahedra.

and at 260 K it becomes antiferromagnetic. By decreasing size, the magnetic domain type structure changes in order multidomain (MD), single domain (SD), pseudosingle domain (PSD) and superparamagnetic (SP). The magnetic susceptibility depends on particle size and domain type. It displays minimum value near the limit SD — PSD type particles where the H_C reaches its maximum. Magnetite particles, smaller than 6 nm,[64] and hematite particles of size less than 8 nm,[64–66] are superparamagnetic at room temperature. The magnetic behaviour of magnetite with different particle sizes, has been discussed by Goya *et al.*[67] The authors have compared the magnetic characteristics (coercivity H_C, saturation magnetization M_S, remanent magnetization M_R and the ratio M_R/M_S) for particles with diameters of 4, 10, 55 and 150 nm. It was found that for a given temperature, M_S decreased as the particles become smaller from bulk to nano- size. Moreover, the coercivity decreases from its maximum value to zero with smaller size too, due to superparamagnetic relaxation effects.

Table 1.2.: Magnetic properties of the iron oxides.[64]

Oxides, oxide-hydroxides and hydroxides	Formula	Temperature, [K]	Magnetic properties	M_S[i] at 300 K $[\mathrm{Am^2kg^{-1}}]$[ii]
Goethite	α-FeOOH	400 T_N	antiferromagnetic	0.01–1
Lepidocrocite	γ-FeOOH	77 T_N	antiferromagnetic	–
Akaganéite	β-FeOOH	290 T_N	antiferromagnetic	–
Feroxyhyte	δ-FeOOH	440–460 T_N	ferrimagnetic	7–20
HP[iii] FeOOH	FeOOH	470 T_N	antiferromagnetic	
Ferrihydrite	$Fe_5HO_8 \cdot 4\,H_2O$	350 T_N	speromagnetic	
Bernalite	$Fe(OH)_3$	427 T_N	weakly ferromagnetic	–
Hematite	α-Fe_2O_3	956 T_C	weakly ferromagnetic	0.3
		260 T_M[iv]	antiferromagnetic	
Magnetite	Fe_3O_4	850 T_C	ferrimagnetic	92–100
		120 Verwey transition	ferrimagnetic	
Maghemite	γ-Fe_2O_3	820–986 T_C	ferrimagnetic	60–80
	ϵ-Fe_2O_3	1026 T_N	antiferromagnetic	–
	$Fe(OH)_2$	34 T_N	planar anti-ferromagnetic	–
Wüstite	FeO	203–211 T_N	antiferromagnetic	

[i] M_S–saturation magnetization; [ii] $[\mathrm{Am^2kg^{-1}}]$ is identical to $[\mathrm{JT^{-1}kg^{-1}}]$; [iii] HP–high pressure; [iv] T_M–Temperature of Morin transition.

Similar trend of higher M_S for bigger magnetite and maghemite particles, was observed by Roca *et al.*[68] (5 nm superparamagnetic and weak superparamagnetic 17 nm particles for biomedical application) and Mürbe *et al.*[69] (particles beteween 15–130 nm).

Single-molecule magnets The bulk magnetism is a 3D property since only if a 3D lattice of interacting magnetic centres is assembled and hence the materials can show spontaneous magnetization below a critical temperature. The low symmetry of individual molecules tends to favour 1D or 2D arrangements. With the discovery that compounds with large and finite number of magnetic centres (transition metals or rare-earth ions) may have unique magnetic properties[70,71] (quantum size effects in magnets), room-temperature coordination single-molecule magnets were synthesized by the means of coordination chemistry (mainly). Molecular-based materials are systems built on discrete molecules. They exhibit similar or even better properties (magnetic and optical) than the classical crystalline materials and allow the modelling of optical, electrical and magnetic properties of the materials with selection of the constituent molecules. The molecular approach to materials was developed mainly in the recent years.[8,57,72,73] The history of molecular magnetism began in 1951 with the study of a binuclear complex, Copper(II) acetate,[74] but the strong advancement in the field began with the discovery of the first molecular-based solids that exhibit spontaneous magnetization.[70,75] At the beginning of the 90's a molecule with 12 Mn ions with ground state $S = 10$ was discovered: $[Mn_{12}O_{12}(CH_3COO)_{16}(H_2O)_4] \cdot 2\,CH_3COOH \cdot 4\,H_2O$[76] ($Mn_{12}$ or Mn_{12}ac, *ac* = acetate). Eight of the Mn ions of the Mn cluster are in state +3 ($S = 2$) and four are in +4 state ($S = \frac{3}{2}$) (Fig. 1.10). This molecule was the first single-molecule like magnet reported in the literature.* It shows enormous relaxation of the magnetization at low temperature (2 K) meaning that a single molecule can become a magnet, since it can stay magnetized during days after applying magnetic field.[76] Such molecules with large number of coupled paramagnetic centres behave as classical magnets, showing properties intermediate between those of simple paramagnets and classical bulk magnets, but they are already small enough to show quantum effects at the same time, such as tunnelling of magnetization. Their behaviour is similar, but not strictly analogous, to that of bulk ferromagnet, in which the hysteresis result from motion of domain walls while in the case of the single-molecular magnet the slow relaxation of the magnetization gives rise to hysteresis effects with molecular origin. This makes possible the information storage in one single molecule.[75] Another example of a single-molecule magnets is the strong ferromagnet Fe_8 ring wheel with $S = 10$ state, $[Fe_8O_2(OH)_{12}(tacn)_6]Br_8$, where tacn = 1,4,7–triazacyclononane, which gives rise of spin frustration effects.[78] Many discoveries have been made since then: synthesis of first bimetallic molecular magnets[79,80] and organic magnets[81,82] with the highest Curie temperature; discovery of spin cross-over materials that occur with large hysteresis at room temperature;[83] the synthesis of the first molecular-based magnetic superconductors;[84,85] materials exhibiting large, negative magnetizations,[34] among others.[57,72,73,86]

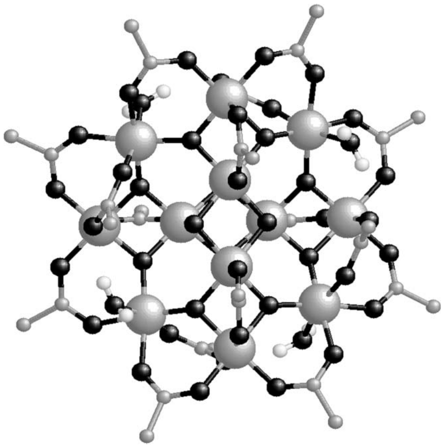

Figure 1.10.: The structure of the molecular magnet $[Mn_{12}O_{12}(CH_3COO)_{16}(H_2O)_4]$. The manganese atoms ($Mn^{3+}$ and Mn^{4+}) are represented by large grey spheres, oxygen atoms — by black spheres and carbon atoms — by small grey spheres (the hydrogen atoms of the methyl groups and the crystallization water and acetic acid molecules are not shown).[87]

---

[*] According to Gatteschi *et al.*[77] the name is not entirely correct, because in a magnet is necessary to be present a number of coupled centres.

This thesis aimed to connect concepts of coordination chemistry with molecular magnetism and to explore the synthesis of bulk finite units of metal-ligand complexes and infinite coordination polymers as well as the synthesis and surface modification of iron oxide nanoparticles. The approach was to use chemistry to produce new molecular assemblies and materials with different structures, dimensionalities and sizes, and to study their magnetic behaviour. The magnetic results in this work are interpreted in the frame of magnetochemistry. Hence, in the next section are described some magnetic foundations, associated with the magnetic characterization of the compounds reported in this work.

1.2. Magnetism: foundations and applications

The synthetic chemistry designs molecules and molecular assemblies which exhibit useful physical and chemical properties. Magnetism is associated with the presence of unpaired electrons and permanent magnetic moment. The magnetic phenomena at all, originate at the microscopic level by magnetic interactions with an external magnetic field. In this way the energy levels of chemical entities are altered. A completed description of the energy levels for a microobject with or without the presence of external magnetic field can be obtained from the principles of quantum mechanics.

1.2.1. Molecular magnetism

The molecular magnetism deals with magnetic properties of isolated molecules and assemblies of molecules involving open-shell molecules and polymeric structures synthesized from molecular precursors. These molecules can contain one or more magnetic centres; the important being to assemble the open-shell units within the lattice in a way that the interactions between such units lead to cooperative phenomena[†] and yield bulk magnetic properties. Various aspects of molecular magnetism are covered by anisotropic and macroscopic approaches deriving directly from the basic concepts of quantum mechanics. Many models used in other fields, such as molecular orbital, are applied. But very often they are incomplete and limited. Hence, models from molecular and solid state physics, theoretical chemistry, physics and materials science are used.[8] The chemistry of the 1st row transition elements is more simple than the one of the other transition metals and this makes easier to use and apply the crystal field theory when explaining the magnetic properties of their complexes. To first approximation, the *d*-block elements complexes are either ionic or covalent. In practice, usually the bonds are between the two. The crystal field theory is a useful ionic treatment while molecular orbital theory provides covalent treatment.

[†] When cooperative phenomenon is present, the lattice will exhibit properties which are more than the sum of the physical properties of the units.

1.2.2. Crystal field theory — the point charge dipole model

One of the most commonly used descriptions for bonding in transition metal compounds is derived from crystal field theory. The crystal field theory was proposed by Hans Bethe in 1929 and modified latter by Van Vleck. The pure theory (ideal case) treats the ligands as point charges or dipole and the metal-ligand interactions are only electrostatic or purely ionic. The five d-orbitals in an isolated gaseous metal ion are degenerate. If a spherical symmetric field of negative charges (ligand with highest symmetry) is around the metal, the orbitals remain degenerate, but as result of the repulsion between the negative ligand field and electrons in the orbitals, they will rise in energy. If the field is not spherical (e.g. the case of octahedral or tetrahedral field), the symmetry of ligands is lower and the five-fold degeneracy of the d-orbitals will be removed. This results in the splitting of the d-orbital energies, i.e. the crystal field terms, and is the basis of the crystal field theory.[9]

1.2.2.1. Octahedral complexes

Let consider an octahedral complex ML_6 in a chosen coordination system as shown in Fig. 1.11. The electrostatic field of the ligands will induce a splitting of the atomic d-level into two well separated levels e_g and t_{2g} (Fig. 1.12). The d-orbitals are destabilized by the ligand field but some more than the others. The lobes of electron density of the $d_{x^2-y^2}$ orbital are orientated directly toward the ligands so that this orbital suffers greater perturbation than d_{xy} (Fig. 1.13). The lobes of the electron density of the d_{xy} orbital point between the axes of the ligand. The orbitals d_{xz}, d_{yz} and d_{xy} are equivalent (with respect to the ligand array) and they remain the same energy, constituting a three-fold degenerate or t set. The orbital d_{z^2} is linear superposition of the two following orbitals:[9]

$$d_{z^2-x^2} + d_{z^2-y^2} \sim d_{z^2}$$

Each of those orbitals are equivalent in octahedral ligand field. So the d_{z^2} and $d_{x^2-y^2}$ orbitals suffer the same destabilization and they form doubly-degenerate or e set of orbitals.

1.2.2.2. Tetrahedral complexes

In Fig. 1.14 is shown a tetrahedral transition metal complex ML_4 in a chosen coordination system. The splitting of the perturbed d-orbitals is shown in Fig. 1.15. In this case none of the metal d-orbitals points directly at the ligands, but each lobe of d_{xy} is close to one ligand (Fig. 1.16). $d_{x^2-y^2}$ has lobes directly orientated between the ligands and thus does not suffer the maximum effect of the ligand. So, d_{xy} is more destabilized from the tetrahedral field than the orbital $d_{x^2-y^2}$. d_{xz} and d_{yz} are equivalent to d_{xy}. As in the previous case, the orbitals $d_{z^2-x^2}$, $d_{z^2-y^2}$, and $d_{x^2-y^2}$ are equivalent and $d_{z^2-x^2} + d_{z^2-y^2} \sim d_{z^2}$, so d_{z^2} remain degenerate with the $d_{x^2-y^2}$ orbital.

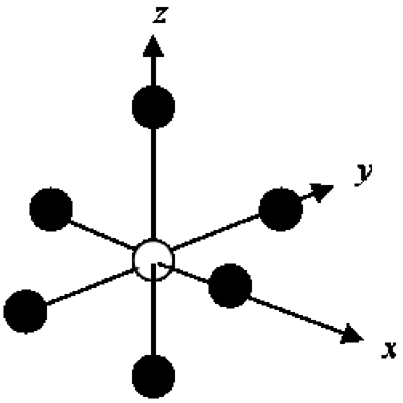

Figure 1.11.: Coordinate system for an octahedral complex ML_6 (the ligands are taken to lie on the cartesian axes).

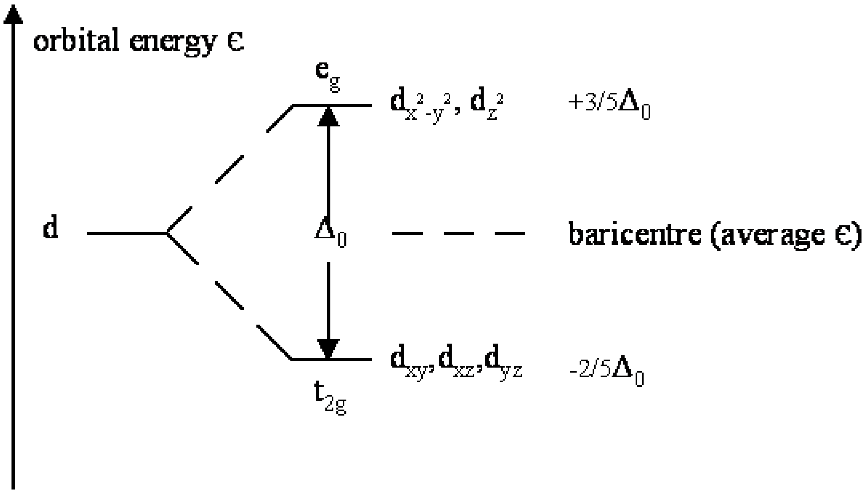

Figure 1.12.: Splitting of the metal *d*-orbitals in an octahedral transition metal complex.[9] (Δ is splitting energy.)

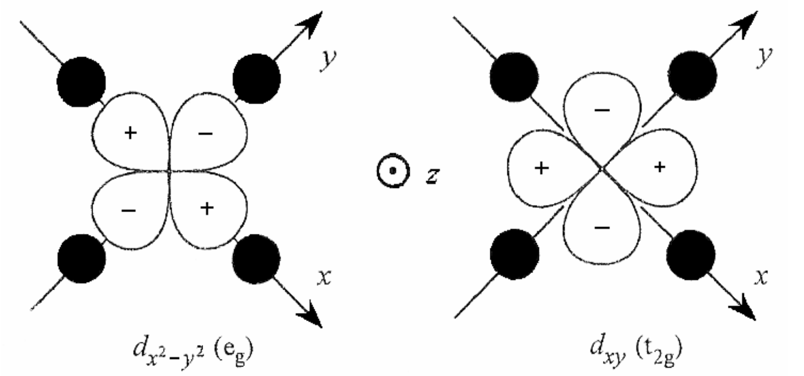

Figure 1.13.: Projection of the *d*-orbitals $d_{x^2-y^2}$ and d_{xy} in relation to the octahedral array of ligands.

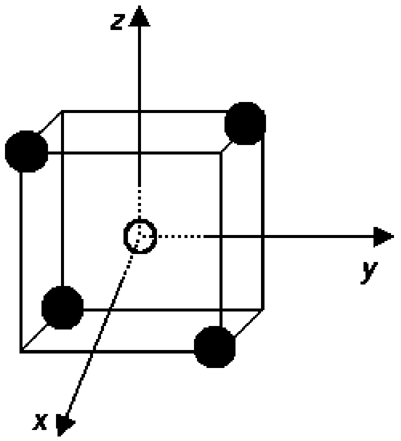

Figure 1.14.: Coordinate system for a tetrahedral complex ML_4 located in the cube.

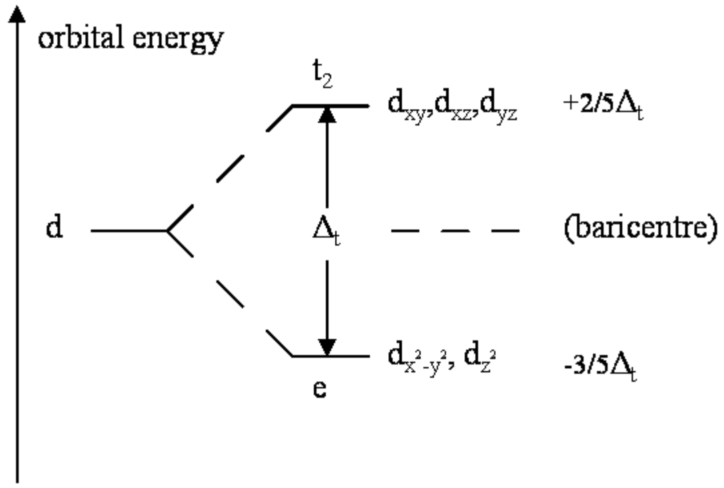

Figure 1.15.: Splitting of the metal *d*-orbitals in a tetrahedral transition metal complex.[9] (Δ is splitting energy.)

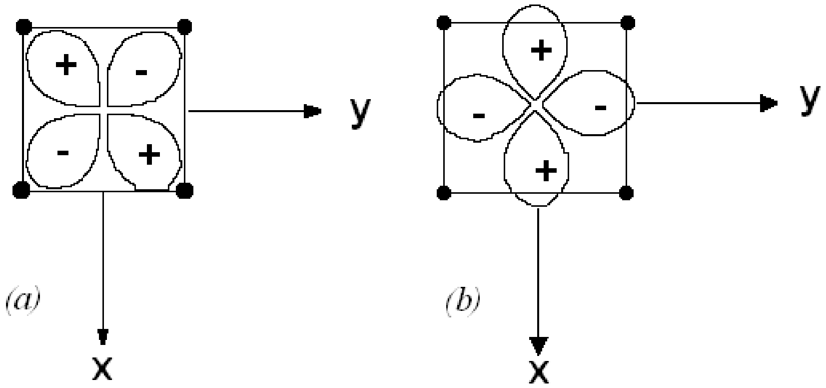

Figure 1.16.: Planar view of the *d*-orbitals $d_{x^2-y^2}$ and d_{xy} in relation to the tetrahedral array of ligands. (a) $d_{xy}(t_2)$, (b) $d_{x^2-y^2}$ (e).[9]

1.2.2.3. Variation of the splitting energy Δ

The orbital splitting parameter Δ (*D*) varies with some factors:

- Coordination number of metal ion

The size of Δ reflects the number of ligands perturbing the *d*-orbitals. For a metal ion M, ligand L and a constant distance between them M−L, the orbital splitting that occurs in a tetrahedral complex ML_4 will be less than in an octahedral complex ML_6. According to the elementary point charge / dipole model, the splittings are related by $\Delta_t = -4/9\Delta_o$.

- Oxidation state of the metal ion

For a given transition element and a ligand, Δ increases with the oxidation state of the metal.

- Location of the transition element in the subgroup

For a complex from any coordination type, with a given ligand and a constant formal charge on the metal ion, Δ increases on going down the column in the transition metal block (3*d*<4*d*<5*d*). The complexes of the 2nd and 3d transition series have higher tendency to be low spin than those of the 1st row metals.

- The nature of the ligands

The values of the splitting energy Δ from $d - d$ spectra depend on the ligand involved. Its magnitude varies with the ligand according to the sequence from the spectrochemical series: CO >CN^- >H^- ∼$[CH_3]$ ∼$[C_6H_5]^-$ >$[NO_2]^-$ >bpy ∼phen >en >NH_3 >py >$[NCS]^-$ >OH_2 >O^{2-} ∼$[ox]^{2-}$>OH^- >urea >F^- >$[N_3]^-$ >$[NO_3]^-$ > Cl^- >$[SCN]^-$ >S^{2-} >Br^- >I^-. (bpy — 2,2′–bipyridine, phen — 1,10–phenanthroline, en — ethylenediamine, py — pyridine, ox — oxalate)
According to the position in this series the ligands can be strong or weak.[7,9]

1.2.2.4. High spin and low spin complexes

Octahedral complexes, involving the particular electron configurations d^4, d^5, d^6 and d^7 have alternative ground states, depending on the strength of the ligand field. In relatively weak ligand fields such complexes may be more stable if the e_g orbitals are populated sufficiently to secure the optimal spin configuration (with maximum *S*) as in the free ion. The energy needed to promote one or two electrons from the t_{2g} level to e_g may be more than recovered through the reduction in inter-electronic repulsion occasioned by increasing the number of pairs of electrons with parallel spins. Those complexes of d^4—d^7 ions that display the maximum possible spin *S* in their ground states are described as high-spin. The effective moment (μ_{eff}) depends on the spin state of the metal centre. Its variation at ambient temperature among low-spin octahedral complexes from the 1st transition series is in Fig. 1.17 and among high-spin complexes: in Fig. 1.18 (calculated and experimental values of μ_{eff} for high-spin ions in octahedral environments are shown in Table 1.5 on p. 25).

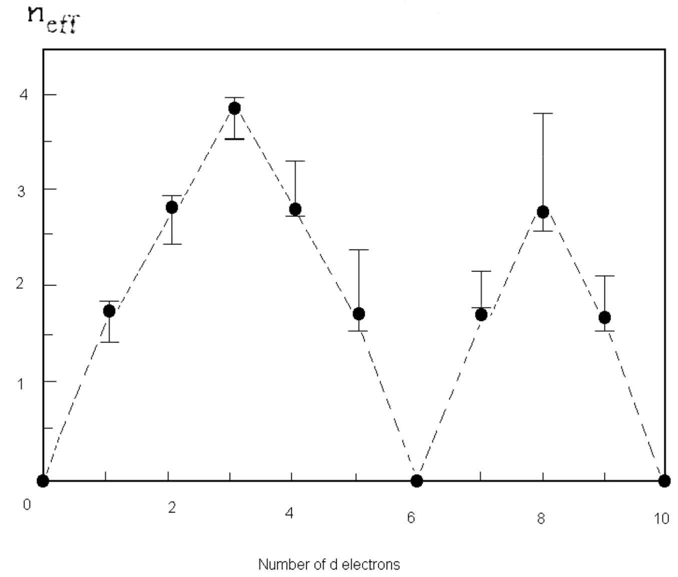

Figure 1.17.: μ_{eff} ($= n_{\text{eff}}$) data (300 K) for octahedral complexes of the 1st row transition elements low spin in the case of $d^4 - d^7$, compared with the predictions (•) of the spin-only formula[9] (spin-only values $n_{\text{eff}} = g_e \left[S\left(S+1\right)\right]^{\frac{1}{2}} = \mu_{\text{eff}}/\mu_B$).

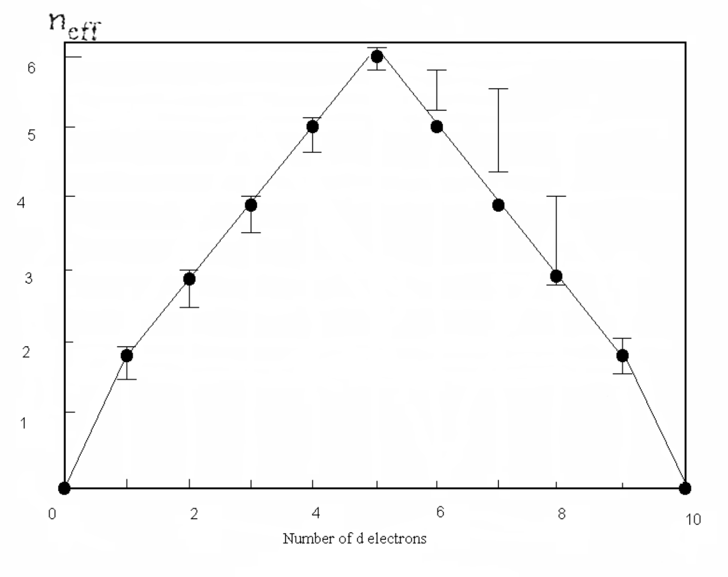

Figure 1.18.: μ_{eff} ($= n_{\text{eff}}$) data (300 K) for octahedral complexes of the 1st row transition elements high-spin in the case of $d^4 - d^7$, compared with the predictions (•) of the spin-only formula[9] (spin-only values $n_{\text{eff}} = g_e \left[S\left(S+1\right)\right]^{\frac{1}{2}} = \mu_{\text{eff}}/\mu_B$) (for the values see Table 1.5 on p. 25).

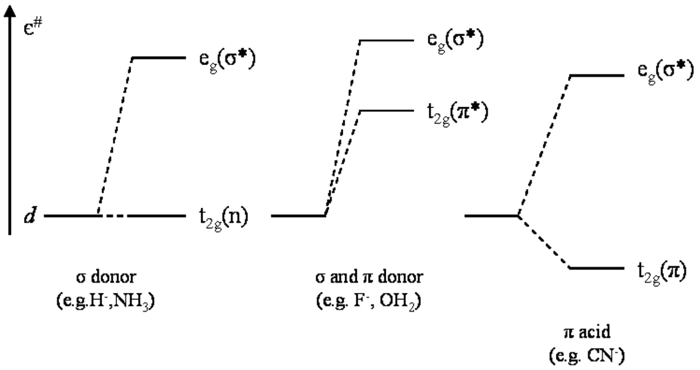

Figure 1.19.: The relative energies of the frontier orbitals of octahedral complexes with different types of ligand.[9]

1.2.3. Molecular orbital theory

The crystal field theory explains successfully many of the properties of the transition elements, especially the magnetic ones but it has some limitations. Other bonding models such as molecular orbital theory can be used for understanding the properties and to explain the orbital splitting Δ. From LCAO—MO (linear combination of atomic orbitals — molecular orbital) point of view, the splitting of the *d*-orbitals is due to covalent bonding between the metal centre and the ligands. This bonding is explained by the molecular orbital theory. The perturbed metal *d*-orbitals of crystal field theory, polarised by the electrostatic field of the point-charge or dipole are substituted by *anti*-bonding MOs which have ligand valence orbital character. The ligands possess valence orbitals of both σ and π type relative to the metal-ligand axes; in such way the bonding is mediated by σ- and π- orbital overlap (σ is larger in most situations). The metal-ligand π bonding involves the transfer of electron and the spectrochemical series, shown above (p. 17), can be interpreted in terms of the σ donor and π donor/acceptor characteristics of the ligands. Depending on the type of their valent orbitals, the ligands can be classified in three categories:

- Purely σ donor ligands (H^-, NH_3);
- Ligands which are σ and π donors (F^-, OH_2);
- π acid (acceptor) ligands (CN^-, bpy, C_6H_6);

The frontier energy levels for octahedral complexes in the different cases are shown in Fig. 1.19. Here follow some basic magnetic fundamentals and theories which were applied in the study of the magnetic properties in this work[‡].

1.2.4. Magnetic phenomena and classification of magnetic materials

There are three principal classes of magnetic materials: diamagnetic, paramagnetic and ordered materials.

[‡] Some basic magnetic definitions and units can be found in Appendix B, p. 181.

Since the magnetization is due to the response of the current loops to the applied magnetic field, which tends to orientate their associated magnetic moments in its direction, the magnetization is positive (for all cases except diamagnetism), as is the susceptibility χ, and the associated field augments the applied field within the sample. This positive magnetization takes various forms, which differ with regard to magnitude and its dependency on temperature and the strength of the applied magnetic field. Classification of main types of magnetic materials is shown in Table 1.3.

Table 1.3.: Summary of different types of magnetic behaviours.[88]

Magnetism	Nature / Origin	Temperature variation
Diamagnetism	closed shell system	
☐ normal diamagnet	compensated spin	Temperature invariance
☐ superconductor		→ to diamagnet above T_C
Paramagnetism	isolated spin system	
☐ normal paramagnet	temperature disorder of isolated spin	Curie (Weiss) law
☐ temperature-independent paramagnetism	low-lying excited states	Temperature invariance
☐ spin crossover system	spin transition	→ to high spin above T_C
☐ dimmers and clusters	exchanged coupled spins	continuous variation
☐ Pauli paramagnetism	field induced band shift	small variation
☐ superparamagnetism	temperature disorder of small ferromagnetic particles	
Ferromagnetism	spontaneous spin ordering	
☐ collinear ferromagnet	complete alignment of spins	→ to paramagnet above T_C
☐ asperomagnetism	random ferromagnet	
☐ helimagnetism	crystalline asperomagnetism	
☐ modulated structures	sine modulation	
☐ itinerant ferromagnetism	electron delocalisation	
☐ metamagnetism	field-induced spin flop	
☐ incipient ferromagnetism		
Antiferromagnetism	spontaneous spin compensation	

Continued on next page

Magnetism	Nature / Origin	Temperature variation
☐ collinear antiferromagnet	complete compensation	→ to paramagnet above T_N → to ferromagnet above H_C
☐ speromagnetism	random antiferromagnet, concentrated spin glass	
Ferrimagnetism	incomplete spin compensation	
☐ collinear ferrimagnet	partial spin compensation	→to paramagnet above T_C
☐ sperimagnetism	canted ferrimagnetism, random ferrimagnet	
Spin glasses	random, frozen-in structural disorder	
Mictomagnetism	cluster glass	

1.2.4.1. Diamagnetism

If the intensity of magnetization is negative, the material is said to be diamagnetic. Such a material, when placed in an inhomogeneous magnetic field will tend to move to the region of lowest field or the sample is simply repelled by the magnetic field. Diamagnetism is a property of all matter, and arises from interaction of paired electrons with magnetic field. It reflects the fact that the ground state is of a single spin multiplicity and there are not thermally populated states of higher spin multiplicity. The molar susceptibility of a diamagnetic material is negative and usually very small, of the order –1 to 100×10^{-6} $\mathrm{cm^3mol^{-1}}$ and this of weak diamagnetic materials has values close to zero (Fig. 1.20). Diamagnetic susceptibility does not depend on applied field strength and usually is independent of temperature (Fig. 1.21). The susceptibility of such atoms in molecules is additive and this is of use in estimating the diamagnetic susceptibilities of ligand atoms and counter-ions in a transition metal complexes. Empirical formulas have been proposed to estimate its value. It can be calculated either from atomic susceptibilities and constitutive corrections, or from group susceptibilities (ligand or counter-ion). The constitutive corrections are generally positive.

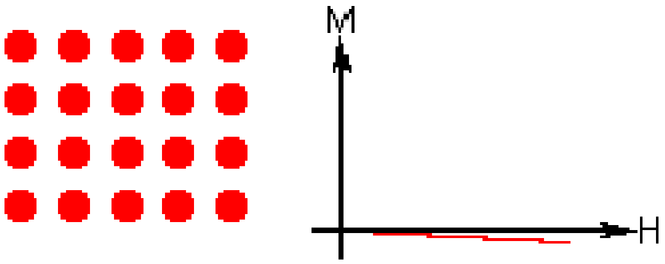

Figure 1.20.: Diamagnetic behaviour. (The atoms have not magnetic moments.)

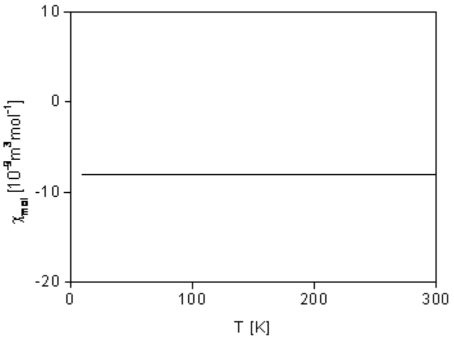

Figure 1.21.: Temperature behaviour of magnetic susceptibility for normal diamagnets.[88]

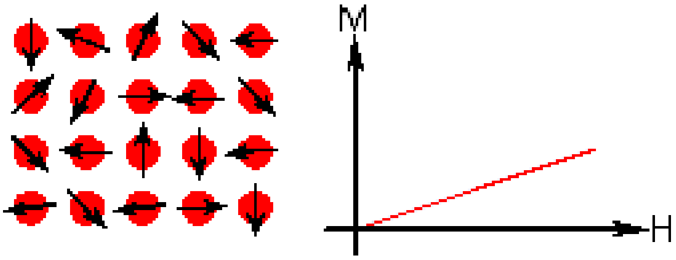

Figure 1.22.: Paramagnetic behaviour. (The ions have randomly oriented magnetic moments.)

They account for the fact that a molecule with multiple or conjugated bonds is less diamagnetic than a similar molecule with only single bond.

A lot of work of establishing the additivity of atomic susceptibilities was carried out by Pascal and the quantities are commonly referred to as Pascal's constants.[8] He applies values for neutral atoms. For more complicated molecules, particularly when aromatic rings are present, it is more convenient to measure the susceptibility of the ligand either free, or complexed with diamagnetic metal. The following equation can be used:

$$\chi^D = kM \times 10^{-6}\mathrm{cm}^3\mathrm{mol}^{-1}, \tag{1.1}$$

where M is the molecular weight of the compound and k is a factor between 0.4 and 0.5.[8] For instance, in order to estimate the underlying diamagnetism in paramagnetic metal complexes such as Mn(II) and Cu(II), their diamagnetic analogues Mg(II) and Zn(II) can be measured.

Some substances with diamagnetic behaviour can switch to the paramagnetic state when the temperature is increased and such systems are called spin-crossover.

1.2.4.2. Paramagnetism

The intensity of magnetization of a paramagnet is positive (see Fig. 1.22) and such material tends to move to regions of maximum field strength in an inhomogeneous magnetic field or in other words the sample is attracted by the applied magnetic field. The paramagnetics have a positive magnetic susceptibility which follows the Curie law at high temperature. It is generated by impaired electrons without correlation between each other. In other words, the ensemble of ions or molecules possesses only spin or orbital angular momentum in their ground state and do not interact magnetically. This might be a fluid material or a crystal containing well separated open-shell ions. It is assumed that no excited electronic state is thermally accessible. The values of χ_{M} are in the range 100 to $100000 \times 10^{-6}\mathrm{cm}^3\mathrm{mol}^{-1}$. These susceptibilities do not depend on the strength of the magnetic field, but depend on the temperature. In fact, paramagnetism is a consequence of the interaction of orbital and/or spin angular moments of unpaired electrons with the applied field. The spin state is determined by measurement of bulk susceptibility, a basic first step in the electronic characterization of new synthesized compounds.

Curie law The tendency for angular momentum to be aligned parallel with the field direction is in competition with the thermal disorder. It means that the higher the temperature (the higher the thermal disorder), the lower the degree of alignment and the susceptibility drops inversely with temperature. This law is fundamental to most considerations of the magnetic properties of atomic systems. The simplest magnetic behaviour (as in gaseous O_2), is reciprocal dependency on temperature as shown in Equation 1.2, known as the Curie law.

$$\chi_m = \frac{C}{T} \tag{1.2}$$

The parameter C, the Curie constant (unit = K), is characteristic of the atomic or molecular species and depends on the spin multiplicity of the ground state. The law was proposed in 1910 from experimental data before the introduction of quantum mechanics and can have the form:

$$\chi = \frac{N g_J^2 \beta^2}{3 k_B T} J\left(J+1\right), \tag{1.3}$$

where:

N — number of Avogadro; $N = 6.022 \times 10^{23}$ mol^{-1}

g_J — g-factor (Landé factor), $g_J = 3/2 + \left[S\left(S+1\right) - L\left(L+1\right)\right]/2J\left(J+1\right)$;

β or μ_B — electronic Bohr magneton; $\beta = 9.27 \times 10^{-21}$ erg.T^{-1} (in *cgs emu* system), $\beta = 9.27 \times 10^{-24}$ J.T^{-1} (in SI system)

k_B or k — Boltzman constant; $k_B = 1.38 \times 10^{-16}$ erg.K^{-1} (in *cgs emu* system), $k_B = 1.38 \times 10^{-23}$ J.K^{-1}

T — temperature

J — total angular moment

S — spin quantum number

L — orbital quantum number;

In the *cgs emu* system $N\beta^2/3k$ is equal to 0.12505 cm^{3}mol^{-1}. Sometimes magnetic susceptibility data are given in the form of the temperature dependence of so called effective

Table 1.4.: Quenching of the orbital contribution to the magnetic moment, due to the ligand field.[89]

		Stereochemistry					
		Octahedral			Tetrahedral		
N° of *d*-electrons	Free ion ground term	$t_{2g}^n e_g^m$ ground configuration	Ligand field ground term	Quenching of orbital contribution (if expected)	$t^n t_2^m$ ground configuration	Ligand field ground term	Quenching of orbital contribution (if expected)
1	^2D	t_{2g}^1	$^2T_{2g}$	No	e^1	^2E	Yes
2	^3F	t_{2g}^2	$^3T_{1g}$	No	e^2	$^3A_2$	Yes
3	^4F	t_{2g}^3	$^4A_{2g}$	Yes	$e^2t_2^1$	$^4T_1$	No
		—	—	—	e^3	E_2	Yes
4	^5D	$t_{2g}^3e_g^1$	^5E_g	Yes	$e^2t_2^2$	$^5T_2$	No
		t_{2g}^4	$^3T_{1g}$	No	e^4	$^1A_1$	Yes
5	^6S	$t_{2g}^3e_g^2$	$^6A_{1g}$	Yes	$e^2t_2^3$	$^6A_1$	Yes
		t_{2g}^5	$^2T_{2g}$	No	$e^4t_2^1$	$^2T_2$	No
6	^5D	$t_{2g}^4e_g^2$	$^5T_{2g}$	No	$e^3t_2^3$	^5E	Yes
		t_{2g}^6	$^1A_{1g}$	Yes	$e^4t_2^2$	$^3T_1$	No
7	^4F	$t_{2g}^5e_g^2$	$^4T_{1g}$	No	$e^4t_2^3$	$^4A_2$	Yes
		$t_{2g}^6e_g^1$	^2E_g	Yes	—	—	—
8	^3F	$t_{2g}^6e_g^2$	$^3A_{2g}$	Yes	$e^4t_2^4$	$^3T_1$	No
9	^2D	$t_{2g}^6e_g^3$	^2E_g	Yes	$e^4t_2^5$	$^2T_2$	No

magnetic moment μ_{eff}, defined as:

$$\mu_{\text{eff}} = \left(3kT\chi/N\beta^2\right)^{1/2} = \sqrt{J\,(J+1)}\beta \tag{1.4}$$

Sometimes the angular magnetic moment can be quenched and it does not contribute to the measured magnetic moment of an open-shell system. So, the observed magnetic moment of an open-shell molecule, or ion in a crystal lattice is due mainly to spin-only values. In this case, when the $^{2S+1}\Gamma$ ground state has no first-order angular momentum and has a large separation in energy from the first excited states so that any coupling between ground and excited states can be neglected (L is quenched), J is replaced in Equation 1.3 by S, and g_J — by the factor for free electron g_e = 2.0023. In Table 1.4 is shown when such quenching can be considered for different ground states. Values of magnetic moment for different metal ions are in Table 1.5. The first order spin orbit coupling has effect in paramagnetic properties, especially in their temperature dependence and in the zero-field splitting. The effective magnetic moment, arisen from the respective ground term (see Table 1.4) of transition metal complex ions, is often presented graphically as a function of temperature. The obtained curves make possible to compare the results of measurements of the magnetic susceptibility of powder or crystal specimens over a range of temperature with the existing theories. The mononuclear complexes with or without first-order angular momentum can be theoretically treated in different degrees of complexity and various theoretical models

Table 1.5.: Comparison of experimental room temperature magnetic moments with those calculated within the ground terms for octahedral symmetry. Experimental data (a) for aqueous ions (Pauling, 1940), (b) typical values for octahedral coordination. $\mu = \mu_{\text{eff}}$.[90]

Ions	μ spin-only	μ calc.	μ exp. (a)	μ exp. (b)
d^1: V^{4+}, Ti^{3+}	1.73	1.95	—	1.9–1.9
d^2: V^{3+}	2.83	2.72	3.8–3.9	2.7–2.9
d^3: V^{2+}, Cr^{3+}	3.87	3.87	4.8–4.9	3.8–3.9
d^4: Cr^{2+}, Mn^{3+}	4.90	4.90	4.8–4.9	4.8–4.9
d^5: Mn^{2+}, Fe^{3+}	5.92	5.92	5.9	5.8–5.9
d^6: Fe^{2+}	4.90	5.64	5.3	5.2–5.5
d^7: Co^{2+}	3.87	4.67	5.0–5.2	4.8–5.1
d^8: Ni^{2+}	2.83	2.83	3.2	2.8–3.3
d^9: Cu^{2+}	1.73	1.73	1.9–2.0	1.8–2.0

can be distinguished and applied for the fitting of experimental results. Such models are those of Van Vleck,[8,9,90,91] Kotani,[9,92] Griffith,[90] Këning and Kremer,[93–96] Figgis *et al.*[97–101]

The most convenient way to establish experimentally that a compound obeys the Curie law is to obtain a horizontal straight line on the χT *vs.* T plot (Fig. 1.23). Normal paramagnets are organic radicals, transition metal complexes and lanthanide compounds. As the p-block elements may have a maximum of 3 unpaired electrons, d-block — 5 and f-block — 7, these numbers determine the normally attainable spins. The clear condition for the high spin state is that the unpaired electrons occupy orthogonal orbitals; in the opposite case the pairing occurs. Some organic radicals can keep their spin even after combination with metal centres. Under certain circumstances the spin state of the central metal atom can be increased by ligand radicals. Ideal paramagnets obey the Curie law. This law implies that the function $\chi^{-1} = f(T)$ (Fig. 1.24) is a straight line intercepting zero and that the function (χT)=$f(T)$ is linear with value of the Curie constant (Fig. 1.23). Deviations from the Curie law may originate in:

- Zero-field splitting
- Orbital contribution to the angular momentum
- Presence of exchange interactions
- Long range ordering (effective molecular field approximation)

Brillouin theory The Curie law is valid only when H/kT is small enough. In this case the macroscopic molar magnetization is linear in field H. When H/kT is large, it is calculated by the sum of the miscroscopic magnetizations according to Boltzman distribution law. After mathematical transformations, the molar magnetization can be expressed by Equation 1.5, where $g_J \beta J B_J(y)$ is the mean molecular or atomic magnetic moment induced in the field direction. $B_J(y)$ is the Brillouin function (see Equation 1.6). In this Equation $y = Jx =$

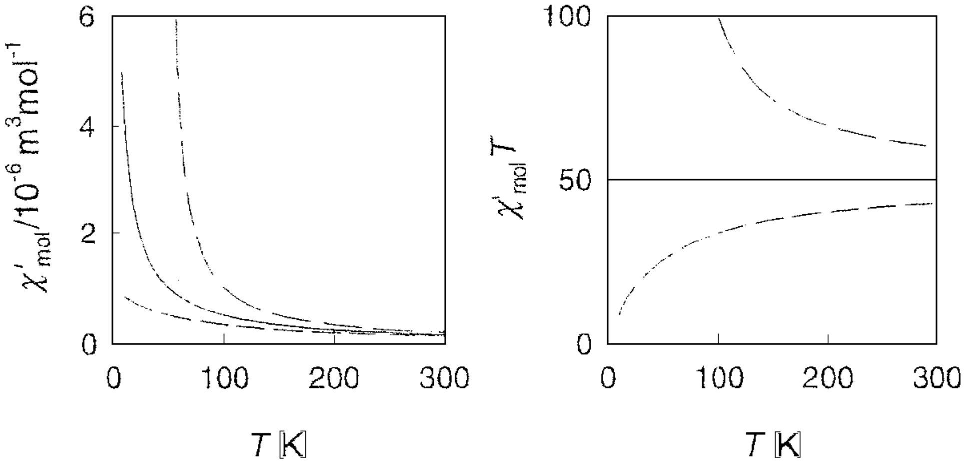

Figure 1.23.: Temperature behaviour of a paramagnet compared with the behaviour of ferro- and antiferromagnet: solid — the perfect Curie law; long dashed — a ferromagnetic interaction ($\Theta > 0$); short dashed — an antiferromagnetic interaction ($\Theta < 0$).[88]

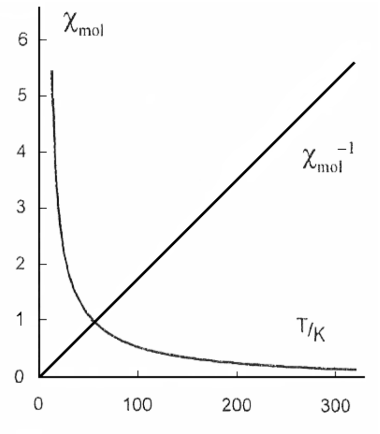

Figure 1.24.: Molar susceptibility scheme of a paramagnet.[9]

$g_J\beta JB/kT$.

$$M = N_A g_J \beta J B_J\left(y\right) \tag{1.5}$$

$$B_J\left(y\right) = \frac{2J+1}{2J}\coth\left[\frac{2J+1}{2J}y\right] - \frac{1}{2J}\coth\left[\frac{y}{2J}\right] \tag{1.6}$$

This can be rewritten with introducing the μ_{eff} as:

$$\mu_{\text{eff}} = \mu_B g_J \sqrt{J(J+1)} \tag{1.7}$$

The saturation limit $M_{sat} g_J \beta J B_J\left(y\right)$ is confirmed by the fact that $\coth y \rightarrow 1$, therefore $B_J\left(y\right) \rightarrow 1$ when $y \rightarrow \infty$. The Brillouin function is a function that arises in the calculation of the magnetization of an ideal paramagnet. This function describes the dependency of the magnetization M on the applied magnetic field H and the total angular momentum quantum number J of the magnetic moments of a material. The variations of M in $N\beta$ units

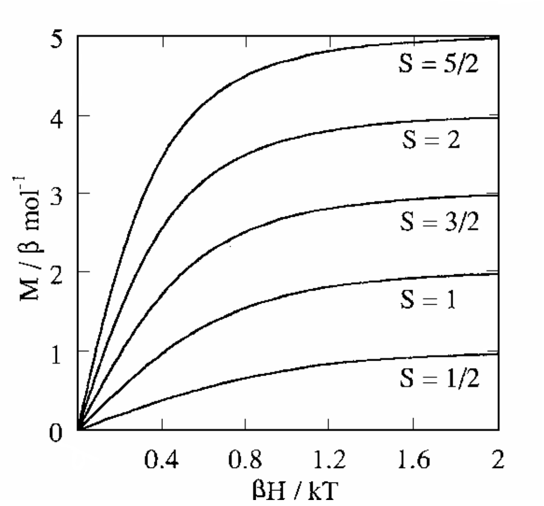

Figure 1.25.: Magnetization M in $N\beta$ units *vs.* $\beta H/kT$ plots for molecules with a $^{2S+1}\Gamma$ ground state. The g-factor is taken equal to 2.[8]

for $g = 2$ and different values of S, when there is no first-order angular momentum or coupling between ground and excited states, are shown in Fig. 1.25.

Other kinds of paramagnetism Sometimes a different, weak form of paramagnetic is observed in metals. This is known as Pauli paramagnetism and is independent of temperature. It is due to itinerant electrons that promote metallic conductivity. An applied field induces marginal spin polarisation of the electrons resulting in small positive magnetization.

In addition to the temperature-independent diamagnetism, any substance possesses a temperature-independent paramagnetism (TIP). Experimentally TIP is attainable in high temperature limit and is estimated only for some typical cases. As an example, is accepted that each Cu(II) centre in a complex/cluster brings the value of $\chi_{\text{TIP}} = 0.75 \times 10^{-9}$ m^3/mol.[88] TIP becomes substantive when the system has close lying states, which is frequent in metal complexes.

1.2.4.3. Superparamagnetism

Superparamagnetism is a result of magnetic anisotropy[§]. For instance, the preferred direction for magnetite is [111]. If a sufficient energy is applied to the system, the magnetism can be reversed along these axes. The relaxation time τ is the time required for spin reversal. It depends on the energy barrier ΔE, which is function of particle size, between the two directions of the spin and the temperature (see Equation 1.8; V is the particle volume, K_{eff} — anisotropy constant). Iron oxides with size < 10 nm exhibit often superparamagnetism at room temperature.

$$\tau = \tau_0 exp\left(\Delta E/k_B T\right), \Delta E = K_{\text{eff}} V \tag{1.8}$$

[§] Existence of preferred crystallographic directions along which the spins are easily aligned and the material is more easily magnetized.

If the temperature is decreasing, τ increases and the superparamagnetic relaxation is counteracted. Below a temperature, called blocking (T_B; Equation 1.9), the thermal excitation is insufficient and the magnetic particles are ordered.

$$T_B = K_{\text{eff}} V / 25 k_B \tag{1.9}$$

In principle superparamagnetism occurs when the material is composed of very small crystallites (1–10 nm). The smaller the crystallite size, the smaller its anisotropy energy barrier and the lower the temperature at which the material becomes superparamagnetic.

1.2.4.4. Cooperative and ordered magnetism; magnetic interactions

The magnetically ordered materials include the numerous classes of the ferromagnetics and the anti-ferromagnetics. The incomplete compensation of the magnetic moments occurs in ferrimagnetics. The temperature behaviour of magnetization in these materials is complex. There are several other classes of ordered materials where the spatial distribution of the microscopic magnetic moments is more complex.

In summary, the paramagnetic centres in "magnetically diluted" compound[¶] are quite independent of one another because they are separated by a distance of many Angström units (Å) by diamagnetic atoms, which are not capable of transmitting magnetic effects between them. Thus the properties of the system are sum of those for each of the centres. If the behaviour of adjacent magnetic centres is not independent, the compound is said to be "magnetically concentrated" and its magnetic behaviour is determined by the nature of the interactions between centres. In this case the magnetic properties of the system are not sum of the properties of the individual centres. Such compounds exhibit magnetic exchange. Many systems such as oxides and halides are magnetically concentrated, where the electron spins on adjacent paramagnetic centres are strongly coupled to each other. This coupling between the spins is ferromagnetic when the spins are aligned parallel. When the spins are aligned anti-parallel, the coupling is antiferromagnetic.

There is a large number of polynuclear transition metal complexes which are intermediate systems between magnetically diluted and magnetically concentrated. In those systems the exchange interactions take place over small number of paramagnetic centres. The types of exchange interactions are summarised in Table 1.6. Principle types of behaviour of magnetic interaction are ferromagnetism, antiferromagnetism, and ferrimagnetism. At ordinary temperature most of the metals are diamagnetic, paramagnetic or antiferromagnetic, except the ferromagnetic Fe, Co, Ni and Gd.

[¶] When the magnetic behaviour of an individual paramagnetic atom is independent of that of its neighbours, the compound is called magnetically dilute. The magnetic behaviour is determined by a thermal distribution among available states.

Table 1.6.: Types of exchange interaction.[88]

Type	Nature
Direct exchange	Coupling of localized magnetic moments in insulators through space
Superexchange	Coupling of localized magnetic moments in insulators through diamagnetic groups
Indirect exchange	Coupling of localized magnetic moments in metals with the conduction electrons
Itinerant exchange	Coupling of itinerant electrons in metals
Double exchange	Coupling in two localized magnetic moments through an itinerant electron

Curie-Weiss law In case of intermolecular interactions, after some modifications[8] in order to account for weak intermolecular interactions, the Curie law (Equation 1.2, p. 23) becomes:

$$\chi = \frac{C}{T - \Theta}, \tag{1.10}$$

which is known as the Curie-Weiss law. C is the Curie constant, Θ is Weiss temperature (or Weiss constant) defined by Equation 1.11, where z is the number of nearest neighbours around a given magnetic molecule in the crystal lattice, J is interaction parameter (exchange energy coupling constant) between two nearest neighbours magnetic species. According to whether J is positive or negative, the intermolecular interaction is said to be ferromagnetic or antiferromagnetic, respectively.

$$\Theta = \frac{zJS\left(S+1\right)}{3k}, \tag{1.11}$$

1.2.4.5. Ferromagnetism

Ferromagnetism is observed when the the electron spins tend to align parallel to each other (Fig. 1.26). The susceptibility obeys a Curie-Weiss law with positive Θ (Figs. 1.23, 1.27 and Equation 1.10). Ferromagnetic substances have an overall net spontaneous magnetic moment below a critical temperature (Curie temperature, T_C), large magnetic permeability and large positive susceptibility. As the temperature is decreased, the susceptibility follows an abrupt, very large increase (Fig. 1.27 (c)). The point at which $\partial\chi/\partial T$ is maximum is called the Curie temperature, T_C. T_C is characteristic for any material. Below T_C, the susceptibility becomes field dependent. At T_C the bulk magnetization of the solid switches from paramagnetic to ferromagnetic type with increase in the susceptibility. The existence of exchange interactions implies that the Curie-Weiss law is obeyed and the Curie constant differs from the spin-only formula. The ordering can be described by the molecular field theory.[88] A

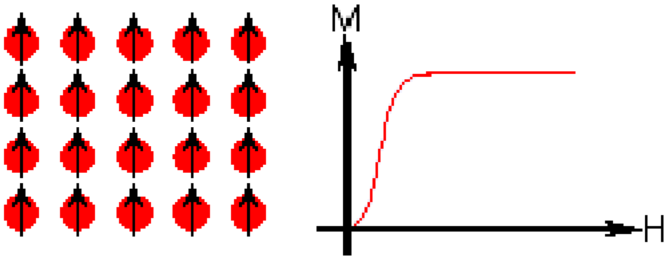

Figure 1.26.: Ferromagnetic behaviour. (The atoms have parallel aligned magnetic moments.)

ferromagnetic substance may be demagnetized by heating above its T_C (see Fig. 1.27).

Materials which display ferromagnetism are usually transition (Fe, Co, Ni, etc.) and some rare-earth (Gd) metals. Such materials display magnetic hysteresis (explained below) as characteristic.

1.2.4.6. Antiferromagnetism

Antiferromagnetism arises if the magnetic vectors of neighbouring centres tend to couple antiparallel magnetic moments. The antiparallel configuration is repeated throughout the lattice (Fig. 1.28). An antiferromagnet have zero overall magnetic moment, positive permeability and small positive susceptibility. In an isotropic solid, where there are equivalent interpenetration sub-lattices with oppositely directed dipoles, this would give a diamagnetic susceptibility at 0 K. When a magnetic field of moderate force is applied, most of the dipoles tend to orientate in the field direction, while the minority of them are oppositely directed. The coupling between the two sets is stronger than interaction of any dipole with the field. The increasing of the temperature will tend to randomize the alignment and the susceptibility rises (the antiparallel ordering is destroyed) to a maximum at the Néel point T_N (Fig. 1.29). Above T_N the thermal energy available to the system is sufficient to overcome the aligning forces resulting in a usual paramagnetic behaviour with negative deviation from the Curie-Weiss law (see Equation 1.10 on p. 29) giving rise to negative Weiss constant Θ. Below T_N the susceptibility is only weakly field-dependent. In the same figure can be seen that the magnetic susceptibility depend on the temperature and the plot $1/\chi$ *vs.* T will give a straight line which intercepts the temperature axis at $-\Theta$.

The antiferromagnetic interactions can be divided in two groups: one when the exchange occurs between centres in the same molecule which is intramolecular antiferromagnetism (or exchange direct interactions) and one when the exchange interactions extends over many centres in a crystal lattice — this is intermolecular antiferromagnetism (or superexchange). Usually polynuclear transition metal complexes are in the first group and the halides and oxide systems belong to the second one. The difference is that the maximum in the susceptibility is much broader in the case of intramolecular interactions and the magnetic susceptibilities are not usually dependent on the strength of the applied magnetic field. The intramolecular antiferromagnetism is associated with direct overlap between the

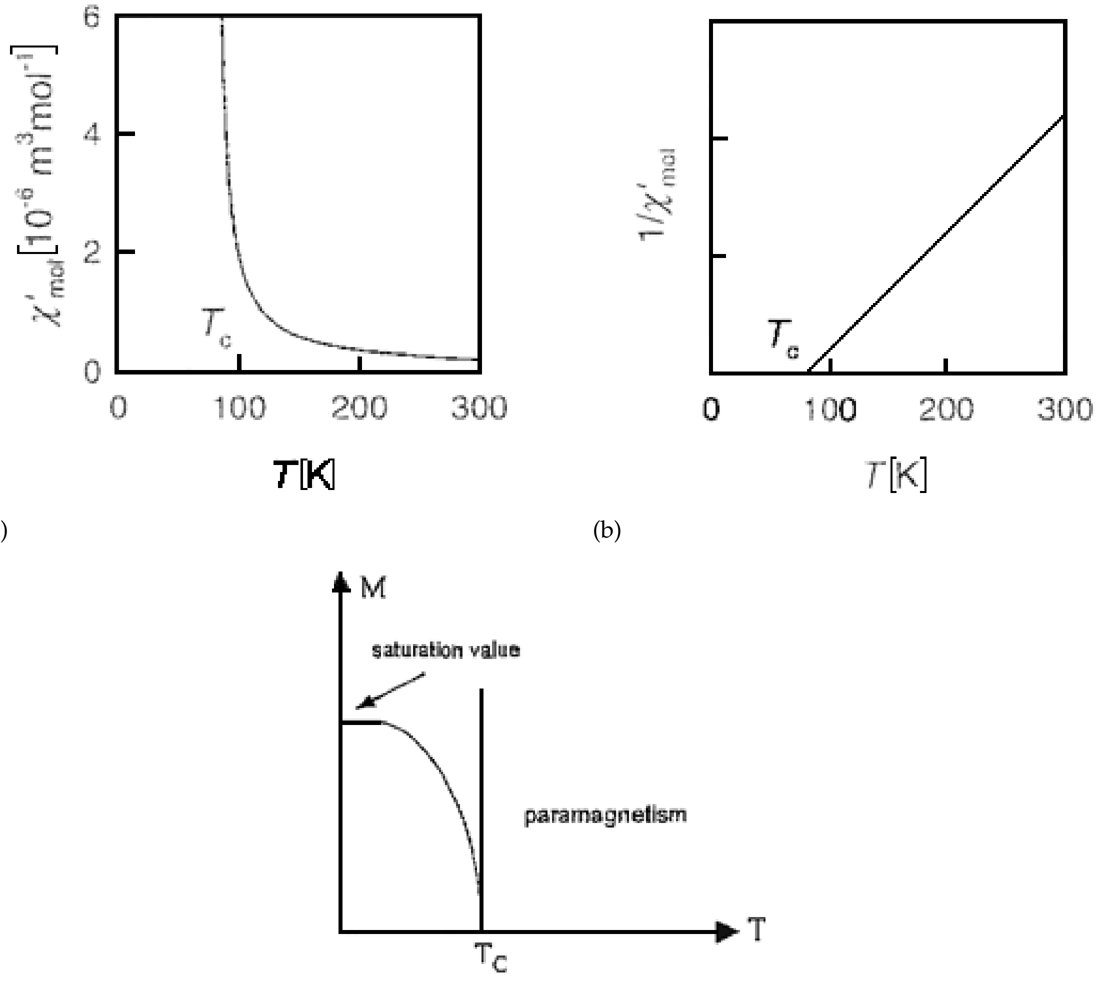

(a)

(b)

(c)

Figure 1.27.: Temperature behaviour of a ferromagnet.[9,88] (a) $\chi = f(T)$;[88] (b) $\chi^{-1} = f(T)$;[88] (c) $M = f(T)$. The switch from paramagnetism to ferromagnetism with decrease of temperature.[9]

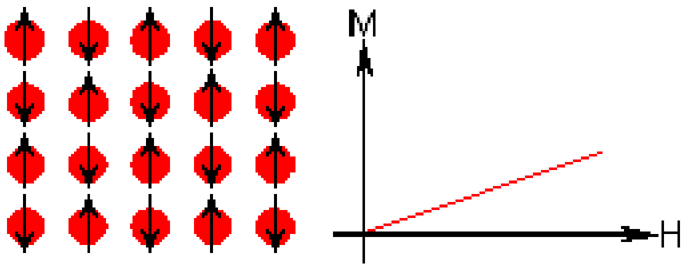

Figure 1.28.: Antiferromagnetic behaviour. (Atoms have mixed parallel and anti-parallel aligned magnetic moments.)

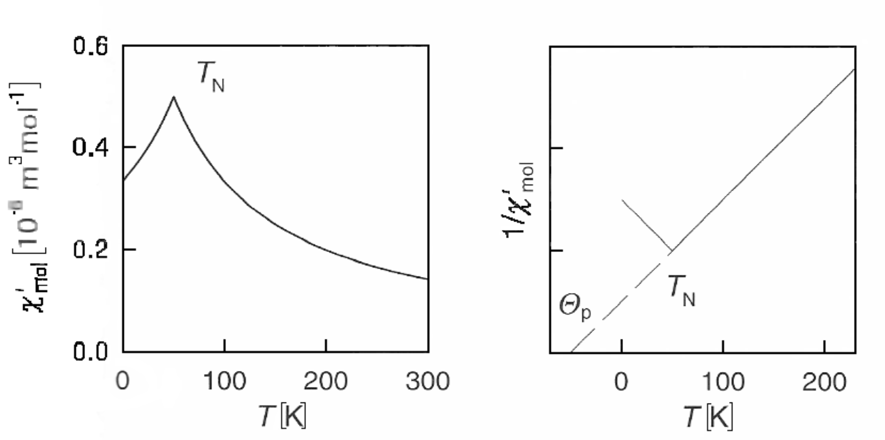

Figure 1.29.: Temperature behaviour of an antiferromagnet. (a) $\chi = \frac{C}{T+\Theta}$; (b) $\frac{1}{\chi} = \frac{1}{C}(T + \Theta)$. The paramagnetism ↔ antiferromagnetism transition (the maximum of χ at T_N is not usually so sharp);[88] $\Theta_p = C(W_f - W_a)$, $|\Theta_p| < T_N$.

orbitals of the magnetic centres with unpaired electrons, leading to mutual pairing in the ground state (metal-metal bonding). The second category is typical for structures with cubic bivalent transition metal oxide lattice where each atom is surrounded by six oxygen atoms, each of which transmits the magnetic interaction to another metal atom. The first category may be treated exactly by theory, the second may only be approached by approximate methods.

Superexchange The mechanism involves interaction of electrons of metal ions with opposite spins through diamagnetic anion (ligand). For a system $M^{n+}-O^{2-}-M^{n+}$ overlap occurs between each d-orbital of the metal and the (filled) p-orbital of the ligand. This gives partial electron density to the metal site (Fig. 1.30). The covalency has influence on T_N. T_N increases with the nuclear charge Z and with the atomic number of the 1st row transition series. T_N tends to be higher for M(III) compounds than those of M(II), and it is higher for oxides than for fluorides. The strength of exchange coupling through bridging ligands depend on the M−L−M bonding angle. The superexchange shown in Fig. 1.30 is weaker with diminishing of the orbital overlap when the bond angle is reduced to 90°. Superexchange leads more often to antiferromagnetic ordering and rarely to ferromagnetic interaction between cations. For configuration M−L−M the coupling is presented in Fig. 1.31.

An antiferromagnet can be viewed as a system composed of two interpenetrating sublattices. Each of them is uniformly magnetised with parallel spins, but the magnetizations of the sublattices are cancelled exactly. The total magnetization $\vec{M}_p$ in a molecular field approximation is the sum of the magnetizations $\vec{M}_A$ and $\vec{M}_B$ of the two sublattices A and B,

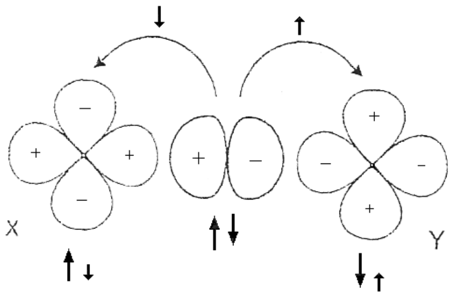

Figure 1.30.: A simple view of superexchange in a linear M−L−M system. The exchange is mediated by σ-bonding with p-orbitals on the bridging ligand.[9]

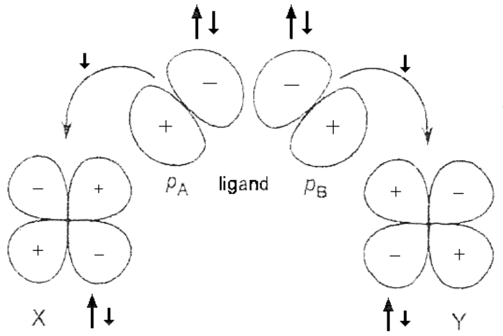

Figure 1.31.: Ferromagnetic coupling driven by covalency in a 90° M−L−M array. (The orthogonal ligand p_σ orbitals A and B are separated for clarity).[9]

respectively:

$$\begin{aligned} \vec{M}_p &= \vec{M}_A + \vec{M}_B = \\ &= \frac{C}{T}\left(\vec{H}_{ext} - W_f\vec{M}_p + W_f\vec{M}_A\right) + \frac{C}{T}\left(\vec{H}_{ext} - W_a\vec{M}_A + W_f\vec{M}_A\right) = \\ &= \frac{C}{T}\left[2\vec{H}_{ext} + \left(W_f - W_a/\vec{M}_p\right)\right], \end{aligned} \tag{1.12}$$

where $\vec{H}_{ext}$ is external applied magnetic field, W_a — negative field coefficient between the two sublattices (antiferromagnetic contribution $W_a > 0$) and W_f — positive field coefficient within each sublattice (ferromagnetic contribution $W_f > 0$). The form of the Curie-Weiss law for the temperature above T_N is in Equation 1.13, where the Weiss constant for the paramagnetic state is expressed by Equation 1.14.

$$\chi_{int} = \frac{\vec{M}_p}{\vec{H}} = \frac{2C}{T - \Theta_p}, (T > T_N) \tag{1.13}$$

$$\Theta_p = C\left(W_f - W_a\right), \left(\left|\Theta_p\right| < T_N\right). \tag{1.14}$$

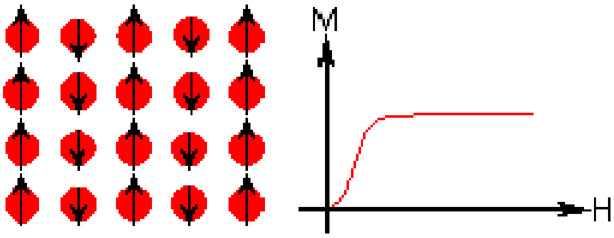

Figure 1.32.: Ferrimagnetic behaviour. (The ions have anti-parallel aligned magnetic moments of different intensities.)

1.2.4.7. Ferrimagnetism

This phenomenon can be seen in Fig. 1.32. When two or more magnetic lattices are not equivalent the compensation of magnetic moments is only partial. The spins alignment is still antiparallel. The different spins have unequal moments so that the net magnetic moment remains (ferromagnetic-like ordering remains) and the material is ferrimagnetic. The temperature variation of the magnetization near the transition temperature becomes very complex. A typical example for such material is magnetite Fe_3O_4. The temperature below which the substance orders ferrimagnetically is called ferrimagnetic Néel temperature T_{fN}.[88,102]

The temperature behaviour of a typical ferrimagnet is shown in Fig. 1.33. There is a non-linearity of the $1/\chi$ *vs.* T curve near the critical temperature. Above the ordering temperature the susceptibility obeys the following relationship (Néel hyperbole):

$$\frac{1}{\chi} = \frac{T + \Theta_p}{C} - \frac{\gamma}{T - \Theta}, \tag{1.15}$$

where C is the Curie constant and Θ_p and Θ determine the asymptotes, and are related to the interactions within and between the magnetic sublattices.

$\gamma = W^2 \frac{C_A C_B}{(C_A + C_B)^3} \left[C_A (1 + \alpha) - C_B (1 + \beta)\right]^2$, ($C = C_A + C_B$ is the mean value of the Curie constant of the assembly of $\mu_{(A)}$ and $\mu_{(B)}$ moments).

Domains and hysteresis loop The ferro- antiferro- and ferrimagnetic materials have domain structures. The particles of size 50–500 nm consist of single domains. The spins inside a domain could be parallel or antiparallel, but different domains have different spin orientation. When a high magnetic field is applied, the domains are eliminated. The stronger the applied field, the more domain spins are aligned. At high field the magnetization is saturated and the spin of all domains are parallel. Fig. 1.34 shows the plot of magnetization M *vs.* external field H (H_{ext}), which forms a hysteresis loop. Each part of it corresponds to magnetization or demagnetization. At zero field the spontaneous magnetization exists within domains of certain nuclearity and shape; the domains are orientated randomly and this brings compensation effect. With increasing the field, the magnetization rises from its spontaneous, zero-field value to a saturation limit M_S where all available spins are aligned

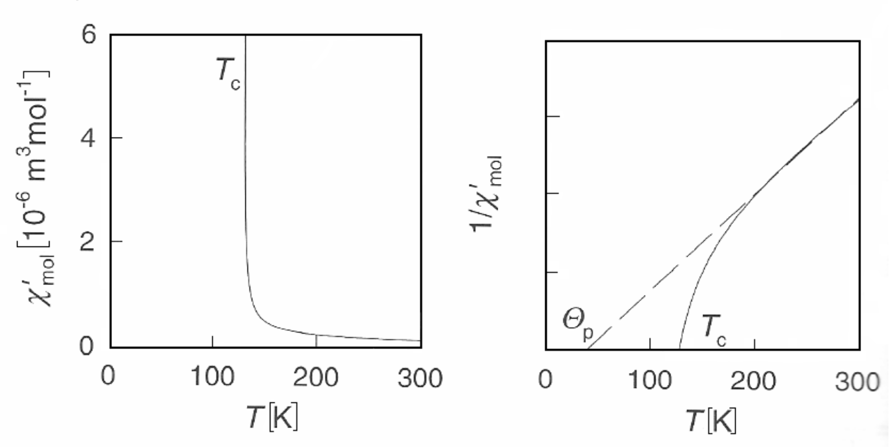

Figure 1.33.: Temperature behaviour of a ferrimagnet.[88]

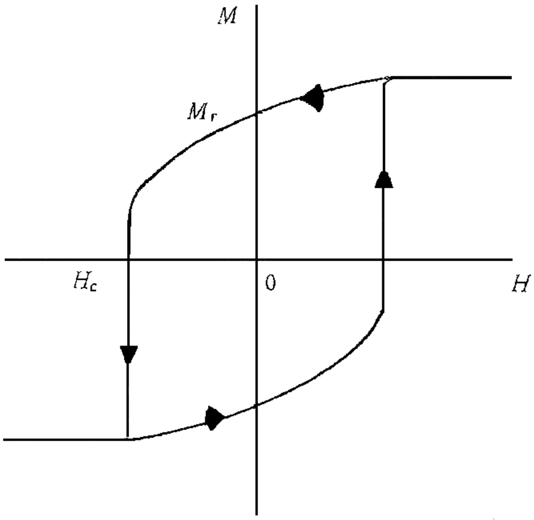

Figure 1.34.: Schematic magnetic hysteresis loop.[102]

with the field direction. With decreasing the field, the magnetization curve drops slightly and crosses the zero-field at the value of the remanent magnetization M_R. When a field of the opposite direction is applied, again the saturation value of magnetization — now with opposite sign — is reached. The reverse field needed to demagnetize a substance is called coercivity H_C, which is zero magnetization appearing at a positive field strength. Ferromagnetic or ferrimagnetic materials show generally remanent magnetization M_R after removing the applied field H. The magnetization curve $M(H)$ is irreversible, giving rise to this hysteresis loop (Fig. 1.34). The magnetic properties can be compared by the type and direction of the remanent magnetization strength; they can help the identification of the remanence carrier and the magnetic domain type of the particles. Ferromagnets, which display very low coercivity are named "soft" and can be easily distinct. Soft ferromagnets are iron and iron-based alloys (Fe/Si). The "hard" ferromagnets exhibit high coercivity and high remanent magnetization (e.g. alloys based on Fe with Co, Ni, etc.). They are not easily demagnetized.

Table 1.7.: Ground state of the d^n ions, n = 4 to 7, in octahedral environment.[8]

	$\Delta >>$P	$\Delta <<$P
d^4	$^3T_{1g}$	^5E_g
d^5	$^2T_{2g}$	$^6A_{1g}$
d^6	$^1A_{1g}$	$^5T_{2g}$
d^7	^2E_g	$^4T_{1g}$

1.2.4.8. Low-spin (*LS*) — high-spin (*HS*) transition

When a transition metal ion of configuration d^n (n = 4–7), is in an octahedral surroundings, its ground state may be *LS* or *HS*, depending on the magnitude of the Δ energy gap between e_g and t_{2g} metal orbitals as was explained (see Fig. 1.12 on p. 15), relative to the mean spin pairing energy P. For $\Delta >> P$, the ground state arises from the configuration where d electrons occupy first the t_{2g} orbitals of lowest energy and then, if there are more than six electrons, the e_g orbital of highest energy. The ground state is then *LS*. For $\Delta <<P$ Hund's rule is obeyed. The *HS* ground state has the same spin multiplicity as the free metal ion. The nature of the ground state for d^n ions in octahedral symmetry is in Table 1.7. This phenomenon is associated with positive enthalpy change. When the conditions $\Delta <<$ or $\Delta >>P$ are not fulfilled, a *LS* $\leftrightarrow$ *HS* transition may occur and the physical properties may be very interesting.[8] A spin transition may be induced either by temperature, applied field and pressure or by the sample composition itself. The condition for a spin transition to occur is defined by $|\Delta - P| \approx kT$ (Fig. 1.35). A thermally induced *LS* $\leftrightarrow$ *HS* transition is characterized by $x = f(T)$ curve, where x is molar fraction of *HS* molecules and *(1-x)* is that of *LS* molecules. There are several techniques to obtain such curves. It is considered that if the origin of the spin transition phenomenon is molecular, it is due to a small balance between enthalpy and entropy factors and the phenomenon is influenced by cooperativity[‖] within the assembly of molecules.

1.2.4.9. Intermediate spin-states

In particular case of octahedral complexes involving d^5 and d^6 configurations there is possibility of ground terms which have intermediate spin states (S = 3/2 for $(t_{2g})^4(e_g)^1$ and S = 1 for $(t_{2g})^5(e_g)^1$ in which the e_g orbital is occupied by only one electron.

1.2.5. Understanding experimental magnetic data

There are some effects which perturb the electronic energy levels and their presence must be always considered in the models for estimation of magnetic susceptibility. These are the Zeeman effect, zero-field splitting, magnetic moment.

[‖] Cooperativity leads to thermal hysteresis. In mononuclear metal complexes it is influenced by nature of anion, hydrogen bonding, $\pi - \pi$ stacking, etc. Clusters or infinite networks of spin-crossover centres should show cooperativity too.

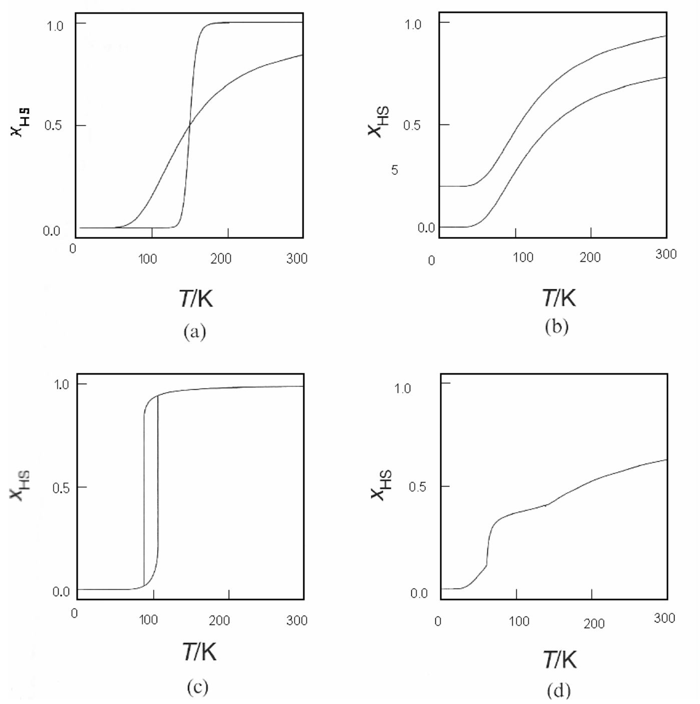

Figure 1.35.: Various types of spin transitions: (a) smooth or abrupt; (b) incomplete at low or high temperature; (c) with hysteresis on heating / cooling; (d) two-steps spin transition.[88]

1.2.5.1. Zeeman effects

The term Zeeman effect derives from atomic spectroscopy. The first order effect is splitting of certain lines when a strong magnetic field is applied to an emitting atom.[8] The splitting is proportional to the field strength (Fig. 1.36). The second order or quadratic effect usually requires very strong fields.

1.2.5.2. Zero-field splitting

When the ground state has a spin multiplicity larger than 2, its coupling with the excited states through the spin-orbit coupling may provoke a splitting of its Zeeman components in a zero applied magnetic field, i.e. the zero-field splitting of energy levels appears for systems with $S \geq 1$. Such systems may exhibit an increase of magnetization (the temperature should be low and the magnetic fields high). Several techniques allow the direct measurements of magnetic-field splitting:

- Magnetic anisotropy measurements on single crystals;
- Magnetization measurements;
- Far-infrared spectroscopy;
- Calorimetric measurements on Schottky anomalies;
- Electron spin resonance (electron paramagnetic resonance);
- Inelastic neutron scattering;

In this work the zero-field splitting was estimated from the fitting to the experimental data from the magnetic measurements.

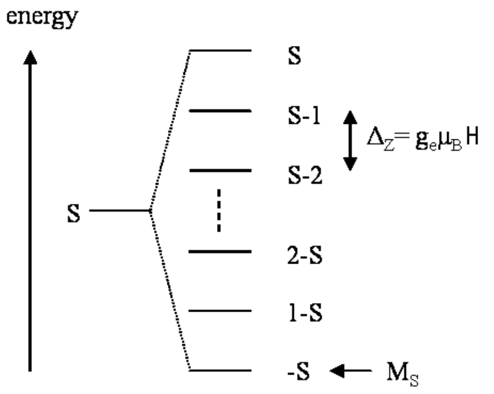

Figure 1.36.: Zeeman effect for pure states.[9]

1.2.5.3. Treatment of experimental data

The interpretation of the susceptibility is the principal source of magnetic information for a material. The molar susceptibility of a compound can be worked out from the measured experimental magnetization (see Equation B.5, p. 183). Its deviation from linear behaviour increases with increasing the magnetic field. The initial calculation always must consider this fact, together with other existing phenomena such as temperature independent paramagnetism and diamagnetism. In initial stages of interpretation the susceptibility must be converted (if needed) in appropriate units.

Transition metal centres with magnetic angular momentum, i.e. systems with ground T-terms, exhibit a variance of magnetic susceptibilities which is better visualised with the product function ($\chi_{\text{mol}}T$). Its field dependence becomes very noticeable with increasing magnetic field at low temperature.

The exhibition of different phenomena can be determined if a compound has typical Curie behaviour or there are deviations. Important steps are the determination of the Curie constant and the magnetic moment, because they allow to deduce the spin state and then the properties can be analysed. The Curie constant can be experimentally determined from the slope of the function χ^{-1}=f(T) (Fig. 1.24, p. 26) or from the ordinate of the function (χT) = f (T) (Fig. 1.23, p. 26) at high temperatures where the Curie law is obeyed. Another way to express Equation 1.4 (p. 24) for deducing the effective magnetic moment,[8] is shown in Equation 1.16, where at high temperature is considered that $\chi T \approx C$.

$$C = \frac{N_A\beta}{3k}\mu_{\text{eff}}^2 \tag{1.16}$$

The interpretation of the experimental data can be done by the application of the final results of the theories to the actual system. The magnetization and consequently the magnetic susceptibility can be calculated by several methods. Among them Van Vleck formula is the most popular. Most of the equations described below are derived from this method.

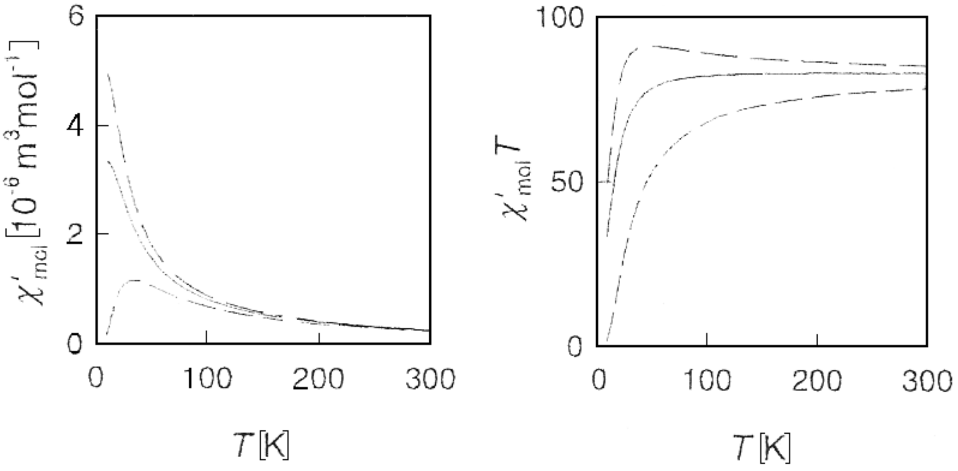

Figure 1.37.: Components of paramagnetic susceptibility: long dashed — perpendicular; short dashed — parallel; solid — average.[88]

The magnetic parameters are expressed of the (sum over the states) perturbation theory, in which the appropriate perturbation operators, individual for the given type of magnetic interaction, occur. All the equations comprise the contribution to the energy of the system (as was mentioned: TIP diamagnetic term, tensors, first- and second- order perturbation theory terms, Zeeman and other effects, if present). They are derivative of *ab initio* calculations of the magnetic parameters. In the final, each equation implies a set of fixed and variable parameters which can be solved through matching with the experimental data by iterative procedure. Then, one can compare how much the theoretical model fits with the experimental data. It is important to try fitting the theoretical formula to the observed data in order to see how well those formula agree with experiments and also to obtain values for the parameters from the calculations. Better agreement is always obtained by taking configuration interactions, spin-orbit coupling, zero-field splitting.

The observed magnetic moment of an open shell molecules or ion in a crystal lattice, is more often due mainly or entirely to electron spin. When magnetic properties are discussed, the effects of consecutive perturbation by spin-orbit coupling and magnetic fields on the crystal field terms are discussed.

Molecules containing a unique magnetic centre without first-order orbital momentum In crystalline solids the magnetic susceptibility forms a tensor. In the presence of axial symmetry two different susceptibility components are experimentally distinguishable (see Fig. 1.37): parallel (χ_z) and perpendicular (χ_x) to the field direction and the mean magnetic susceptibility then is:[8]

$$\chi = \chi_{z(\mathrm{II})} + 2\chi_{x(\perp)}/3 \tag{1.17}$$

When the symmetry is even lower, three components of susceptibility tensor should be considered. When the measurements are performed on high fields, the microcrystals may tend to orient themselves and that's why the measured susceptibility is no longer correct average, but higher than the powder average. Each susceptibility has its own characteristic temperature dependence and usually at low temperature their evolution may be completely different (Fig. 1.37).

Anisotropy of *g*-factor In most cases the magnetic data are collected for polycrystalline samples and the *g*-factor is interpreted as an average value (Equation 1.18). Usually *g* is considered to be $g \approx g_x \approx g_z \approx 2$.[8]

$$g^2 = \left(g_x^2 + g_y^2 + g_z^2\right)/3 \tag{1.18}$$

When in magnetochemistry there is no matching of *g*-factors, EPR studies are necessary. Usually for a Co(II) systems the magnetochemical *g*-values may be either close to the free-electron value g_e = 2.0023 (as was mentioned above; when the active space is extended enough to more magnetic levels) or close to EPR values which are higher (g_{eff} = 4–13) when only a few magnetic levels are included in the active space.

The following examples concern the magnetic properties of molecular species with a unique magnetic centre (a transition metal ion), with deviation from Curie law resulting from a zero-field splitting (*D*).

Examples *Ni(II) ion with d^8 configuration in axially distorted octahedral surroundings*[8] According to the Van Vleck formula the parallel and perpendicular susceptibilities are:

$$\chi_z = \frac{2Ng_z^2\beta^2}{kT}\frac{exp\left(-x\right)}{1+2exp\left(-x\right)} \tag{1.19}$$

$$\chi_x = \frac{2Ng_x^2\beta^2}{D}\frac{1-exp\left(-x\right)}{1+2exp\left(-x\right)} \tag{1.20}$$

where $x = D/kT$. The plots of χ_z and χ_x *vs.* *T* for *D* = +-5 cm^{-1} and $g_z = g_x$ = 2 are shown in Fig. 1.38. Whatever is the sign of *D*, χ_x tends to a finit value when approaches 0. χ_z tends to zero for $D > 0$ and diverges for $D < 0$. Fig. 1.39 shows $\chi_z T$ and $\chi_x T$ *vs.* $kT/\left|D\right|$ plots for $D > 0$ and $D < 0$. For $D > 0$, $\chi_z T$ and $\chi_x T$ tend to zero when $kT/\left|D\right|$ approaches zero; $\chi_z T$ continuously decreases while $\chi_x T$ passes through a maximum. For $D < 0$, $\chi_z T$ slightly increases on cooling and tends to the finite value $Ng_z^2\beta^2/k$ when $kT/\left|D\right|$ approaches zero, $\chi_x T$ tends to zero. In Fig. 1.39 also can be seen the curves χT *vs.* $kT/\left|D\right|$, where χ in this case is the average magnetic susceptibility (see also Equation 1.17).

Cr(III) with d^3 configuration in axially distorted octahedral surroundings[8] (After simplification, the model for this electronic configuration can interpret the magnetic properties of Co(II) (high-spin d^7) ion in octahedral environment, too.) According to Van Vleck, the susceptibilities can be evaluated by Equations 1.21 and 1.22, where $x = D/kT$.

$$\chi_z = \frac{Ng_z^2\beta^2}{4kT}\frac{1+9exp(-2x)}{1+exp(-2x)} \tag{1.21}$$

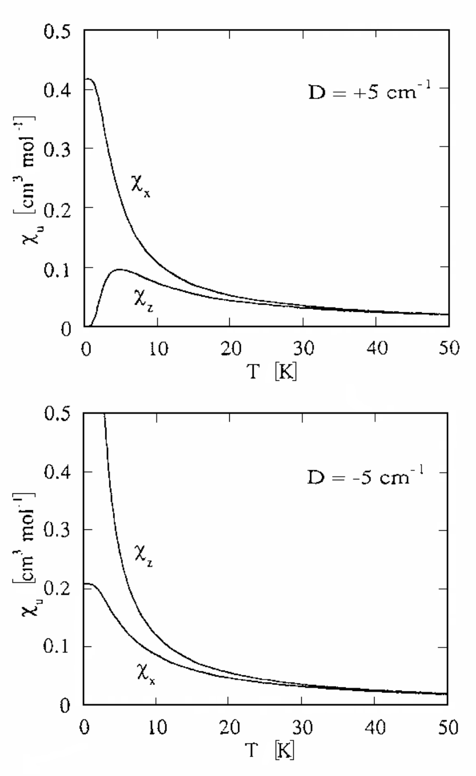

Figure 1.38.: Principal susceptibilities χ_z and χ_x *vs.* T plots for a spin triplet molecule with an axial anisotropy; top — the axial zero-field splitting parameter D is equal to 5 cm^{-1}; bottom $-D = -5$ cm^{-1}; g_z and g_x are taken equal to 2.[8]

$$\chi_x = \frac{Ng_x^2\beta^2}{kT}\frac{1+(3/4x)[1-exp(2x)]}{1+exp(-2x)}. \tag{1.22}$$

d^5 ion [Fe(III) or Mn(II)] in axially distorted octahedral surroundings[8] The Van Vleck equations in this case are:

$$\chi_z = \frac{Ng_z^2\beta^2}{4kT}\frac{1+9exp\,(-2x)+25exp\,(-6x)}{1+exp\,(-2x)+exp\,(-6x)} \tag{1.23}$$

$$\chi_x = \frac{Ng_x^2\beta^2}{4}\frac{(9/kT+8/D)-11exp(-2x)/2D-5exp(-6x)/2D}{1+exp(-2x)+exp(-6x)}, \tag{1.24}$$

where again $x = D/kT$.

Molecules containing a unique magnetic centre with a first-order orbital momentum

First-order orbital momentum and spin-orbit coupling As it was already mentioned that in some cases the first-order orbital momentum cannot be ignored (see Table 1.4, p. 24). It couples with the spin momentum, which partially removes the degeneracy of the respective ground state and the magnetic properties may be different than those in the described above cases. The magnetic anisotropy is often much more important and the average susceptibility may not follow the Curie law, even at high temperature. An acceptable approach for

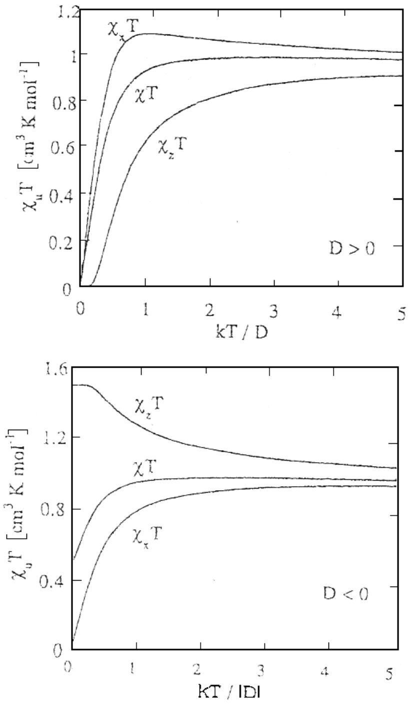

Figure 1.39.: $\chi_u T$ ($u = z, x$) and χ *vs.* $kT/\,|D|$ plots for a spin triplet molecule with an axial anisotropy; top — the axial zero-field splitting D is positive; bottom — D is negative. Both g_z and g_x are taken equal to 2.[8]

calculation was developed by Figgis[97,99–101] and Griffith.[90] The following examples are generalised equations by Mabbs & Machin,[89] Griffith[90] and Figgis.[103] The equations comprise the action of spin-orbit coupling term, the magnetic field term and the crystal field terms.

More examples *The magnetic susceptibility of the* $^2T_2$ *term arising from a free ion* ^2D *term (transition ion in weak distored octahedral and tetrahedral crystal fields);* d^1 *configuration (ex. V(IV), S = 1/2) (Fig. 1.40).* The expressions[8,88,89] for susceptibility and magnetic moment are:

$$\bar{\chi}_A = \frac{N\beta^2}{3kT}\frac{\left[8 + (3x-8)\,exp\left(-\frac{3x}{2}\right)\right]}{x\left[2 + exp\left(-\frac{3x}{2}\right)\right]} \tag{1.25}$$

or

$$\bar{\mu}^2 = \frac{\left[8 + (3x-8)\,exp\left(-\frac{3x}{2}\right)\right]}{x\left[2 + exp\left(-\frac{3x}{2}\right)\right]}, \tag{1.26}$$

where $x = \lambda/kT$. $\bar{\chi}_A$ is average magnetic susceptibility per mole of atoms and λ is a spin-orbit coupling constant for the term. Similar treatment can be applied for cases of d^2 configuration, low-spin d^4, low-spin d^5, high-spin d^6 and high-spin d^7 in octahedral surrounding.[8,97,99–101] The equation is:

$$\chi_{z(x)} = \frac{Ng^2_{z(x)}\beta^2}{4kT} + C_{z(x)}, \tag{1.27}$$

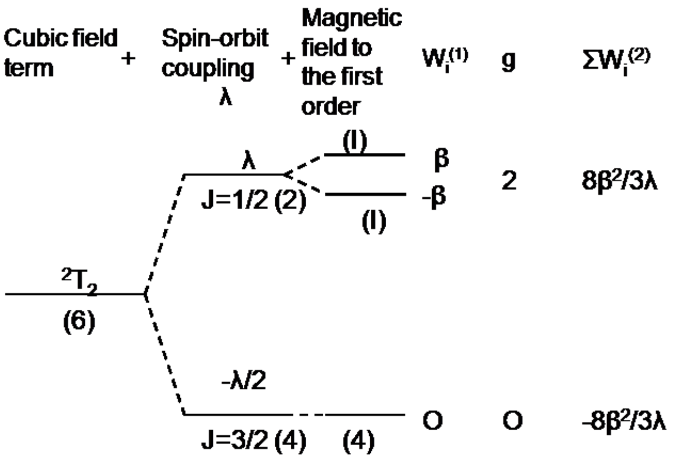

Figure 1.40.: The splitting diagram for the $^2T_2$ term under the action of spin-orbit coupling and a magnetic field.[89] (The numbers in brackets under each energy level are total degeneracies of the levels).

where $C_{z(x)}$ are positive temperature-independent contributions.

The magnetic behaviour of the $^4T_1$ term arising from a free ion ^4F term (transition ion in weak octahedral and tetrahedral crystal fields); d^7 configuration (ex. high-spin Co(II)). The expression is:

$$\mu_{\text{eff}}^2 = \frac{300(x+5) + 6(45x-88)e^{-\frac{1}{2}x} + 12(35x-81)e^{-\frac{4}{3}x}}{25x(1+2e^{-\frac{1}{2}x}+3e^{-\frac{4}{3}x})}, \tag{1.28}$$

where $x = \lambda/kT$.

The magnetic behaviour of the $^5T_2$ term arising from a free ion ^5D term (transition ion in weak octahedral and tetrahedral crystal fields); d^4 configuration (ex. Fe(II)). The applicable equation is:

$$\bar{\mu}^2 = \frac{3\left[28x + 9.33 + (22.5x+4.17)\,exp\,(-3x) + (24.5x-13.5)\,exp\,(-5x)\right]}{x\left[7+5exp\,(-3x)+3exp\,(-5x)\right]}, \tag{1.29}$$

where again $x = \lambda/kT$.

The magnetic behaviour of the $^3T_1$ term arising from a free ion ^3F term (transition ion in weak octahedral and tetrahedral crystal fields); d^8 configuration (ex. V(III)).

$$\bar{\mu}^2 = \frac{3\left[0.625x + 6.8 + (0.125x+4.09)\,exp\,(-3x) - 10.89exp\left(-\frac{9x}{2}\right)\right]}{x\left[5+3exp\,(-3x)+exp\left(-\frac{9x}{2}\right)\right]}, \tag{1.30}$$

where $x = \lambda/kT$.

The magnetic behaviour of the A_2 terms arising from a free ion F term (transition ion in weak octahedral and tetrahedral crystal fields)

In certain cases a cubic crystal field may split the free ion F term in such way that an orbitally non-degenerate A_2 term lies lowest. There is no orbital angular momentum associated with this term and there is nothing for the spin angular momentum to couple with. Thus spin-orbit coupling cannot raise any degeneracy. As consequence of the lack of orbital angular momentum the values for the magnetic susceptibilities must be the spin-only values. In the cases of $^3A_2$ term (arising from ^3F term, d^2 configuration) and of $^4A_2$ term (arising form ^4F term; d^7) although spin-orbit coupling does not split the A_2 term, there are non-zero matrix element with ^3T terms arising from the free ion ^3F term. Thus for d^7 configuration (ex. Co(II)) according to Griffith[90] we have:

$$\mu_{\text{eff}}^2 = \frac{300\,(x+5) + 6\,(45x-88)\,e^{-\frac{1}{2}x} + 12\,(35x-81)\,e^{-\frac{4}{3}x}}{25x\left(1+2e^{-\frac{1}{2}x}+3e^{-\frac{4}{3}x}\right)} \tag{1.31}$$

where $x = \lambda/kT$ and λ is spin-orbit coupling constant for the term.

The magnetic behaviour of the $^6A_1$ term arising from a free ion ^6S term (transition ion in weak octahedral and tetrahedral crystal fields)

Examples are Ni(II) and Cu(II) and the equation given by Griffith[90] is:

$$\mu_{\text{eff}}^2 = \frac{3\,(49x+108) + 5\,(27x-20)\,e^{-\frac{1}{2}x} + 56\,(3x-4)\,e^{-\frac{5}{4}x}}{2x\left(3+5e^{-\frac{1}{2}x}+7e^{-\frac{5}{4}x}\right)}, \tag{1.32}$$

where $x = \lambda/kT$ and λ being spin-orbit coupling constant for the term.

The ^6S term which arises from the spin-free d^5 configuration is not splited by crystal fields of any symmetry, but gives rise to a $^6A_1$ term. This term is an orbital singlet and it has no orbital momentum associated with it. The spin-orbit coupling cannot raise the degeneracy of this term. Since there are no excited terms with the same multiplicity as the ground term there isn't second-order mixing due to the spin-orbit coupling, nor can there be any second-order Zeeman effect. The magnetic properties are simplified to the spin contribution which is independent of temperature and:

$$\bar{\mu} = (4S\,(S+1))^{\frac{1}{2}}\,\mu_B = 5.92\mu_B. \tag{1.33}$$

The best example of complexes with the $^6A_1$ ground term are provided by spin-free octahedral or tetrahedral Mn(II) or Fe(III).

Intermolecular interactions A plot of $\chi^{-1} = f\,(T)$ for a system obeying the Curie-Weiss law gives a straight line of which the slope is C^{-1}. The intercept with the T axis yields the sign and the value of Θ (see Fig. 1.41). According to this model, $\Theta > 0$ indicates ferromagnetic intermolecular interactions and $\Theta < 0$ indicates antiferromagnetic intermolecular interactions (as was mentioned above). In the former case ($\Theta > 0$) the Curie-Weiss law is limited to the temperature range $T > \Theta$. If the magnetic data are represented in the form of χT *vs.* T plot, positive Θ leads to an increase and negative Θ — to a decrease of $\chi_M T$ on cooling (Figs. 1.23 on p. 26 and 1.42). The lower the temperature, the stronger is this effect. The deviation from the Curie law may have other origins than intermolecular interactions, such as zero-field splitting and spin-orbit coupling as was explained above. Sometimes a wrong assumption can be made that a large value if Θ is due to presence of antiferrimagnetic in-

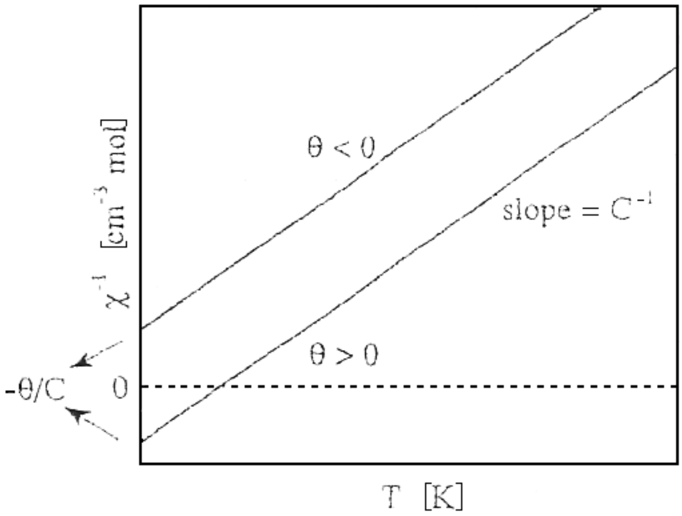

Figure 1.41.: χ^{-1} *vs.* T plot for an assembly of molecules obeying the Curie-Weiss law.[8]

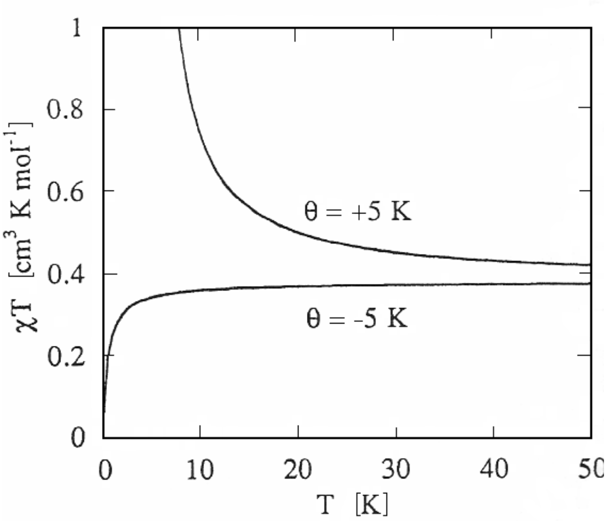

Figure 1.42.: χT *vs.* T plot for an assembly of molecules obeying the Curie-Weiss law with a Curie constant $C = 0.375$ cm^{3}K/mol and the Weiss constant Θ=5 K (top) and –5 K (bottom).[8]

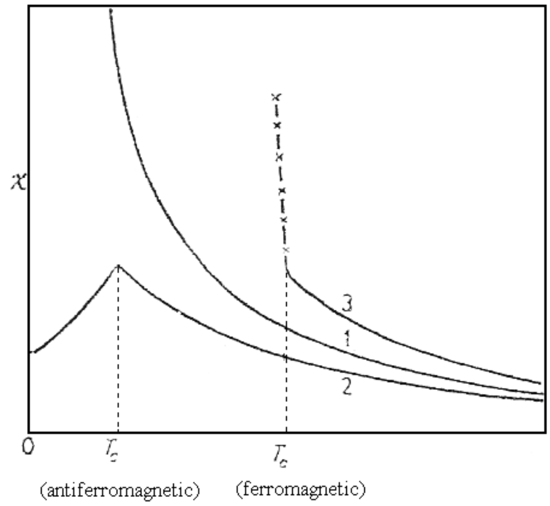

Figure 1.43.: Behaviour of typical (1) paramagnetic, (2) antiferromagnetic and (3) ferromagnetic compounds as function of temperature.[103]

teractions. When there is not an occurrence of a maximum in the susceptibility as is shown in Fig. 1.29 (p. 32), or another additional information is not available, the same feature can be observed in magnetically dilute systems (paramagnetic behaviour without interactions). Hence, if the temperature is reduced sufficiently, a sharp maximum in the magnetic susceptibility is reached at the temperature T_N, below which the susceptibility decreases rapidly with temperature (Fig. 1.29).

Compounds with several interaction magnetic centres The interpretation of the magnetic susceptibilities of polynuclear transition metal complexes involves two complementary approaches: molecular orbital theory and bipolar coupling approach of Van Vleck. Molecular orbital theory takes into account the mechanism of the exchange interaction and bonding in the complex. It is not possible to predict or rationalize only the spin multiplicity of the ground state of the molecule. On the other hand, the bipolar coupling approach only assumes the presence of an exchange interaction without reference to the mechanism, but it make easy the calculation of the variation of magnetic susceptibility with temperature (Fig. 1.43). The equations that describe this behaviour are elaborated by different authors.[8,74,88]

References

1. Winter MJ, d-Block chemistry, Oxfod University Press, 1994.
2. URL `http://physics.nist.gov/PhysRefData/PerTable/index.html`.
3. McCleverty J, Chemistry of the first-row transition metals, 1st ed., Oxfod University Press, 1999.
4. Cotton FA and Wilkinson G, Advanced inorganic chemistry. A comprehensive text., 3rd ed., John Wiley & Sons, Inc., 1972.
5. Huheey JE, Keiter EA and Keiter RL, Inorganic chemistry. Principles of structure and reactivity, 4th ed., HaprepCollinsCollegePublishers, 1993.
6. Miessler GL and Tarr DA, Inorganic chemistry, 3rd ed., Prentice Hall, 2003.
7. Shriver DF, Atkins PW and Langford CH, Inorganic chemistry, 1st ed., Oxford university Press, 1990.
8. Kahn O, Molecular magnetism, Wiley–VCH, 1993.
9. Orchard AF, Magnetochemistry, 1st ed., Oxford chemistry primers, Oxford: University Press, 2003.
10. Mayoh B and Day P, *J. Chem. Soc., Dalton Trans.* (15) (1976), 1483–1486.
11. Ferlay S, Mallah T, Ouahes R, Veillet P and Verdaguer M, *Nature* 378(6558) (1995), 701–703.
12. Entley WR and Girolami GS, *Science* 268(5209) (1995), 397–400.
13. Holmes SM and Girolami GS, *J. Am. Chem. Soc.* 121(23) (1999), 5593–5594.
14. Chapman KW, Southon PD, Weeks CL and Kepert CJ, *Chem. Commun.* (26) (2005), 3322–3324.
15. Kaye SS and Long JR, *J. Am. Chem. Soc.* 127(18) (2005), 6506–6507.
16. Boxhoorn G, Moolhuysen J, Coolegem JGF and Vansanten RA, *J. Chem. Soc., Chem. Commun.* (19) (1985), 1305–1307.
17. Sato O, Iyoda T, Fujishima A and Hashimoto K, *Science* 272(5262) (1996), 704–705.
18. Salah El Fallah M, Rentschler E, Caneschi A, Sessoli R and Gatteschi D, *Angew. Chem, Int. Ed. Engl.* 35(17) (1996), 1947–1949.
19. Dong W, Zhu LN, Song HB, Liao DZ, Jiang ZH, Yan SP, Cheng P and Gao S, *Inorg. Chem.* 43(8) (2004), 2465–2467.
20. Larionova J, Gross M, Pilkington M, Andres H, Stoeckli-Evans H, Güdel H and Decurtins S, *Angew. Chem., Int. Ed.* 39(9) (2000), 1605–1609.
21. Ferlay S, Mallah T, Vaissermann J, Bartolome F, Veillet P and Verdaguer M, *Chem. Commun.* (21) (1996), 2481–2482.
22. Ohba M, Okawa H, Fukita N and Hashimoto Y, *J. Am. Chem. Soc.* 119(5) (1997), 1011–1019.
23. Thetiot F, Triki S, Pala JS, Gomez-Garcia CJ and Golhen S, *Chem. Commun.* (10) (2002), 1078–1079.

24. Kou HZ, Liao DZ, Cheng P, Jiang ZH, Yan SP, Wang GL, Yao XK and Wang HG, *J. Chem. Soc., Dalton Trans.* (9) (1997), 1503–1506.
25. Rogez G, Parsons S, Paulsen C, Villar V and Mallah T, *Inorg. Chem.* 40(16) (2001), 3836–3837.
26. Shatruk M, Dragulescu-Andrasi A, Chambers KE, Stoian SA, Bominaar EL, Achim C and Dunbar KR, *J. Am. Chem. Soc.* 129(19) (2007), 6104–6116.
27. Klein CL, Majeste RJ, Trefonas LM and O'Connor CJ, *Inorg. Chem.* 21(5) (1982), 1891–1897.
28. Inoue M and Kubo M, *Coord. Chem. Rev.* 21(1) (1976), 1–27.
29. Lu JY, Lawandy MA, Li J, Yuen T and Lin CL, *Inorg. Chem.* 38(11) (1999), 2695–2704.
30. Ismayilov RH, Wang WZ, Lee GH and Peng SM, *J. Chem. Soc., Dalton Trans.* (3) (2006), 478–491.
31. Liu CM, Gao S, Zhang DQ, Huang YH, Xiong RG, Liu ZL, Jiang FC and Zhu DB, *Angew. Chem., Int. Ed.* 43(8) (2004), 990–994.
32. Zhao W, Song Y, Okamura TA, Fan J, Sun WY and Ueyama N, *Inorg. Chem.* 44(9) (2005), 3330–3336.
33. Tamaki H, Zhong ZJ, Matsumoto N, Kida S, Koikawa M, Achiwa N, Hashimoto Y and Okawa H, *J. Am. Chem. Soc.* 114(18) (1992), 6974–6979.
34. Mathoniere C, Nuttall CJ, Carling SG and Day P, *Inorg. Chem.* 35(5) (1996), 1201–1206.
35. Hernández-Molina M, Lloret F, Ruiz-Pérez C and Julve M, *Inorg. Chem.* 37(16) (1998), 4131–4135.
36. Tamaki H, Mitsumi M, Nakamura K, Matsumoto N, Kida S, Okawa H and Iijima S, *Chem. Lett.* (10) (1992), 1975–1978.
37. Wernsdorfer W, «Quantum dynamics in single-molecule magnets triggered by microwave pulses», Oral presentatin in Conference on single molecule magnets and hybrid magnetic nanostructures, ICTP–Trieste, Italy, 2005.
38. URL `http://www.chim1.unifi.it/LAMM/smm.htm`.
39. Batlle X and Labarta A, *J. Phys. D: Appl. Phys.* 35(6) (2002), R15–R42.
40. Cox DM, Trevor DJ, Whetten RL, Rohlfing EA and Kaldor A, *Phys. Rev. B: Condens. Matter Mater. Phys.* 32(11) (1985), 7290–7298.
41. Feng L, Press MR, Khanna SN and Jena P, *Phys. Rev. B: Condens. Matter Mater. Phys.* 39(10) (1989), 6914–6924.
42. De Heer WA, Milani P and Chtelain A, *Phys. Rev. Lett.* 65(4) (1990), 488–491.
43. Bucher JP, Douglass DC and Bloomfield LA, *Phys. Rev. Lett.* 66(23) (1991), 3052–3055.
44. Khanna SN and Linderoth S, *Phys. Rev. Lett.* 67(6) (1991), 742–745.
45. Douglass DC, Cox AJ, Bucher JP and Bloomfield LA, *Phys. Rev. B: Condens. Matter Mater. Phys.* 47(19) (1993), 12874–12889.
46. Reddy BV, Khanna SN and Dunlap BI, *Phys. Rev. Lett.* 70(21) (1993), 3323–3326.
47. Cox AJ, Louderback JG and Bloomfield LA, *Phys. Rev. Lett.* 71(6) (1993), 923–926.

48. Chen JP, Sorensen CM, Klabunde KJ and Hadjipanayis GC, *Phys. Rev. B: Condens. Matter Mater. Phys.* 51(17) (1995), 11527–11532.
49. Kaiming D, Jinlong Y, Chuanyun X and Kelin W, *Phys. Rev. B* 54(3) (1996), 2191–2197.
50. Apsel SE, Emmert JW, Deng J and Bloomfield LA, *Phys. Rev. Lett.* 76(9) (1996), 1441–1444.
51. Respaud M, Broto JM, Rakoto H, Fert AR, Thomas L, Barbara B, Verelst M, Snoeck E, Lecante P, Mosset A, Osuna J, Ould Ely T, Amiens C and Chaudret B, *Phys. Rev. B: Condens. Matter Mater. Phys.* 57(5) (1998), 2925–2935.
52. Luis F, Torres JM, García LM, Bartolomé J, Stankiewicz J, Petroff F, Fettar F, Maurice JL and Vaurés A, *Phys. Rev. B* 65(9) (2002), 094409–1–094409–10.
53. Kodama RH, *J. Magn. Magn. Mater.* 200(1-3) (1999), 359–372.
54. Chaudret B, *C. R. Phys.* 6(1) (2005), 117–131.
55. Jena P and Castleman Jr AW, *Proc. Natl. Acad. Sci. U. S. A.* 103(28) (2006), 10560–10569.
56. Sun CQ, *Prog. Solid State Chem.* 35(1) (2007), 1–159.
57. Miller JS and Drillon M, Magnetism: molecules to materials. Nanosized magnetic materials, vol. III, 1st ed., Wiley-V C H Verlag Gmbh, 2002.
58. Eberhardt W, *Surf. Sci.* 500(1-3) (2002), 242–270.
59. Billas IML, Châtelain A and De Heer WA, *Science* 265(5179) (1994), 1682–1684.
60. Billas IML, Chatelain A and deHeer WA, *J. Magn. Magn. Mater.* 168(1-2) (1997), 64–84.
61. Ahn Y, Choi E and Kim E, *Rev. Adv. Mater. Sci.* 5(5) (2003), 477–480.
62. Christodoulides J, Bonder M, Huang Y, Zhang Y, Stoyanov S, Hadjipanayis G, Simopoulos A and Weller D, *Phys. Rev. B: Condens. Matter Mater. Phys.* 68(5) (2003), 544281–544287.
63. Iida H, Takayanagi K, Nakanishi T and Osaka T, *J. Colloid Interface Sci.* 314(1) (2007), 274–280.
64. Cornell RM and Schwertmann U, The iron oxides, 2nd ed., Wiley-VCH Verlag Berlin GmbH, 2003.
65. Berkowitz AE, Schuele WJ and Flanders PJ, *J. Appl. Phys.* 39(2) (1968), 1261–1263.
66. Morales MP, Veintemillas-Verdaguer S, Montero MI, Serna CJ, Roig A, Casas LI, Martínez B and Sandiumenge F, *Chem. Mater.* 11(11) (1999), 3058–3064.
67. Goya GF, Berquo TS, Fonseca FC and Morales MP, *J. Appl. Phys.* 94(5) (2003), 3520–3528.
68. Roca AG, Marco JF, Morales MD and Serna CJ, *J. Phys. Chem. C* 111(50) (2007), 18577–18584.
69. Mürbe J, Rechtenbach A and Töpfer J, *Mater. Chem. Phys.* 110(2-3) (2008), 426–433.
70. Gatteschi D, Caneschi A, Pardi L and Sessoli R, *Science* 265(5175) (1994), 1054–1058.
71. Chudnovsky EM, *Science* 274(5289) (1996), 938–939.
72. Miller JS and Drillon M, Magnetism: molecules to materials. Models and experiments, vol. I, 1st ed., Wiley-V C H Verlag Gmbh, 2001.

73. Miller JS and Drillon M, Magnetism: molecules to materials. Molecule-based materials, vol. II, 1st ed., Wiley-V C H Verlag Gmbh, 2001.
74. Bleaney B and Bowers KD, *Proc. R. Soc. London, Ser. A* 214(1119) (1952), 451–465.
75. Sessoli R, Gatteschi D, Caneschi A and Novak MA, *Nature* 365(6442) (1993), 141–143.
76. Lis T, *Acta Crystallogr., Sect. B: Struct. Sci.* 36(9) (1980), 2042–2046.
77. Gatteschi D and Sessoli R, *Angew. Chem., Int. Ed.* 42(3) (2003), 268–297.
78. Wieghardt K, Pohl K, Jibril I and Huttner G, *Angew. Chem, Int. Ed. Engl.* 23(1) (1984), 77–78.
79. Larionova J, Kahn O, Gohlen S, Ouahab L and Clerac R, *J. Am. Chem. Soc.* 121(14) (1999), 3349–3356.
80. Kahn O, Larionova J and Ouahab L, *Chem. Commun.* (11) (1999), 945–952.
81. Rajca A, *Chem. Rev.* 94(4) (1994), 871–893.
82. Iwamura H, Inoue K and Hayamizu T, *Pure Appl. Chem.* 68(2) (1996), 243–252.
83. Krober J, Codjovi E, Kahn O, Grolière F and Jay C, *J. Am. Chem. Soc.* 115(21) (1993), 9810–9811.
84. Ouahab L, *Chem. Mater.* 9(9) (1997), 1909–1926.
85. Kurmoo M and Kepert CJ, *New J. Chem.* 22(12) (1998), 1515–1524.
86. Miller JS and Drillon M, Magnetism: molecules to materials. Nanosized magnetic materials, vol. IV, Wiley-V C H Verlag Gmbh, 2002.
87. Moroni R, Buzio R, Chincarini A, Valbusa U, de Mongeot FB, Bogani L, Caneschi A, Sessoli R, Cavigli L and Gurioli M, *J. Mater. Chem.* 18(1) (2008), 109–115.
88. Bǒca R, Theoretical foundations of molecular magnetism, vol. 1 of *Current methods on inorganic chemistry*, 1st ed., Elsevier, 1999.
89. Mabbs FE and Machin DJ, Magnetism and transition metal complexes, Chapman & Hall, London, 1973.
90. Griffith JS, The theory of transition - metal ions, 3rd ed., Cambridge University Press, 1971.
91. Van Vleck JH, The theory of electronic and magnetic susceptibility, Oxford, 1932.
92. Kotani M, *J. Phys. Soc. Jpn.* 4(4–6) (1949), 293–297.
93. König E and Kremer S, *Ber. Bunsenges. Phys. Chem.* 76(9) (1972), 870.
94. König E and Kremer S, *Ber. Bunsenges. Phys. Chem.* 78(3) (1974), 268–276.
95. König E and Kremer S, *Ber. Bunsenges. Phys. Chem.* 78(8) (1974), 786–795.
96. König E and Kremer S, Magnetism diagrams for transition metal ions, Plenum Press, New York, 1979.
97. Figgis BN, *Trans. Faraday Soc.* 57(2) (1961), 198–203.
98. Figgis BN, Introduction to ligand fields, Wiley, New York, Interscience Publishers, 1966.
99. Figgis BN, Lewis J, Mabbs FE and Webb CA, *J. Chem. Soc. A* (10) (1966), 1411–1421.
100. Figgis BN, Lewis J, Mabbs FE and Webb GA, *J. Chem. Soc. A* (3) (1967), 442–447.

101. Figgis BN, Gerloch M, Lewis J, Mabbs FE and Webb GA, *J. Chem. Soc. A* (9) (1968), 2086–2093.
102. Barbara B, Gignoux D and Vettier C, Lectures on modern magnetism, Springer-Verlag, 1988.
103. Figgis BN and Lewis J, The magnetic properties of transition metal complexes, vol. 6 of *Progress in inorganic chemistry*, John Wiley & Sons, Inc., 1964.

COORDINATION COMPOUNDS OF 1ST ROW TRANSITION METALS AND AMBIDENTATE AROMATIC LIGANDS

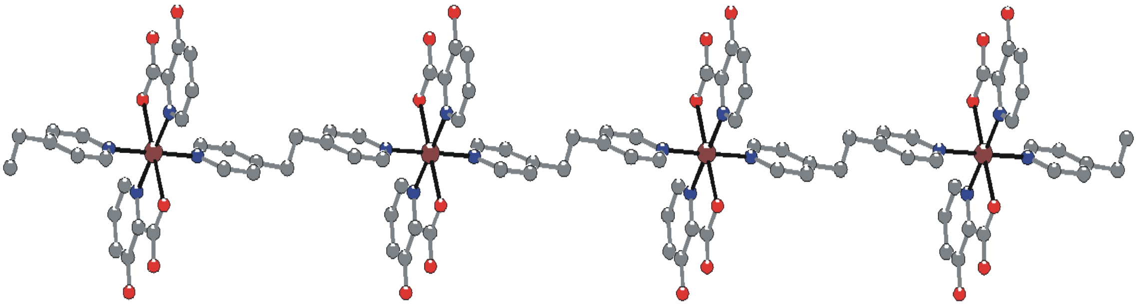

CHAPTER II

Chapter 2.

Coordination compounds of 1^{st} row transition metals and ambidentate aromatic ligands

2.1. Chemistry and complexes of derivatives of pyridine-carboxylic acids

The diversity of ligands and the metal-ligand coordination chemistry give many opportunities for synthesizing compounds with novel architectures. For the construction of hybrid inorganic-organic polymer network, the choice of the ligand which form the basic building block is very important. In this work ambidentate ligands were chosen, whose donor atoms in most of the cases are located in a pyridine ring (Fig. 2.1). The ligands contain carboxyl and amino-, hydroxy- and thio- functionalities and are known to have different behaviour towards metal centres because of differences in their hard-soft donor characteristics. Additional functional groups in the heterocyclic ring give other coordination possibilities so that can result in different supramolecular architectures, held together via hydrogen bonding, $\pi - \pi$ interactions, Van der Waals forces or electrostatic forces. When using transition metals with low coordination numbers in combination with nitrogen heterocyclic ligands of different geometry, discrete supramolecular assemblies and 1D polymers are formed. Extended structures can be obtained by including bridging ligands in the coordination sphere of the metal. The bridging ligands used in the work and reported in this chapter are the N– donors 1,2–bis (4–pyridyl) ethane and 1,10–phenanthroline. Their geometry and chemical properties, together with the affinity of the transition metals to coordination with the nitrogen atoms, turns them suitable to build extended crystalline structures.

The purpose of the work reported in this chapter was to synthesize coordination compounds of 1^{st} row transition metals with different ligands derivative of pyridine-carboxylic acids; then to include a second ligand in the metal coordination sphere and to investigate the resulting magnetic properties of the new compounds.

2–Hydroxynicotinic acid (HnicOH, $C_6H_5NO_3$[*]) HnicOH was first synthesized by Fibel and Spoerri.[1] The pyridine nitrogen usually undergoes protonation from the neighbouring hydrogen atom of the hydroxyl group thus establishing keto-enol tautomerism on the analogy of 2–mercaptonicotinic acid (see Figs. 2.2 and 2.3). The acid-base equilibria in water-ethanol medium have the form:

$$\mathrm{HnicOH} \rightleftharpoons \mathrm{HnicO^-} + \mathrm{H^+},\ \mathrm{HnicO^-} \rightleftharpoons \mathrm{nicO^{2-}} + \mathrm{H^+}$$

The dissociation constants pK_a for the carboxyl and the phenol OH groups at 20 °C are 6.20 and 9.65 respectively.[2] The dissociation of HnicOH was also studied by Stephens and Orvig[3] (see also Fig. 2.2) and the acid dissociation constants at 25 °C were found to be re-

---

[*] IUPAC name: 2–hydroxypyridine–3–carboxylic acid.

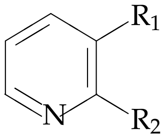

R_1	R_2	Name
OH	COOH	3–Hydroxypicolinic acid
COOH	OH	2–Hydroxynicotinic acid
H	COOH	Picolinic acid
COOH	SH	2–Mercaptonicotinic acid

Figure 2.1.: Derivatives of pyridine-carboxylic and benzoic acids, used in the present work.

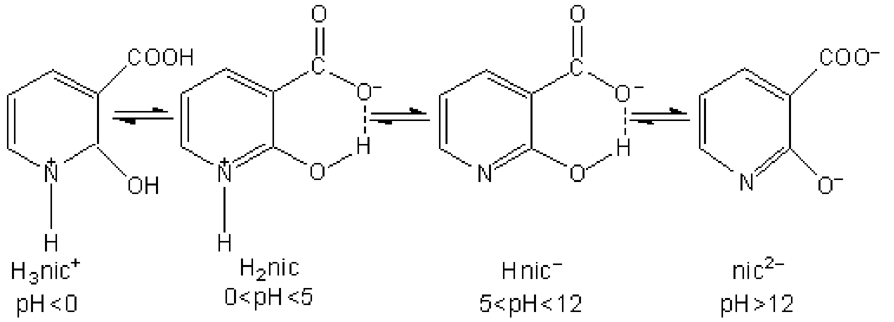

Figure 2.2.: Deprotonation process of 2–hydroxynicotinic acid as a function of pH. The process is analogous for 2–mercaptonicotinic and 3–hydroxypicolinic acid.[3]

spectively 4.98 and 11.96. The decrease of the acidity of the carboxyl group might be due to the formation of intramolecular hydrogen bonding between the COO^- and OH groups.

Similarly to other ligands derived from pyridine-carboxylic acid, HnicOH can coordinate in various fashions depending on the type of solvent, the pH of the solution or the affinity to the metal. As shown in Fig. 2.4 this ligand displays various coordination modes: monodentate, NO bidentate chelating (with the oxygen from the hydroxyl group) or COO^-,O^- (the oxygens from the carboxyl and hydroxyl groups). COO^-,O^-– chelation is observed in various complexes with transition metals[4–8] and lanthanides.[9–11] N,O–coordination mode with transition metals have also been reported in the litterature,[4,11–14] while coordination through only the N atom is unusual.[13] Coordination through the two oxygens from the carboxyl group is possible but not very common.[11]

3–hydroxypicolinic acid (HpicOH, $C_6H_5NO_3$[†]) HpicOH is a positional isomer of HnicOH which combines two types of coordinating groups in such a way that acts as a versatile

---

[†] IUPAC name: 3–hydroxypyridine–2–carboxylic acid.

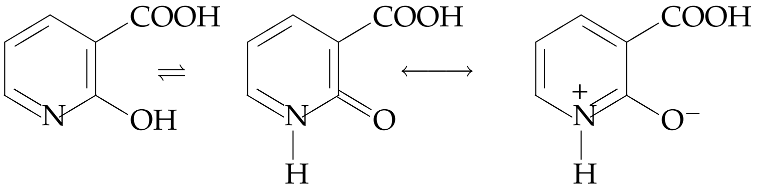

Figure 2.3.: Tautomeric equilibrium of 2–hydroxynicotinic acid.

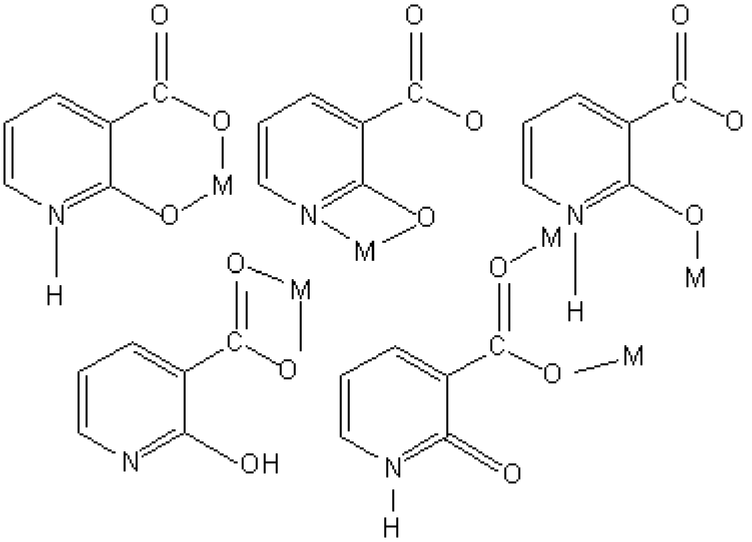

Figure 2.4.: Coordination modes of 2–hydroxynicotinic acid.

ambidentate ligand (Fig. 2.5). It was first synthesized by Kirpal[15] and years latter by Fibel and Spoerri.[1] For the two acid-base equilibria:

$$\mathrm{HpicOH} \rightleftharpoons \mathrm{picOH}^- + \mathrm{H}^+, \mathrm{picOH}^- \rightleftharpoons \mathrm{picO}^{2-} + \mathrm{H}^+$$

the values of $\mathrm{pK_a}$ were found as follows: 3.91 for the carboxyl group and 9.22 for the hydroxyl group,[2] at 20 °C. The deprotonation process as function of pH is analogous to that of HnicOH (see Fig. 2.2), according to Stephens and Orvig[3] who found dissociation constants of 5.03 and 11.06, respectively.

The mono-deprotonated ligand ($\mathrm{picOH^-}$) can form a five-membered chelate ring via the pyridine nitrogen atom and the carboxyl group ($\mathrm{N,COO^-}$– picolinate-type chelation) with this coordination mode being the most commonly found in complexes.[6,7,16–30] The deprotonation of the carboxyl and hydroxyl groups makes O,O– chelation (salicylate-type coordination mode, $\mathrm{COO^-,O^-}$) possible with the consequent formation of a typical six-membered chelate ring.[5,21–23,26] It can also coordinate in a tridentate way via the ($\mathrm{N, COO^-, O^-}$) donor set, forming tetrameric species.[23] There is only one report for single coordination through the pyridine nitrogen atom,[19] but there is an example of coordination through the oxygen atoms of the deprotonated carboxyl and hydroxyl groups and also through the pyridine nitrogen.[31] No examples are known so far for single coordination via the deprotonated

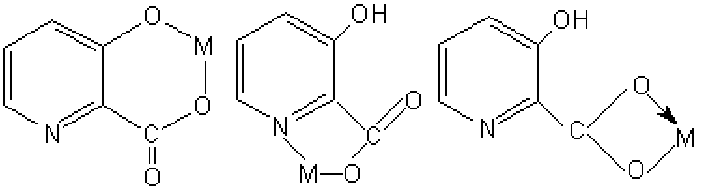

Figure 2.5.: Coordination modes of 3–hydroxypicolinic acid.

hydroxyl group.

Versatile chelating properties of HpicOH have been exploited to synthesize a series of lanthanide complexes, and the role of this ligand in the photoluminescence of materials containing these complexes have been investigated.[10,22] However, HpicOH is commonly used with 2nd and 3d row transition metal centres,[17–20,29] and new structures with magnetic and insulino-mimetic properties of 1st row transition cations can be found in the literature.[16,21,23,24,26]

2–Mercaptonicotinic acid (HnicSH, $C_6H_5NO_2S$‡) The ligand HnicSH was synthesized for first time in 1932.[32] It is a soft ligand (if coordinated through the S atom) with pK_a of the thiol group equal to 8.82 and of the carboxyl group, equal to 5.78,[2] determined at 20 °C for the equilibria:

$H_2nicS \rightleftharpoons HnicS^- + H^+$ and $HnicS^- \rightleftharpoons nicS^{2-} + H^+$

The acid shows the characteristic thione-thiol tautomerism of the heterocyclic thiones[33] (Fig. 2.6). The thione form is the more common and exists as zwitterionic species (see Fig. 2.7). Heterocyclic thiolates are known as ambidentate ligands that are capable to involve either the sulphur or/and the nitrogen atoms in monodentade, chelating or bridging coordination. Depending on the pH conditions,[2] HnicSH coordinates in different modes (see Fig. 2.8): via the sulphur donor atom only,[34] via the sulphur and nitrogen from the pyridine ring forming a four membered chelate;[34–38] via the sulphur and the oxygen atom from the carboxyl group,[36,37,39] and via the carboxyl group in chelating mode.[36,38]

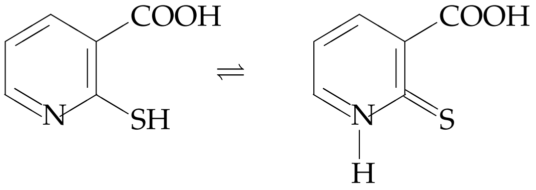

Figure 2.6.: Thione-thiol tautomerism of 2–mercaptonicotinic acid.

Several complexes of HnicSH with transition metals have been reported, including with Mo(VI),[34] Pd(II) and Pt(II),[40] Ag(I) and Au(I),[41,42] Pt(III),[43] Ru(III),[44] Os cluster com-

---

‡IUPAC name: 2–mercaptopyridine–3–carboxylic acid.

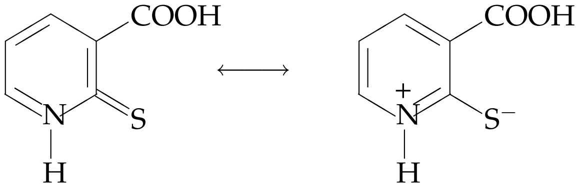

Figure 2.7.: The thione form of 2–mercaptonicotinic acid and its Zwitterion.

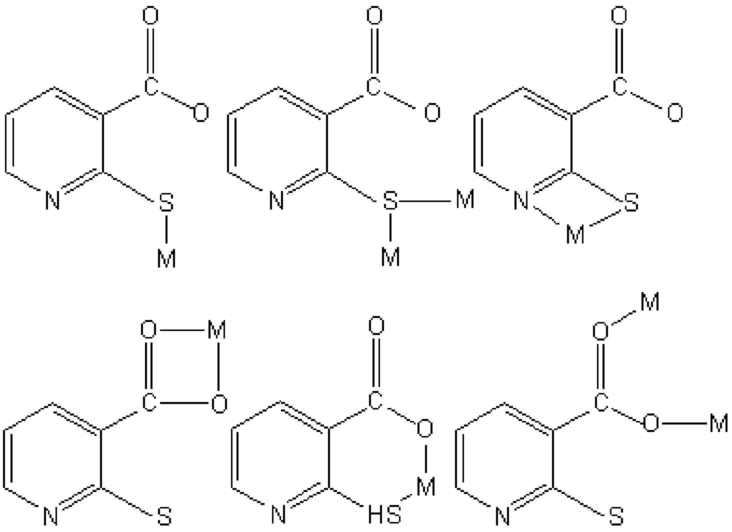

Figure 2.8.: Coordination modes of 2–mercaptonicotinic acid.

plexes,[45] Cr(III);[46] Pd(II), Pt(II) Rh(III). In these structures, HnicSH acts as either monodentate or bidentate ligand and in all the examples the sulphur atom is involved in the coordination.

2.2. Structural aspects of complexes of 1st row transition metals and ambidentate aromatic ligands

2.2.1. Crystal structures of complexes of 3–hydroxypicolinic acid

2.2.1.1. Compound [Co(picOH)$_2$(H$_2$O)$_2$] (I)

The reaction in aqueous media between Co^{2+} and HpicOH led to the formation of a highly crystalline, air- and light-stable product formulated as [Co(picOH)$_2$(H$_2$O)$_2$] on the basis of single-crystal X-ray diffraction and elemental analysis (see Tables 2.1 on p. 72 and C.1 (in Appendix C, p. 185)). This structure shares striking similarities with those reported by Jin and co-workers,[24] containing 1st row transition metal cations — [Zn[picOH]$_2$(H$_2$O)$_2$] and [Mn[picOH]$_2$(H$_2$O)$_2$].

Compound **I** is formed by neutral centrosymmetric [Co(picOH)$_2$(H$_2$O)$_2$] complexes, in which the Co^{2+} centre is located at an inversion centre and six-coordinated to two N,O–

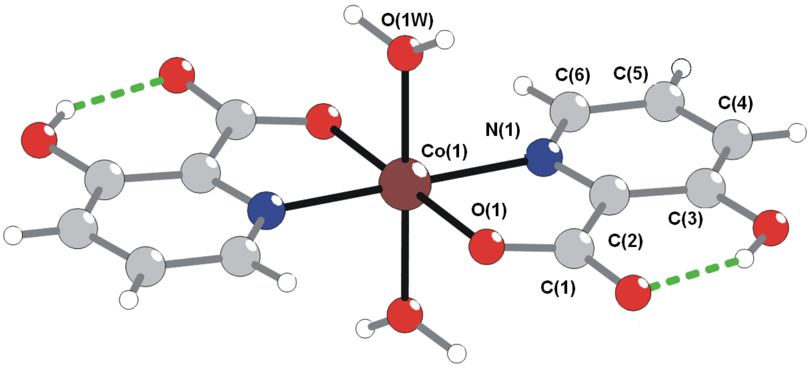

Figure 2.9.: Representation of the neutral complex $[Co(picOH)_2(H_2O)_2]$ (**I**), emphasizing the slightly distorted octahedral coordination environment for the Co^{2+} metal centre. The marked atoms belong to the asymmetric unit. For selected bond lengths and angles see Table D.1 (in Appendix D, p. 191). For details on the hydrogen-bonding geometry see Table E.1 in Appendix E, p. 201.

chelating $picOH^-$ anionic ligands [bite angle of 78.24°] plus two water molecules, $\{CoN_2O_4\}$, with coordination geometry resembling a slightly distorted octahedron (Fig. 2.9 and Table D.1 (in Appendix D, p. 191)). As found in the structures containing Zn^{2+} and Mn^{2+},[24] the water molecules are *trans*-coordinated (Fig. 2.9) with the $O_{water}-Co-O_{water}$ vector not being exactly perpendicular to the $\{N_2O_2\}$ plane of the octahedron formed by the two $picOH^-$ anionic ligands (Table D.1). The vector is indeed tilted by a combination of *ca.* 3.1° and 0.9° in both directions of the $\{N_2O_2\}$ plane, values comparable with those registered for $[Zn[picOH]_2(H_2O)_2]$ and $[Mn[picOH]_2(H_2O)_2]$ (*ca.* 2.9/0.8 and 2.5/1.2, respectively).[24] This distortion seems to be driven by the presence of extensive hydrogen-bonding networks in the crystal structures of these compounds. In fact, apart from the homonuclear, intramolecular and strong O−H···O hydrogen bond between the hydroxyl and the carboxyl groups (Fig. 2.9 and Table E.1 in Appendix E, p. 201), each $[Co(picOH)_2(H_2O)_2]$ moiety is further strongly hydrogen-bonded via the coordinated water molecules to another four neighbouring complexes.

2.2.1.2. Compound *mer*−$[N(CH_3)_4][Co(picOH)_3] \cdot H_2O$ (II)

The substitution of the coordinated water molecules from the coordination sphere of **I** by a third 3–hydroxypicolinate ligand leads to the formation of *mer*-isomer $[Co(picOH)_3]^-$ complex anion (Fig. 2.10) which co-exists in the asymmetric unit of **II** with a tetramethylammonium cation plus a crystallization water molecule, corresponding to the empirical formula of *mer*−$[N(CH_3)_4][Co(picOH)_3] \cdot H_2O$ (**II**).

As in the previous structure, the crystallographically unique Co^{2+} centre appears six-coordinated, $\{CoN_3O_3\}$ (Fig. 2.10), with a geometry resembling a distorted octahedron due to the geometrical constraints of the $picOH^-$ ligand. On the one hand, the chelating nature of 3–hydroxypicolinate leads to an average bite angle of *ca.* 78.7 which, although comparable with the analogous value for **I** [78.23(5)°], imposes some strain in the octahedral geometry; on the other, the presence of three large substituent ligands within the first coordination

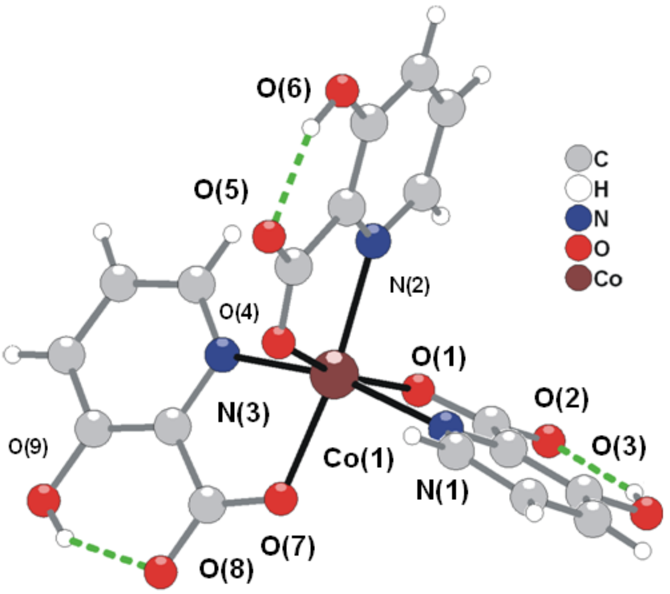

Figure 2.10.: Schematic representation of the anionic *mer*$-[Co(picOH)_3]^-$ complex in *mer*$-[N(CH_3)_4][Co(picOH)_3] \cdot H_2O$ (**II**), showing the slightly distorted octahedral coordination environment for the Co^{2+} metal centre. The marked atoms are the non-hydrogen atoms belonging to the asymmetric unit. For selected bond lengths and angles see Table D.1. For details on the hydrogen-bonding geometry see Table E.1.

sphere leads to an inherent steric hindrance directly affecting the global geometry of the complex. In fact, these distortions are reflected in the ranges of the *cis* and *trans* angles of the octahedron which can be found within the 78.45(8)–98.22(9) and 163.84(9)–171.45(9) ranges, respectively (Table D.1). The average Co−O and Co−N distances are almost identical (*ca.* 2.07 and 2.14 Å, respectively) and comparable with those found in related compounds.[47,48]

The hydrogen-bonding network present in the crystal structure of **II** is not so extensive as that described for **I**. However, physical bridges via homonuclear and relatively strong O−H···O hydrogen bonds between neighbouring *mer*-$[Co(picOH)_3]^-$ complex anions are assured by the crystallization water molecules (Fig. 2.11 and Table E.1) which, along with interactions of the intra-molecular nature, lead to the formation of a supramolecular hydrated {*mer*$-[Co(picOH)_3] \cdot H_2O\}^-$ anionic tapes running along the *a* direction (Fig. 2.11, perpendicular to the plane of the representation).

2.2.1.3. Compound $[Cu(picOH)_2]$ (III)

Compound (**III**) contains centrosymmetric $[Cu(picOH)_2]$ neutral complexes (Fig. 2.12) in which the metal centre is coordinated to two N,O− chelating $picOH^-$ anionic ligands with bite angle O(1)−Cu(1)−N(1) 83.96(6)° and exhibits a distorted square planar coordination geometry (Table D.1). The crystal structure of this compound has been described by Sun *et al.*[24] The bond length Cu−O is equal to 1.95 Å and is slightly shorter than the Cu−N, equal to 1.97 Å. Other two hydroxyl oxygen atoms from two neighbouring $picOH^-$ ligands

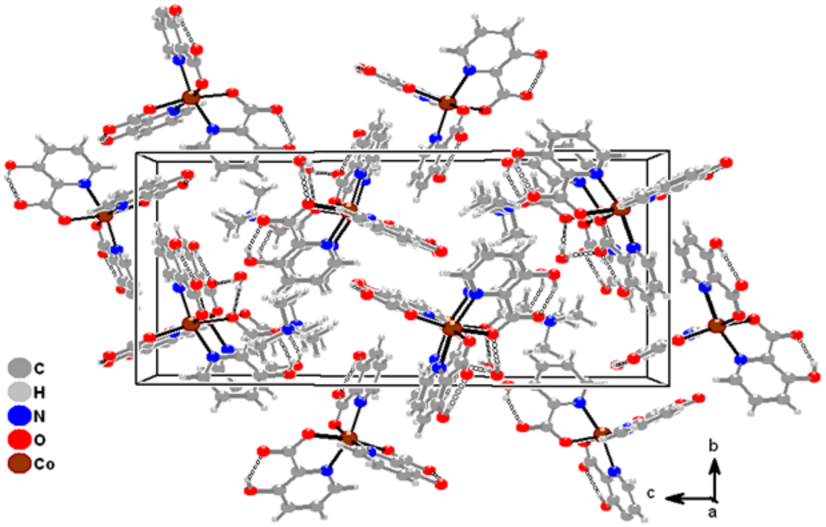

Figure 2.11.: Crystal packing of *mer*−$[N(CH_3)_4][Co(picOH)_3] \cdot H_2O$ (**II**) viewed in perspective along the *a* direction, with the O−H···O hydrogen-bonding interactions represented as dashed white-filled bonds. The crystallization water molecule establishes a physical link between neighbouring anionic *mer*−$[Co(picOH)_3]^-$, leading to the formation of supramolecular hydrated $\{mer{-}[Co(picOH)_3] \cdot H_2O\}^-$ anionic tapes running along the *a* direction. For details on the hydrogen-bonding geometry see Table E.1.

might interact weakly with the Cu^{2+} ion (see Fig. 2.13). These two oxygen atoms occupy axial positions of a distorted octahedron equally distant from the metal centre (at 2.73 Å). The axis connecting the two hydroxyl atoms and the metal centre are almost perpendicular to the coordinating square-plane of the Cu^{2+} ion (with angles O−Cu−N of 91° and O−Cu−O — 80°). The crystal packing along *a* direction can be seen in Fig. 2.13.

2.2.1.4. Compound $[Cu(picOH)_2(BPE)]_2 \cdot [Cu(picOH)_2(BPE)_2] \cdot 8\,H_2O$ (IV)

The typical square planar coordination geometry of Cu^{2+} in the neutral complex **III** leaves the axial positions available for further coordination, which was achieved by using the bridging ligand 1,2–bis(4–pyridyl)ethane (BPE),[49–68] a derivative of the widely used 4,4'-

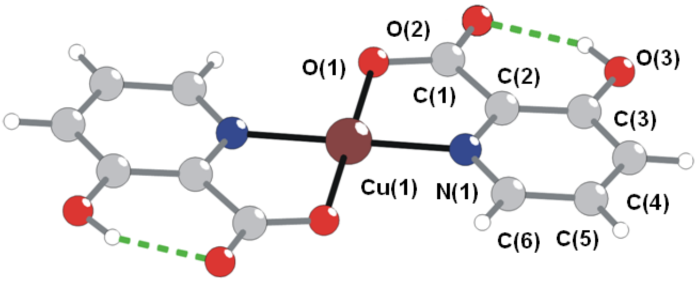

Figure 2.12.: Schematic representation of the neutral complex $[Cu(picOH)_2]$ (**III**), emphasising the slightly distorted square planar coordination environment for the Cu^{2+} metal centre. Non-hydrogen atoms belonging to the asymmetric unit are represented with thermal ellipsoids drawn at 50% probability. For selected bond lengths and angles see Table D.1. For details of hydrogen-bonding geometry see Table E.1.

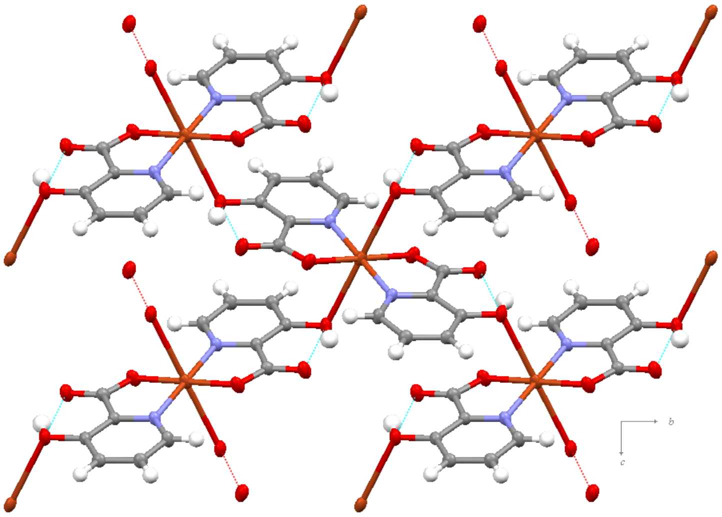

Figure 2.13.: Crystal packing of compound [Cu(picOH)$_2$] (**III**) viewed in perspective along the *a* direction with hydrogen-bonding interactions represented with dashed lines. For details of hydrogen-bonding geometry see Table E.1.

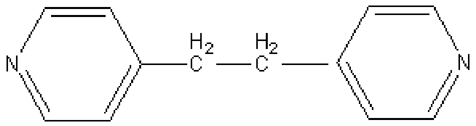

Figure 2.14.: 1,2–bis(4–pyridyl)ethane.

bipyridine rod-like organic ligand in which two methylene groups have been introduced between the 4-pyridyl groups (Fig. 2.14). The inclusion of BPE in the reactive mixture from which compound **III** was isolated led to the formation of a novel material, isolated in the crystalline solid-state and formulated as $[Cu(picOH)_2(BPE)]_2 \cdot [Cu(picOH)_2(BPE)_2] \cdot 8\,H_2O$ (**IV**) (Tables 2.1 and C.1).

Individual [Cu(picOH)$_2$] neutral complexes in **IV** are axially bridged by the highly flexible BPE organic ligand, leading to the formation of centrosymmetric secondary building units (Fig. 2.15 (a) and (b)), which are further interconnected along the *b* direction to form [Cu(picOH)$_2$(BPE)] 1D coordination polymers (Fig. 2.16). Within the unit cell there are two crystallographically independent types of 1D polymers, each one associated with a unique Cu^{2+} metal centre [Cu(1) and Cu(2) in Fig. 2.15 (a) and (b)]. Although topologically identical, the formation of these two polymers essentially arises from the high flexibility of the BPE ligands imposed by the presence of two methylene groups between the coordinating 4–pyridyl aromatic rings: while in [Cu^1(picOH)$_2$(BPE)] the ditopic BPE ligands adopt the typical *anti* conformation as described by Hennigar *et al.*,[68] with the two 4–pyridyl rings lying in parallel planes separated by *ca.* 0.8 Å (Fig. 2.15 (a)), in [Cu^2(picOH)$_2$(BPE)] this same conformation is not so markedly observed with rotations about the methylene groups

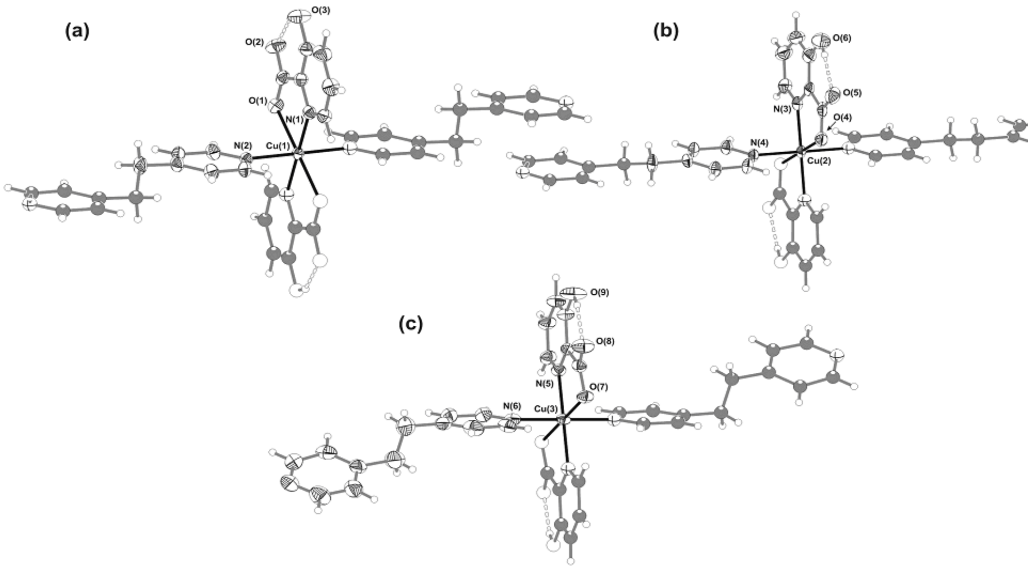

Figure 2.15.: Schematic representation of the secondary building units of the (a) and (b) 1D [Cu$^{1 \text{ and } 2}$(picOH)$_2$(BPE)] polymers and of the (c) neutral [Cu(picOH)$_2$(BPE)$_2$] complex present in [Cu(picOH)$_2$(BPE)]$_2$ · [Cu(picOH)$_2$(BPE)$_2$] · 8 H$_2$O **IV**, emphasising the slightly distorted octahedral coordination environment (showing Jahn-Teller distortion) of each crystallographically independent Cu^{2+} centre. Non-hydrogen atoms belonging to the asymmetric unit are represented with thermal ellipsoids drawn at 50% probability. For selected bond lengths and angles see Table D.1. For details of the hydrogen-bonding geometry see Table E.1.

leading to a closer approximation of *ca.* 0.4 Å between parallel planes (Fig. 2.15 (b)). However, such flexibility does not lead to variations for the intermetallic distances with both Cu(1)···Cu(1)$^{\text{i}}$ (Fig. 2.16) and Cu(2)···Cu(2)$^{\text{i}}$ distances being 13.42 Å.

Apart from these 1D polymers, the structure of compound **IV** also contains discrete [Cu(picOH)$_2$(BPE)$_2$] neutral complexes in which BPE molecules act as unidentate ligands (via the N(6) donor atom; Fig. 2.15 (c)), leaving the second 4–pyridyl group uncoordinated but engaged in a $\pi - \pi$ interaction with another neighbouring and crystallographically related aromatic ring (Fig. 2.17; distance between rings of *ca.* 3.6 Å). We note that these weak interactions, on the one hand, are responsible for a prominent rotation about the methylene groups leading to a significant dihedral angle of *ca.* 33° between the two 4–pyridyl rings (Fig. 2.15 (c)) and, on the other, lead to the formation of a third type of weakly $\pi - \pi$

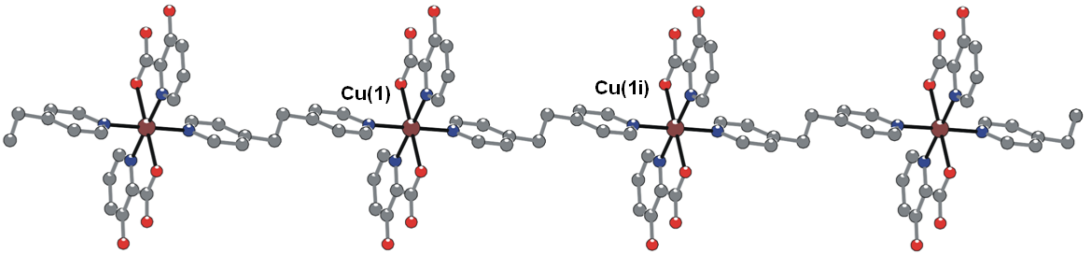

Figure 2.16.: View of the 1D [Cu^1(picOH)$_2$(BPE)] coordination polymer. Individual complexes identical to those in compound **III**, [Cu(picOH)$_2$], are bridged along the *b* direction via ditopic BPE ligands, imposing Cu(1)···Cu(1)$^{\text{i}}$ distances of 13.42 Å (symmetry code: (i) $x, 1 + y, z$).

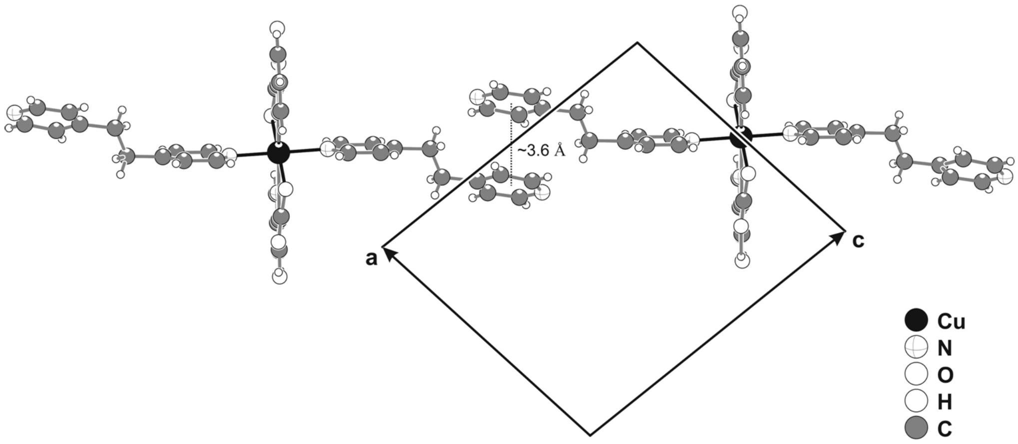

Figure 2.17.: Perspective view along the *b* direction showing the $\pi - \pi$ stacking between neighbouring 4–pyridyl groups belonging to adjacent neutral [Cu(picOH)(BPE)$_2$] complexes (compound **IV**).

bounded polymer (Fig. 2.17).

The three crystallographically unique Cu^{2+} centres in **IV** exhibit a slightly distorted octahedral geometry, {CuO$_4$N$_2$}, due to the typical Jahn-Teller effect usually observed in complexes containing this type of metal centre (Fig. 2.15 and Table D.1). In fact, although in compound **III** the Cu−O and Cu−N are statistically identical to *ca.* 1.96 Å (Table D.1), upon coordination to the BPE ligands these distances become significantly different with average values of *ca.* 2.28 Å and 2.03 Å, respectively (Table D.1). With the increase in the Cu−O bond lengths the average bite angle of picOH$^-$ in **IV** (*ca.* 78°; Table D.1) is significantly smaller than those observed for **III** (*ca.* 84°; Table D.1) and in related complexes.[24]

The structure of compound **IV** is formed by the previously described coordination polymers [Cu(picOH)$_2$(BPE)] which run along the *b* direction [Cu^1(picOH)$_2$(BPE)] through the middle of the unit cell intersecting the *ac* plane; [Cu^2(picOH)$_2$(BPE)] run along the *b*-edge and close-pack with the space-filling discrete neutral [Cu(picOH)$_2$(BPE)$_2$] moieties (Fig. 2.18 (a)). The four crystallographically unique crystallization water molecules are involved in an extensive hydrogen-bonding network composed of strong homonuclear hydrogen bonds O−H···O which, along with the related intramolecular (picOH$^-$) interactions between hydroxyl and carboxyl groups (Table E.1), further establish physical links between complexes and 1D polymers, and generally contribute to the global cohesion of the crystal structure (Fig. 2.18 (b)).

2.2.1.5. Compound Ni(picOH)$_2$(H$_2$O)$_2$ (V)

Another coordination compound, with general empirical formula Ni(picOH)$_2$(H$_2$O)$_2$, was isolated and characterised in the solid-state as homogeneous phase-pure material. An aqueous solution containing Ni^{2+} was allowed to diffuse into a silica gel matrix containing HpicOH. Thus, a crystalline material, which could be manually isolated in the form of large single-crystals, was formed in some days (see Chapter 7). Information concerning crystallographic data collection for compound **V** is summarised in Table C.2.

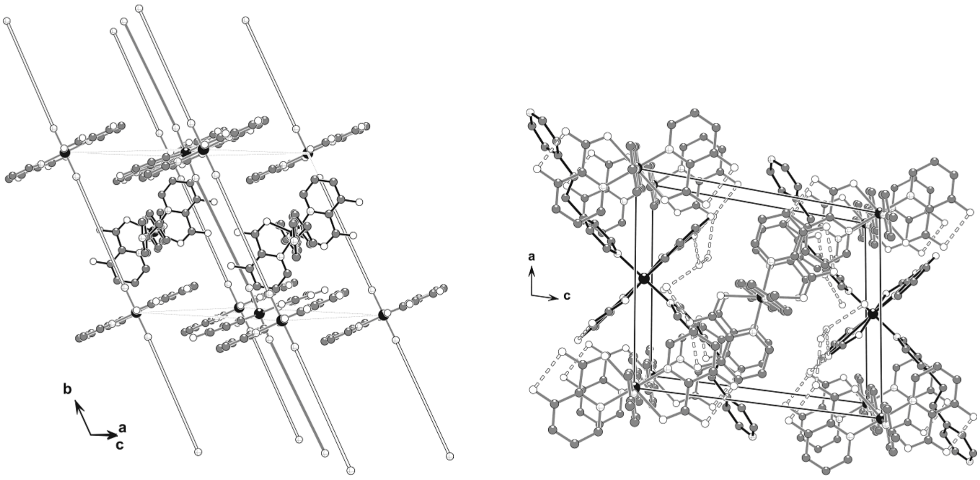

(a) (b)

Figure 2.18.: (a) 1D [$Cu^{1 \text{ and } 2}(picOH)_2(BPE)$] coordination polymers along the *b* direction: BPE molecules are replaced by grey-filled rods for [$Cu^1(picOH)_2(BPE)$] and white-filled rods for [$Cu^2(picOH)_2(BPE)$]; (b) Crystal packing of compound **IV** viewed along the *b* direction. 1D [$Cu^{1 \text{ and } 2}(picOH)_2(BPE)$] polymers are represented with grey-filled bonds. Hydrogen bonds are represented as dashed bonds (Table E.1). (a) and (b): Neutral [$Cu(picOH)_2(BPE)_2$] complexes are represented with black-filled bonds. Water molecules and hydrogen atoms have been omitted for clarity.

In compound **V** the Ni^{2+} centre is located at an inversion centre and six-coordinated to two N,O− chelating $picOH^-$ anionic ligands [bite angle of 80.57(2)°] plus two water molecules, {NiN_2O_4}, with the coordination geometry resembling a slightly distorted octahedron (see Fig. 2.19). Selected bond lengths and angles are given in Tables D.1 and E.1. This structure (like compound **I**) shares similarities with those reported by Jin and co-workers,[24] also containing 1st row transition metal cations — [$Zn[picOH]_2(H_2O)_2$] and [$Mn[picOH]_2(H_2O)_2$].

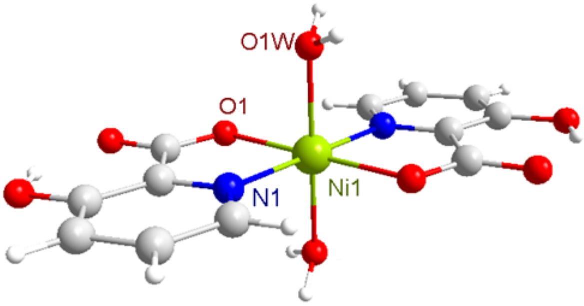

Figure 2.19.: Schematic representation of the neutral complex $Ni(picOH)_2(H_2O)_2$ (**V**), showing the slightly distorted octahedral coordination environment for the Ni^{2+} metal centre. For selected bond lengths and angles see Table D.1. For details on the hydrogen-bonding geometry see Table E.1.

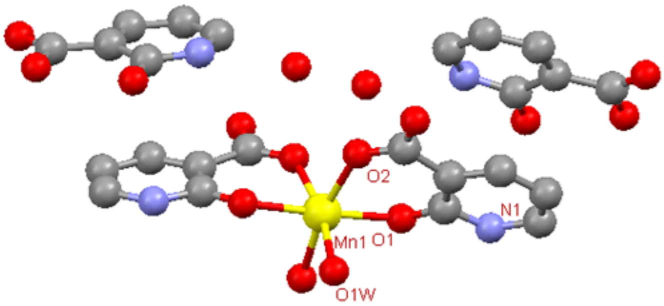

Figure 2.20.: Representation of the neutral complex $[Mn(H_2nicO)_2(H_2O)_2](H_2nicO)_2 \cdot 2\,H_2O$ (**VI**). For selected bond lengths and angles see Table D.1.

2.2.2. Crystal structures of complexes of 2–hydroxynicotinic acid

2.2.2.1. Compound $[Mn(H_2nicO)_2(H_2O)_2](H_2nicO)_2 \cdot 2\,H_2O$ (VI)

The hydrothermal reaction between Mn^{2+} and HnicOH led to the formation of a crystalline coordination compound, formulated as $[Mn(H_2nicO)_2(H_2O)_2](H_2nicO)_2 \cdot 2\,H_2O$ (see Table 2.2 and C.2).

Compound **VI** is formed by neutral complex $[Mn(H_2nicO)_2(H_2O)_2](H_2nicO)_2 \cdot 2\,H_2O$, containing the centrosymmetric unit $[Mn(H_2nicO)_2(H_2O)_2]$ (Figs. 2.20 and 2.21), in which the Mn^{2+} cation is located at the C_2 axis of the space group and six-coordinated to two O,O−chelating H_2nicO^- anionic ligand in ketone tautomeric form [bite angle of 82.46°] (to one carboxyl and one hydroxyl oxygen atoms) plus two water molecules, $\{MnO_6\}$. The coordination geometry resembles a distorted octahedron, with bond angles represented in Table D.1. In this complex, the water molecules are *cis*-coordinated with the $O_{(water)}-Mn-O_{(water)}$ angle being of 90.18° (Table D.1). The $Mn-O_{(carboxyl)}$ (2.13 Å) and $Mn-O_{(water)}$ (2.22 Å) bonds are slightly longer than $Mn-O_{(hydroxyl)}$ (2.14 Å). This complex coexists with two neutral H_2nicO residues in ketone tautomeric form and two water molecules. The strong $O-H\cdots O$ hydrogen bonds between the neutral units are assured by the hydrogens, bonded to the pyridine nitrogen atoms, and the carboxyl and carbonyl oxygens. The strong network of hydrogen bonds is completed from the coordinated water molecules (see Fig. 2.22 and Table E.1). The neutral H_2nicO residues are connected via hydrogen bonding to two waters and two neutral units.

2.2.2.2. Compound $M[HnicO]_2[H_2O]_2$, where M = Ni^{2+} (VII) and Mn^{2+} (VIII)

Two identical crystalline, air- and light-stable compounds of HnicOH and Mn and Ni with formula $M[HnicO]_2[H_2O]_2$, where M = Ni^{2+} (**VII**) and Mn^{2+} (**VIII**) were crystallized in gel media (for details see Tables 2.2 and C.2). Identical structures with the same ligand have already been reported: for Mn(II),[8,69] Zn(II),[70] Co(II),[70,71] and Cu(II) and Ni(II).[72]

Compound **VII** is formed by neutral centrosymmetric $Ni[HnicO]_2[H_2O]_2$ complex (Fig. 2.23), in which the Ni^{2+} cation is located at an inversion centre and six-coordinated

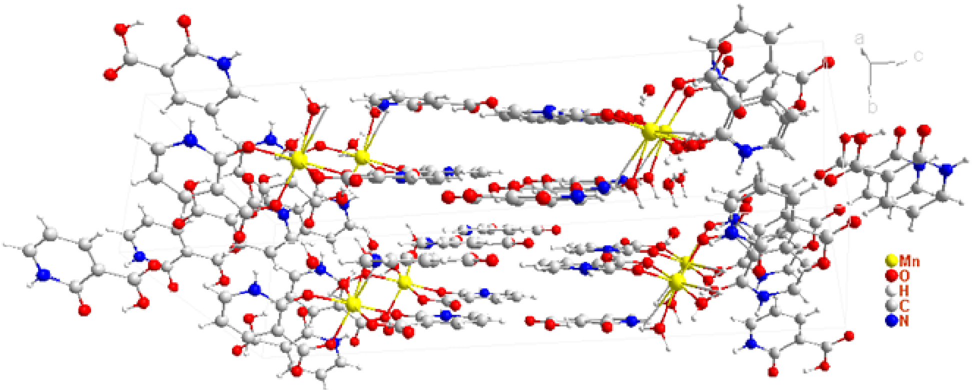

Figure 2.21.: Crystal packing of compound $[Mn(H_2nicO)_2(H_2O)_2](H_2nicO)_2 \cdot 2\,H_2O$ (**VI**).

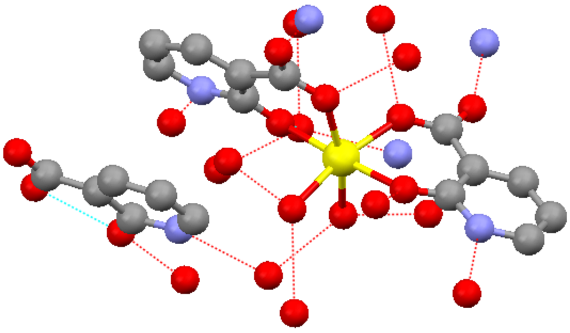

Figure 2.22.: Representation of the neutral complex $[Mn(H_2nicO)_2(H_2O)_2](H_2nicO)_2 \cdot 2\,H_2O$ (**VI**) with hydrogen-bondings (for details see Table E.1).

to two symmetry-related O,O− chelating $HnicO^-$ anionic ligands in ketone tautomeric form [bite angle of 89.05°]: one carboxyl and one carbonyl oxygen atoms, plus two water molecules, $\{NiO_6\}$. The coordination geometry resembles a slightly distorted octahedron (Fig. 2.23 and Table D.1), according to the registered bond angles ($O_{(water)}-Ni-O_{(carboxyl)}$ = 87.35°, $O_{(hydroxyl)}-Ni-O_{(carboxyl)}$ = 89.05°, etc.) and lengths. As found in other structures containing Mn^{2+},[8,69] the water molecules are *trans*-coordinated (Fig. 2.23) with the $O_{water}-Ni-O_{water}$ vector being approximately perpendicular to the $\{O_4\}$ plane formed by the two $HnicO^-$ anionic ligands (angles O(1W)−Ni(1)−O(3) and O(1W)−Ni(1)−O(1)^{i} are *ca.* 93°, and O(1W)−Ni(1)−O(1) and O(1W)−Ni(1)−O(3)^{i} are *ca.* 87°) (Table D.1). The bond $Ni-O_{(carboxyl)}$ (1.987 Å) is a slightly shorter than $Ni-O_{(hydroxyl)}$ (2.074 Å) and Ni−O (H_2O), nevertheless both are comparable to these of the reported $Mn-O_{(carboxyl)}$ (2.2 Å), and $Mn-O_{(hydroxyl)}$ and Mn−O (H_2O) approximatively equal to 2.20 Å.[8]

Each $[Ni(HnicO)_2(H_2O)_2]$ unit is strongly hydrogen-bonded via the coordinated water molecules to the non-coordinated carboxyl oxygens of another four neighbouring complex units, leading to an expansion of the dimensionality of the structure into the two dimensions (see Fig. 2.24). Meanwhile hydrogen bonds between the hydrogen bonded to the pyridine nitrogen, the uncoordinated carboxyl, the carbonyl oxygens and the coordinated water

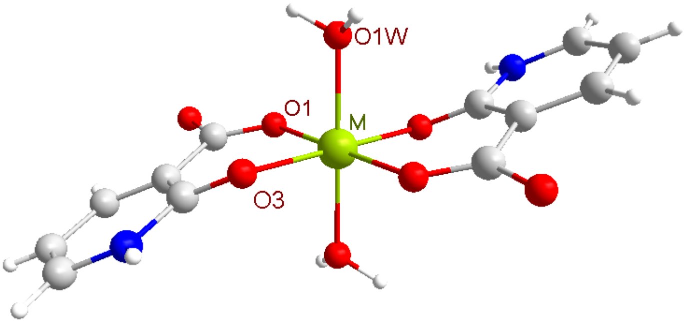

Figure 2.23.: Representation of the neutral complex $M[HnicO]_2[H_2O]_2$, where M = Ni^{2+} (VII) and Mn^{2+} (VIII), emphasizing the slightly distorted octahedral coordination environment for the metal centre. For selected bond lengths, angles and hydrogen-bonding see Tables D.1 and E.1.

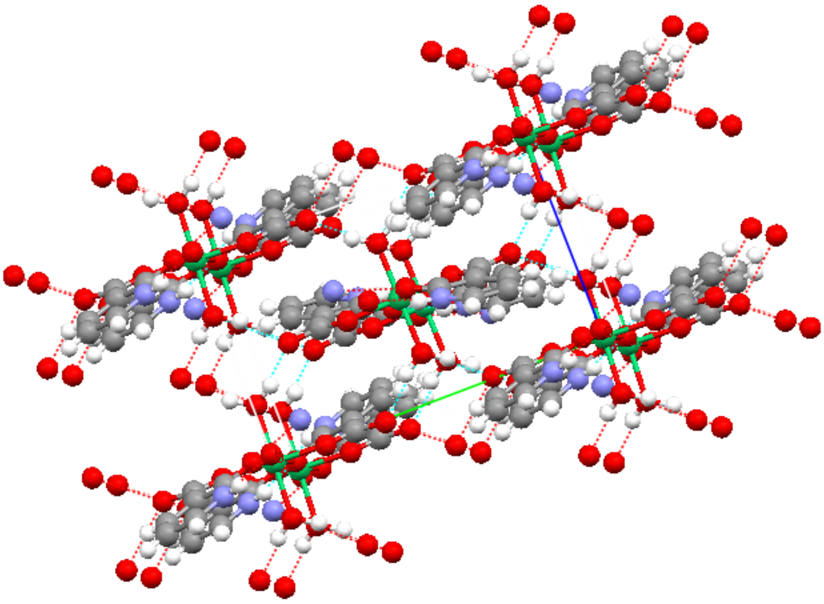

Figure 2.24.: Crystal packing of compound $M[HnicO]_2[H_2O]_2$, where M = Ni^{2+} (**VII**) and Mn^{2+} (**VIII**), viewed in perspective along the *a* direction with hydrogen-bonding (dashed lines).

molecules (see Table E.1) are formed.

The details of the crystallographic data can be seen in Table C.2 and the bond lengths and angles for the identical compound $Mn[HnicO]_2[H_2O]_2$ (**VIII**) are presented in Table E.1.

2.2.2.3. Compounds $Co[HnicO]_2[H_2O]_2$ (IX), $Mn[HnicO]_2[H_2O]$ (X) and $Cu[HnicO]_2$ (XI)

The efforts to obtain single crystals of these three new compounds were not successful so far. The powder samples of $Co[HnicO]_2[H_2O]_2$, $Mn[HnicO]_2[H_2O]$ and $Cu[HnicO]_2$ were characterised with powder XRD, elemental analyses, FT–IR and TGA (see Table 2.2) and the data are analysed bellow. The results indicate that compound **IX** is structurally identical to the compound **VII**. Apart the crystals of $[Mn(H_2nicO)_2(H_2O)_2](H_2nicO)_2 \cdot 2\,H_2O$ (**VI**) and $Mn[HnicO]_2 \cdot 2\,H_2O$ (**VIII**), the reactions between Mn^{2+} and H_2nicOH gave rise to powder

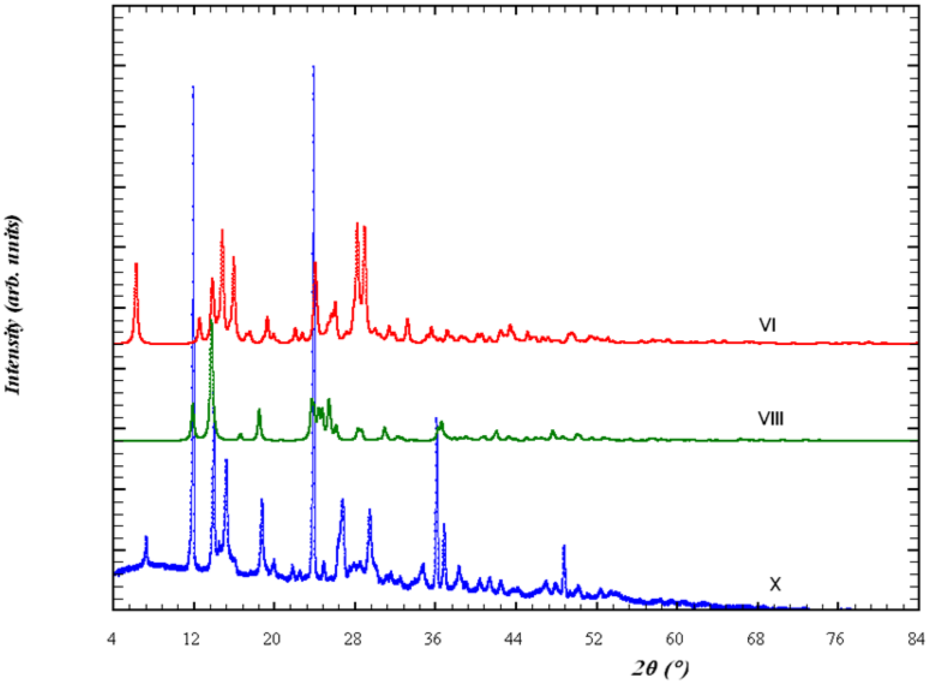

Figure 2.25.: Powder XRD patterns of the Mn^{2+} and HnicOH compounds (**VI**, **VIII** and **X**).

of compound **X**, formulated as $[Mn(HnicO)_2] \cdot H_2O$, whose powder XRD pattern does not match the simulated powder XRD pattens of the crystals (see Fig. 2.25).

2.2.3. Crystal structures of complexes of 2–mercaptonicotinic acid

2.2.3.1. Compound $[Ni(phen)_3](H_2nic_2S_2)_2 \cdot 2\,H_2O$ (XII)

The compound $[Ni(phen)_3](H_2nic_2S_2)_2 \cdot 2\,H_2O$ was isolated in trace amounts as small single-crystals (see crystallographic data in Table C.3; in the molecular formula phen is 1,10–phenanthroline and $H_2nic_2S_2$ is 2,2′–dithiobisnicotinic acid[§]). The structure revealed by X-ray diffraction contains a Ni^{2+} octahedral cation with the first coordination sphere composed of three phen ligands (bond lengths and angles are presented in Table D.1). Each phen acts as bidentate chelating ligand through the nitrogen atoms with the Ni−N bond lengths being of *ca.* 2.1 Å (see Fig. 2.26). The planes between the phen molecules are almost perpendicular to each other (89.6° and 84.7°). During the reaction a conversion of the thiolate ligand and formation of disulphide anion of mercaptonicotinic anions is observed. Each chemical moiety has only one deprotonated carboxyl group, thus balancing the crystal charge. Two extra crystallization water molecules complete the asymmetric unit. The anionic moieties interact between each other via a series of hydrogen bonds also involving the water molecules of crystallization (for details see Fig. 2.27 and Table E.1).

[§] IUPAC name: bis(2-carboxyphenyl) disulphide.

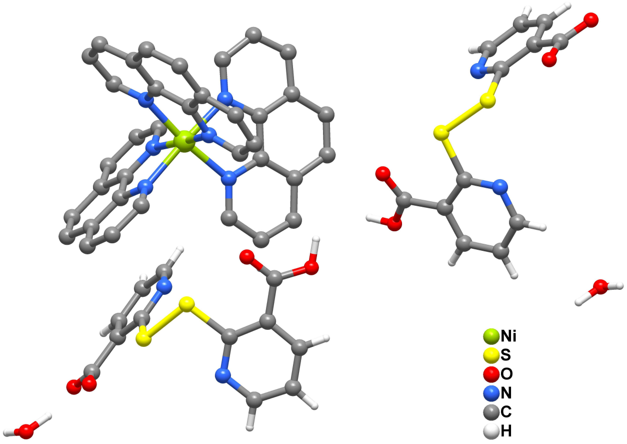

Figure 2.26.: Representation of the neutral complex [Ni(phen)$_3$](H$_2$nic$_2$S$_2$)$_2 \cdot 2\,H_2O$ (**XII**). For selected bond lengths, angles and hydrogen-bonding see Tables D.1 and E.1.

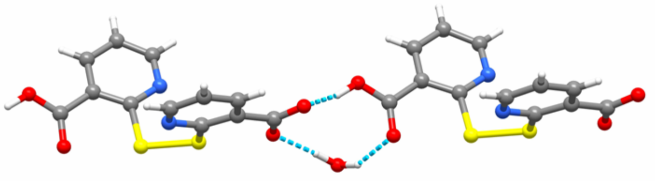

Figure 2.27.: Hydrogen-bonding in the complex [Ni(phen)$_3$](H$_2$nic$_2$S$_2$)$_2 \cdot 2\,H_2O$ ((**XII**)) (see also Table E.1).

2.2.3.2. Compound [Co(phen)(HnicS)(nicS)] (XIII)

The hydrothermal reaction between HnicSH, phen and Co^{2+} resulted in the formation of the neutral complex [Co(phen)(HnicS)(nicS)] (see crystallographic data in Table C.3). Noteworthy, X-ray diffraction evidence support the presence of Co^{3+} in the final structure which is feasible to understand considering *in situ* oxidation of the metallic centre under hydrothermal conditions. The Co^{3+} metal is six-coordinated to one phen ligand, one protonated and one deprotonated HnicSH ligands with distorted octahedral coordination geometry (see Fig. 2.28; bond lengths and angles are presented in Table D.1). The phen acts as a bidentate chelating ligand through its two nitrogen atoms, with bond lengths to the Co^{3+} atom being approximately equal (1.94 and 1.95 Å). The anionic HnicS$^-$ and nicS^{2-} ligands appear as bidentate ligands coordinated to the metal centre through the pyridinic nitrogen and the sulphur atoms, forming two four-membered chelate rings with equal bond distances between the metal and the nitrogen atoms (*ca.* 1.925 Å), and approximately equal distances between the metal and the sulphur atoms (*ca.* 2.284 and 2.290 Å). These values are closer to the values for Co(III), found in the literature[36] and in Cambridge structural database rather than to the values for Co(II) (CCDC: Co(II)−N: 2.112 Å and Co(III)−N: 1.966 Å; Co(II)−S: 2.343 Å and Co(III)−S: 2.247 Å).

While the dihedral angle between the planes of the two mercapto- ligands is of about 82.6°, that, relating the deprotonated nicS^{2-} and the phen molecule is instead of 81.1° which

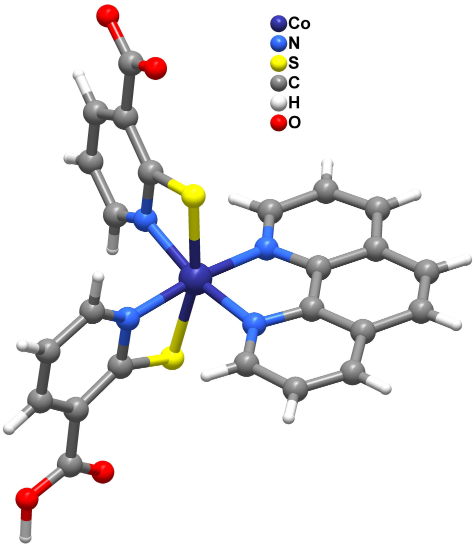

Figure 2.28.: Schematic representation of the complex [Co(phen)(HnicS)(nicS)] (**XIII**), emphasizing the slightly distorted octahedral coordination environment for the Co^{3+} metal centre. For selected bond lengths, angles and hydrogen-bonding see Tables D.1 and E.1.

is smaller than the angle between phen and the $HnicS^-$ (*ca.* 85.3°).

2.2.3.3. Compound $[Mn(phen)_2(C_{12}H_7N_2O_5)](C_{12}H_8N_2O_4S_2) \cdot 2\,H_2O$ (XIV)

The compound $[Mn(phen)_2(C_{12}H_7N_2O_5)](C_{12}H_8N_2O_4S_2) \cdot 2\,H_2O$ is a Mn^{2+} complex in which the octahedral metallic centre is coordinated to two phen ligands and by one *in situ* generated anionic $(C_{12}H_7N_2O_5)_2^-$ moiety (crystal structure data can be seen in Table C.3, and bond lengths and angles are presented in Table D.1). Under the hydrothermal conditions the HnicSH ligand is decomposed in a way that one *ortho* thiol group is substituted by another perpendicularly-bonded carboxypyridine residue, which was also modified at the vacant *ortho* position (see Fig. 2.29). Instead of the SH group an oxygen atom is coordinated to the metal centre. During the reaction a conversion of the thiolate ligand and formation of disulphide anion of mercaptonicotinic anions is also observed, corresponding to the other two identical charge balancing anionic units of bis(2-carboxyphenyl) disulphide in the crystal structure, with one deprotonated carboxyl group in each of them. The structure is completed with two crystallization water molecules.

Each of the two phen molecules acts as bidentate chelating ligand through its two nitrogen atoms with bond lengths of about 2.3 Å. Contrary to that observed for the two previous complexes, the planes between phen are not perpendicular to each other, forming an angle of about 70.0°. Noteworthy, this value is identical to the dihedral angles between the coordinated pyridine ring and the two phen residues. The *in situ* generated ligand forms a six-membered chelate ring with Mn^{2+} via the carboxyl and phenol oxygen atoms.

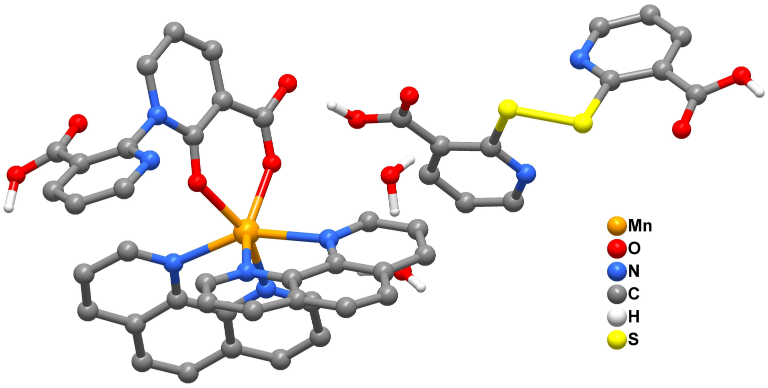

Figure 2.29.: Schematic representation of the neutral complex $[Mn(phen)_2(C_{12}H_7N_2O_5)](C_{12}H_8N_2O_4S_2) \cdot 2\,H_2O$ (**XIV**), emphasizing the slightly distorted octahedral coordination environment for the Mn^{2+} metal centre. For selected bond lengths, angles and hydrogen-bonding see Tables D.1 and E.1.

2.3. Spectroscopic and thermo-analytical results

2.3.1. Vibrational spectroscopy

Selected FT–IR data for compounds **I**, **II**, **III**, **IV** and **V** are given in Table 2.1 (only bands of HpicOH acid sensitive to metal coordination are reported). Infrared spectroscopy confirms the coordination of $picOH^-$ to the metal centres via the carboxyl group, with the asymmetric stretching $\nu_{asym}(-CO_2^-)$ mode showing shifts up to 70 cm^{-1} to lower wavenumbers when compared with the values registered for the free ligand. Furthermore, the measured values of $\Delta[\nu_{asym}(-CO_2^-)-\nu_{sym}(-CO_2^-)]$ for **I** (301 cm^{-1}), **II** (298 cm^{-1}), **III** (319 cm^{-1}), **IV** (327 cm^{-1}) and **V** (306 cm^{-1}), are clear evidence for the presence of carboxyl groups coordinated to the M^{2+} centres in unidentate fashion,[73,74] in agreement with the N,O− chelation described before (Figs. 2.9, 2.10, 2.12, 2.15 and 2.19). The $\nu(C-O)_h$ mode for **I** and **II** shows significant shifts up to *ca.* 14 and 34 cm^{-1}, and for **III**, **IV** and **V** — up to 30 cm^{-1}, respectively, when compared with the band present in the spectra of HpicOH, possibly due to hydrogen-bonding involving the carboxyl groups and the water molecules (Table E.1). The typical stretching $\nu(C-N)$ vibrational mode of substituted pyridines appears for the uncoordinated ligand at 1609 cm^{-1} and shows small shifts (up to 7 cm^{-1} (**I** and **II**) and up to 6 cm^{-1} for **III**, **IV** and **V**; see Table 2.1), in good agreement with N,O− chelation involving the nitrogen atom of $picOH^-$.

The infrared spectra (Fig. 2.30) of the complexes of HnicOH (compounds **VI**, **VII**, **VIII**, **IX**, **X** and **XI**) clearly suggest that the ligand in all compounds exist in the ketone form. It can be assumed from the existence of the weak band at about 3246 cm^{-1}, assigned to the $\nu(N-H)$ stretch, and from the $\delta(N-H)$ and γ bands at around 1607 and 539 cm^{-1} respectively, confirming that the pyridine nitrogen is protonated and after the reaction it is not directly involved in the coordination to the metal. The very strong band in the spectrum of HnicOH at 1742 cm^{-1}, which is not observed in the spectra of the complexes (except for com-

Table 2.1.: Analytical and spectroscopic data for 3–hydroxypicolinic acid and its compounds (**I–V**).

	Elemental composition (%)[a]			Vibrational data (cm^{-1})[b]			
Compound	C	N	H	$\nu_{asym}(-CO_2^-)$	$\nu(C-N)$	$\nu_{sym}(-CO_2^-)$	$\nu(C-O)_h$
HpicOH				1701s	1609s	1322s	1282vs
I	38.05	7.38	3.55	1644s	1602s	1343s	1268s
	(38.83)	(7.55)	(3.26)				
II	46.31	9.93	4.83	1631s	1602s	1333s	1248s
	(46.73)	(9.91)	(4.63)				
III	41.90	7.94	2.00	1647vs	1608s	1328s	1274s
	(42.00)	(8.25)	(2.37)				
IV	55.60	10.83	4.50	1637s	1615s	1310s	1252s
	(55.01)	(10.69)	(3.85)				
V	34.16	6.63	3.01	1650s	1614m	1344m	1253m
	(38.86)	(7.55)	(3.26)				

(a) Calculated values in parentheses; (b) vs — very strong; s — strong; m — medium

pound **VI**), is assigned to the $\nu(C{=}O)$ stretch. The ligands display the same (O,O−) coordination modes in the six compounds (not evident for compound **VI**), shown by the shift of the band at 1742 cm^{-1} ($\nu(C{=}O)$ stretch) to lower wavenumbers (see Table 2.2). The symmetric mode $\nu_{sym}(-CO_2^-)$ shows shift up to 58 cm^{-1}. In the spectrum of compound **VI** a very strong band at 1752 cm^{-1} and a characteristic band of the symmetric stretch $\nu_{sym}(-CO_2^-)$ are present, which confirm the presence of the uncoordinated ligand in the structure.

Spectroscopic data for the complexes of HnicSH are shown in Table 2.3. The assignments are based on those existing in the literature for HnicSH,[40,42,75] heterocyclic thiones[76–78] and thiosalicylic acid complexes.[79,80] HnicSH shows the characteristic thione-thiol tautomerism of the heterocyclic thiones[33] as was mentioned before (Fig. 2.6). In the infrared spectra of the free HnicSH ligand, the presence of the stretching $\nu(C{=}S)$ at 1143 cm^{-1} and of the $\nu(N-H)$ at around 3065 cm^{-1},[77,81] and the absence of the $\nu(S-H)$ absorption band at 2500 cm^{-1},[78,79] suggest that the solid ligand exist in the thione form rather than in the thiol form. The shifts of the positions of the bands assigned to the stretching $\nu(C{=}O)$ in the spectra of the complexes to lower wavenumbers — for compound **XII** (1654 cm^{-1}), and to higher — for compounds **XIII** (1716 cm^{-1}) and **XIV** (1682 cm^{-1}, very similar to the free ligand — 1679 cm^{-1}) indicate the existence of hydrogen bonding in the HnicSH (with participation of deprotonated hydroxyl oxygen) in compounds **XIII** and **XIV**. This is also seen from the presence of bands around 3000 cm^{-1}, which for the case of compound **XIII** indicate the presence of non-ionized hydroxyl group. The weak band at 1598 cm^{-1} of the free ligand is assigned to the $\nu(C{=}N)$ stretching mode and in the complexes we observe that there is a shift of this stretching band to lower wavenumbers: to 1590 cm^{-1} for compound **XII**, to 1576 cm^{-1} for **XIII** and to 1588 cm^{-1} for **XIV**. The nitrogen atom from HnicSH in complex **XII** is not involved in the coordination (see crystal structure), but we assign the small shift of the stretching to the (C=N) in the phen molecules.

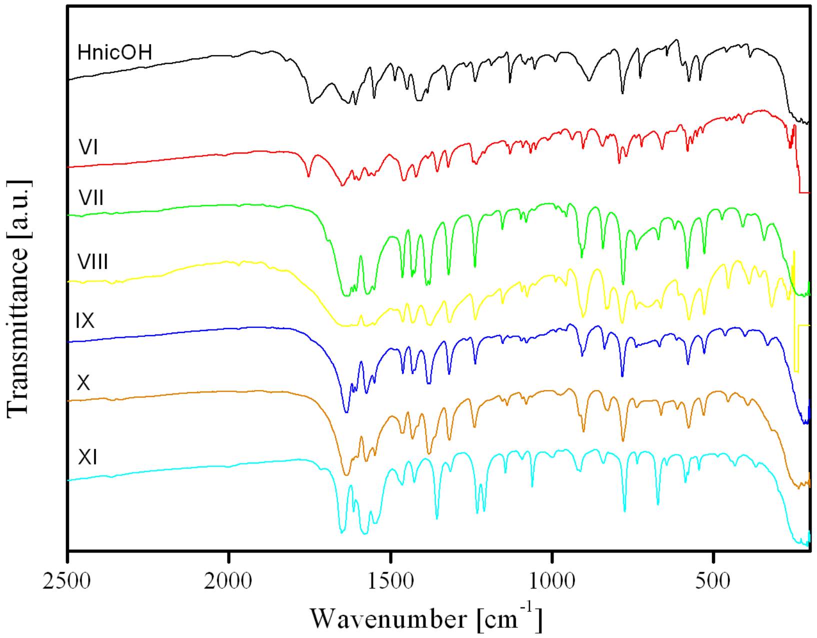

Figure 2.30.: Infrared spectra of HnicOH and its coordination compounds (**VI–XI**).

Table 2.2.: Analytical and spectroscopic data for 2–hydroxynicotinic acid and its compounds (**VI–XI**).

	Elemental composition (%)^{a}			Vibrational data (cm^{-1})^{b}		
Compound	C	N	H	$\nu_{asym}(-CO_2^-)$	$\nu(C-N), \nu(C-C)$	$\nu_{sym}(-CO_2^-)$
HnicOH	—	—	—	1630vs	1550vs	1413vs
VI	42.57 (42.30)	8.24 (8.22)	3.86 (3.85)	1645s	1549m	1420m, 1354m
VII	39.53 (38.86)	7.78 (7.55)	3.43 (3.26)	1640vs	1550vs	1384vs
VIII	40.02 (39.25)	8.22 (7.63)	3.20 (3.29)	1631s	1549m	1376s
IX	37.42 (37.23)	8.17 (7.24)	3.60 (3.12)	1634vs	1549s	1377vs
X^{c}	41.38 (41.28)	8.02 (8.02)	2.98 (2.89)	1639vs	1548s	1375vs
XI	43.09 (42.42)	8.52 (8.25)	2.28 (2.37)	1649vs	1548vs	1355

(a) Calculated values in parentheses; (b) vs — very strong; s — strong; (c) According to ICP analysis: Mn — 16% (*ca.* 15.73);

Table 2.3.: Analytical and spectroscopic data for complexes of 2–mercaptonicotinic acid (**XII–XIV**).
(a) Calculated values in parentheses; (b) vs — very strong; s —strong; m — medium; w — weak.

	Elemental composition (%)^a			Vibrational data (cm^{-1})^b					
				HnicSH					phen
Compound	C	N	H	ν(C=O)	ν(C=N)	ν(C−O)	ν(C=S)	ν(M−N)	ν(M−N)
HnicSH	—	—	—	1679vs	1598w	1332w	1142	—	—
phen	—	—	—	—	—	—	—	—	—
XII	— (62.35)	— (12.12)	— (3.60)	1679	1590m	1321w	1143	—	1497
XIII	51.74 (52.75)	10.18 (10.25)	2.80 (2.77)	1716m	1576m	1344w	1153w	390	1602w 1514w 1489w
XIV	56.10 (56.75)	10.93 (11.03)	3.54 (3.18)	1682vs	1588s	1344	1144	—	1495w

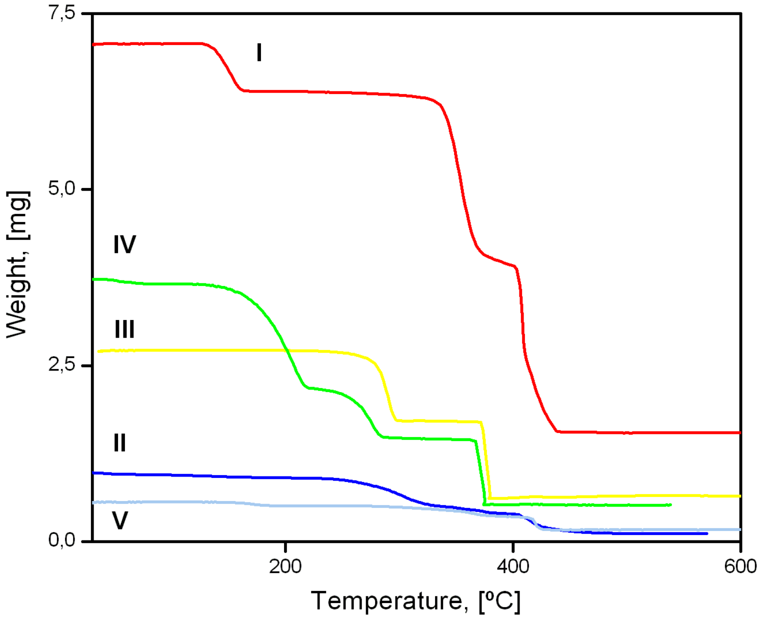

Figure 2.31.: TGA thermograms of complexes of 3–hydroxypicolinic acid (**I–V**).

2.3.2. Thermal analysis

The TGA thermograms of the compounds **I–V**, **VII**, **IX–XIV** are presented in Figs. 2.31, 2.32 and 2.33.

Thermal decomposition of compound **I** occurs in a multi-step process between ambient temperature and *ca.* 500 °C leading to the formation of the stoichiometric amount of CoO (total weight loss of 78%, calculated *ca.* 80%). The first weight loss of 10% occurs in the 80–180 °C temperature range (DTG peak at 150 °C) and is attributed to the release of the two coordinated water molecules (calculated weight loss of 10%). Between 180 and 500 °C a total weight loss of *ca.* 69% (DTG peaks at 353, 409, 418 and 432 °C) corresponds to the release of the organic component.

The thermal decomposition of **II** between ambient temperature and *ca.* 550 °C is more complex than that of **I** with more overlapping decomposition steps corresponding to the oxidation of the organic molecules. However, as for **I**, at *ca.* 550 °C only the stoichiometric CoO residue remains with a total weight loss of *ca.* 89% (calculated *ca.* 87%).

Thermal decomposition of compound **III** occurs in a multi-step process between *ca.* 95 and 395 °C, leading to the formation of the stoichiometric quantity of CuO (total weight loss of *ca.* 78%, calculated *ca.* 76%).

For compound **IV** the thermal decomposition starts in the 36–85 °C temperature range, most probably due to the release of some crystallization water molecules. Between 85 and *ca.* 402 °C the decomposition of **IV** occurs in a multi-step process due, on the one hand,

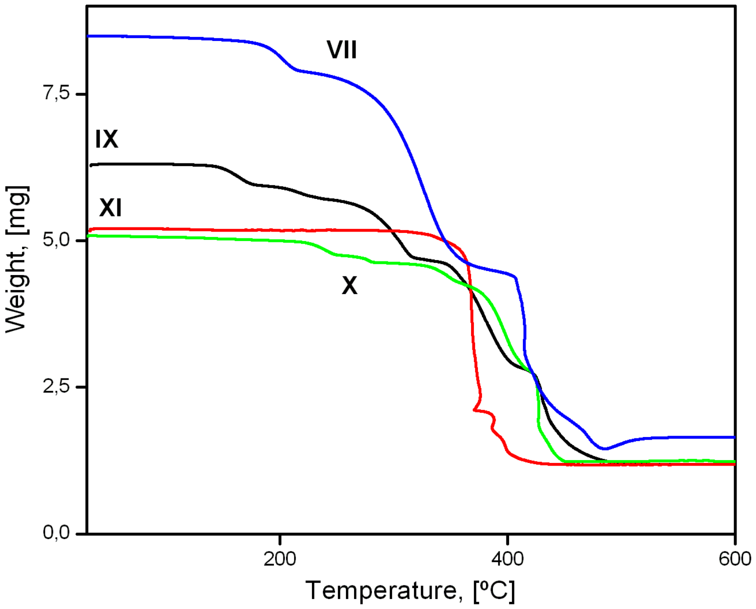

Figure 2.32.: TGA thermograms of complexes of 2–hydroxynicotinic acid (**VII, X–XI**).

to release of the remaining water molecules and, on the other, to oxidation of the organic component. The residue for **IV** is also formed by the stoichiometric quantity of CuO (total weight loss of *ca.* 86%, calculated *ca.* 88%).

Thermal decomposition of compound **V** occurs in a multi-step process between ambient temperature and *ca.* 700 °C leading to the formation of the stoichiometric amount of NiO (total weight loss of 72%, calculated *ca.* 80%). The first weight loss of 9% occurs in the 57–196 °C temperature range (DTG peak at 173 °C) and is attributed to the release of the two coordinated water molecules (calculated weight loss of 10%). Between 180 and 486 °C a total weight loss of 62% (calculated *ca.* 74%) (DTG peaks at 365 and 420 °C) corresponds to the release of the organic component.

Thermal decomposition of compound **VII** occurs in a multi-step process between *ca.* 38 and 487 °C , leading to the formation of the stoichiometric quantity of NiO (total weight loss of *ca.* 84%, calculated *ca.* 80%). The weight loss during the first decomposition step corresponds to the loss of two water molecules (weight loss 8% with calculated *ca.* 10%). The next two steps between 240 and 485 °C correspond of the releasing of the organic components (weight loss 76%, calculated *ca.* 70%).

The thermal decomposition of **IX** between 45 and *ca.* 633 °C is a five-step process. At *ca.* 633 °C only the stoichiometric CoO residue remains with a total weight loss of *ca.* 82% (calculated *ca.* 81%). The releasing of the three water molecules begins at 44 °C and continues the first three steps. During the third step (at 249 °C) a part of the organic component starts being released. The DTG peaks are at 164, 217, 307, 380 and 429 °C.

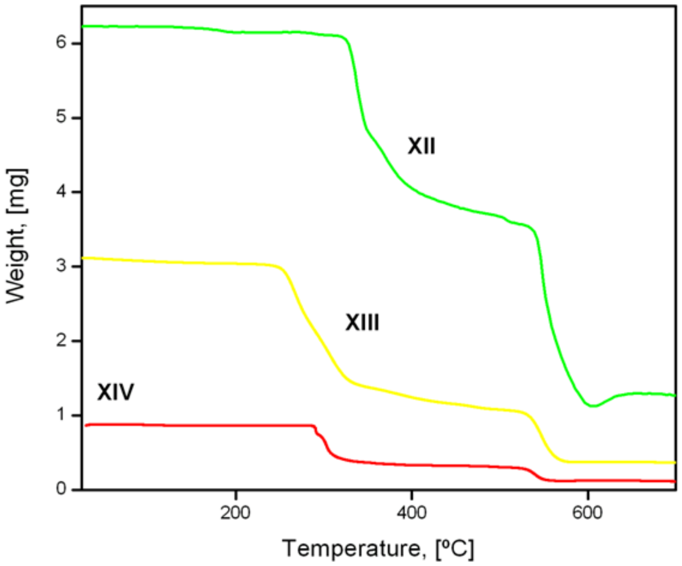

Figure 2.33.: TGA thermograms of complexes of 2–mercaptonicotinic acid (**XII–XIV**).

Thermal decomposition of compound **X** occurs in a multi-step process between 41 and 523 °C leading to the formation of the stoichiometric amount of MnO (total weight loss of 76%, calculated *ca.* 70%). The first weight loss of 7% occurs in the 40–258 °C temperature range (DTG peak at 242 °C) and is attributed to the release of one molecule of water (calculated weight loss of 5%). The release of the organic components consisting of two ligands occurs is a multi-step process between 259 and 523 °C (DTG peaks at 278, 348, 396 and 426 °C).

For compound **XI** thermal decomposition starts in the 56–473 °C temperature range. The decomposition occurs in a two-step process due to release of the organic part consisting in two ligand molecules thus confirming the suggested structure of the powder compound. The residue for **XI** is also formed by the stoichiometric quantity of CuO (total weight loss of *ca.* 78%, calculated *ca.* 77% with DTG peaks at 369 and 395 °C).

Thermal decomposition of compound **XII** occurs in a multi-step process from ambient temperature to 700 °C, to yield NiO as the final residue (total weight loss: 89%; calculated: 80%). The weight losses occur in the temperature range 42–699 °C (DTG peaks at 289, 303 and 539 °C) and is attributed to the release of one molecule of water (2%, calculated *ca.* 2%), the organic components: the three molecules of phen (62%, calculated weight loss of 64%) and the molecule of new modified ligand (25%, calculated weight loss of 29%).

The thermal decomposition of compound **XIII** occurs in a multi-step process from ambient temperature to 650 °C, to yield CoO as the final residue (total weight loss: 82%; calculated: 86%). The weight losses occur in the temperature range 58–606 °C (DTG peaks at 337, 507 and 548 °C) and is attributed to the release of one molecule of crystallization water (2%), the organic components: the molecule of phen (38%, calculated weight loss of

36%) and the two molecules of HnicSH.

The thermal decomposition of compound **XIV** occurs in a multi-step process from ambient temperature to 900 °C, to yield MnO as the final residue (total weight loss: 90%; calculated: 90%). The weight losses occur in the temperature range 23–899 °C (DTG peaks at 267, 304, 547 and 734 °C) and is attributed to the release of two molecules of crystallization water, and the organic components (56%, *ca.* 64%): the two molecules of phen, one molecule of the new formed bisulphide ($C_{12}H_6N_2O_4S_2$) and one molecule of the new formed ligand ($C_{12}H_6N_2O_5$).

2.4. Magnetic properties

The magnetic properties of coordination compounds with the described ligands were studied. It was found that the complexes with HpicOH and HnicSH are paramagnetic, with deviations from the Curie law at low temperature, due to the influence of the crystal field splitting of the *d*–orbitals, usually together with weak antiferromagnetic interactions. There is a strong influence of the coordination environment around the metal centres (dimensionality, geometry of ligands, number of coordinated metal sites, presence of bridging ligands and nature of substitution groups, bond angles and lengths) on the strength of the ligand field, resulting in different values of splitting energies. The substitution of one metal with another, even in the cases of identical structures (see compounds **I** and **V**) did not give rise to magnetic interactions, neither the presence of second ligand played role as a pathway for propagation of such exchanges. Some of the coordination compounds of HnicOH, though, have performed different behaviours, although HnicOH is only a positional isomer of HpicOH. For example, compounds **VII** (Ni^{2+}) and **XI** (Cu^{2+}) are paramagnetic, while compound **IX** (Co^{2+}) is antiferromagnetic. Compound **X** (Mn^{2+}) surprisingly is metamagnetic revealing almost complete transition from antiferromagnetic to ferromagnetic behaviour. A good metal-ligand orbital overlap is expected to increase the strength of magnetic exchange in the structures containing HnicSH (**XII**, **XIII** and **XIV**), due to a greater degree of spin delocalisation onto the ligand.[35,36,82–84] But such success is limited due to the formation of disulphide for this thiolate ligand. The three compounds do not display interactions between the metal ions in the measured temperature ranges.

2.4.1. Compounds performing magnetic interactions

2.4.1.1. Compound $Co[HnicO]_2[H_2O]_2$ (IX)

Fig. 2.34 displays the plots of magnetic susceptibility as a function of temperature (χ *vs.* T) and of the field dependence of magnetization (M *vs.* H) of the powdered compound **IX** at 5 K. The fit to the Curie-Weiss law at high temperatures indicates antiferromagnetic interactions with Weiss constant –18 K. From the constant of Curie for the effective moment was found $\mu_{\text{eff}} = 4.86\mu_B$ (higher than the spin-only value $3.87\mu_B$[85] expected for high-spin Co(II) $S = 3/2$). More detailed measurements of lower temperature were not performed but

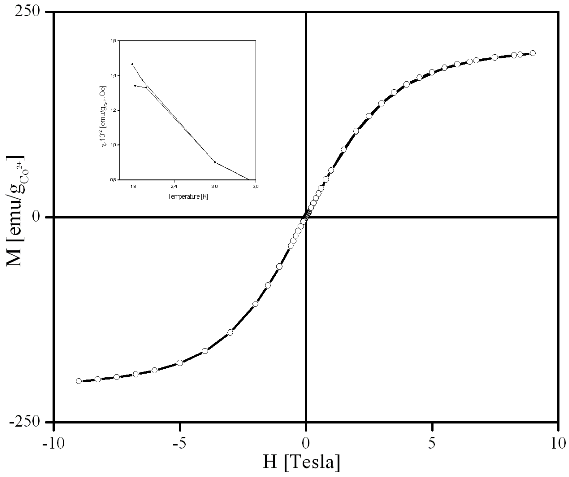

Figure 2.34.: Magnetization loop as a function of applied field at 5 K and χ *vs.* T (inset) of compound $Co[HnicO]_2[H_2O]_2$ (**IX**).

the inset of Fig. 2.34 shows the irreversibility (up to 3 K) of the magnetic susceptibility at ZFC and FC regime.

2.4.1.2. Compound $Mn[HnicO]_2[H_2O]$ (X)

The temperature dependence of the susceptibility of compound **X** shows thermal irreversibility between 1.9 and 5.3 K after cooling from ambient temperature to 1.9 K in zero applied magnetic field and after cooling under the measurement field (1000 Oe), due to existance of magnetic interactions (Fig. 2.35). At low temperature the susceptibility increases and at $T > 5.3$ K starts decreasing. The best fit of the plot χ^{-1} *vs.* T to the Curie-Weiss law (Equation 1.10 on p. 29) at high temperature gave as a result $\Theta = -9.0$ K and $C = 0.22$ emu.K/Oe.g$_{Mn^{2+}}$. The measurements of the field dependence of the magnetization at 1.9, 5 and 15 K (Fig. 2.36) show that the magnetization increases to very high values and does not reach saturation. This, together with the results from the fitting to the Curie-weiss law indicate dominant antiferromagnetic interactions over canting of magnetic moments or the incipient ferromagnetism ($H_C = 20$ Oe, M_R (at 1.9 and 5 K) = 0.28 emu/g$_{Mn^{2+}}$, M_R (15 K) = 0.19 emu/g$_{Mn^{2+}}$). After removing of the linear component of the antiferromagnetic curve (Fig. 2.37) and working out the magnetic moment by the Equation 1.5 on p. 26, was found that the magnetization tends to saturate with value of maximum magnetic moment, very close to the theoretical value: calculated $gS = 4.52\mu_B$; theoretical $gS = 5\mu_B$ for $S = 5/2$ (Fig. 2.38). Such behaviour can be interpreted as metamagnetic where appears transition from antiferromagnetic to a ferromagnetic state. Some similar compounds with such behaviour have been reported.[86–88] The plots of M *vs.* H at 1.9 and 5 K coincide at low filed while this at 15 K exhibit lower magnetization. This is in agreement with the transition temperature of 5.3 K on the plot of ZFC-FC.

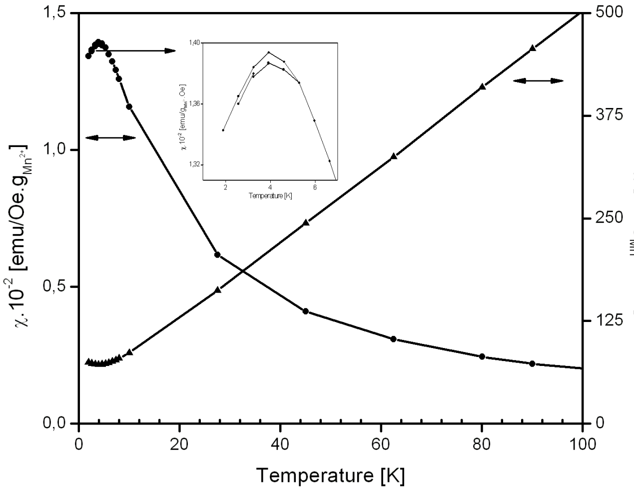

Figure 2.35.: Plots of χ *vs.* T and χ^{-1} *vs.* T of compound Mn[HnicO]$_2$[H$_2$O] (**X**). Magnification at low temperature is shown in the inset.

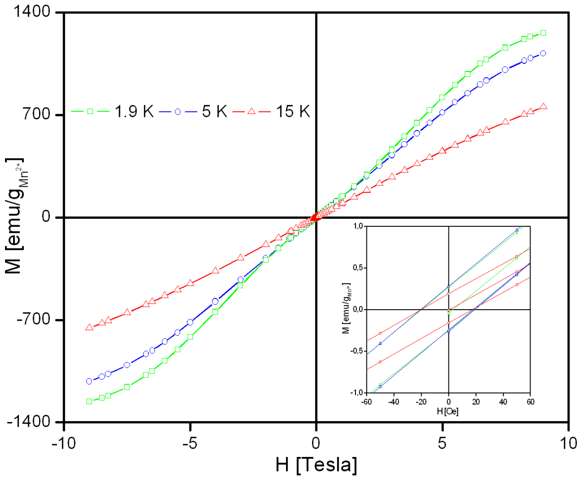

Figure 2.36.: Plot of magnetization *M* *vs.* applied field *H* of compound Mn[HnicO]$_2$[H$_2$O] (**X**) at 1.9, 5 and 15 K.

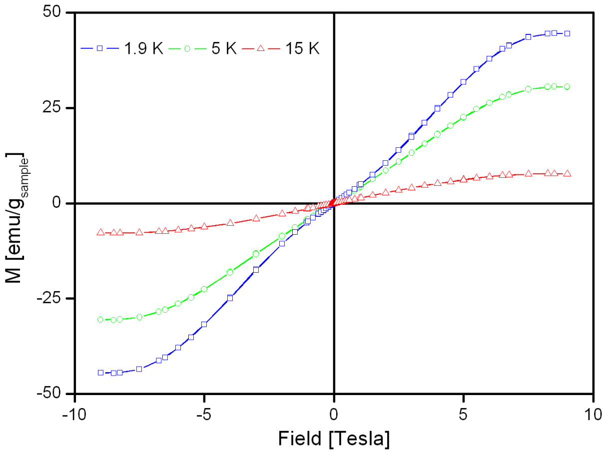

Figure 2.37.: Magnetization loops of compound Mn[HnicO]$_2$[H$_2$O] (**X**) without linear component.

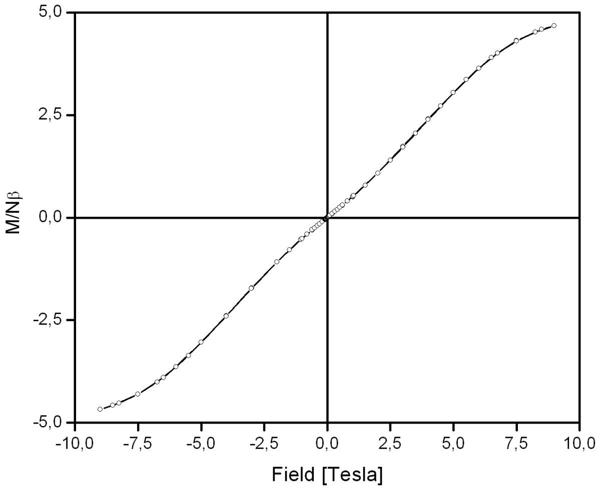

Figure 2.38.: Reduced magnetization $M/N\beta$ *vs.* applied field H at 1.9 K of compound Mn[HnicO]$_2$[H$_2$O] (**X**).

2.4.2. Paramagnetic compounds

No thermal irreversibility was observed for the following compounds: **I**, **II**, **III**, **IV**, **V**, **VII**, **XI**, **XII**, **XIII**[¶] and **XIV**, as measurements taken with decreasing temperature gave the same results, either after cooling from room temperature to 1.9 K in zero applied magnetic field (zero field cooling) or after cooling under the measurement field.

2.4.2.1. Compounds of Co^{2+}

Fig. 2.39 represents the magnetic susceptibility multiplied by the temperature (χT, with $\chi = M/H$) for compounds **I** and **II**. The temperature dependence indicates deviation from simple paramagnetic (Curie-like) ion behaviour. Such is ascribed to the influence of crystal field of **I** and **II**, just like it is also observed in several mononuclear systems containing high-spin Co^{2+} ions in an octahedral coordination geometry.[82] The lowest energy levels of the Co^{2+} cations are Γ_6 and Γ_7 doublets, and in a first approximation one can consider that only these two are thermally populated. Hence, the total susceptibility can be described by Equation 1.17, where χ_z and χ_x are expressed in Equations 1.21 and 1.22, respectively (see Chapter 1, p. 39 and p. 40). Within this approximation, D includes the Γ_6 and Γ_7 energy gap and the influence of the orbital momentum.[82] Fitting the data to Equation 1.17 (solid lines in Fig. 2.39) we obtain D = 24 and 65 cm^{-1} for samples **I** and **II**, respectively, in good agreement with the values expected for Co^{2+} cations.[82] From the fitting it is also feasible to calculate g_x = 2.1, g_z = 2.3 (**I**) and g_x = 1.8, g_z = 1.7 (**II**). (Small variations of these parameters are not critical for the quality of the fit, and are subject to absolute errors of the order of 0.1.) Although at present we do not have a plausible explanation for the difference between these values for the two compounds, the ratio g_z/g_x is *ca.* 1.1, in good agreement with the values reported for similar compounds.[82] The differences registered for the crystal field splitting can be attributed to the influence of the donor atoms present in the Co^{2+} first coordination shell. In fact, compound **II** has one more pyridine ring bound to the metal, which increases the crystal field splitting for the former compound, in agreement with the spectrochemical series.

2.4.2.2. Compounds of Cu^{2+}

Fig. 2.40 reveals the temperature dependence of the reciprocal magnetic susceptibility ($\chi^{-1} = H/M$) for samples **III**, **IV** and **XI**. The observed linear temperature dependences indicate simple paramagnetic ion behaviour. The results were fitted to a Curie law (Equation 1.2, p. 23). From the values of the fitted Curie constants, the calculated effective magnetic moments per copper cation in samples are $\mu = 1.8\mu_B$, $\mu = 1.6\mu_B$ and $\mu = 1.8\mu_B$ per cation for **III**, **IV** and **XI**, respectively. These values are very close to the free Cu^{2+} ion spin-only (quenched orbital moment L = 0) value $\mu = 1.73\mu_B$. The magnetic measurements show that

---

[¶] This paramagnetic compound gave a very low signal so that the magnetic properties will be not discussed here in details.

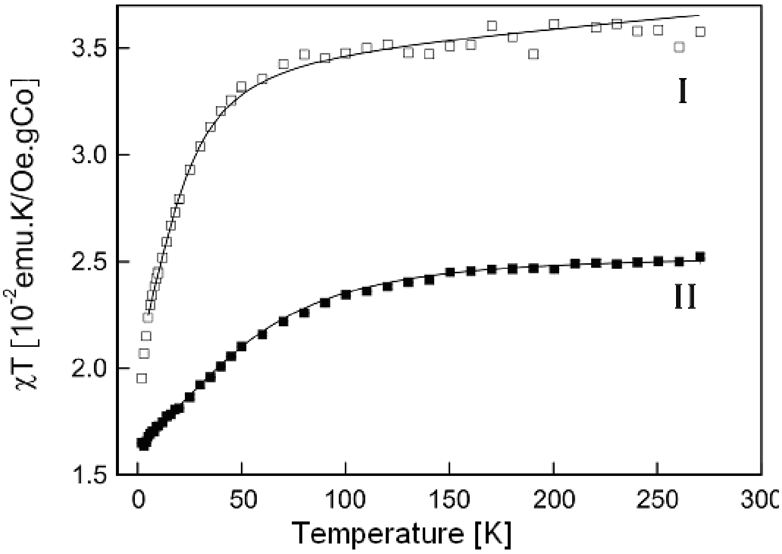

Figure 2.39.: Temperature dependence of the magnetic susceptibility multiplied by temperature (χT *vs.* T) for compounds $[Co(picOH)_2(H_2O)_2]$ and *mer*$-[N(CH_3)_4][Co(picOH)_3] \cdot H_2O$ (**I** and **II**). Solid lines are fits to Equations 1.21, 1.22 (p. 40) and 1.17 on p. 39.

the magnetic interactions between Cu^{2+} are negligible, essentially due to the large interionic distance (see crystal structure descriptions above).

2.4.2.3. Compounds of Ni^{2+} and Mn^{2+}

The magnetic susceptibilities multiplied by the temperature as functions of temperature for compounds **V** and **VII** are presented in Figs. 2.41 and 2.42, respectively. The obtained effective magnetic moments of these compounds after fittings to the Curie law are $\mu_{\text{eff}} = 2.77\mu_B$ for compounds **V** and $\mu_{\text{eff}} = 3.01\mu_B$ for compound **VII**, which are very close to the free Ni^{2+} ion spin-only (quenched orbital moment $L = 0$) values which vary between $2.83\mu_B$ and $3.5\mu_B$.[85,89] The temperature dependences of the magnetic susceptibilities indicate deviation from simple paramagnetic ion behaviour, again ascribed to the influence of crystal field of the compounds in both cases. For Ni^{2+} ($S = 1$) in octahedral coordination geometry, the lower energy levels are E and A triplet states, as observed in several mononuclear systems containing these ions.[82,90] In a first approximation only these levels are thermally populated, and the total susceptibility for Ni^{2+} can be described by Equations 1.17, 1.19 and 1.20 (Chapter 1, on ps. 39 and 40). Within this approximation, the model includes the ligand field distortions. After fitting the data to the total susceptibility (Equation 1.17), were obtained for the crystal field splitting $D = 8$ cm^{-1} (compound **V**) and $D = 7.7$ cm^{-1} (compound **VII**). From the fitting also were calculated $g_x = 4.3$, $g_z = 4.1$ for compound **V**[‖] and for compound **VII**: $g_x = 2$, $g_z = 1.4$. (The values are subject to absolute errors of the order of 0.1.)

[‖] We do not find a physical explanation for such high values of g_z and g_x, although the model describes well the magnetic behaviour; the high number of parameters might turn the values of some of the parameters less reliable.

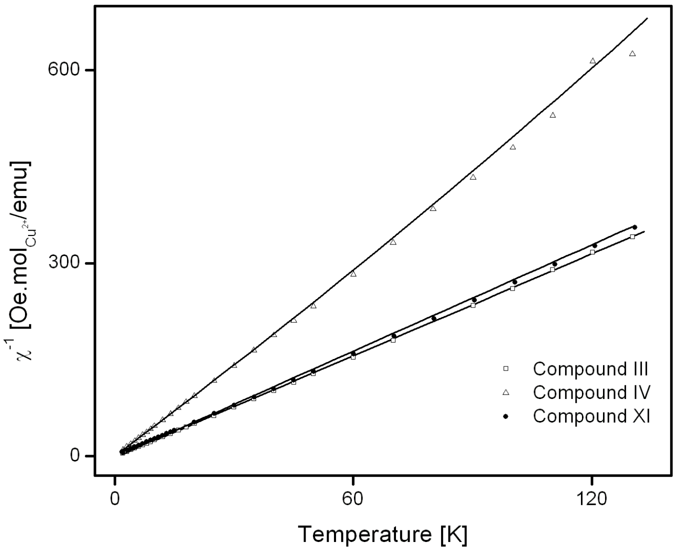

Figure 2.40.: Temperature dependence of the inverse magnetic susceptibility ($\chi^{-1} = H/M$) for compounds [Cu(picOH)$_2$] (**III**), [Cu(picOH)$_2$(BPE)]$_2 \cdot$ [Cu(picOH)$_2$(BPE)$_2$] $\cdot$ 8 H_2O (**IV**) and Cu(HnicOH)$_2$ (**XI**). Solid lines are fits to the Curie law.

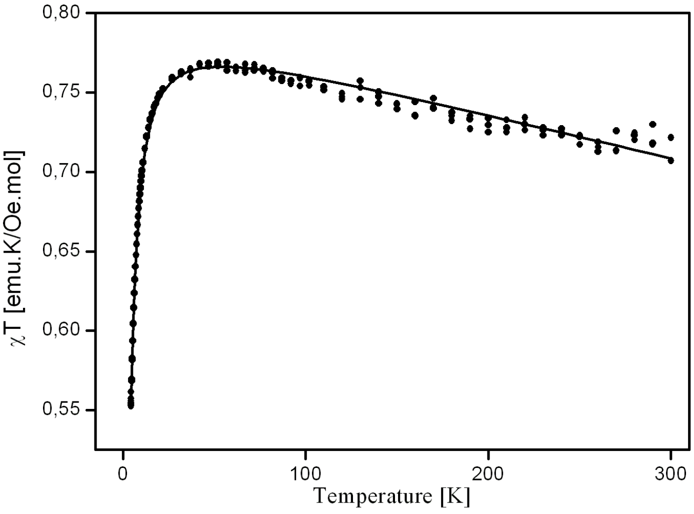

Figure 2.41.: Temperature dependence of the magnetic susceptibility multiplied by temperature (χT *vs.* T) for compound Ni(picOH)$_2$(H_2O)$_2$ (**V**). Solid line is the fit to Equation 1.17, where χ_x and χ_z are the expressions shown in Equations 1.19 and 1.20 on p. 40.

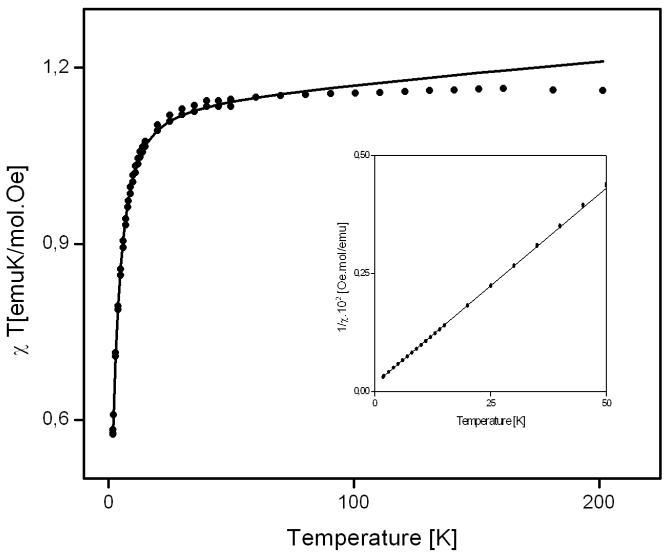

Figure 2.42.: Temperature dependence of the magnetic susceptibility multiplied by temperature (χT *vs.* T) for compound Ni[HnicO]$_2$[H$_2$O]$_2$ (**VII**). Solid lines are fits to Equation 1.17, where χ_x and χ_z are are the expressions shown in Equations 1.19 and 1.20 on p. 40. The inset shows the fit of χ^{-1} *vs.* T to the Curie law.

Fig. 2.43 represents the magnetic susceptibilities for compounds **XII** (a) and **XIV** (b). This observed temperature dependence indicates simple paramagnetic ion behaviour. The results were fitted to the Curie law. From the values of the fitted Curie constants, the calculated effective magnetic moment per nickel cation (**XII**) is $\mu = 2.6\mu_B$ and $\mu = 6.0\mu_B$ per manganese cation (**XIV**). These values are very close to the free Ni^{2+} and Mn^{2+} ions spin-only values $\mu = 2.8$–$3.3\mu_B$ for the former and $\mu = 5.6$–$6.1\mu_B$ — for the latter. The magnetic measurements show that the magnetic interactions between Mn^{2+} and Ni^{2+} in the corresponding compounds are negligible, essentially due to the large interionic distance (see crystal structure descriptions).

2.5. Final remark

The compounds with HpicOH, HnicSH and these with Cu^{2+}, Ni^{2+} and HnicOH reported in this chapter do not exhibit magnetic interactions, but showed paramagnetism with deviations from the Curie law at low temperatures. Their magnetic properties were analysed with physical models, which describe paramagnetic behaviours of transition metals systems where the electronic configurations and ligand environments differ. Metamagnetic behaviour was revealed by the coordination complex with Mn^{2+} and HnicOH. At low temperatures (< 6 K) the compound entirely changes the interactions from antiferro- to ferromagnetic. We cannot be certain about interaction paths since single-crystal were not obtained so that the structure was deduced from elemental analysis, infrared spectroscopy

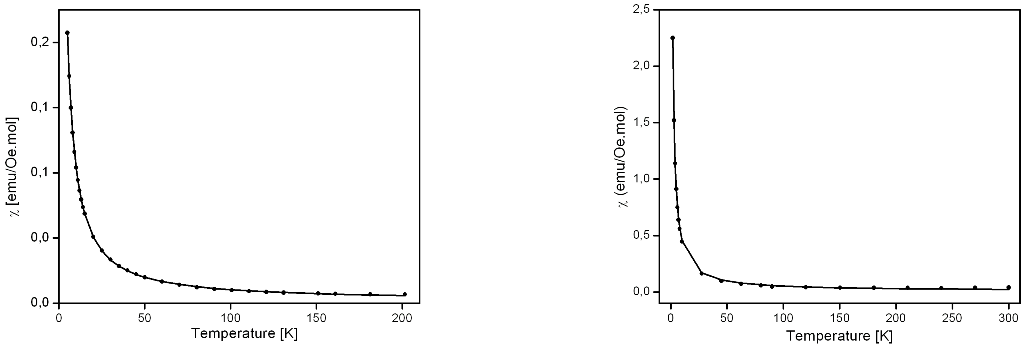

(a) (b)

Figure 2.43.: Temperature dependence of the magnetic susceptibility (χ *vs.* T) for: (a) Compound $[Ni(phen)_3](H_2nic_2S_2)_2 \cdot 2\,H_2O$ (**XII**); (b) Compound $[Mn(phen)_2(C_{12}H_7N_2O_5)](C_{12}H_8N_2O_4S_2) \cdot 2\,H_2O$ (**XIV**).

and thermo-analytical measurements. Another antiferromagnetic compound is with Co and HnicOH.

We can speculate that the position of the hydroxyl group (of HpicOH and HnicOH) and the coordination mode of the ligand (mono- or polydentate) has a crucial influence on the magnetic properties. These results show that the materials containing 1st row transition metals and ligands, derivative of pyridine-carboxylic acids (in particular HnicOH) can show magnetic interactions and a future work in this direction can be of scientific interest.

References

1. Fibel LR and Spoerri PE, *J. Am. Chem. Soc.* 70(11) (1948), 3908–3911.
2. Saleh MS, Idriss KA, Abu-Bakr MS and Hashem EY, *The Analyst* 117(6) (1992), 1003–1007.
3. Stephens AKW and Orvig C, *Inorg. Chim. Acta* 273 (1998), 47–53.
4. Kukovec BM, Popović Z, Pavlović G and Linarić MR, *J. Mol. Struct.* 882(1–3) (2008), 47–55.
5. Kiss E, Petrohán K, Sanna D, Garribba E, Micera G and Kiss T, *Polyhedron* 19(1) (2000), 55–61.
6. Pazderska-Szablowicz M, Bialkowska A and Kita E, *Transition Met. Chem.* 31(3) (2006), 413–420.
7. Szablowicz M and Kita E, *Transition Met. Chem.* 29(7) (2004), 762–768.
8. Yue YF, Sun W, Gao EQ, Fang CJ, Xu S and Yan CH, *Inorg. Chim. Acta* 360(5) (2007), 1466–1473.
9. Soares-Santos PCR, Nogueira HIS, Rocha J, Félix V, Drew MGB, Ferreira RAS, Carlos LD and Trindade T, *Polyhedron* 22(27) (2003), 3529–3539.
10. Soares-Santos PCR, Paz FAA, Ferreira RAS, Klinowski J, Carlos LD, Trindade T and Nogueira HIS, *Polyhedron* 25(12) (2006), 2471–2482.
11. Gu XJ and Xue DF, *CrystEngComm* 9(6) (2007), 471–477.
12. Di Marco VB, Tapparo A, Dolmella A and Giorgio Bombi GG, *Inorg. Chim. Acta* 357(1) (2004), 135–142.
13. Quintal SMO, Nogueira HIS, Félix V and Drew MGB, *Polyhedron* 21(27-28) (2002), 2783–2791.
14. Chattopadhyay S, Fanwick PE and Walton RA, *Inorg. Chim. Acta* 357(3) (2004), 764–768.
15. Kirpal A, *Monatsh. Chem.* 29(2) (1908), 227–231.
16. Shaver A, Ng JB, Hall DA, Lum BS and Posner BI, *Inorg. Chem.* 32(14) (1993), 3109–3113.
17. Dar A, Moss K, Cottrill SM, Parish RV, Mc Auliffe CA, Pritchard RG, Beagley B and Sandbank J, *J. Chem. Soc., Dalton Trans.* (12) (1992), 1907–1913.
18. Gatto S, Gerber TIA, Bandoli G, Perils J and Du Preez JGH, *Inorg. Chim. Acta* 269(2) (1998), 235–240.
19. Quintal SMO, Nogueira HIS, Félix V and Drew MGB, *New J. Chem.* 24(7) (2000), 511–517.
20. Quintal SMO, Nogueira HIS, Carapuca HM, Félix V and Drew MGB, *J. Chem. Soc., Dalton Trans.* (21) (2001), 3196–3201.
21. Yano S, Nakai M, Sekiguchi F, Obata M, Kato M, Shiro M, Kinoshita I, Mikuriya M, Sakurai H and Orvig C, *Chem. Lett.* (9) (2002), 916–917.
22. Soares-Santos PCR, Nogueira HIS, Félix V, Drew MGB, Ferreira RAS, Carlos LD and Trindade T, *Chem. Mater.* 15(1) (2003), 100–108.
23. Kiss E, Bényei A and Kiss T, *Polyhedron* 22(1) (2003), 27–33.

24. Sun C, Zheng X and Jin L, *J. Mol. Struct.* 646(1-3) (2003), 201–210.
25. Dakternieks D, Duthie A, Smyth DR, Stapleton CPD and Tiekink ERT, *Appl. Organomet. Chem.* 18(1) (2004), 53–54.
26. Nakai M, Sekiguchi F, Obata M, Ohtsuki C, Adachi Y, Sakurai H, Orvig C, Rehder D and Yano S, *J. Inorg. Biochem.* 99(6) (2005), 1275–1282.
27. Popović Z, Pavlović G, Vinković M, Vikić-Topić D and Linarić MR, *Polyhedron* 25(12) (2006), 2353–2362.
28. Popović Z, Matković-Čalogović D, Popović J, Vicković I, Vinković M and Vikić-Topić D, *Polyhedron* 26(5) (2007), 1045–1052.
29. Kukovec BM, Popović Z, Pavlović G, Vinković M and Vikić Topić D, *Polyhedron* 27(5) (2008), 1479–1488.
30. Casas JS, Castellano EE, Ellena J, García-Tasende MS, Sánchez A, Sordo J and Toma M, *Polyhedron* 27(4) (2008), 1296–1302.
31. Constantino VRL, De Oliveira LFC, Santos PS and Toma HE, *Transition Met. Chem.* 19(1) (1994), 103–107.
32. Sucharda and Troszkiewicz, *Roczniki Chem.* 12 (1932), 493.
33. Raper ES, *Coord. Chem. Rev.* 153 (1996), 199–255.
34. Quintal SMO, Nogueira HIS, Félix V and Drew MGB, *J. Chem. Soc., Dalton Trans.* (23) (2002), 4479–4487.
35. Humphrey SM, Mole RA, Rawson JM and Wood PT, *J. Chem. Soc., Dalton Trans.* (11) (2004), 1670–1678.
36. Humphrey SM, Alberola A, García CJG and Wood PT, *Chem. Commun.* (15) (2006), 1607–1609.
37. Toma M, Sánchez A, García-Tasende MS, Casas JS, Sordo J, Castellano EE and Ellena J, *Cent. Eur. J. Chem.* 2(3) (2004), 534–552.
38. Ma C, Jiang Q and Zhang R, *J. Organomet. Chem.* 678(1-2) (2003), 148–155.
39. Yang Q, Chen S and Gao S, *J. Therm. Anal. Calorim.* 90(3) (2007), 881–885.
40. Marchal S, Moreno V, Aullón G, Alvarez S, Quirós M, Font-Bardia M and Solans X, *Polyhedron* 18(27) (1999), 3675–3682.
41. Nomiya K, Noguchi R, Shigeta T, Kondoh Y, Tsuda K, Ohsawa K, Chikaraishi-Kasuga N and Oda M, *Bull. Chem. Soc. Jpn.* 73(5) (2000), 1143–1152.
42. Nomiya K, Takahashi S and Noguchi R, *J. Chem. Soc., Dalton Trans.* (13) (2000), 2091–2097.
43. Cervantes G, Marchal S, Prieto MJ, Pérez JM, González VM, Alonso C and Moreno V, *J. Inorg. Biochem.* 77(3–4) (1999), 197–203.
44. Rein FN and Toma HE, *Polyhedron* 17(9) (1998), 1439–1448.
45. Ainscough EW, Brodie AM, Coll RK, Kotch TG, Lees AJ, Mair AJA and Waters JM, *J. Organomet. Chem.* 517(1–2) (1996), 173–181.
46. Armijo L and Arancibia V, *Anal. Chim. Acta* 298(1) (1994), 91–98.
47. Abe K, Matsufuji K, Ohba M and Okawa H, *Inorg. Chem.* 41(17) (2002), 4461–4467.

48. Liang YC, Hong MC, Liu JC and Cao R, *Inorg. Chim. Acta* 328(1) (2002), 152–158.
49. Dong YB, Smith MD, Layland RC and Zur Loye HC, *Inorg. Chem.* 38(22) (1999), 5027–5033.
50. Plater MJ, Foreman MRS, Howie RA and Skakle JMS, *Inorg. Chim. Acta* 318(1-2) (2001), 175–180.
51. Vaid TP, Sydora OL, Douthwaite RE, Wolczanski PT and Lobkovsky EB, *Chem. Commun.* (14) (2001), 1300–1301.
52. Lu JY and Babb A, *Inorg. Chim. Acta* 318(1-2) (2001), 186–190.
53. Hernández ML, Urtiaga MK, Barandika MG, Cortes R, Lezama L, De la Pinta N, Arriortua MI and Rojo T, *J. Chem. Soc., Dalton Trans.* (20) (2001), 3010–3014.
54. Fu ZY, Wu XT, Dai JC, Wu LM, Cui CP and Hu SM, *Chem. Commun.* (18) (2001), 1856–1857.
55. Carlucci L, Ciani G, Proserpio D and Rizzato S, *Chem. Commun.* (13) (2001), 1198–1199.
56. Bourne SA, Lu J, Moulton B and Zaworotko MJ, *Chem. Commun.* (9) (2001), 861–862.
57. Nel A, Chapman J, Long N, Kolawole G, Motevalli M and O'Brien P, *Polyhedron* 19(13) (2000), 1621–1626.
58. Moon M, Kim I and Lah MS, *Inorg. Chem.* 39(13) (2000), 2710–2711.
59. Hernández ML, Barandika MG, Urtiaga MK, Cortés R, Lezama L and Arriortua MI, *J. Chem. Soc., Dalton Trans.* (1) (2000), 79–84.
60. Carlucci L, Ciani G, Proserpio DM and Rizzato S, *Chem. Commun.* (14) (2000), 1319–1320.
61. Carlucci L, Ciani G, Proserpio DM and Rizzato S, *J. Chem. Soc., Dalton Trans.* (21) (2000), 3821–3827.
62. Wang QM, Guo GC and Mak TCW, *Chem. Commun.* (18) (1999), 1849–1850.
63. Sharma CVK and Rogers RD, *Chem. Commun.* (1) (1999), 83–84.
64. Hong C, Son SK, Lee Y, Jun MJ and Do Y, *Inorg. Chem.* 38(24) (1999), 5602–5610.
65. Hernández ML, Barandika MG, Urtiaga MK, Cortés R, Lezama L, Arriortua MI and Rojo T, *J. Chem. Soc., Dalton Trans.* (9) (1999), 1401–1404.
66. Ferbinteanu M, Marinescu G, Roesky HW, Noltemeyer M, Schmidt HG and Andruh M, *Polyhedron* 18(1-2) (1998), 243–248.
67. Power KN, Hennigar TL and Zaworotko MJ, *Chem. Commun.* (5) (1998), 595–596.
68. Hennigar TL, MacQuarrie DC, Losier P, Rogers RD and Zaworotko MJ, *Angew. Chem, Int. Ed. Engl.* 36(9) (1997), 972–973.
69. Li YM, Che YX and Zheng JM, *Chin. J. Struct. Chem.* 25(5) (2006), 572–576.
70. Yan HY and Hu TQ, *Acta Crystallogr., Sect. E: Struct. Rep. Online* 63 (2007), M2325–U728.
71. Yan HY and Hu TQ, *Acta Crystallogr., Sect. E: Struct. Rep. Online* 63 (2007), M2326–U737.
72. Wen DC and Liu SX, *Chin. J. Struct. Chem.* 26(11) (2007), 1281–1286.
73. Deacon GB and Phillips RJ, *Coord. Chem. Rev.* 33(3) (1980), 227–250.
74. Oldham C, Comprehensive coordination chemistry, vol. 2, S. G. Wilkinson Pergamon Press Oxford, 1987.

75. Nogueira HIS, *Spectrochim. Acta, Part A* 54(10) (1998), 1461–1470.
76. Kovala-Demertzi D, Kyrkou P and Zakharoba I, *Polyhedron* 10(13) (1991), 1507–1512.
77. Pérez-Lourido PA, García-Vázquez JA, Romero J, Louro MS, Sousa A, Chen Q, Chang Y and Zubieta J, *J. Chem. Soc., Dalton Trans.* (10) (1996), 2047–2054.
78. Banerji S, Byrne RE and Livingstone SE, *Transition Met. Chem.* 7(1) (1982), 5–10.
79. McCaffrey LJ, Henderson W, Nicholson BK, Mackay JE and Dinger MB, *J. Chem. Soc., Dalton Trans.* (15) (1997), 2577–2586.
80. Mitra S, Biswas H and Bandyopadhyay P, *Polyhedron* 16(3) (1997), 447–451.
81. Constable E, Elder SM, Palmer CA, Raithby PR and Tocher DA, *Inorg. Chim. Acta* 252(1–2) (1996), 281–291.
82. Kahn O, Molecular magnetism, Wiley–VCH, 1993.
83. Humphrey SM, Mole RA, McPartlin M, McInnes EJL and Wood PT, *Inorg. Chem.* 44(17) (2005), 5981–5983.
84. Cave D, Gascon JM, Bond AD, Teat SJ and Wood PT, *Chem. Commun.* (10) (2002), 1050–1051.
85. Griffith JS, The theory of transition - metal ions, 3rd ed., Cambridge University Press, 1971.
86. Das A, Rosair GM, El Fallah MS, Ribas J and Mitra S, *Inorg. Chem.* 45(8) (2006), 3301–3306.
87. Johnson MT, Arif AM and Miller JS, *Eur. J. Inorg. Chem.* (8) (2000), 1781–1787.
88. Maji TK, Kaneko W, Ohba M and Kitagawa S, *Chem. Commun.* (36) (2005), 4613–4615.
89. McCleverty J, Chemistry of the first-row transition metals, 1st ed., Oxfod University Press, 1999.
90. Orchard AF, Magnetochemistry, 1st ed., Oxford chemistry primers, Oxford: University Press, 2003.

COORDINATION COMPOUNDS OF LANTHANIDES WITH PICOLINIC ACID AND GLUTARIC ACID AS BRIDGING LIGAND

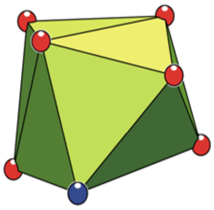

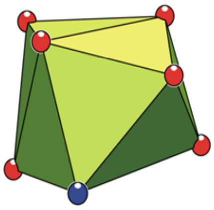

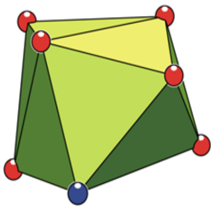

CHAPTER III

Chapter 3.

Coordination compounds of lanthanides with picolinic acid and glutaric acid

3.1. Introduction

The design of functional units from the molecular scale to macroscopic assemblies has emerged as a new paradigm in materials synthesis, resulting in an interplay between conventional molecular chemistry and solid-state science. This has been particularly clear in the development of functional materials using coordination compounds in the field of semiconductors technology, supramolecular machinery, catalysis, micro-porous and hybrid materials.[1–7] In some cases, the development of these functional materials is based on the chemistry of well-known coordination compounds, e.g. by the assembly of inorganic-organic extended lattices[8] or by thermolysis of metal thiolates to produce thin films or nanoparticles.[9–13]

1st row transition metals coordinated to aromatic ambidentate ligands form a class of compounds with a wide variety of coordination modes that has attracted the attention of chemists.[14–20] Griffith and co-workers extended this type of chemistry to the 2nd row transition metals and, in particular, to their applications in catalysis.[21–23] More recently, in our research group studies on metal complexes with aromatic ambidentate ligands have been exploited.[24–27] In particular, the coordination chemistry of 3–hydroxypicolinic acid and its derivatives, and the role of this ligand in the photoluminescence of lanthanide complexes[28] were investigated. Picolinic complexes of lanthanides, particularly those of Eu^{3+} and Tb^{3+}, show interesting photoluminescent behaviour because energy transfer from the aromatic groups close to the lanthanide ions may enhance the luminescent efficiency of the lanthanide (Ln) ion.[29] Even dispersed in solid matrices they can produce efficient luminescent materials, such as those in SiO_2 nanoparticles obtained by the sol-gel method.[28] Therefore, in principle, it should be possible to fine tune the luminescence of such nanocomposites by working out the coordination chemistry of the Ln complexes. Lanthanide coordination polymers, including those synthesized in the presence of dicarboxylic ligands have attracted considerable interest and many examples can be found in the literature.[30] Here is reported a distinct approach which involves the simultaneous use of a highly flexible bridging ligand (glutaric acid) with a chelating aromatic ligand (picolinic acid) which, on the one hand, might function as an antenna, efficiently transferring energy to the Ln centre or, on the other hand, may remove available coordination sites thus controlling to some extent the dimensionality of the final product. Examples in the literature of Ln–containing coordination compounds with this type of ligands and an aromatic antenna were not found so far.

All the lanthanides can be considered as hard acids.[31] Therefore among the donor atoms, they bond preferentially to fluoride, oxygen and other atoms in order O>N>S, i.e. to hard bases. The water molecules and hydroxide ions (OH^-) are strong ligands, so that in aqueous solution only ligands containing donor groups with negatively charged oxygen (e.g. in carboxyl and phosphate groups) can bind strongly. In neutral to basic aqueous solution, ligands containing such donor groups can bind sufficiently strongly the Ln metal and prevent the precipitation of $Ln(OH)_3$. Lanthanide complexes of ligands containing nitrogen, sulphur and halogen donors are not generally stable in water. Donor groups with neutral oxygen or nitrogen atoms usually bind or occupy Ln^{3+} coordination sites only when present in multidentate ligands, which contain at least one other donor group with negatively charged oxygen.

The lanthanide coordination geometry is determined by many aspects, mainly by ionic character of Ln^{3+} — ligand interactions and by relatively low ionic potentials of the Ln^{3+} ions. The lanthanide complexes exhibit coordination numbers (CNs) from 6 to 12 (in solid state and in solution); the most common CNs are 8 and 9. The coordination geometries vary and depend on the ionic radius, ligand conformation, competition between ligand donor groups and solvent molecules for available coordination sites. The smaller Ln centres provide shorter and stronger coordination. Since the Lns exhibit low polarity ability and ionic nature of the interactions with the ligand therefore those ions do not induce changes in the electronic charge distributions at the biding sites.

In relation to the magnetic behaviour, the metal-centred magnetic properties of the Ln compounds result from the $[Xe]4f^n$ electronic configurations of Ln(III) which can be exploited to design functional devices. The existence of seven $4f$ orbitals provides metals and/or ions with a large number of unpaired electrons and considerable associated electronic magnetic moments for the Lns in the range Gd−Er. Specific functions are enhanced by the peculiar symmetric electronic ground state ^8S of Gd(III). For instance, its unique long electronic relaxation time opens perspectives for enhancing nuclear relaxation of peripheral atoms via contact, dipolar, or spin—Curie interactions.[32] The recent development of MRI (magnetic resonance imaging) contrast agents takes advantage of the strong dipolar coupling between the electronic magnetic moment of paramagnetic Gd(III) and the nuclear magnetic moment of water molecules entering in the first coordination sphere of the Ln complex, in order to enhance proton relaxivity of the solvent close to the paramagnetic metal.[33–35] Thus the paramagnetic metal complexes can be in general more efficient contrast agents for medical MRI. The development of new generation of "smart" MRI contrast agents sensitive to external stimuli (pH, pO_2, intracellular concentrations of specific analytes) is currently the subject of research.[33,36,37] For the lanthanides with large orbital contributions, the weak crystal-field splitting induced by the coordinated ligands is sufficient to produce magnetic anisotropies of larger magnitude than those obtained for diamagnetic materials. Thus Ln–containing liquid crystals or matrices are used for their capability to align proteins in magnetic fields and to give access to residual dipolar N−H couplings, an important point for conformational studies of biological materials in solution.[38] The large magnetic anisotropies induce also through-space paramagnetic hyperfine NMR shifts (i.e. pseudocontact shifts), which were originally used for assigning structures of complicated organic molecules at low magnetic fields (shift reagents).[39] There are new perspectives open for improving the structural characterization of supramolecular lanthanide complexes in solution and for designing paramagnetic probes monitoring temperature in biological media.[40]

3.1.1. Magnetic consideration

The f-block elements, namely the lanthanides, display peculiar magnetic properties of their f-orbital spins and large magnetic moments. The ground configuration of the rare earth ions is $4f^n5s^25p^6$. These ions are generally trivalent (although divalent (Eu^{2+}, Yb^{2+}) or tetravalent (Ce^{4+}, Tb^{4+}) also exist. The $5s$ and $5p$ orbitals are fully occupied and shield the partly occupied by magnetically active electrons $4f$ orbitals. The influence of the ligands on the magnetic properties is not as strong for the complex of f-elements as for the $3d$ ion compounds. The spin-orbit coupling is considered to play an essential role in their magnetic properties, since the f-electrons are well shielded. The magnitude of the spin-orbit coupling is larger than for a $3d$ ion and increases from La to Lu. Their total magnetic moments J, are expressed as $J = L + S$, where L denotes an angular moment and S — spin moment. The ground states of Ln ions are $J = L \pm S$, where the sign depends on the number of f electrons ($J = L - S$ for lighter elements than Gd; $J = L + S$ for heavier elements than Gd). The lowest state has the smallest J for the configurations $4f^1 - 4f^6$, and the highest J for the configurations $4f^8 - 4f^{13}$. For the configuration $4f^7$ (Eu^{3+}) there is no first-order angular momentum. The energy separation between the state of lowest energy (the ground free ion state $^{2S+1}\Gamma_J$ arising from $4f^n$ configuration) and the first excited state varies from few hundreds to thousands cm^{-1} of wavenumbers.[41] When this energy separation is weak, the first excited state may be thermally populated; when it is large — only the ground state is thermally populated. The ground electronic configuration with ground and first excited states of Ln ions, and their energy separation, according to Kahn,[41] are presented in Table 3.1. For most trivalent lanthanide ions only the ground state is thermally populated at room temperature and below (since it is largely separated from the first excited state). In free-ion approximation the molar susceptibility for a mononuclear compound can be given by the Equation 1.3 on p. 23 (Chapter 1). In this approximation the magnetic susceptibility obeys the Curie law. The values of g_J and χT calculated from Equation 1.3 for different ions[41] are given in Table 3.1 too. If the energy of the excited states is not too larger than the energy of the ground state, it is necessary to add a significant temperature independent contribution to the magnetic susceptibility of Equation 1.3. This contribution is:

$$\chi' = \frac{2N\mu_B^2 \left(g_J - 1\right) \left(g_J - 2\right)}{3\lambda}, \tag{3.1}$$

where λ is spin-orbital coupling parameter. For rare earth mononuclear compounds the χT *vs.* T plot is general deviated from the predicted with the sum of the Equations 1.3 and 3.1.[41,45]

The free-ion approximation does not interpret all the details of the magnetic properties

Table 3.1.: Ground configuration, ground and first excited states, energy separation between these states, magnetic moments, values of g_J and χT for rare earth ions in the free-ion approximation.[41–44]

Ion	Configuration $4f^n, n =$	Number of unpaired e^-	Colour of Ln^{3+}	Ground state	First excited state	Energy state separation [cm^{-1}]	g_J	μ_{theor}[42]	μ_{obs}[43] μ_{eff}/μ_B	$\chi_M T$ [cm^{3}Kmol^{-1}]
Ln(III)	0	0	colourless	$^1S_0$			6/7	0	0	
Ce(III)	1	1	colourless	$^2F_{5/2}$	$^2F_{7/2}$	2200	6/7	2.54	2.3–2.5	0.80
Pr(III)	2	2	green	$^3H_4$	$^3H_5$	2100	4/5	3.58	3.4–3.6	1.60
Nd(III)	3	3	lilac	$^4I_{9/2}$	$^4I_{11/2}$	1900	8/11	3.62	3.5–3.6	1.64
Pm(III)	4	4	pink	$^5I_4$	$^5I_5$	1600	3/5	2.68	—	0.90
Sm(III)	5	5	yellow	$^6H_{5/2}$	$^6H_{7/2}$	1000	2/7	0.85	1.4–1.7	0.09
Eu(III), Sm(II)	6	6	pale pink	$^7F_0$	$^7F_1$	300	5	**0**	**3.3–3.5**	0.00
Gd(III), Eu(II)	7	7	colourless	$^8S_{7/2}$	$^6P_{7/2}$	30000	2	**7.94**	**7.9–8.0**	7.88
Tb(III)	8	6	pale pink	$^7F_6$	$^7F_5$	2000	3/2	9.72	9.5–9.8	11.82
Dy(III)	9	5	yellow	$^6H_{15/2}$	$^6H_{13/2}$	–	4/3	10.63	10.4–10.6	14.17
Ho(III)	10	4	yellow	$^5I_8$	$^5I_7$	–	5/4	10.60	10.4–10.7	14.07
Er(III)	11	3	rose-pink	$^4I_{15/2}$	$^4I_{13/2}$	6500	6/5	9.57	9.4–9.6	11.48
Tm(III)	12	2	pale green	$^3H_6$	$^3H_5$	–	7/6	7.63	7.1–7.6	7.15
Yb(III)	13	1	colourless	$^2F_{7/2}$	$^2F_{5/2}$	10000	8/7	4.50	4.3–4.9	2.57
Lu(III)	14	0	colourless	$^1S_0$				0	0	

of the systems with rare earth ions. In most of the cases the situation is more complicate. With the decrease of the temperature, the components of higher energy are depopulated and this approximation becomes less valid. As a consequence: the magnetic susceptibility does not follow the Curie law and the system becomes more anisotropic on cooling. When the multiplet width is larger, the components of higher energy arising from free-ion ground state are not statistically populated, even at room temperature and the compound may present a significant magnetic anisotropy. In such case, the fact that the average value of χT is close to the value predicted in the free-ion approximation might be occasional. But the magnetic anisotropy always increase by decreasing the temperature.

3.1.2. Photoluminescent properties

3.1.2.1. Antenna effect

Lanthanide coordination chemistry has been especially relevant in the development of photoluminescent materials. In particular, the research of efficient light-converting devices based on rare earth coordination compounds. The importance of the luminescence of Ln ions is related to their long lifetime emission and narrow emission bands, which make them unique among other luminescent species. Those features are due to the fact that the emitting excited states and the ground state have f^n electronic configuration and therefore the same equilibrium geometry. This makes the $f - f$ transitions strictly forbidden (radiative lifetimes in milliseconds range[46,47] and small absorption coefficients). The lanthanide ions show weak absorption in the UV and visible region. This problem is solved by using complexes where light is absorbed by a ligand that coordinates to the ion. Such systems can exhibit the antenna effect and to show strong luminescence. Hence, the $4f - 4f$ luminescence intensity of the Ln compounds is the result of a balance between strong absorption by the ligands, ligand-rare earth ion energy transfer rates, non-radiative decays and radiative emission rates involved. In this way in a Ln–ligand complex the emitting $4f$ level is in general populated much more efficiently than by direct excitation of the excited levels of the rare earth ion. In the light conversion via antenna effect a key step is the ligands-to-metal energy transfer. The basis of this concept is a process of light conversion via absorption-energy transfer-emission, with an absorbing component — ligand — and an emitting component — metal ion[48] (Fig. 3.1). In such systems the quantities that contribute to the overall luminescence intensity are the efficiency of the ligand absorption, the efficiency of the ligand-to-metal energy transfer and the efficiency of the metal luminescence upon ligand excitation. The efficiency of this process cannot be measured directly but it appears in the luminescence quantum yield, which includes also the efficiency of the emission of the metal ion itself.

3.1.2.2. Jablonski diagram

The various energy levels involved in the absorption and emission of light by a fluorescent material and the transitions between the electronic states are classically presented by a Jablonski energy diagram (Fig. 3.1).

For any particular molecule, several different electronic singlet states exist (in the Fig. 3.1 – S_0, S_1, and S_2), depending on the total electron energy and the symmetry of various electron spin states. Each electronic state is further subdivided into a number of vibrational and rotational energy levels associated with the atomic nuclei and bonding orbitals. The ground state for most organic ligand molecules is an electronic singlet in which all electrons are spin-paired. At room temperature excitation processes usually originate from the lowest vibrational level of the ground state.

In Fig. 3.1, transitions between the states are shown as solid-line and dashed-line arrows, depending upon whether the transition is associated with absorption or emission of a photon (solid-line arrow) or results from a molecular internal conversion or non-radiative relaxation process (dashed-line arrows). Vertical upward arrows indicate the instantaneous nature of excitation processes, while the dashed-line arrows represent phenomena that occur on a much longer time scale.

With ultraviolet or visible light, a fluorescent compound is excited to higher vibrational levels of the first (S_1) or second (S_2) singlet energy state. One of the absorption (or excitation) transitions presented in Fig. 3.1 (process 1) occurs from the lowest vibrational energy level of the ground state to a higher vibrational level in the second excited state (a transition denoted as $S_0 = 0$ to $S_2 = 3$). A second excitation transition is depicted from the second vibrational level of the ground state to the highest vibrational level in the first excited state (denoted as $S_0 = 1$ to $S_1 = 5$). In a typical fluorescent material, irradiation with a wide spectrum of wavelengths will generate an entire range of allowed transitions that populate the various vibrational energy levels of the excited states. Some of these transitions will have a much higher degree of probability than others, and when combined, will constitute the absorption spectrum of the molecule.

Three non-radiative deactivation processes occur with varying probabilities following the absorption of a photon: internal conversion (IC; in Fig. 3.1, transition 4a), intersystem crossing (ISC; path 5) and vibrational energy relaxation (VR; path 4b). IC is the non-radiative conversion (or transition) between energy states of the same spin state (compare with fluorescence - a radiative process). The most probable will be relaxation to the lowest vibrational energy level of the first excited state ($S_1 = 0$; Fig. 3.1; the molecule returns to the electronic ground state, transition 6a). VR, the most common of the three, for most molecules, occurs very quickly ($< 1 \times 10^{-12}$ seconds) and is enhanced by physical contact of an excited molecule with other particles with which energy, in the form of vibrations and rotations, can be transferred through collisions. In other words, this process involves the dissipation of energy, in the absence of light emission, from the molecule to its surroundings and thus it cannot occur for isolated molecules. The excess energy is converted to vibrational energy (IC), and so the molecule is placed in an extremely high vibrational level of the electronic ground state.

ISC is a non-radiative transition between different spin states or transition to a state with a different spin multiplicity, when the spin of an excited electron is reversed (a crossing

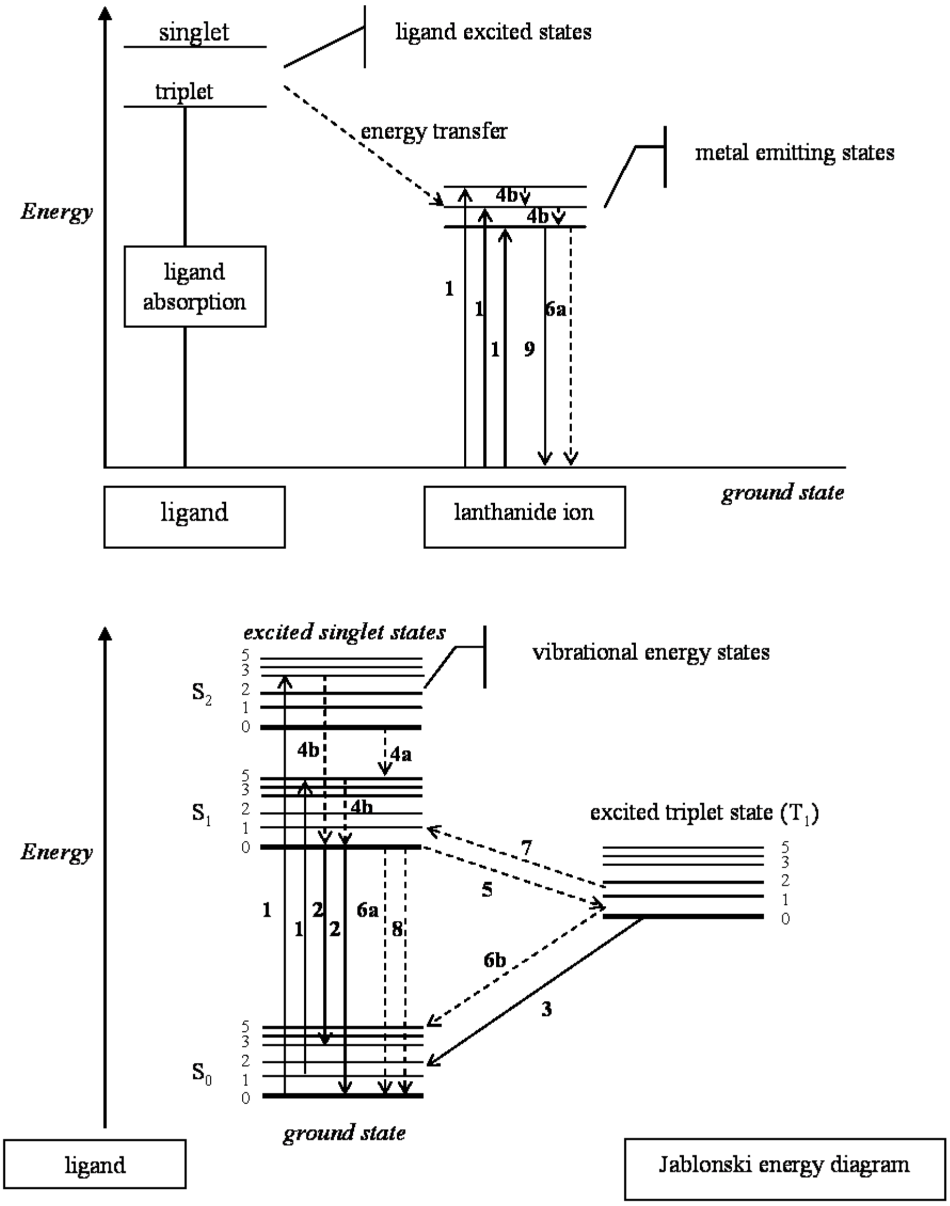

Figure 3.1.: Schematic representation of the antenna effect (above) and Jablonski diagram (below).[48–51] The states are arranged vertically by energy and grouped horizontally by spin multiplicity. The vibrational ground states of each electronic state are indicated with thicker lines, the higher vibrational states with thinner lines (rotational energy states are ignored). The following processes are observed: **1**–Excitation (absorption), 10^{-15} sec; **2**–Ligand fluorescence, 10^{-9}–10^{-7} sec; **3**–Phosphorescence, 10^{-3}–10^{2} sec; **4**–(**a**) Internal conversion, (**b**) Vibrational relaxation, 10^{-14}–10^{-11} sec; **5**–Intersystem crossing; **6**–(**a**) Non-radiative relaxation, (**b**) Non-radiative relaxation (triplet); **7**–Delayed fluorescence; **8**–Quenching; **9**–Metal luminescence.
$\rightarrow$ radiative processes, $\dashrightarrow$ non-radiative processes

to the lowest excited triplet state occurs, path 5). This process is relatively rare*, but results either in emission of a photon through phosphorescence (path 3) or in transition back to the excited singlet state that yields delayed fluorescence (second ISC, path 7) after which the molecule returns to the lowest vibrational level of the electronic ground state by VR. Transitions from the triplet excited state to the singlet ground state are forbidden, which results in rate constants for triplet emission that are several orders of magnitude lower than those for fluorescence. This type of non-radiative transition can give rise to phosphorescence.

Some other pathways compete with the fluorescence emission. The excited state energy can be dissipated non-radiatively as heat (path 7) or the excited probe can collide with another molecule to transfer energy in a second type of non-radiative process (e.g. quenching, path 8).

The photons of a laser monochromatic† beam are absorbed by the probe. Usually, for every photon that is absorbed, one will come out. But the energy (frequency) of the emitted photon will vary since the emitted photon's energy (frequency) depends on which S_0 level the probe relaxes to. As a result, light, emitted by the specimen that is made up of a lot of different wavelengths, will be seen. The shape of the emission spectrum of a probe generally does not depend on the wavelength of light used to excite the fluorescence.

Quantum yield (F) The fluorescence quantum yield gives the efficiency of fluorescence emission relative to all of the possible pathways for relaxation and is generally expressed as the (dimensionless) ratio of number of photons emitted to the number of photons absorbed (Equation 3.2).

$$F = \frac{Photons_{emitted}}{Photons_{absorbed}} \tag{3.2}$$

In other words, F represents the probability that a given excited probe will produce an emitted photon (fluorescence). Quantum yields typically range between a value of zero and one ($F = 1$ – every photon absorbed results in a photon emitted). Another way to define the quantum yield of fluorescence, is by the rates excited state decay (Equation 3.3), where k_f is the rate of spontaneous emission of radiation and $\sum_i k_i$ is the sum of all rates of excited state decay. Other rates of excited state decay are caused by the non-radiative mechanisms. Thus, if the rate of any pathway changes, this will affect both the excited state lifetime and the fluorescence quantum yield.

$$\frac{k_f}{\sum_i k_i} \tag{3.3}$$

Fluorescence lifetime (τ) or k_r The fluorescence lifetime is the characteristic time during which a molecule remains in an excited state before returning to the ground state. During

---

[*] The molecules must first undergo spin conversion to produce unpaired electrons which is an unfavourable process, thus there is lower probability of ISC occurrence.

[†] All the photons are with the same frequency.

the excited state lifetime, a probe can undergo conformational changes as well as interact with other molecules and diffuse through the local environment. The decay of fluorescence intensity as a function of time in a uniform population of molecules excited with a brief pulse of light is described by an exponential function (Equation 3.4), where $I(t)$ is the fluorescence intensity measured at time t; t_0 is the initial delay; I_0 is the initial intensity observed immediately after excitation at $t = t_0$, and t is the fluorescence lifetime.

$$I\left(t\right) = I_0 exp\left[\left(t - t_0\right)/\tau\right] \tag{3.4}$$

Because the level of fluorescence is directly proportional to the number of molecules in the excited singlet state, lifetime measurements can be conducted by measuring fluorescence decay after a brief pulse of excitation.

Quantitative fluorescence lifetime measurements permit to distinguish probes that have similar spectral characteristics but different lifetimes, and can also yield information for the local environment.

Quantum efficiency (q) The quantum efficiency is described with Equation 3.5, where $(k_{rad} + k_{nrad})$ corresponds to the inverse lifetime $1/\tau = k_{rad} + k_{nrad}$ and express the probability of transition k_{exp}, k_{rad} being the probability of radiative transition and k_{nrad} being the probability of non-radiative transition.

$$q = \frac{k_{rad}}{k_{rad} + k_{nrad}} \tag{3.5}$$

The idea presented in this chapter was to extend with bridging ligands some of the new structures of lanthanide complexes, previously obtained in our research group[52–55] and to study the modification of the structural, optical and magnetic properties of the new compounds. The same ligands derivatives of pyridine-carboxylic and benzoic acids were used in the coordination of the 1st row transition metals (some reported in the previous Chapter 2), namely 3–hydroxypicolinic, 2–hydroxynicotinic and picolinic. Details about the different approaches of synthesis with Lns can be found in Chapter 7 (p. 161). The choice of the bridging ligands was made by different criteria, such as: affinity to Ln ion and facility to coordination in aqueous solution (O donor ligands were preferred: aliphatic dicarboxylic acids with growing chains from C_2 to C_7; geometry and electronic configuration (polydentate); to enhance the optical properties and to allow spatially and electronically magnetic interactions. We have focused our attention to synthesis and properties of new coordination compounds with picolinic acid and aliphatic dicarboxylic bridging ligand.

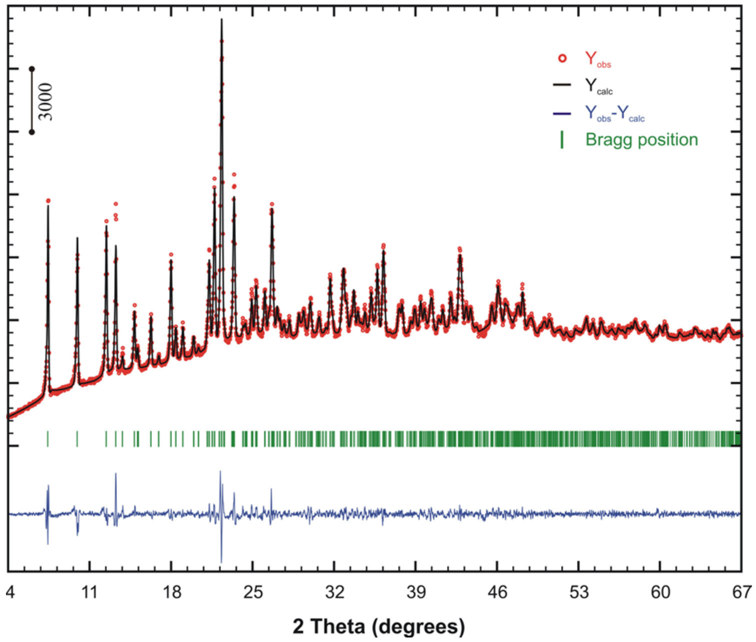

Figure 3.2.: Experimental data (red circles), calculated (upper solid black line) and difference (lower solid blue line) powder X-ray diffraction patterns for compound $[Eu(glu)(pic)(H_2O)_2]$. Vertical bars indicate the angular positions of the allowed Bragg reflections for space group $P2_1/c$. M(20) = 44.4 and F(20) = 97.6. Refined unit cell parameters (after Le Bail profile fitting with FullProf.2k): a = 12.025(1) Å, b = 13.376(1) Å, c = 8.480(1) Å, β = 96.862(5), (R_{Bragg} = 1.54% and χ^2 = 6.81).

3.2. Structural aspects of compounds $[Ln(glu)(pic)(H_2O)_2]$ (Ln^{3+} = Sm^{3+} (compound XV), Tb^{3+} (compound XVI) and Eu^{3+} (compound XVII))

A triad of isostructural lanthanide-organic one-dimensional coordination polymers, with general empirical formula $[Ln(glu)(pic)(H_2O)_2]$ (where Ln = Sm^{3+}, Tb^{3+} and Eu^{3+}), were isolated and characterised (by elemental analyses, infrared spectroscopy and thermoanalytical measurements) in the solid-state as homogeneous phase-pure materials. Phase identification of the Sm^{3+} and Tb^{3+} materials was performed using single-crystal X-ray diffraction whereas for the microcrystalline Eu^{3+} complex (Fig. 3.2) only powder studies could be undertaken.

3.2.1. Crystal structure of compound $[Sm(glu)(pic)(H_2O)_2]$ (XV)

When an aqueous solution with Sm^{3+} or Tb^{3+} ions diffuses into a gel containing glutaric acid ($H_2glu = C_5H_8O_4$) and picolinic acid ($Hpic = C_6H_5NO_2$), crystalline materials, which could be manually isolated in the form of large single-crystals shown in Fig. 3.3 (a) and (b), respectively, were formed (see Chapter 7). Information concerning crystallographic data collection and structural refinement details for $[Sm(glu)(pic)(H_2O)_2]$ is summarised in Table C.4 (in Appendix C, p. 188).

The crystal structure of $[Sm(glu)(pic)(H_2O)_2]$ contains a single crystallographically unique Sm^{3+} metallic centre, which appears coordinated to two water molecules, three glutarate anions (glu^{2-}) and one picolinic acid residue (pic^-), in a typical eight-coordination

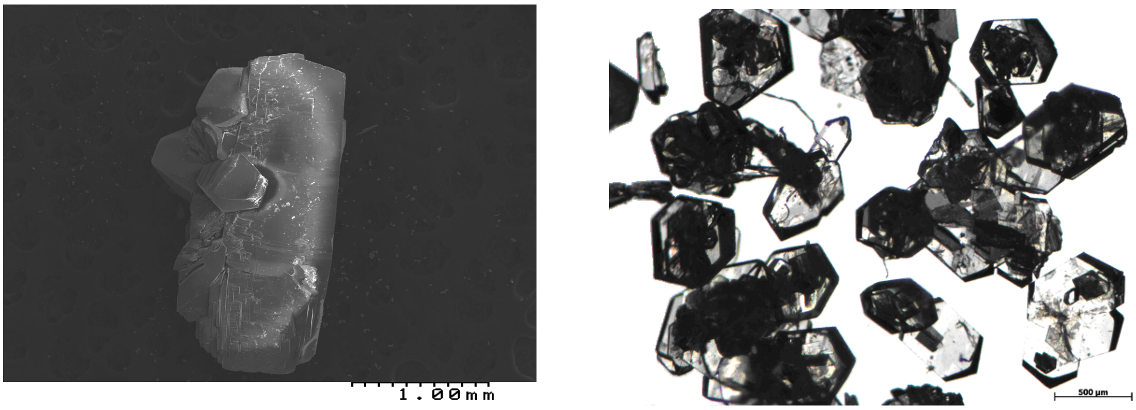

(a) (b)

Figure 3.3.: (a) SEM image of the crystal [Sm(glu)(pic)(H_2O)$_2$] (**XV**); (b) Optical microscope image of [Tb(glu)(pic)(H_2O)$_2$] (**XVI**).

fashion (Fig. 3.4 (a), {$SmNO_7$}) best described as a highly distorted dodecahedron (Fig. 3.4 (b)): while one trapezoid of this polyhedron is composed of two water molecules [O(1*W*) and O(2*W*)] and two oxygen atoms from distinct glutarato residues [O(4)^{i} and O(6)^{ii}], the other is instead formed by the N,O− chelate of the picolinic acid moiety plus another two oxygen atoms from glutarate anions [O(3) and O(5)^{ii}] (Fig. 3.4 (a) and (b); symmetry codes: (i) $2 - x, 1 - y, -z$; (ii) $2 - x, 1 - y, 1 - z$). The Sm−O bond lengths for the coordinated water molecules and the carboxyl groups [found in the 2.407(3)–2.410(3) and 2.355(3)–2.508(3) Å ranges, respectively — see Table D.2] are in good agreement with those typically found in related compounds, as revealed by a search of the Cambridge Structural Database (CSD, Version 5.27, November 2005),[56,57] while the typical Sm−O_{water} can be found in the 2.32–2.89 Å range (from 41 entries with a median of 2.44 Å). The Sm−$O_{carboxylate}$ are instead in the 2.19–3.08 Å range. It is of considerable interest to mention that the lack of regularity in the dodecahedral coordination environment arises, mainly, because of the various binding modes of the ligands composing the first coordination sphere, which is reflected in the internal angles of the polyhedron (Table D.2).

The compound contains a single crystallographically independent glutarato residue, which appears with its two carboxyl groups having very distinct coordination modes (see Fig. 3.5 (a) and (b)). On the one hand, the carboxyl group composed of O(5) and O(6) (Fig. 3.4, a) coordinates to the Sm^{3+} centre through a typical bidentate *syn,syn* chelating fashion with a bite angle of 52.33(9)°, which is in good agreement with the values reported for analogous materials (from 35 entries in the CSD with a median of 51.2°). On the other hand, the opposite carboxyl group, composed of O(3) and O(4)(Fig. 3.4, a), appears instead forming a *syn,anti* bridge with a neighbouring Sm^{3+} cation, thus imposing a Sm(1)···Sm(1)^{i} separation of 4.626(1) Å. This *syn,anti* bridge leads to the formation of a centrosymmetric binuclear moiety, which can be further envisaged as the building block of the polymeric structure of the material, a structural feature only found in few other structures also containing lanthanide centres and glutarato anions, namely with Nd^{3+},[58,59] Ho^{3+},[59] and Tb^{3+},[60] all of which are 1D materials. Interestingly, in those compounds, the glutarato anions exhibit

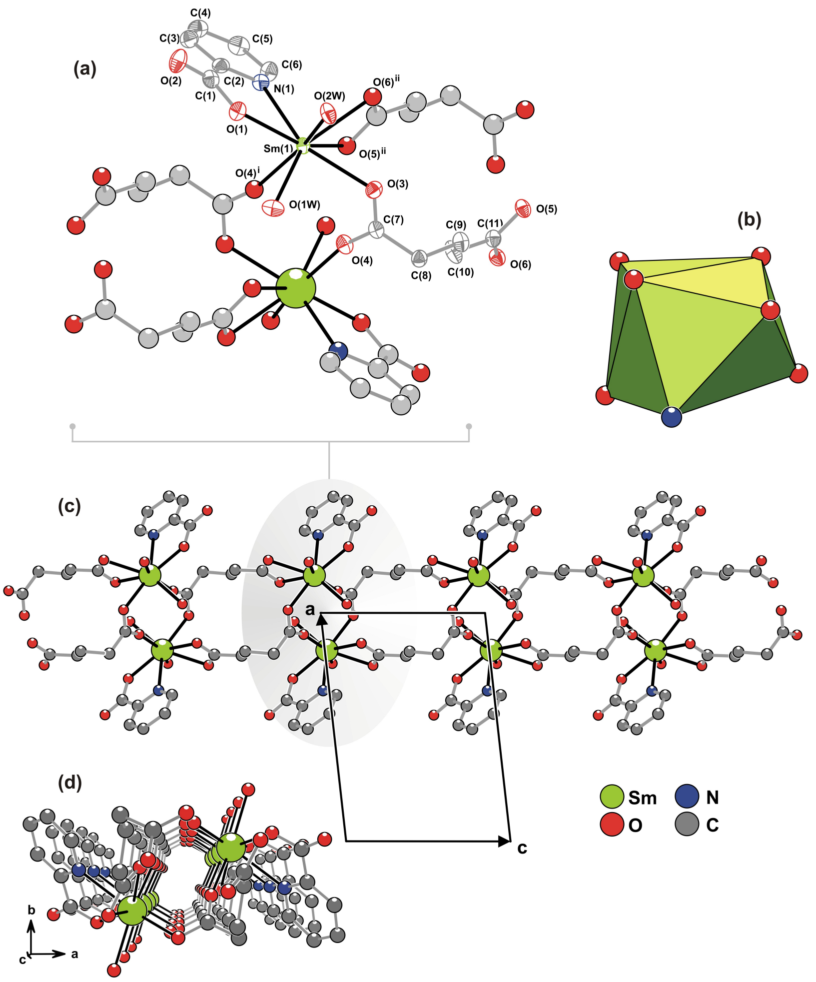

Figure 3.4.: (a) Centrosymmetric binuclear secondary building unit of the coordination polymer, showing the labelling scheme for all non-hydrogen atoms belonging to the asymmetric unit. Thermal ellipsoids are shown at the 50% probability level; (b) Polyhedral representation of the coordination sphere of the Sm^{3+} centre, $\{\mathrm{SmNO_7}\}$, resembling a highly distorted dodecahedron; (c and d) Perspective views of the $1\mathrm{D}^{1}_{\infty}$ $[\mathrm{Sm(pic)(glu)(H_2O)_2}]$ molecular tape running parallel to the *c* axis of the unit cell. Hydrogen atoms have been omitted for clarity. For selected bond lengths and angles see Table D.2 in Appendix D, p. 196. Symmetry transformations used to generate equivalent atoms: (i) $2-x, 1-y, -z$; (ii) $2-x, 1-y, 1-z$.

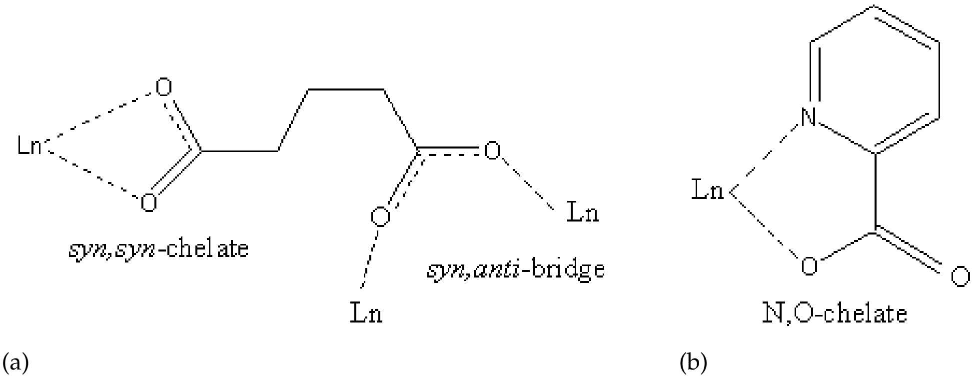

Figure 3.5.: Schematic representation of the ligands' coordination modes in $[\mathrm{Sm(glu)(pic)(H_2O)_2}]$: (a) glutaric acid; (b) picolinic acid.

markedly distinct coordination geometries compared with those registered for compound **XV**. This is particularly notable for the bridging groups which appear as *syn,anti* bridges, while in those 1D compounds[58,59] one oxygen atom is simultaneously involved in a *syn,syn* chelate and in a *syn,anti* bridge. Moreover, this structural aspect exhibited by one carboxyl oxygen atom is repeatedly found in all the remaining known 2D[60] and 3D[61–66] lanthanide-organic materials containing glutaric acid residues, thus rendering the present compound the first example of a glutarato-lanthanide material in which an inter-lanthanide bridge via a carboxyl group is enforced by a *syn,anti* bridge. Apart from structurally creating the aforementioned bimetallic units, the glutarato anionic residues further establish physical links interconnecting the two Sm^{3+} centres of one unit [Sm(1) plus Sm(1)^{i} — Fig. 3.4, a] with a third metallic centre of a neighbouring moiety [Sm(1)^{iii}], imposing Sm(1)$\cdots$Sm(1)^{iii} and Sm(1)$^{i}\cdots$Sm(1)^{iii} separations of 8.480(2) and 9.074(2) Å, respectively [symmetry code: (iii) $x,\ y,\ -1+z$]. This leads to the formation of a 1D $^{1}_{\infty}$ [Sm(glu)(pic)(H_2O)$_2$] molecular tape running parallel to the [001] direction of the unit cell (Fig. 3.4, c and d).

As reported by Zhang *et al.*[59] for the 1D $^{1}_{\infty}$ [Ln(glu)(phen)Cl] (where Ln^{3+} = Tb^{3+} and Ho^{3+}, phen = 1,10–phenanthroline) materials, the $^{1}_{\infty}$ [Sm(glu)(pic)(H_2O)$_2$] molecular tape present in the crystal structure also contains, external to the glu/Sm core, chelating aromatic organic ligands (picolinato residues) which seem to prevent the growth of the hybrid polymer in more than one direction by removing available coordination sites in the metallic centres (Fig. 3.4). Indeed for all known and related compounds, when these chelating moieties are not present 2D[60] and 3D[61–68] materials are typically isolated. The picolinic acid residues appear coordinated to the Sm^{3+} metallic centres in a typical N,O− chelating fashion (Fig. 3.5 (b)) with a bite angle of 64.97(10)°, a value consistent with those reported for similar compounds.[29,52,55,69]

Individual neutral 1D $^{1}_{\infty}$ [Sm(glu)(pic)(H_2O)$_2$] molecular tapes close-pack in the solid state, mediated by weak interactions, such as homonuclear O−H$\cdots$O hydrogen bonds and $\pi-\pi$ stacking to form a 3D supramolecular structure. Strong and highly directional [all interaction angles <(DHA) are well above 150° — see Table E.2 in Appendix E, p. 204] O−H$\cdots$O hydrogen bonds involving the coordinated water molecules and the carboxyl groups interconnect neighbouring tapes in the *bc* plane of the unit cell leading to a 2D supramolecular framework (Fig. 3.6, a). One of these interactions is particularly important for the structural integrity of the binuclear secondary building unit of the molecular tape, as represented in Fig. 3.6, b. The coordinated O(1W) water molecule donates one hydrogen atom in a strong hydrogen bonding interaction with a neighbouring carboxyl group [D$\cdots$A of 2.753(4) Å with <(DHA) of 175(4)°]. In fact, for all other closely related compounds, connections between adjacent lanthanide centres are usually assured by four carboxyl groups, either belonging to the glutarato[58–60,62,64–67] or oxalato[61,63] anions, in a pseudo-paddlewheel motif. For the $^{1}_{\infty}$ [Sm(glu)(pic)(H_2O)$_2$] molecular tape, only two carboxyl groups bridge the metallic centres (Fig. 3.6, b), with structural stability being achieved when the aforementioned hydrogen bonds are taken into account. Hydrogen-bonded supramolecular layers are in turn arranged in an orderly fashion along the [100] direction of the unit cell, medi-

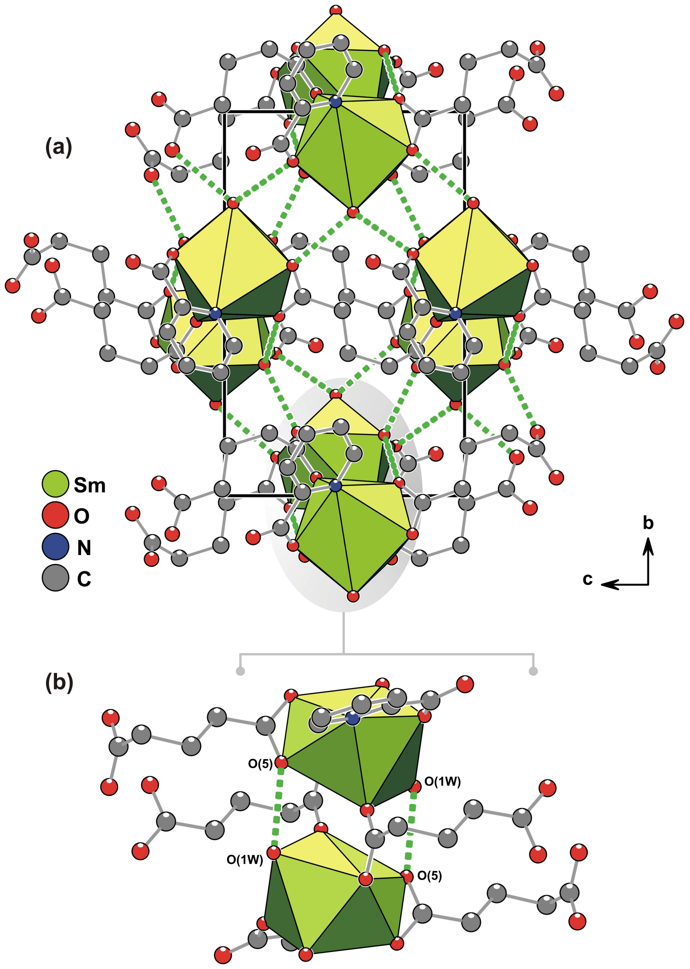

Figure 3.6.: (a) Crystal packing of [Sm(pic)(glu)(H_2O)$_2$] viewed along the [100] direction of the unit cell; (b) Intra-dimer hydrogen bonds involving the coordinated O(1) water molecule and the *syn,syn* chelating carboxyl group. Hydrogen atoms and symmetry codes used to generate equivalent atoms have been omitted for clarity. Hydrogen bonds are represented as black-filled dashed lines. For hydrogen bonding geometric details see Table E.2 in Appendix E, p. 204.

ated by offset $\pi - \pi$ stacking interactions between neighbouring coordinated picolinic acid residues (Fig. 3.7).

3.2.2. Spectroscopic and thermo-analytical results

The CHN elemental and diagnostic FT–IR and Raman spectroscopic data for the synthesized compounds are summarised in Table 3.2.

Compounds XV, XVI and XVII The elemental data agree well with the expected composition based on the single-crystal X-ray studies performed. FT–IR spectroscopy confirms the coordination of both ligands to the metal centres: pic$^-$ by means of the carboxyl group and the nitrogen atom from the aromatic ring, and glu^{2-} via its carboxyl groups. The asymmetric stretching $\nu_{asym}(-CO_2^-)$ mode shows shifts up to 33 cm^{-1} (40 cm^{-1} in the Raman spectra) to lower wavenumbers when compared with the values reported for the free picolinic acid.

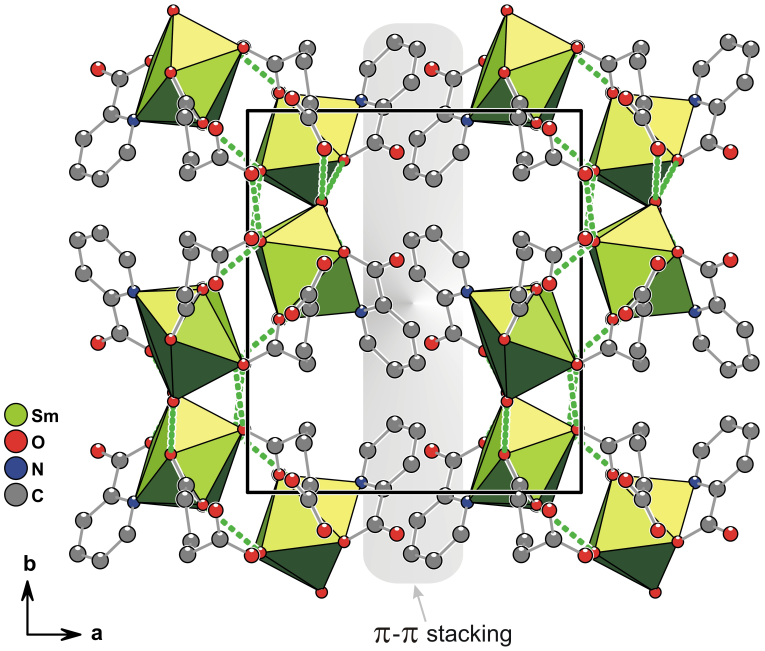

Figure 3.7.: Mixed ball-and-stick and polyhedral (for the {$SnNO_7$} coordination environments) representations of the crystal packing of [$Sm(pic)(glu)(H_2O)_2$] viewed along [001] direction of the unit cell. Hydrogen atoms have been omitted for clarity, and hydrogen bonds are represented as black-filled dashed lines.

Furthermore, the measured values of $\Delta[\nu_{asym}(-CO_2^-)-\nu_{sym}(-CO_2^-)]$ for the Sm (281 cm^{-1}), Eu (283 cm^{-1}) and Tb (283 cm^{-1}) compounds are further evidence for the presence of carboxyl groups coordinated to the metal centres. The typical stretching $\nu(C-N)$ vibrational mode of substituted pyridines appears for the uncoordinated picolinic acid at 1594 cm^{-1} and shows small shifts (up to 13 cm^{-1} in the FT–IR spectra and up to 30 cm^{-1} in the Raman spectra) for all compounds, in agreement with N,O− chelation involving the nitrogen atom of pic^- group. The typical stretching $\nu(C-O)$ vibrational mode of the carboxyl group of glutaric acid at 1265 cm^{-1} is shifted for all compounds by 26 cm^{-1}, confirming the bond formed between the deprotonated carboxyl group of glutaric acid and lanthanide ion.

The thermal decomposition of compound **XV** occurs in a multi-step process from ambient temperature to 800 °C, to yield Sm_2O_3 as the final residue (total weight loss: 57%; calculated: 60%). The first weight loss of *ca.* 8.4% occurs in the 57–230 °C temperature range (DTG peak at 182 °C) and can be attributed to the release of the two coordinated water molecules (calculated weight loss of 8.2%). Between 230 and 747 °C a total weight loss of *ca.* 49% corresponds to the thermal decomposition of the organic components (calculated 57%). The other Ln compounds exhibit similar thermal properties: for compound **XVI** the total weight loss between 72 °C and 700 °C was 58% (calculated value of 59%). For compound **XVII** the total weight loss was 57% with a calculated value of 60% between 22 °C and 800 °C.

Table 3.2.: Analytical and spectroscopic data for the lanthanide complexes.
(a) Calculated values in parentheses. (b) Infrared and Raman data (in italics).

	Elemental composition (%)[a]			Vibrational data (cm^{-1})[b]				
Compound	C	N	H	Picolinic acid			Glutaric acid	
				$\nu_{as}(CO_2)$	$\nu(CC), \nu(CN)$	$\nu_{sym}(CO_2)$	$\nu(C-O)$	$\nu(C=O)$
Hpic	—	—	—	1722	1608,1594	1344	—	—
				1692	*1620,1596*	*1358*		
H_2glu	—	—	—	—	—	—	1250	1697
[Sm(glu)(pic)(H_2O)$_2$]	29.20	2.71	3.23	1689	1599,1581	1407	1276	1563
	(30.12)	(3.19)	(3.22)	*1652*	*1598,1566*	*1351*		
[Tb(glu)(pic)(H_2O)$_2$]	29.58	2.83	3.15	1691	1601,1589	1408	1276	1563
	(29.55)	(3.16)	(3.13)	*1654*	*1600,1568*	*1354*		
[Eu(glu)(pic)(H_2O)$_2$]	29.99	2.99	3.19	1690	1600,1584	1407	1276	1563
	(30.01)	(3.18)	(3.21)	*1653*	*1600,1567*	*1353*		

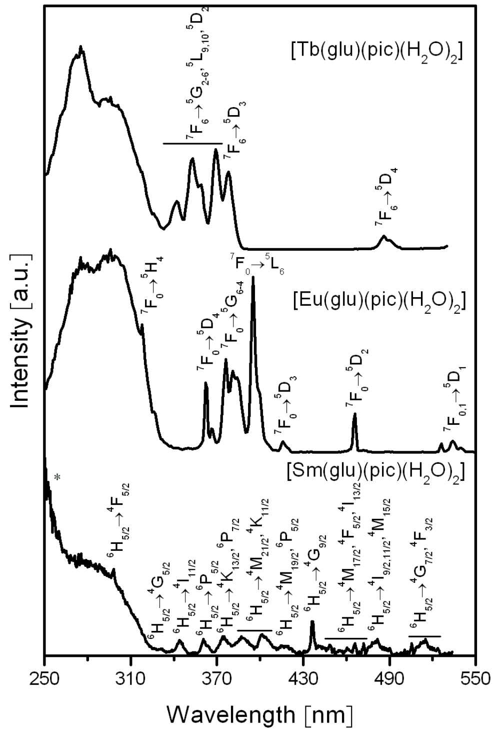

Figure 3.8.: Excitation spectra of [Ln(glu)(pic)(H_2O)$_2$] monitored at 597, 614, and 545 nm for the Sm^{3+}, Eu^{3+} and Tb^{3+} complexes, respectively.

3.3. Photoluminescence of compounds XV, XVI and XVII

The excitation spectra of the Sm^{3+}, Eu^{3+} and Tb^{3+} compounds represented in Fig. 3.8, were monitored around the cation's more intense line which can be found at 597 nm for Sm^{3+}, 614 nm for Eu^{3+} and 545 nm for Tb^{3+}. Each spectrum displays a large broad band in the range of 250–345 nm and a series of sharp lines characteristic of the Sm^{3+}, Eu^{3+} and Tb^{3+} energy levels. The large broad bands can be ascribed to the excited levels of the ligands[29,55] and are mainly formed of two components, peaking around 275 and 295 nm, being most evident for the Eu^{3+} and Tb^{3+} compounds. The assignment of the intra-$4f^5$ transition was based on the published literature.[70–73] Although the $^7F_1$ level of the Eu^{3+} complex is populated at room-temperature, the $^7F_1 \rightarrow^5 D_0$ transition was only explicitly assigned. It was also noted that the intensity at lower wavelengths (250—260 nm) for the Sm^{3+} complex is artificial due to the correction for the spectroscopic distribution of the lamp intensity (marked with an asterisk in Fig. 3.8).

Fig. 3.9 shows the emission spectra of the compounds **XV**, **XVI** and **XVII**. No changes could be detected in the lines of the cations by varying the excitation wavelength, suggesting that the lanthanide centre has only one local environment. The emission spectra of the Sm^{3+},

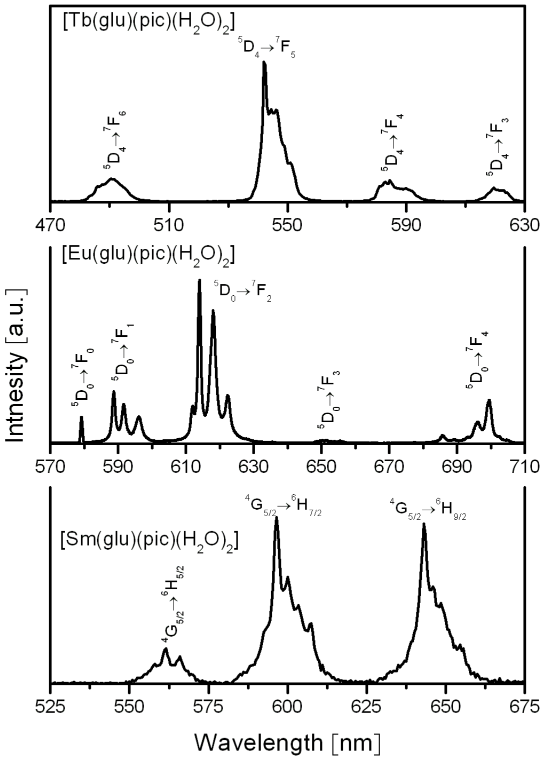

Figure 3.9.: Emission spectra of [Ln(glu)(pic)(H_2O)$_2$] (Ln = Sm, Eu and Tb), excited at 277, 305 and 277 nm for the Sm^{3+}, Eu^{3+} and Tb^{3+} complexes, respectively.

Eu^{3+} and Tb^{3+} complexes are composed by the intra–4f^5 (Sm^{3+}), intra–4f^6 (Eu^{3+}) and intra–4f^8 (Tb^{3+}) transitions ($^4G_{5/2} \rightarrow ^6H_{5/2,7/2,9/2}$, $^5D_0 \rightarrow ^7F_{0-4}$, and $^5D_4 \rightarrow ^7F_{6-3}$, respectively).

The $^5D_0$ (Eu^{3+}) and $^5D_4$ (Tb^{3+}) lifetimes were monitored within the more intense line of the $^5D_0 \rightarrow ^7F_2$ and $^5D_4 \rightarrow ^7F_5$ transitions, respectively, under the excitation which maximises the Eu^{3+} and Tb^{3+} emissions. The emission decay curves (not shown) reveal a single-exponential behaviour yielding to lifetimes values of 0.385 ± 0.002 ($^5D_0$) and 1.024 ± 0.005 ms^{-1} ($^5D_4$), respectively. The quantum efficiency, q, of the emission arising from the $^5D_0$ level in the complex [Eu(glu)(pic)(H_2O)$_2$] has been estimated assuming that only non-radiative and radiative processes are essentially involved in the depopulation of the excited state, as has already been reported.[28,74] We obtained a q value of *ca.* 10%, with a corresponding k_r value of 0.253 ms^{-1}. These lifetimes and quantum efficiency values, although lower when compared with those obtained by Sendor *et al.* for the europium picolinato complexes,[29] are of the same order of magnitude as those obtained for the Eu^{3+} emission in the 3–hydroxypicolinato[28] and 2–hydroxynicotinato complexes.[54]

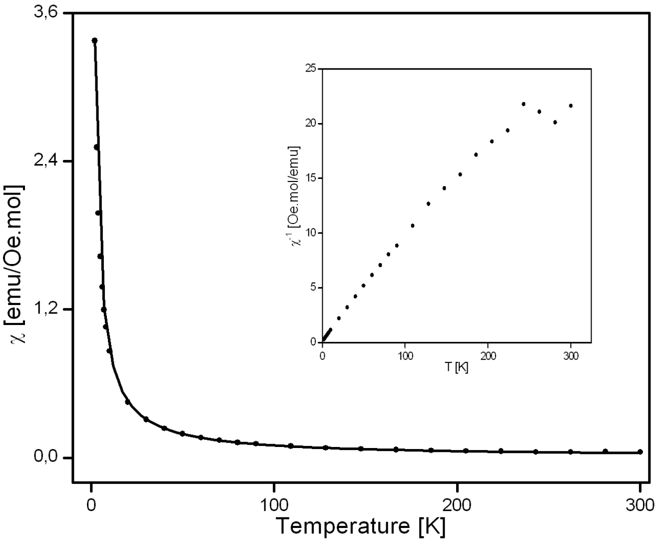

Figure 3.10.: Magnetic susceptibility χ as function of temperature T of [Tb(glu)(pic)(H_2O)$_2$]. The straight line is the fit of the experimental data to the Curie-Weiss law. The inset shows the inverse magnetic susceptibility χ^{-1} as a function of temperature.

3.4. Magnetic properties of compound [Tb(glu)(pic)(H_2O)$_2$] (XVI)

No thermal irreversibility was observed for the compound [Tb(glu)(pic)(H_2O)$_2$] since measurements taken with decreasing temperature gave identical results, either after cooling from ambient temperature to 2 K in zero applied magnetic field (zero field cooling), or after cooling under the measurement field (Fig. 3.10). Fig. 3.11 presents the magnetic susceptibility multiplied per temperature as function of the temperature. The plot show decreasing of the χT with the decreasing of the temperature. This tendency might be due to zero-field splitting (although usually very weak for lanthanides) of the Tb^{3+} ion, because of strong spin-orbit coupling, and partially contributed to the possible antiferromagnetic coupling between the Ln ions at lower temperatures (the distance between the Sm^{3+} ions in compound **XV** is about 4.6 Åand could be of approximatively similar value for compound **XVI**, since the complexes are structurally identical (see Section 3.2)).

The temperature dependence of the inverse of susceptibility follows the Curie-Weiss law (the inset in Fig. 3.10). The experimentally obtained effective magnetic moment of the Tb^{3+} ion is $8.71\mu_B$, which in this case is lower than the theoretical value of $9.72\mu_B$.[42] Since the high distance between the ground and excited levels of the terbium[41] (2000 cm^{-1}; see Table 3.1), we can assume that only the ground state $^7F_6$ is thermally populated.

The fitting of the experimental data to the Curie-Weiss law (Equation 1.10 on p. 29; see Fig. 3.10) gave the values: Curie constant, $C_{\text{mol}} = 9.48$ emu.K/mol; Weiss constant: $\Theta = -0.9$ K and residual temperature independent which accounts for diamagnetic contributions is equal of $\chi_0 = 0.007$ emu/mol.K.Oe. Such independent was added to the Curie-

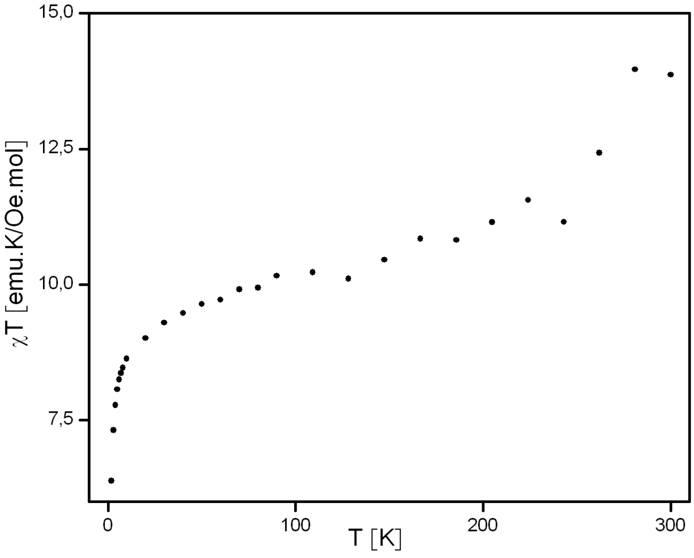

Figure 3.11.: Plot of magnetic susceptibility multiplied per temperature χT as a function of temperature for [Tb(glu)(pic)(H_2O)$_2$].

Weiss law as a fitting variable as shown in Equation 3.6. The value of C is close to the value already reported for Tb^{3+} complex.[75] From C (Equation 1.16 on p. 38), the value of the g-factor g_J was found: $g_J = 2.5$, which is higher than the theoretically calculated for Tb^{3+} ion, $g_J = 3/2$ (by Equation 3.7).[41] For the f^8 electrons of the Tb^{3+}, the quantum numbers are $S = L = 3$, and $J = 6$.

$$\chi_M = \frac{C}{T - \Theta} + \chi_0 \tag{3.6}$$

$$g_J = \frac{3}{2} + \frac{[S(S+1) - L(L+1)]}{2J(J+1)} \tag{3.7}$$

3.5. Final remark

Magnetic interactions between the Tb^{3+} ions in its complex with picolinic and glutaric acid were not found. Nevertheless, the possibility to build such picolinic-containing lanthanide-organic polymers in which the length of the bridging ligand could be systematically varied open up some prospects for future work concerning the investigation of the photoluminescent and magnetic behaviour of other similar systems.

References

1. Jones AC and O'Brien P, CVD of compound semiconductors, Wiley-VCH Verlagsgesellschaft mbH, Weinheim, 1997.
2. Cotton FA, *J. Chem. Soc., Dalton Trans.* (13) (2000), 1961–1968.
3. Dinolfo PH and Hupp JT, *Chem. Mater.* 13(10) (2001), 3113–3125.
4. Sanchez C, Lebeau B, Chaput F and Boilot JP, *Adv. Mater.* 15(23) (2003), 1969–1994.
5. Rao CNR, Müller A and Cheetham AK, The Chemistry of nanomaterials: synthesis, properties and applications, Wiley-V C H, Weinheim, 2003.
6. Schmid G, Nanoparticles, Wiley-V C H, Weinheim, 2004.
7. Ozin GA and Arsenaukt AC, Nanochemistry: a chemical approach to nanomaterials, RSC, Cambridge, 2005.
8. Kitagawa S, Kitaura R and Noro S, *Angew. Chem., Int. Ed.* 43(18) (2004), 2334–2375.
9. O'Brien P and Nomura R, *J. Mater. Chem.* 5(11) (1995), 1761–1773.
10. Bochmann M, *Chem. Vapor Depos.* 2(3) (1996), 88.
11. Trindade T, OBrien P and Zhang XM, *Chem. Mater.* 9(2) (1997), 523–530.
12. Monteiro OC, Nogueira HIS, Trindade T and Motevalli M, *Chem. Mater.* 13(6) (2001), 2103–2111.
13. Green M, Prince P, Gardener M and Steed J, *Adv. Mater.* 16(12) (2004), 994–996.
14. Shaver A, Ng JB, Hall DA, Lum BS and Posner BI, *Inorg. Chem.* 32(14) (1993), 3109–3113.
15. Palicová M, Segl'a P, Mikloš D, Kopcová M, Melník M, Dudová B, Hudecová D and Glowiak T, *Polyhedron* 19(28) (2000), 2689–2695.
16. Yano S, Nakai M, Sekiguchi F, Obata M, Kato M, Shiro M, Kinoshita I, Mikuriya M, Sakurai H and Orvig C, *Chem. Lett.* (9) (2002), 916–917.
17. Barman RK, Singh SK and Das BK, *J. Chem. Crystallogr.* 32(10) (2002), 369–375.
18. March R, Clegg W, Coxall RA, Cucurull-Sánchez L, Lezama L, Rojo T and González-Duarte P, *Inorg. Chim. Acta* 353 (2003), 129–138.
19. Sun C, Zheng X and Jin L, *J. Mol. Struct.* 646(1-3) (2003), 201–210.
20. Kiss E, Bényei A and Kiss T, *Polyhedron* 22(1) (2003), 27–33.
21. Griffith WP, Pumphrey CA and Rainey TA, *J. Chem. Soc., Dalton Trans.* (6) (1986), 1125–1128.
22. Griffith WP, Nogueira HIS, Parkin BC, Sheppard RN, White AJP and Williams DJ, *J. Chem. Soc., Dalton Trans.* (11) (1995), 1775–1781.
23. Griffith WP, Nogueira HIS, White AJP and Williams DJ, *Polyhedron* 16(8) (1997), 1323–1329.
24. Quintal SMO, Nogueira HIS, Félix V and Drew MGB, *New J. Chem.* 24(7) (2000), 511–517.
25. Quintal SMO, Nogueira HIS, Félix V and Drew MGB, *Polyhedron* 21(27-28) (2002), 2783–2791.

26. Girginova PI, Paz FAA, Nogueira HIS, Silva NJO, Amaral VS, Klinowski J and Trindade T, *J. Mol. Struct.* 737(2-3) (2005), 221–229.
27. Girginova PI, Paz FAA, Nogueira HIS, Silva NJO, Amaral VS, Klinowski J and Trindade T, *Polyhedron* 24(4) (2005), 563–569.
28. Soares-Santos PCR, Nogueira HIS, Félix V, Drew MGB, Ferreira RAS, Carlos LD and Trindade T, *Chem. Mater.* 15(1) (2003), 100–108.
29. Sendor D, Hilder M, Juestel T, Junk PC and Kynast UH, *New J. Chem.* 27(7) (2003), 1070–1077.
30. Guillou O and Daiguebonne C, Lanthanide-containing coordination polymers, vol. 34 of *Handbook on the Physics and Chemistry of Rare Earths*, 1st ed., North Holland, 2005.
31. Huheey JE, Keiter EA and Keiter RL, Inorganic chemistry. Principles of structure and reactivity, 4th ed., HaprepCollinsCollegePublishers, 1993.
32. Bertini I, Capozzi F, Luchinat C, Nicastro G and Xia ZC, *J. Phys. Chem.* 97(24) (1993), 6351–6354.
33. Tóth E, Burai L and Merbach AE, *Coord. Chem. Rev.* 216 (2001), 363–382.
34. Tóth E, Helm L, Merbach AE, Hedinger R, Hegetschweiler K and Jánossy A, *Inorg. Chem.* 37(16) (1998), 4104–4113.
35. Comblin V, Gilsoul D, Hermann M, Humblet V, Jacques V, Mesbahi M, Sauvage C and Desreux JF, *Coord. Chem. Rev.* 185–186 (1999), 451–470.
36. Moats RA, Fraser SE and Meade TJ, *Angew. Chem, Int. Ed. Engl.* 36(7) (1997), 726–728.
37. Zhang SR, Wu KC and Sherry AD, *Angew. Chem., Int. Ed.* 38(21) (1999), 3192–3194.
38. Bertini I, Felli IC and Luchinat C, *J. Biomol. NMR* 18(4) (2000), 347–355.
39. Hinckley CC, *J. Am. Chem. Soc.* 91(18) (1969), 5160–5162.
40. Zuo CS, Metz KR, Sun Y and Sherry AD, *J. Magn. Reson.* 133(1) (1998), 53–60.
41. Kahn O, Molecular magnetism, Wiley–VCH, 1993.
42. Orchard AF, Magnetochemistry, 1st ed., Oxford chemistry primers, Oxford: University Press, 2003.
43. URL `www.radiochemistry.org`.
44. URL `http://www.chem.ox.ac.uk`.
45. Andruh M, Bakalbassis E, Kahn O, Trombe JC and Porcher P, *Inorg. Chem.* 32(9) (1993), 1616–1622.
46. Judd BR, *Phys. Rev.* 127(3) (1962), 750–761.
47. Ofelt GS, *J. Chem. Phys.* 37(3) (1962), 511–520.
48. Sabbatini N, Guardigli M and Lehn JM, *Coord. Chem. Rev.* 123(1-2) (1993), 201–228.
49. URL `www.shsu.edu`.
50. URL `http://micro.magnet.fsu.edu/`.
51. URL `http://web.uvic.ca/ail/techniques/epi-fluorescence.html`.
52. Soares-Santos PCR, Nogueira HIS, Félix V, Drew MGB, Ferreira RAS, Carlos LD and Trindade T, *Inorg. Chem. Commun.* 6(9) (2003), 1234–1238.

53. Soares-Santos PCR, Nogueira HIS, Paz FAA, Ferreira RAS, Carlos LD, Klinowski J and Trindade T, *Eur. J. Inorg. Chem.* (19) (2003), 3609–3617.
54. Soares-Santos PCR, Nogueira HIS, Rocha J, Félix V, Drew MGB, Ferreira RAS, Carlos LD and Trindade T, *Polyhedron* 22(27) (2003), 3529–3539.
55. Soares-Santos PCR, Paz FAA, Ferreira RAS, Klinowski J, Carlos LD, Trindade T and Nogueira HIS, *Polyhedron* 25(12) (2006), 2471–2482.
56. Allen FH, *Acta Crystallogr., Sect. B: Struct. Sci.* 58(3 PART 1) (2002), 380–388.
57. Allen FH and Motherwell WDS, *Acta Crystallogr., Sect. B: Struct. Sci.* 58(3 PART 1) (2002), 407–422.
58. Legendziewicz J, Keller B, Turowska-Tyrk I and Wojciechowski W, *New J. Chem.* 23(11) (1999), 1097–1103.
59. Zhang LP, Wan YH and Jin LP, *J. Mol. Struct.* 646(1-3) (2003), 169–178.
60. Glowiak T, Legendziewicz J, Dao CN and Huskowska E, *J. Less-Common Met.* 134(2) (1987), 153–168.
61. Thomas P and Trombe JC, *J. Chem. Crystallogr.* 30(10) (2000), 633–639.
62. Benmerad B, Guehria-Laïdoudi A, Dahaoui S and Lecomte C, *Acta Crystallogr., Sect. C: Cryst. Struct. Commun.* 60 (2004), M119–M122.
63. Vaidhyanathan R, Natarajan S and Rao CNR, *J. Solid State Chem.* 177(4-5) (2004), 1444–1448.
64. Glowiak T, Ngoan DC and Legendziewicz J, *Acta Crystallogr., Sect. C: Cryst. Struct. Commun.* 42 (1986), 1494–1496.
65. Serpaggi F and Férey G, *J. Mater. Chem.* 8(12) (1998), 2737–2741.
66. Serpaggi F and Férey G, *J. Mol. Struct.* 656(1-3) (2003), 201–206.
67. Benmerad B, Guehria-Laïdoudi A, Balegroune F, Birkedal H and Chapuis G, *Acta Crystallogr., Sect. C: Cryst. Struct. Commun.* 56 (2000), 789–792.
68. Dolbecq A, Mialane P, Lisnard L, Marrot J and Sécheresse F, *Chem. Eur. J.* 9(12) (2003), 2914–2920.
69. Ma JF, Hu NH and Ni JZ, *Polyhedron* 15(11) (1996), 1797–1799.
70. Faucher MD and Tanner PA, *J. Phys.: Condens. Matter* 18(37) (2006), 8503–8522.
71. Gruber JB, Zandi B and Reid MF, *Phys. Rev. B: Condens. Matter Mater. Phys.* 60(23) (1999), 15643–15653.
72. Wells JPR, Yamaga M, Han TPJ, Gallagher HG and Honda M, *Phys. Rev. B: Condens. Matter Mater. Phys.* 60(6) (1999), 3849–3855.
73. Devi AR, Jayasankar CK and Reid MF, *Phys. Rev. B: Condens. Matter Mater. Phys.* 49(18) (1994), 12551–12555.
74. Fernandes JA, Ferreira RAS, Pillinger M, Carlos LD, Jepsen J, Hazell A, Ribeiro-Claro P and Gonçalves IS, *J. Lumin.* 113(1-2) (2005), 50–63.
75. Cui HB, Otsuka T, Kobayashi A, Takeda N, Ishikawa M, Misaki Y and Kobayashi H, *Inorg. Chem.* 42(19) (2003), 6114–6122.

MAGNETIC BEHAVIOUR OF ORGANIC-INORGANIC HYBRIDS OF N-(PHOSPHONOMETHYL)IMINODIACETIC ACID AND 1ST ROW TRANSITION METALS

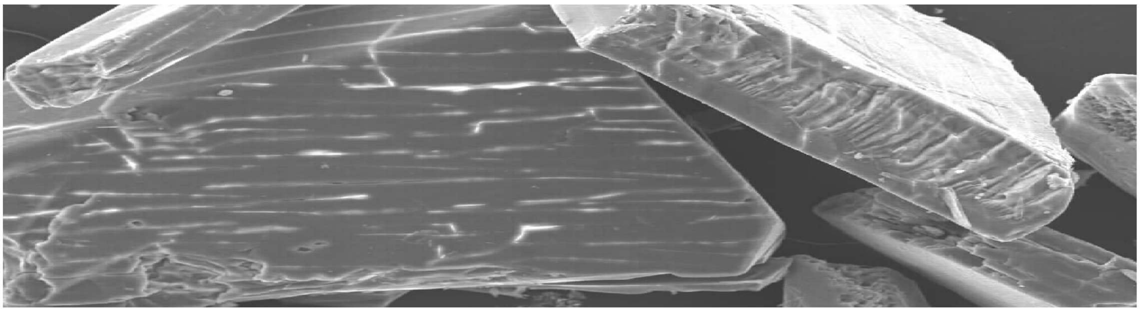

CHAPTER IV

Chapter 4.

Magnetic behaviour of organic-inorganic hybrids of N–(phosphonomethyl)iminodiacetic acid and 1st row transition metals

4.1. Introduction

Since the first multi-dimensional diamondoid-type metal-organic frameworks (known as MOF, coordination polymers or coordination frameworks) have been synthesized by Hoskins and Robson[1] in the early 1990s, the design of extended organic-inorganic hybrid frameworks using aromatic rings (N–donors such as 4,4′–bipyridine or pyrazine), polycarboxylic and polyphosphonic acid groups ligands in combination with various distinct metal centres, has received much attention.[2–11] This great interest is due of their rich and exotic topological architectures, and their interesting properties and potential applications[2,12–22] as functional materials in areas as diverse as catalysis, photonics, gas and shape-selective adsorption, photochemistry, enantioselective processes, optical and magnetic devices. The control of the dimensionality of the final compounds is a major challenge, as the structures are frequently modulated by a combination of various factors[7,23–30] such as the temperature, the kind of counter ion, the coordination geometries of the metal centres, the metal-to-ligand ratios and the solvent, and the type of bridging ligands which might connect different metal centres.

It has been of interest how organic ligands can control the dimensionality of the hybrid materials by selective removal of some coordinative sites through the formation of chelate rings.[31–42] Materials which combine organic bridging ligands traditionally used in this field of research with new highly flexible molecules which join metal centres are of interest to study their magnetic properties. To this end, the multidentate chelating ligand, N–(phosphonomethyl)iminodiacetic acid (H_4pmida; Fig. 4.1) has three distinct coordination functional groups (two carboxylic acid groups and one phosphonic group, plus a central nitrogen atom) with interesting and flexible coordination properties, just like those we have observed for diethylenetriacetate ligands[39] and multiacetate ligands.[33] Metal centres can be located inside three five-membered rings formed by two carboxylate and the phosphonate groups, plus the central N− atom (Fig. 4.2).[43–48] This was first observed by Crans *et al.*[43,44] for the dimeric $[V_2O_2(\text{pmida})_2]^{4-}$ unit which was than used to construct three-dimensional frameworks incorporating Cd^{2+} and Co^{2+}.[34] The structures could be extended by including bridging ligands and thus new polynuclear polymer chains are built. In such way magnetic interactions between different magnetic centres could be propagated all along the chains (mediated by the the aromatic $\pi - \pi$ stacking and dipolar interactions). Those interactions between paramagnetic centres have been investigated for compounds with similar structures and were found to be antiferromagnetic or paramagnetic.[49–51]

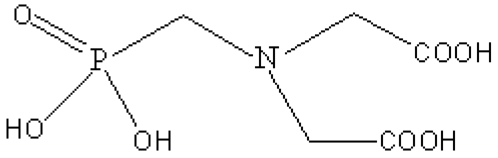

Figure 4.1.: N–(phosphonomethyl)iminodiacetic acid (H_4pmida).

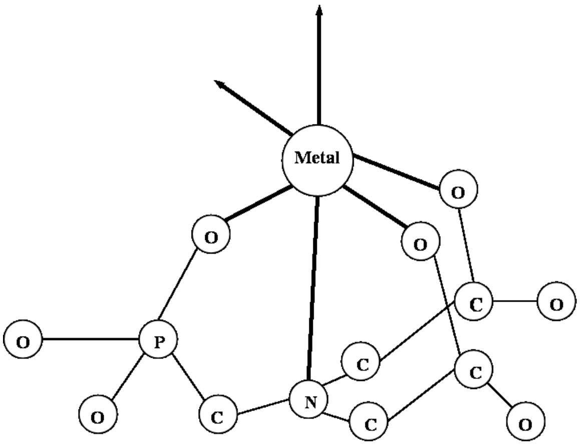

Figure 4.2.: Schematic representation of the three five-membered chelate rings formed by the pmida^{n-4} residues with metal centres. Arrows indicate available coordinative sites.

In the course of studies on transition metals complexes in our group, six new extended organic-inorganic hybrid complexes containing multidentate chelating organic residues of H_4pmida and organic bridging ligands containing nitrogen, have been synthesised using hydrothermal methods.[34,52] They were characterized structurally by single-crystal and powder X-ray diffraction techniques, elemental analysis and infrared spectroscopy. This chapter will focus on the research made on their magnetic properties, associated to structural details gathered from single-crystal X-ray diffraction studies. In particular, the influence of the ligand field and the coordination geometry on the magnetic susceptibility of the hybrid complexes was studied.

4.2. Magnetic properties of compounds with H_4pmida and without bridging ligand

4.2.1. Compound $[Fe(H_2pmida)(H_2O)_2]$ (XVIII)

4.2.1.1. Crystal structure

The hydrothermal reaction, under mild conditions, between ammonium iron(II) sulfate and H_4pmida yielded a highly crystalline compound formulated on the basis of single-crystal X-ray diffraction (Table C.5 in Appendix C, p. 189), elemental analysis and infrared spectroscopy (Table 4.1) as $[Fe(H_2pmida)(H_2O)_2]$. Phase purity and homogeneity of the bulk

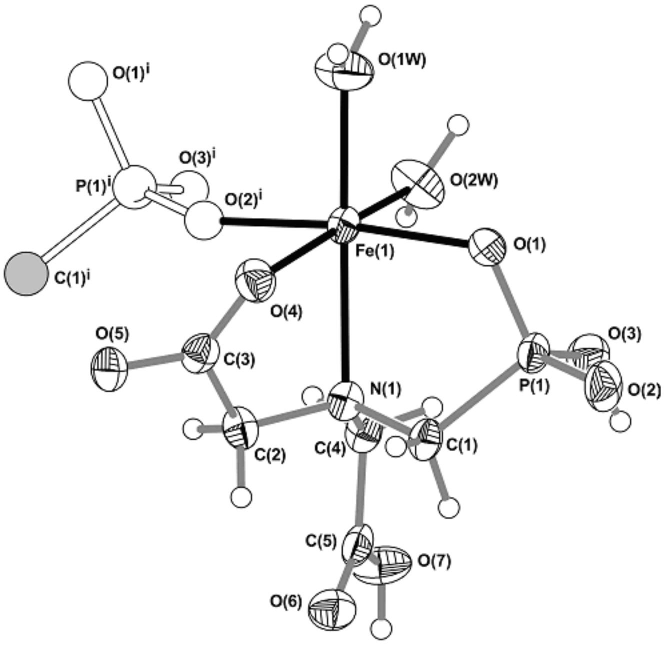

Figure 4.3.: Distorted {$FeNO_5$} octahedral coordination environment of the Fe^{2+} centres in [Fe(H_2pmida)(H_2O)$_2$] (**XVIII**), showing the labelling scheme for all atoms belonging to the asymmetric unit. Thermal ellipsoids are drawn at the 80% probability level and hydrogen atoms are represented as small spheres with arbitrary radius. For selected bond lengths and angles see Table D.3 in Appendix D, p. 197. Symmetry code used to generate equivalent atoms: (i) $x, y, 1 + z$.

sample were confirmed by powder X-ray diffraction (powder XRD) which also revealed the presence of some strong preferential orientation of the crystallites.

The crystal structure contains only one crystallographically unique Fe^{2+} metal centre, which is coordinated to two water molecules [O(1*W*) and O(2*W*), average bond distance *ca.* 2.12 Å], and to three O− and one N− donor atoms from H_2pmida^{2-} residues, leading to a six-coordination environment, {$FeNO_5$}, resembling a distorted octahedron, with the *cis* and *trans* angles within the 74.19(8)–100.68(9)° and 167.21(9)–173.73(8)° ranges, respectively (Fig. 4.3 and Table D.3 in Appendix D on p. 197). The coordination geometry of Fe^{2+} can also be described as a more regular square pyramidal environment [bond distances and angles found within the 2.051(2)–2.182(2) Å and 89.81(1)–96.36(1)° ranges, respectively], with the longer Fe−N bond to the H_2pmida^{2-} residue [2.311(2) Å] capping the base of the polyhedron (Fig. 4.3 and Table D.3).

The H_2pmida^{2-} anion appears in [Fe(H_2pmida)(H_2O)$_2$] as a polydentate organic ligand, which traps the Fe(1) centres inside two five-membered chelate rings, formed by one carboxylate group and the phosphonate moiety, both connected in the usually observed *anti*-unidentate coordinative fashion (Fig. 4.3). The two bite angles of $^{1}_{\infty}$[Fe(H_2pmida)(H_2O)$_2$] are significantly different, a relatively uncommon feature among the known crystal structures containing H_4pmida residues.[44–48,53–55] On the one hand, the bite angle formed with the coordinated carboxylic acid group, 74.19(8)° (Fig. 4.3 and Table D.3 (in Appendix D)), is very close to the angles usually observed for the anionic centrosymmetric [V_2O_2(pmida)$_2$]$^{4-}$ unit (*ca.* 76.2–77.0°),[34,44,56,57] with the small difference being attributed to the slightly higher

Table 4.1.: Analytical and spectroscopic data for the compounds of H_2pmida. *vs — very strong, s — strong, m — medium, w — weak*; (a) Calculated values in parentheses.

	Elemental composition (%)[a]			Vibrational data (cm^{-1})					
Compound				H_4pmida			pyr	4,4′–bpy	
	C	N	H	ν_{as}(C=O)	ν_{sym}(C=O)	ν(P=O)	ν(C=C), ν(C=N)	ν(C=N)	ν(C=C)
H_4pmida	–	–	–	1735	1340	1246	–	–	–
Pyrazine	–	–	–	–	–	–	–	–	–
4,4′–bpy	–	–	–	–	–	–	–	1590	1530
XVIII	18.93	4.42	3.79	1560vs	1401s	1055vs	–	–	–
	(18.95)	(4.44)	(3.82)					–	–
XIX	22.24	8.73	4.12	1622vs	1400s	1052	1622vs	–	–
	(23.27)	(9.08)	(4.12)					–	–
XX	22.57	8.77	4.18	1624s	1410s	1179s	1624vs	–	–
	(23.28)	(9.09)	(4.12)					–	–
XXI	35.88	8.88	4.88	1607vs	1400s	1067s	–	1590vs	1491
	(38.45)	(9.01)	(4.36)				–		
XXII	37.36	8.85	4.05	1608vs	1398s	1068vs	–	1588vs	1490m
	(38.32)	(8.98)	(4.34)				–		
XXIII	34.93	8.62	4.03	1633s	1388m	1247w	–	1601vs	1531m
	(35.60)	(8.30)	(3.66)						

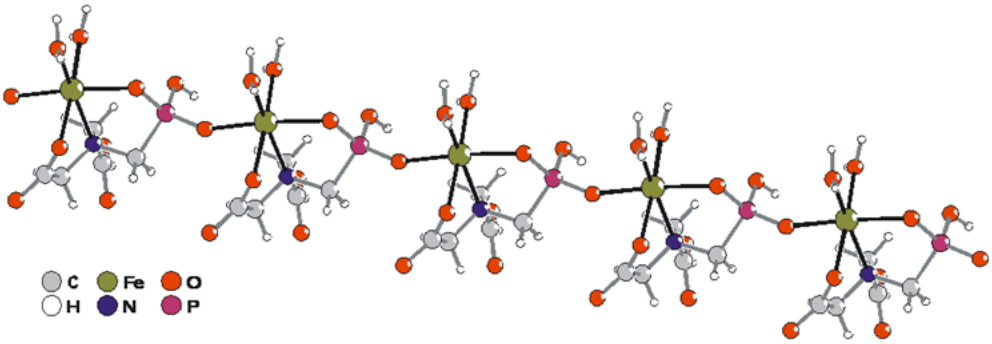

Figure 4.4.: Ball-and-stick representation of the one-dimensional $^1_\infty$[Fe(H_2pmida)(H_2O)$_2$] (**XVIII**) neutral coordination polymer running along the [001] direction.

effective ionic radius of the Fe^{2+} centre (for a typical six-coordination geometry: V^{4+} 0.58 Å; Fe^{2+} 0.61 Å and 0.78 Å, for low- and high-spin complexes, respectively).[58,59] On the other hand, the bite angle formed with the phosphonate group, 83.51(9)° (Fig. 4.3 and Table D.3), is also very similar to the angles observed in similar structures in which this group bridges two adjacent metal centres as, for example, in the polymeric structure $[Co_2(pmida)(H_2O)_5]_n$ (*ca.* 81.4°)[45] and in the cyclic hexameric unit $[C_{30}H_{30}Co_6N_6O_{42}P_6]^{12-}$ (*ca.* 82.3°).[47]

Another interesting feature of compound **XVIII**, not observed in any other structure with H_4pmida or its residues, is that the single H_2pmida^{2-} anion appears with one uncoordinated (and protonated) carboxylic acid group (Fig. 4.3), which is involved in a very strong $O-H\cdots O$ hydrogen bonding interaction with the coordinated carboxylate group of a neighbouring moiety (Table E.3 in Appendix E, p. 205). Furthermore, while for the coordinated carboxylic acid the C−O bonds are equivalent [Δ(C−O) of 0.016 Å], the uncoordinated group exhibits clear differences between the C−OH and the C=O bonds [Δ(C−O) of 0.123 Å], even though this moiety is engaged in the hydrogen bonds mentioned above (Table D.3).

The phosphonate functional group acts as a stabilizing unit, due to the presence of the three coordinating oxygen atoms. Indeed, because of the translational symmetry intrinsically present in the crystal structure, this functional group establishes physical bridges between adjacent Fe^{2+} metal centres, imposing $Fe(1)\cdots Fe(1)^{i}$ separations of 6.325(1) Å [symmetry code: (i) $x, y, 1+z$], leading to the formation of one-dimensional $^1_\infty$[Fe(H_2pmida)(H_2O)$_2$] neutral coordination polymer which runs along the [001] direction of the unit cell (Fig. 4.4). Individual and neighbouring $^1_\infty$[Fe(H_2pmida)(H_2O)$_2$] polymers close-pack to form *pseudo*-layers in the *ac* plane, in which the coordinated water molecules all face each other and are involved in strong and highly directional $O-H\cdots O$ hydrogen bonding interactions (the angles are all above 160°; see Fig. 4.5 and Table E.3). Inter-layer connectivity is assured by hydrogen bonds involving water molecules and by the uncoordinated and pendant carboxylic acid groups which interact with O(5) from the coordinated carboxylate of a neighbouring $^1_\infty$[Fe(H_2pmida)(H_2O)$_2$] polymer (Table E.3).

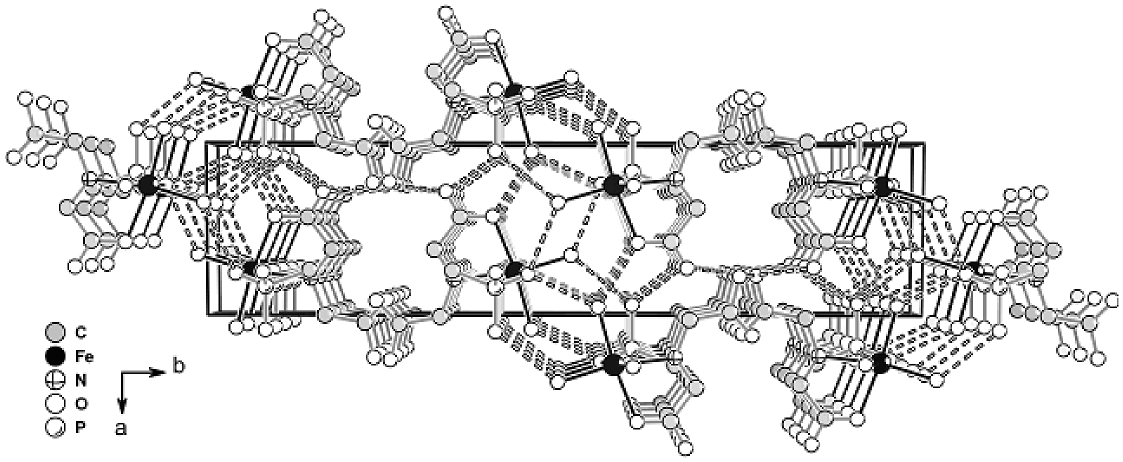

Figure 4.5.: Perspective view along the [001] direction of the crystal packing of [Fe(H_2pmida)(H_2O)$_2$] (**XVIII**). Hydrogen atoms have been omitted for clarity and hydrogen bonds are represented as white-filled dashed lines. For hydrogen bonding geometry see Table E.3 in Appendix E, p. 205.

4.2.1.2. Magnetic studies

The temperature dependence (T) of the magnetic susceptibility ($\chi = M/H$) of **XVIII** is shown at Fig. 4.6*. At high temperature (above about 50 K) the compound shows typical Curie-Weiss behaviour (Weiss constant Θ = 0.9 K) with an effective magnetic moment of 5.8 μ_B/Fe ion and g-factor g = 2.5, as reported for other high-spin iron(II) complexes (S = 2) exhibiting a distorted octahedral geometry.[60] Below 50 K the effective magnetic moment is reduced through first order spin-orbit coupling and the influence of the crystal field. High-spin Fe(II) has a $^5T_{2g}$ ground state and thus the spin-orbit coupling does not quench the orbital moment, leading to large deviations of the g-factor from the free electron value and to large zero-field splitting. The data were tentatively analysed according to existing models that describe the magnetic susceptibility. We have used the models described by Griffith[60] for $^5T_{2g}$ term arising from a free ion ^5D term (transition ion in octahedral crystal fields, where the quenching of the orbital contribution is not complete) and as alternatives, the model of Figgis[61,62] for large axial distortion that considers, besides the spin-orbit coupling, and the effect of ligand field and electron delocalisation, and to the model of Mabbs and Machin[63] for $^5T_{2g}$ in tetrahedral environment where the quenching of the orbital contribution is not complete. All the attempts to describe the experimental data with those models did not allow to obtain a good fit (Fig. 4.7).

The value of the effective magnetic moment is also close to the value of Fe(III) (5.9 μ_B, see Table 1.5 on p. 25). Although the crystallographic data indicate the presence of Fe(II) rather than Fe(III), the magnetic data were fitted to the equations of Van Vleck for high-spin (Equations 1.17 (p. 39), 1.23 and 1.24 on p. 39, and Equation 1.27 (p. 42) for low-spin Fe(III) ion (see Fig. 4.8)). The fits to all applied models for Fe(II) and Fe(III) can be compared in Fig. 4.9.

---

*Details for measurement techniques and conditions can be found in Chapter 7 on p. 161.

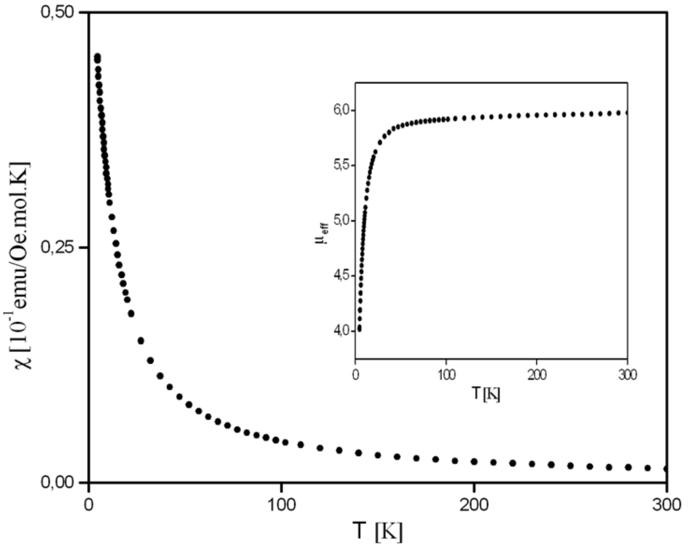

Figure 4.6.: Temperature (T) dependence of the magnetic susceptibility (χ) for compound $[Fe(H_2pmida)(H_2O)_2]$ (**XVIII**) and temperature (T) dependence of the effective magnetic moment μ_{eff}.

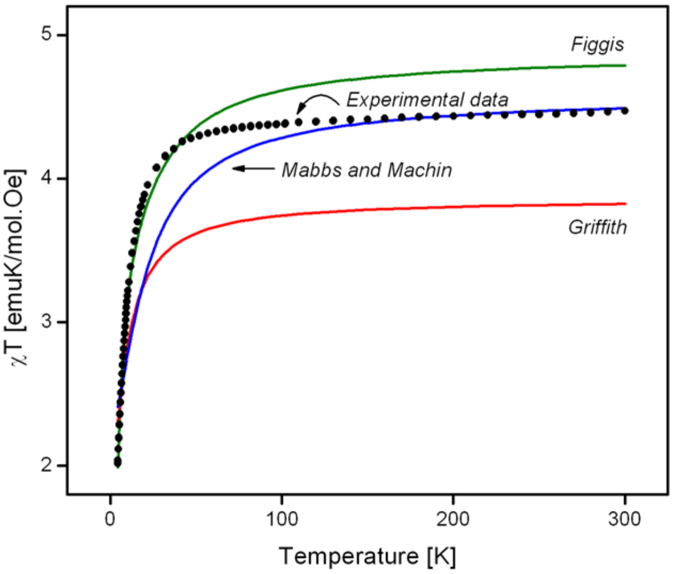

Figure 4.7.: χT *vs.* T: Fits of the experimental data to the models of Griffith,[60] Figgis,[61,62] and Mabbs and Machin[63] (compound $[Fe(H_2pmida)(H_2O)_2]$ (**XVIII**)).

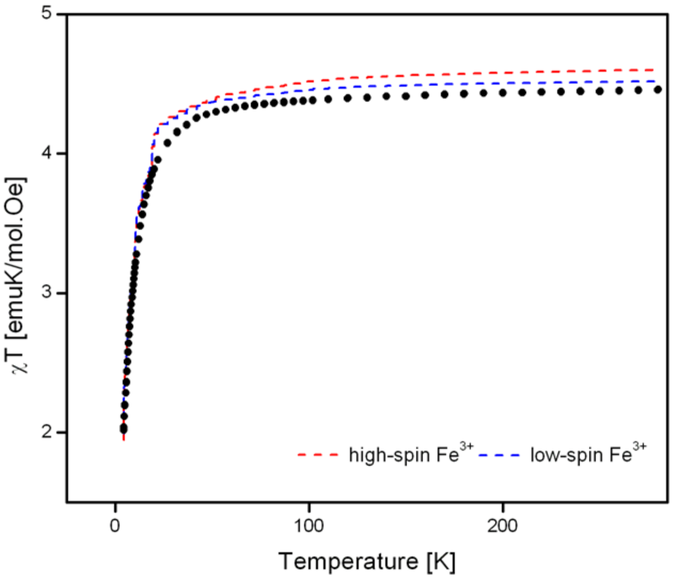

Figure 4.8.: χT *vs.* T: Fits of the experimental data to the models for high-spin and low-spin Fe(III)[64] (compound [Fe(H_2pmida)(H_2O)$_2$] (**XVIII**)).

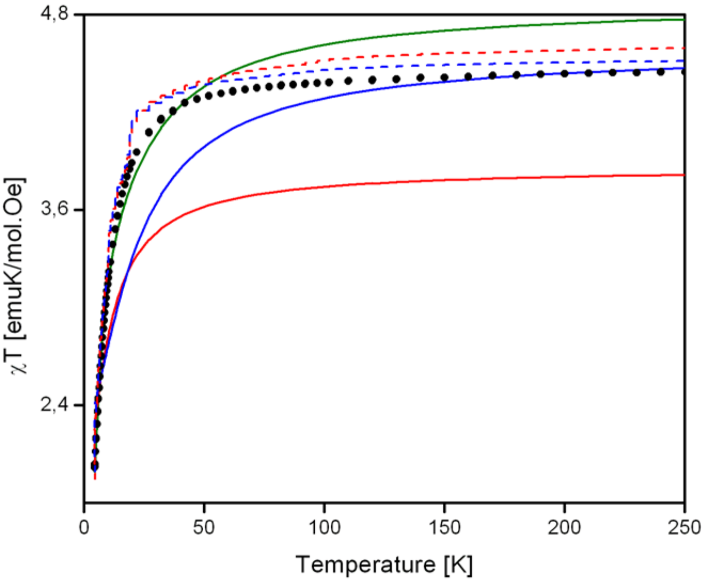

Figure 4.9.: χT *vs.* T: All the fits of the experimental data to models for Fe(II) and Fe(III) (compound [Fe(H_2pmida)(H_2O)$_2$] (**XVIII**)). The solid lines are the fits corresponding to Fe^{2+} and the dashed lines — to Fe^{3+}.

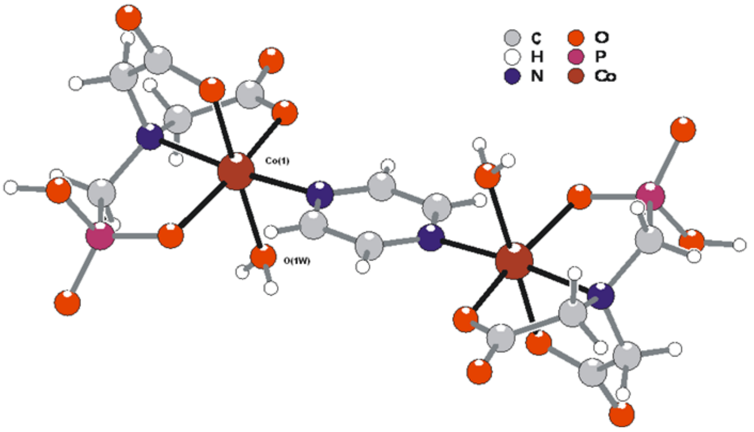

Figure 4.10.: Schematic representation of the anionic $[Co_2(Hpmida)_2(pyr)(H_2O)_2]^{2-}$ moiety in $[Co(pyr)(H_2O)_4][Co_2(Hpmida)_2(pyr)(H_2O)_2] \cdot 2\,(H_2O)$ (**XIX**) showing the labelling scheme for the atoms belonging to the asymmetric unit. For selected bond lengths and angles see Table D.3 in Appendix D.

4.3. Magnetic properties of compounds with H_4pmida and transition metals, containing bridging ligands

4.3.1. Compounds $[M(pyr)(H_2O)_4][M_2(Hpmida)_2(pyr)(H_2O)_2] \cdot 2\,(H_2O)$, where M = Co^{2+} (XIX) and Ni^{2+} (XX)

4.3.1.1. Crystal structures

The hydrothermal reactions, between copper(II) acetate or nickel(II) carbonate basic, H_4pmida and pyrazine yielded highly crystalline materials (see Chapter 7). The compounds were formulated as $[M(pyr)(H_2O)_4][M_2(Hpmida)_2(pyr)(H_2O)_2] \cdot 2\,(H_2O)$ (where M = Co^{2+} or Ni^{2+} for **XIX** and **XX**, respectively) on the basis of single-crystal X-ray diffraction (Table C.5 in Appendix C), elemental analysis and infrared spectroscopy (Table 4.1).

Overall, the crystal structures of **XIX** and **XX** are identical and contain two distinct moieties: anionic $[M_2(Hpmida)_2(pyr)(H_2O)_2]^{2-}$ discrete units (Fig. 4.10) which close pack and interact (via hydrogen bonds) with cationic $[M(pyr)(H_2O)_4]_n^{2n+}$ one-dimensional coordination polymers (Fig. 4.11).

The discrete binuclear anionic $[M_2(Hpmida)_2(pyr)(H_2O)_2]^{2-}$ units are formed by two M^{2+} cations bridged by one pyrazine organic ligand which imposes $Co(1)\cdots Co(1)^{i}$ and $Ni(1)\cdots Ni(1)^{ii}$ separations of 6.93(1) and 6.83(1) Å for **XIX** and **XX**, respectively [symmetry codes: (i) $2-x, 1-y, -z$; (ii) $2-x, 1-y, 2-z$]. The centre of mass of the bridging pyrazine is located at a symmetry centre which leads to inversion symmetry for the discrete individual $[M_2(Hpmida)_2(pyr)(H_2O)_2]^{2-}$ unit (Fig. 4.10). The remaining coordinative sites of M(1) are occupied by one coordinated water molecule [O(1*W*)] and by donor atoms from the $Hpmida^{3-}$ organic ligand (Fig. 4.10) leading to a typical six-coordination fashion, $\{MN_2O_4\}$, resembling a distorted octahedron (Table D.3 in Appendix D): *cis* and *trans* angles within the 80.77(2)–99.45(2)° and 165.23(2)–178.64(2)° ranges (for **XIX**), and 81.76(8)–98.77(9)° and

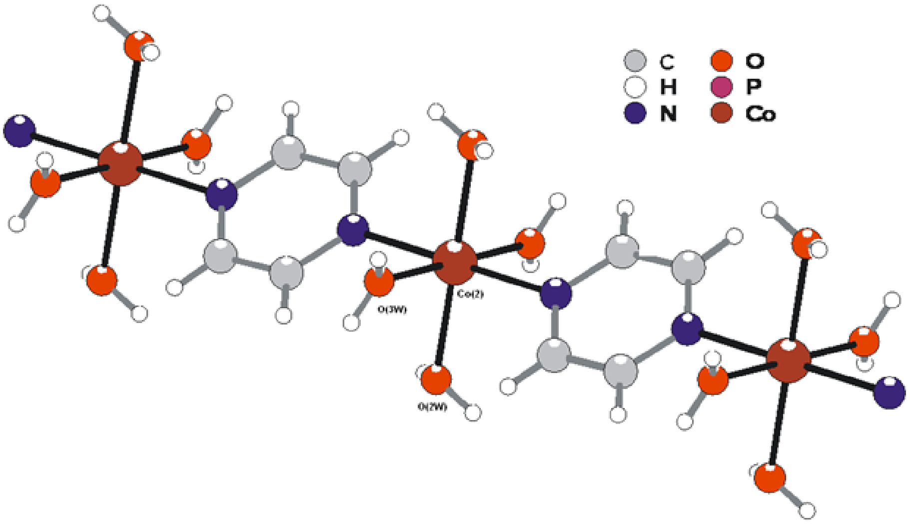

Figure 4.11.: Schematic representation of the one-dimensional cationic $[Co(pyr)(H_2O)_4]_n^{2n+}$ coordination polymer in $[Co(pyr)(H_2O)_4][Co_2(Hpmida)_2(pyr)(H_2O)_2]\cdot2(H_2O)$ (**XIX**), showing the labelling scheme for the atoms belonging to the asymmetric unit. For selected bond lengths and angles see Table D.3 in Appendix D.

168.66(8)–177.82(8)° ranges (for **XX**), respectively. It was observed that neither the high-spin Co^{2+} nor the Ni^{2+} centres exhibit strongly Jahn-Teller distortions and all the M(1)−(O,N) bonds are approximately equivalent (only the bonds to the coordinated water molecules are slightly longer; see Table D.3) and in good agreement with the values typically found in related compounds.[65–67]

The $Hpmida^{3-}$ anion appears in $[M_2(Hpmida)_2(pyr)(H_2O)_2]^{2-}$ as a polydentate organic ligand which completely traps the M(1) centres inside three five-membered chelate rings, formed by the two carboxylate and phosphonate groups connected in an *anti*-unidentate coordinative fashion (Fig. 4.10). The average bite angles are *ca.* 83.3 and 84.5° (for **XIX** and **XX**, respectively; Table D.3), values which are slightly higher than those typically registered for the anionic $[V_2O_2(pmida)_2]^{4-}$ unit (*ca.* 76.2–77.0°),[34,43,44] but in good agreement with those reported for the cyclic $[C_{30}H_{30}Co_6N_6O_{42}P_6]^{12-}$ hexameric unit (*ca.* 82.3°)[47] and for the $[Co_2(pmida)(H_2O)_5]_n$ polymeric structure (*ca.* 81.4°).[45] The variation of these bite angles is related, on the one hand, to the effective ionic radii of the central metal centres (effective ionic radii for 6–coordination geometry: V^{4+} 0.59 Å, high-spin Co^{2+} 0.65 Å, Ni^{2+} 0.70 Å)[58] and, on the other hand, to the coordination geometry of the phosphonate groups. In fact, it seems that if the phosphonate group is engaged in a bridge between two adjacent metal centres (as in $[C_{30}H_{30}Co_6N_6O_{42}P_6]^{12-}$ and $[Co_2(pmida)(H_2O)_5]_n$), geometrically-constrained rotations around the central P-atom preferentially lead to smaller bite angles.

The two compounds possess very similar 1D cationic $[M(pyr)(H_2O)_4]_n^{2n+}$ coordination polymers (Fig. 4.11) running along the [100] direction of the unit cell (Fig. 4.12), with the M^{2+} cations being located at an inversion centre. The crystal structure of such polymer has been previously reported for both Co^{2+},[65,66] Ni^{2+},[65,67] and other metal centres,[65,68] but containing different anions. Pyrazine molecules appear once again as ditopic rod-like *trans*-coordinated

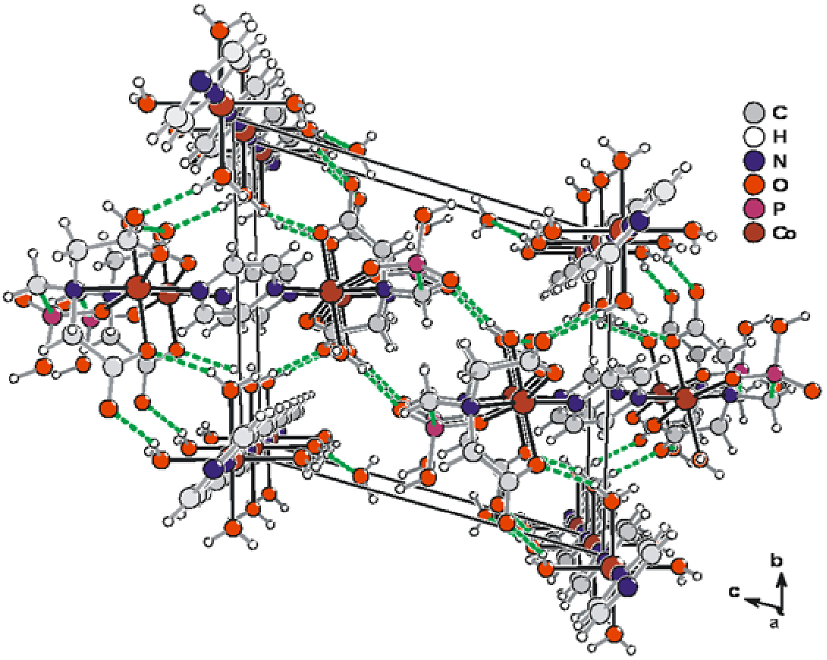

Figure 4.12.: Perspective view along the [100] direction of the crystal packing of $[Co(pyr)(H_2O)_4][Co_2(Hpmida)_2(pyr)(H_2O)_2] \cdot 2\,(H_2O)$ (**XIX**). Hydrogen bonds are represented as green-filled dashed lines (for hydrogen-bonding geometry see Table E.3 in Appendix E).

bridging ligands, establishing the physical links between adjacent $[M(H_2O)_4]^{2+}$ moieties and imposing Co(2)···Co(2)^{iii} and Ni(2)···Ni(2)^{iii} separations of 7.05(1) and 6.96(1) Å for **XIX** and **XX**, respectively [symmetry code: (iii) $-1 + x$, y, z]. The remaining coordination sites are occupied by four water molecules [O(2W) and O(3W)], leading to typical octahedral coordination geometry which are significantly more regular than those observed for the anionic $[M_2(Hpmida)_2(pyr)(H_2O)_2]^{2-}$ moieties: *cis* angles within the 86.4(2)–93.6(2)° and 87.06(10)–92.94(10)° for **XIX** and **XX**, respectively (Table D.3). For the M(2) metallic sites, the typical Jahn-Teller distortion is now observed with the M(2)−N(3) bonds being slightly longer than those registered for the M(2)−O bonds with water molecules (Table D.3).

4.3.1.2. Magnetic studies

Fig. 4.13 shows the plots of the magnetic susceptibility multiplied by temperature (χT) *vs.* temperature for compounds **XIX** (Fig. (a)) and **XX** (Fig. (b)). The decrease of χT with decreasing temperature deviates from a simple paramagnetic Curie-like behaviour, and can be associated to antiferromagnetic interactions between the ions or to single ion anisotropy and crystal field effects. The latter mechanism gives a better description of the data, leading to a zero field splitting of the lowest energy sublevels and therefore to the existence of an energy gap D. For high-spin Co^{2+} ($S = 3/2$) ions in octahedral coordination geometry the lowest energy levels are Γ_6 and Γ_7 doublet states, while for Ni^{2+} ($S = 1$) the levels involved are E and A triplet states, as observed in several mononuclear systems containing these ions.[64,69] In a first approximation only these levels are thermally populated, and the susceptibilities

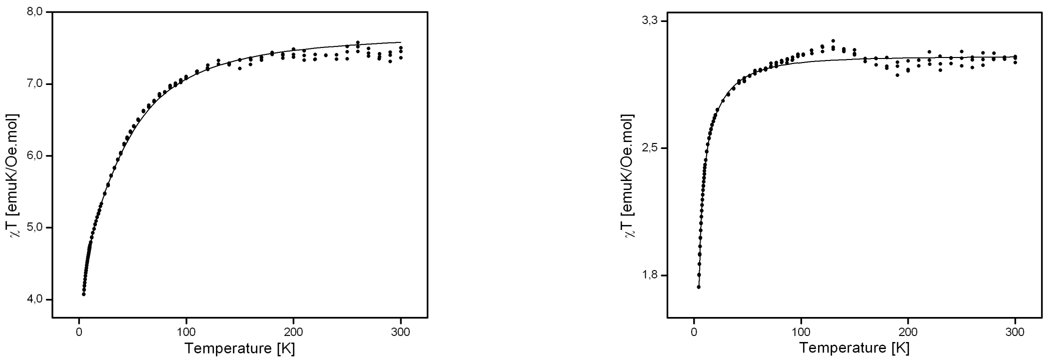

(a) (b)

Figure 4.13.: Plots of χT *vs.* T of compounds $[M(pyr)(H_2O)_4][M_2(Hpmida)_2(pyr)(H_2O)_2] \cdot 2\,(H_2O)$, (M = Co^{2+} (**XIX**) and Ni^{2+} (**XX**)): (a) Compound **XIX**: the solid line corresponds to the fit of the equations for zero field splitting of spin $S = 3/2$ (Equations 1.21, 1.22 and 1.17); (b) Compound **XX**: the solid line corresponds to the fit to the equations of zero field splitting and spin-orbit coupling of three spins $S = 1$ (Equations 1.19, 1.20 and 1.17).

for Co^{2+} ions (in **XIX**) and Ni^{2+} (in **XX**) are described by Equations 1.21 and 1.22, p. 40 and Equations 1.19 and 1.20, p. 40 for Ni^{2+} in Chapter 1, respectively.[64] Within this approximation, the model includes the influence of the orbital momentum for spin-orbit coupling and ligand field distortions. The presence of two distinct environments and three metal centres is accounted for by fitting the sample susceptibility to a sum of the corresponding contributions. A residual temperature independent χ_0 which accounts for diamagnetic contributions was added to the expression for the contribution of the parallel and the perpendicular to the field magnetic susceptibilities (see Equation 1.17 on p. 39). The best fit of the experimental data yields crystal field splitting for two paramagnetic centres of $D_1 = -5.85$ cm^{-1} and $D_2 = -47.74$ cm^{-1} (for **XIX**), and $D_1 = -57.00$ cm^{-1} and $D_2 = 10.89$ cm^{-1} (for **XX**). D_1 corresponds to M(2) metal centres in the cationic moieties (Fig. 4.11) and D_2 corresponds to the environment of the two equivalent M(1) centres in the anionic moieties (Fig. 4.10). From the fitting we also obtain $g_x = 2.97$, $g_z = 2.35$ (**XIX**) and $g_x = 2.16$, $g_z = 2.06$ (**XX**)[†]. Absolute errors of these values are of the order of 0.1. They are in agreement with the values reported for such high-spin ions.[64,69–72] The magnetic properties were interpreted by taking into account only the single ion anisotropy, since in this case there was no evidence for exchange interactions mediated by the pyrazine ligand. The differences observed for the crystal field splitting can be attributed to the influence of the different donor ligands in the M^{2+} coordination shell.

[†] g_z and g_x are the Landé factors associated with z- and x-directions. For details see Chapter 1.

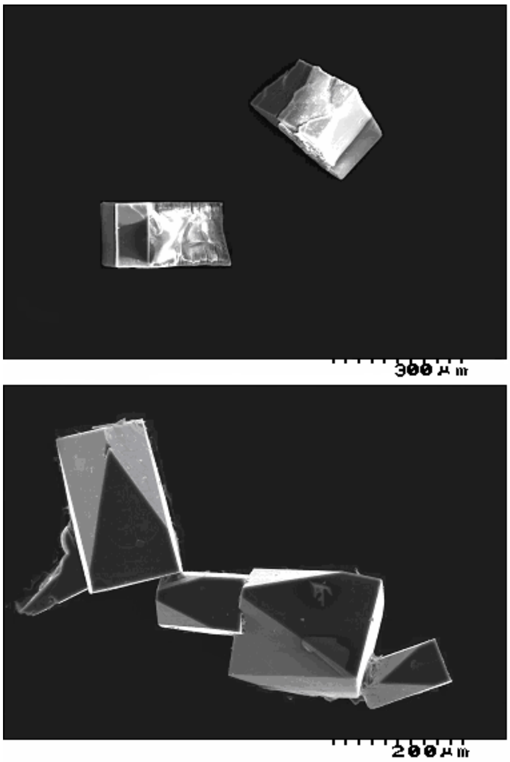

Figure 4.14.: SEM image of compounds **XXI** (top) and **XXII** (bottom).

4.3.2. Compounds $(4,4'\text{−bpyH})_2[\text{M}(4,4'\text{−bpy})(\text{H}_2\text{O})_4][\text{V}_2\text{O}_2(\text{pmida})_2] \cdot 2\,\text{H}_2\text{O}$, where M = Mn^{2+} (XXI) and Co^{2+} (XXII)

4.3.2.1. Crystal structures

Reactions between vanadium(IV) oxide sulfate ($\text{VOSO}_4 \cdot \text{xH}_2\text{O}$) and manganese(II) or cobalt(II) acetate ($\text{M(CH}_3\text{COO)}_2 \cdot 4\,\text{H}_2\text{O}$, M = Mn or Co), H_4pmida and 4,4′–bipyridine (4,4′–bpy) yielded highly crystalline materials (Fig. 4.14) with identical crystal structures, formed by the close packing (mediated by electrostatic interactions) of 1D $[\text{M}(4,4'\text{−bpy})(\text{H}_2\text{O})_4]_n^{2n+}$ cationic polymers (Fig. 4.15) and $4,4'\text{−bpyH}^+$ cations with dimeric centrosymmetric anionic moieties $[\text{V}_2\text{O}_2(\text{pmida})_2]^{4-}$ (Fig. 4.16). An extensive sub-network of hydrogen bonds interconnects in the three dimensions these individual moieties. The isolated compounds were formulated as $(4,4'\text{−bpyH})_2[\text{M}(4,4'\text{−bpy})(\text{H}_2\text{O})_4][\text{V}_2\text{O}_2(\text{pmida})_2] \cdot 2\,\text{H}_2\text{O}$ (M = Mn^{2+} or Co^{2+} for **XXI** and **XXII**, respectively) on the basis of single-crystal X-ray diffraction (Table C.6 in Appendix C), elemental analysis and infrared spectroscopy (Table 4.1).

The structures contain one-dimensional (1D) $[\text{M}(4,4'\text{−bpy})(\text{H}_2\text{O})_4]_n^{2n+}$ cationic coordination polymers (see Fig. 4.15) running along the [010] direction of the unit cell.The structure of such a 1D polymer has been previously described for Mn^{2+},[73–75] Co^{2+}[73,76–79] and other metal centres[80–84] (Ni^{2+}, Cu^{2+}, Zn^{2+}, Cd^{2+}) but crystallising with other anions and/or moieties. 4,4′–bpy molecules appear *trans*-coordinated to the metal centres, acting as rod-like ditopic bridging ligands and imposing physical $\text{M}\cdots\text{M}^{\text{i}}$ separations of 11.576(2) and 11.371 Å (one *b* axis length of the unit cell) for **XXI** and **XXII**, respectively [symmetry code:

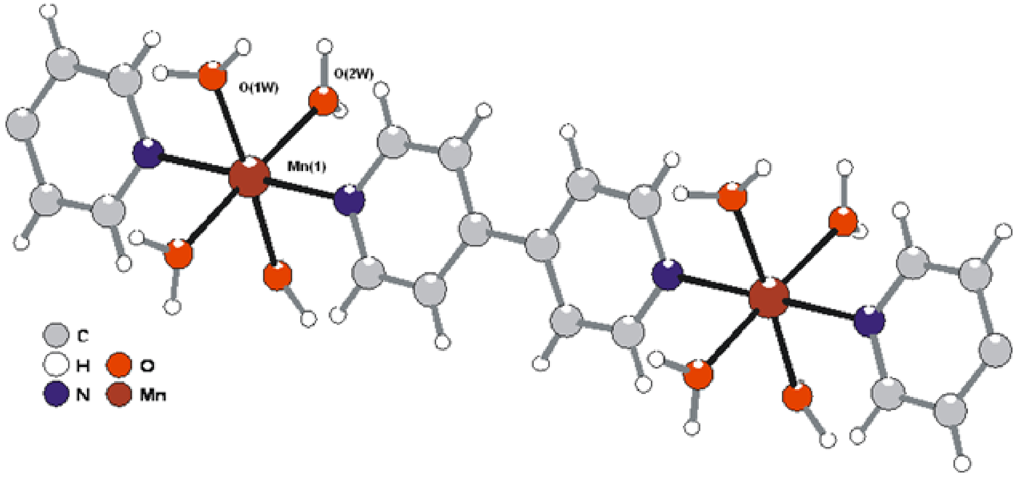

Figure 4.15.: Schematic representation of the cationic one-dimensional $[\mathrm{Mn}(4,4'-\mathrm{bpy})(\mathrm{H_2O})_4]_n^{2n+}$ coordination polymer with twofold rotation symmetry, showing the labelling scheme for the atoms belonging to the asymmetric unit. For selected bond lengths and angles, see Table D.3 in Appendix D.

(i) $x, 1+y, z$]. The remaining coordination sites of the M(1) centres are occupied by four water molecules [O(1W) and O(2W)] (forming the equatorial plane), leading to a typical slightly distorted octahedral coordination environment, $\{\mathrm{MN_2O_4}\}$ (Fig. 4.15): *cis* coordination angles within the 87.57(5)–92.43(5)° and 88.03(5)–91.97(5)° ranges, and *trans* coordination angles in the 175.15(1)–180.0° and 176.07(1)–180.0° ranges for **XXI** and **XXII**, respectively (Table D.3 (in Appendix D) and Fig. 4.15).

The crystal charge is balanced by the inclusion of centrosymmetric dimeric tetravalent anionic $[\mathrm{V_2O_2(pmida)_2}]^{4-}$ moieties identical to those described by Crans *et al.*[44] and Paz *et al.*,[34] in which the $\mathrm{V(1)\cdots V(1)}^i$ distance is 5.154(9) and 5.148(8) Å for **XXI** and **XXII**, respectively [symmetry code: (i) $2-x, 1-y, 2-z$]. In these units, pmida^{4-} appears as a polydentate organic ligands which encapsulates the V^{4+} centres inside three five-membered chelate rings (see Fig. 4.2) through the central nitrogen and the two carboxylate plus the phosphonate groups, which are coordinated in a typical anti-unidentate coordination fashion (Fig. 4.16). The average bite angle is of *ca.* 75.9° for both compounds (Table D.3 in Appendix D), which is in good agreement with those typically registered for this anionic unit.[34,44] The central V^{4+} metal centre shows a typical highly distorted octahedral coordination environment, $\{\mathrm{VNO_5}\}$, resembling the $1+4+1$ arrangement described by Boudin *et al.*,[85] with the oxo group (V=O) markedly showing its strong *trans* influence in the long V−N bond.

The crystal structures of compounds **XXI** and **XXII** are formed by the close packing of all the above mentioned moieties, mediated by electrostatic interactions and hydrogen bonds. The $[\mathrm{V_2O_2(pmida)_2}]^{4-}$ anions are distributed along the [001] direction, placed in the *bc* plane, surrounding channels running along the [010] direction which contain the one-dimensional $[\mathrm{M}(4,4'-\mathrm{bpy})(\mathrm{H_2O})_4]_n^{2n+}$ cationic coordination polymers (Fig. 4.17). Space-filling (and charge-balancing) 4,4'–bpyH$^+$ cations and water molecules of crystallisation

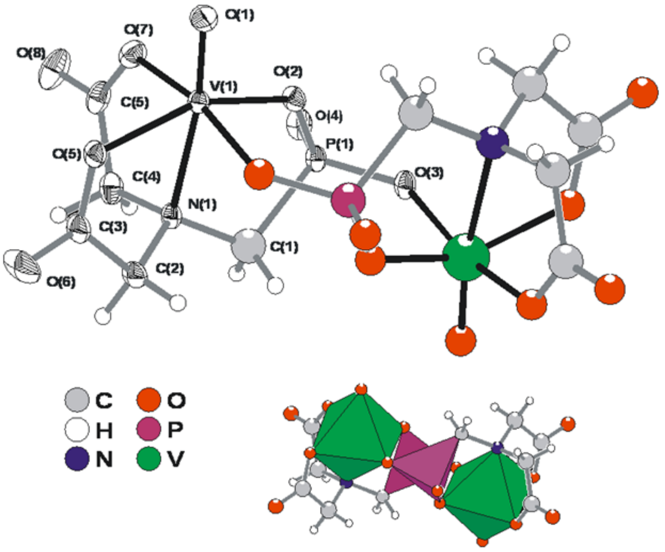

Figure 4.16.: Ball-and-stick (top) and polyhedral (bottom) representations of the dimeric anionic $[V_2O_2(pmida)_2]^{4-}$ moieties present in compounds **XXI** and **XXII**, showing the labelling scheme for all non-hydrogen atoms belonging to the asymmetric unit. Thermal displacement ellipsoids are drawn at the 50% probability level and hydrogen atoms are shown as small spheres. For bond lengths and angles see Table D.3 in Appendix D.

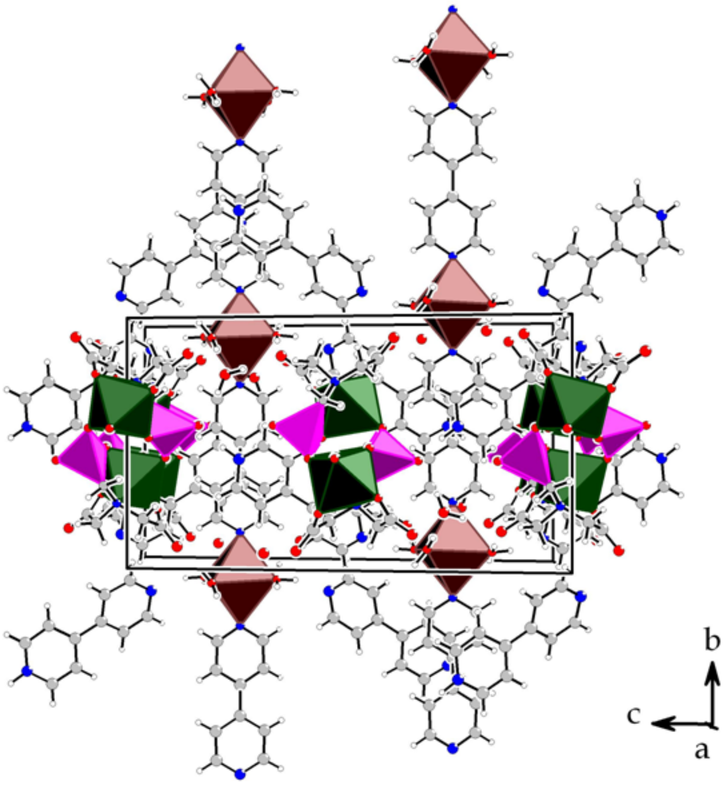

Figure 4.17.: Mixed ball-and-stick (4,4′–bpyH$^+$ cations) and polyhedral representation viewed along *b* direction of the crystal packing of compounds **XXI** and **XXII**. (for hydrogen-bonding geometry see Table E.3 in Appendix E). Hydrogen atoms have been omitted for clarity.

occupy the interstitial spaces. These moieties are interconnected by an extensive hydrogen-bonded sub-network formed by highly directional [<(DHA) greater than 150°] and very strong homonuclear O−H···O and heteronuclear N^+−H···O interactions (Table E.3 in Appendix E).

4.3.2.2. Magnetic studies

Fig. 4.18 shows the plots of the magnetic susceptibilities multiplied by temperature (χT) *vs.* temperature, for compounds **XXI** (a) and **XXII** (b). The decrease on χT with decreasing temperature, deviating from simple paramagnetic Curie-like behaviour. Since there was no evidence for exchange interactions, we assume that the crystal field effects lead to a zero field splitting of the lowest energy sublevels and the existence of an energy gap. The presence of three metal centres in two distinct environments is accounted for by fitting the samples susceptibilities to a sum of the corresponding contributions. Absolute errors are of the order of 0.1.

The magnetic susceptibility of **XXI** was calculated with the sum of the Van Vleck's equations[63,64,86] for manganese d^5 high-spin ion (S = 5/2; Equations 1.23 and 1.24 on p. 41), and for vanadium d^1 ions (S = 1/2; Equation 1.25 on p. 42) in octahedral environment, and a residual temperature independent term χ_0. The model includes the influence of the orbital momentum for spin-orbit coupling and ligand field distortions, as in the previous cases. The best fit of the experimental data yields crystal field splitting of the ${}^6A_{1g}$ ground term for paramagnetic Mn^{2+} ion D = 8.43 cm^{-1}. From the fitting we also obtain g_x = 1.95 and g_z = 2.04. The ${}^2T_2$ ground term of V^{4+} arises from a free ion ${}^2D$ term and, from the fitting, the spin-orbit coupling constant is λ = –2.39 cm^{-1}.

For compound **XXII** the experimental results were fitted to a model for three ions with spin S = 1/2 (two d^1 ions of V^{4+} and one low-spin Co^{2+}ion) in octahedral environment, according to Equation 1.25. From the fitting the spin-orbit coupling constant of V^{4+} is λ_1 = 0.37 cm^{-1} and of Co^{2+} is λ_2 = 7.83 cm^{-1}; $\chi_0 = 0.003$ [emu/Oe.mol]. The low values of the constants for the ${}^2T_2$ terms of both Co^{2+} and V^{4+} ions show that spin-orbit coupling effects are very weak so that the energy splitting is given only by the magnetic fields as sequential perturbations.

4.3.3. Compound $[Cu_5(pmida)_2(4,4'-bpy)_3] \cdot 6.5H_2O$ (XXIII)

4.3.3.1. Crystal structure

The hydrothermal reaction between copper(II) carbonate basic, H_4pmida and 4,4′–bipyridine led to the isolation of a new material solely composed by single crystals and formulated as $[Cu_5(pmida)_2(4,4'-bpy)_3] \cdot 6.5H_2O$ on basis of single-crystal X-ray diffraction (see Table C.6 in Appendix C) and CNH elemental analysis (Table 4.1).

The structure contains two crystallographically independent $pmida^{4-}$ anions, five metallic centres (with +2 and +1 oxidation states) and ten crystallographic independent sites

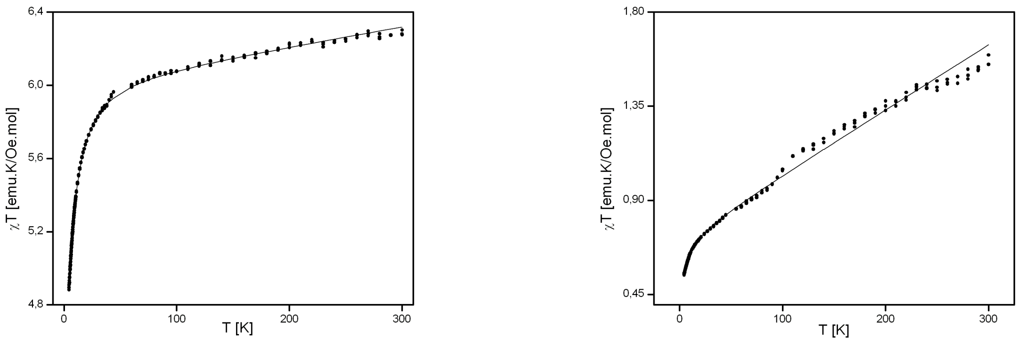

(a)

(b)

Figure 4.18.: Plots of χT *vs.* T: (a) Compound **XXI**: the solid line corresponds to the fit of the equations for zero field splitting of spin $S = 5/2$, and for zero field splitting and spin-orbit coupling of two spins $S = 1/2$ (Equations 1.23, 1.24 and 1.25); (b) Compound **XXII**: the solid line corresponds to the fit to the equations of zero field splitting and spin-orbit coupling of three spins $S = 1/2$ (Equation 1.25).

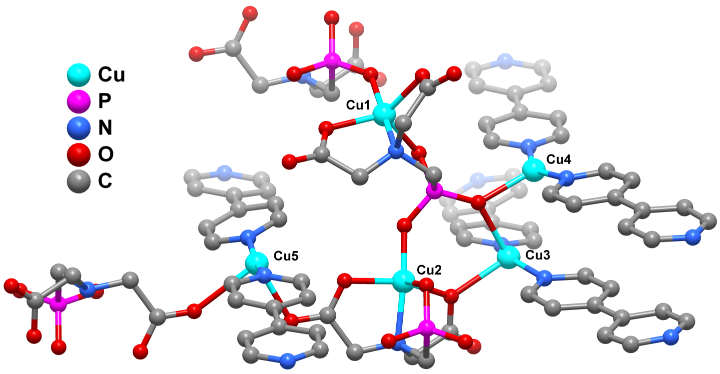

Figure 4.19.: Schematic representation of the neutral complex $[Cu_5(pmida)_2(4,4'-bpy)_3] \cdot 6.5H_2O$ (**XXIII**) showing the different coordination environments of the five metallic centres. For selected bonds and angles see Table D.3 in Appendix D.

for water molecules of crystallization which add up to 6.5 chemical moieties (see the different coordination environments of the copper centres in Fig. 4.19 and the crystal packing in Fig. 4.20). On the one hand, pmida^{4-} anions act as a mono- and multidentate coordination agents through the phosphonate and/or carboxylate groups and through the central nitrogen atom. On the other, the 4,4'–bpy molecules establish physical links between copper Cu(3), Cu(4) and Cu(5) centres: Cu(4)···Cu(5)^{i}, Cu(5)···Cu(3)^{i}, and Cu(5)···Cu(4)^{i} of 10.91 Å (see Table D.3 in Appendix D).

Cu(1) (Fig. 4.19) has an identical coordination environment to Cu(2). It is trapped by three five-membered chelate rings formed by the central nitrogen and three oxygen atoms (two from the deprotonated carboxylic acid groups and one from the deprotonated phosphonic acid group). The Cu(1) centre is further connected and to an adjacent pmida^{4-} anion via one phosphonate group. Thus the coordination environment of these metallic centres

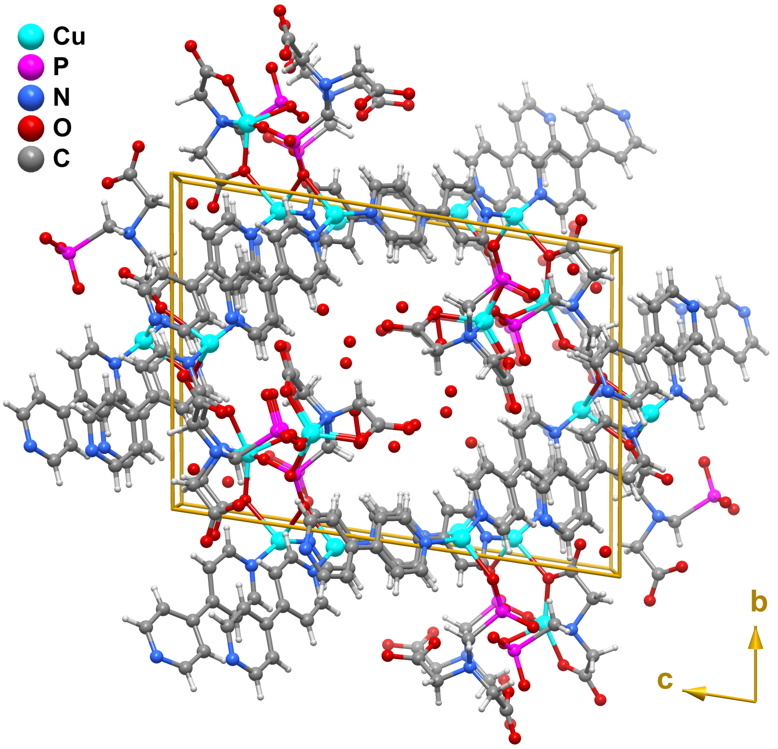

Figure 4.20.: Crystal packing of the neutral complex $[Cu_5(pmida)_2(4,4'-bpy)_3]\cdot 6.5H_2O$ (**XXIII**) viewed in perspective along the *a* direction.

strongly resembles a distorted bipyramid.

Cu(3) is four coordinated to two oxygen atoms from the two distinct pmida^{4-} units plus two nitrogen atoms from 4,4'–bpy bridging molecules, with a coordination environment approaching a strongly distorted tetrahedron. Noteworthy, this connecting phosphonate group is tetradentate, establishing an effective bridges between Cu(1) and Cu(2) and between Cu(3) and Cu(4) (intermetallic distance of 3.01 Å for the latter). Cu(4) has a rather irregular environment being three coordinated (resembling a triangle) to the phosphonate group and two nitrogen atoms from bridging bipy molecules.

Cu(5) appears in the structure as binuclear untis formed by two *syn,anti*–bridges of carboxylate groups, with a Cu(5)···Cu(5)$^{\mathrm{ii}}$ distance of 3.65 Å. [symmetry code: (ii) $1-x$, $1-y$, $-z$]. The remaining coordination sphere is once again composed by two bridging 4,4'–bpy molecules, with the overall geometry resembling a tetrahedron which is significantly more distorted than that of Cu(3) (see above).

4.3.3.2. Magnetic studies

Fig. 4.22 represents the magnetic susceptibility for sample **XXIII**. The observed temperature dependence indicates simple paramagnetic ion behaviour. The results were fitted to a Curie law[87] $\chi = (C/T) + \chi_0$, where the residual temperature independent χ_0 accounts for diamagnetic contributions.

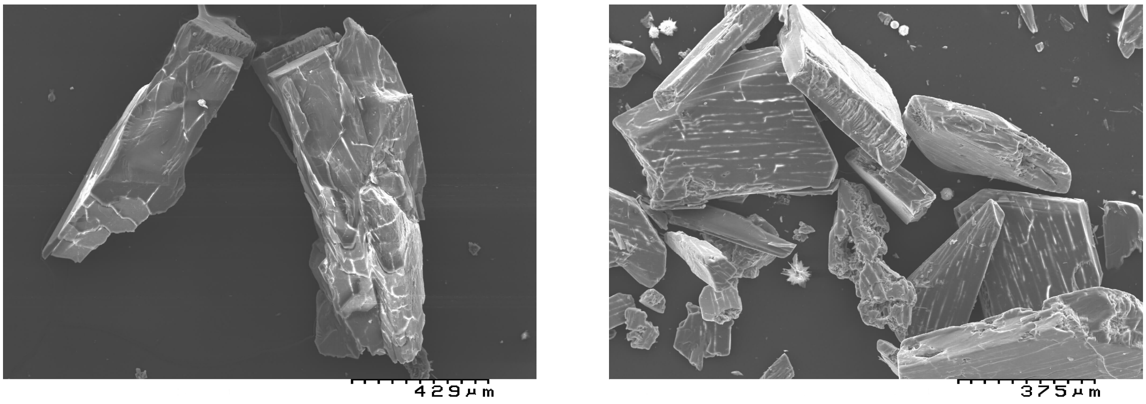

(a)

(b)

Figure 4.21.: SEM image of $[Cu_5(pmida)_2(4,4'-bpy)_3] \cdot 6.5H_2O$ (**XXIII**).

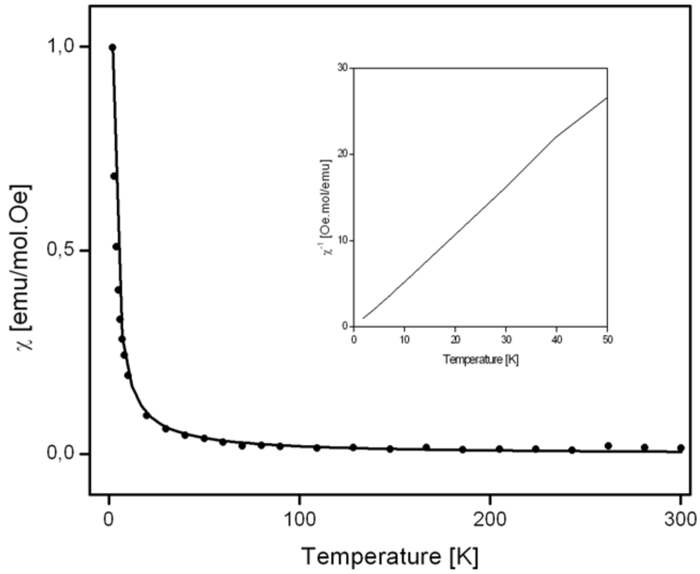

Figure 4.22.: Fit (the solid line) to the temperature dependence of the magnetic susceptibility of compound $[Cu_{10}(pmid)_4^{4-}(4,4'-bpy) \cdot 12\,H_2O]$ (**XXIII**). In the inset is displayed the plot of χ^{-1} *vs. T*.

From the values of the fitted Curie constants, the calculated effective magnetic moment per copper cation is $\mu_{\mathrm{eff}} = 1.8\mu_B$. These value is very close to the free Cu^{2+} ion spin-only (quenched orbital moment L=0) value $\mu_{\mathrm{eff}} = 1.73\mu_B$ (although Cu^{1+} is also present). As expected, due to the large interionic distance (see Table D.3), the magnetic measurements show that the magnetic interactions between Cu^{2+} are negligible.

4.4. Final remark

There are no evidences for exchange interactions in the novel crystal structures of pmida and 1st row transition metals. Their paramagnetic behaviours are due to the presence of the transition metals. Due to the crystal field effects were observed deviations from the Curie law at low temperatures. The values of magnetic parameters were calculated with fittings, which are different depending on the metal electronic configurations and the ligand environments.

References

1. Hoskins BF and Robson R, *J. Am. Chem. Soc.* 112(4) (1990), 1546–1554.
2. Rowsell JLC and Yaghi OM, *Microporous Mesoporous Mater.* 73(1-2) (2004), 3–14.
3. Zaworotko MJ, *Chem. Commun.* (1) (2001), 1–9.
4. Moulton B and Zaworotko M, *Chem. Rev.* 101(6) (2001), 1629–1658.
5. Janiak C, *J. Chem. Soc., Dalton Trans.* (14) (2003), 2781–2804.
6. Batten SR and Robson R, *Angew. Chem., Int. Ed.* 37(11) (1998), 1461–1494.
7. Barnett SA and Champness NR, *Coord. Chem. Rev.* 246(1-2) (2003), 145–168.
8. Khlobystov AN, Blake AJ, Champness NR, Lemenovskii DA, Majouga AG, Zyk NV and Schroöder M, *Coord. Chem. Rev.* 222(1) (2001), 155–192.
9. Blake AJ, Champness NR, Hubberstey P, Li WS, Withersby M and Schröder M, *Coord. Chem. Rev.* 183(1) (1999), 117–138.
10. Rao CNR, Natarajan S and Vaidhyanathan R, *Angew. Chem., Int. Ed.* 43(12) (2004), 1466–1496.
11. Maeda K, *Microporous Mesoporous Mater.* 73(1-2) (2004), 47–55.
12. Mori W, Takamizawa S, Kato C, Ohmura T and Sato T, *Microporous Mesoporous Mater.* 73(1-2) (2004), 31–46.
13. Schlichte K, Kratzke T and Kaskel S, *Microporous Mesoporous Mater.* 73(1-2) (2004), 81–88.
14. Kesanli B and Lin WB, *Coord. Chem. Rev.* 246(1-2) (2003), 305–326.
15. Matsuda K, Takayama K and Irie M, *Chem. Commun.* (4) (2001), 363–364.
16. Noro SI, Kitagawa S, Kondo M and Seki K, *Angew. Chem., Int. Ed.* 39(12) (2000), 2082–2084.
17. Kitaura R, Fujimoto K, Noro SI, Kondo M and Kitagawa S, *Angew. Chem., Int. Ed.* 41(1) (2002), 133–135.
18. Eddaoudi M, Kim J, Rosi N, Vodak D, Wachter J, O'Keeffe M and Yaghi O, *Science* 295(5554) (2002), 469–472.
19. Li H, Eddaoudi M, O'Keeffe M and Yaghi O, *Nature* 402(6759) (1999), 276–279.
20. Rosi N, Eckert J, Eddaoudi M, Vodak D, Kim J, O'Keeffe M and Yaghi O, *Science* 300(5622) (2003), 1127–1129.
21. Matouzenko GS, Molnar G, Bréfuel N, Perrin M, Bousseksou A and Borshch SA, *Chem. Mater.* 15(2) (2003), 550–556.
22. Zang SQ, Tao RJ, Wang QL, Hu NH, Cheng YX, Niu JY and Liao DZ, *Inorg. Chem.* 42(3) (2003), 761–766.
23. Roesky HW and Andruh M, *Coord. Chem. Rev.* 236(1-2) (2003), 91–119.
24. Aakeröy CB and Beatty AM, *Chem. Commun.* (10) (1998), 1067–1068.
25. Tong ML, Zheng SL and Chen XM, *Chem. Commun.* (6) (1999), 561–562.

26. Yaghi OM, Li H, Davis C, Richardson D and Groy TL, *Acc. Chem. Res.* 31(8) (1998), 474–484.
27. De Munno G, Cipriani F, Armentano D, Julve M and Antonio Real J, *New J. Chem.* 25(8) (2001), 1031–1036.
28. Lu J, Paliwala T, Lim SC, Yu C, Niu T and Jacobson AJ, *Inorg. Chem.* 36(5) (1997), 923–929.
29. Lu JY, Lawandy MA, Li J, Yuen T and Lin CL, *Inorg. Chem.* 38(11) (1999), 2695–2704.
30. Eddaoudi M, Moler DB, Li H, Chen B, Reineke TM, O'Keeffe M and Yaghi OM, *Acc. Chem. Res.* 34(4) (2001), 319–330.
31. Paz FAA and Klinowski J, *Chem. Commun.* 9(13) (2003), 1484–1485.
32. Paz FAA, Khimyak Y, Bond A, Rocha J and Klinowski J, *Eur. J. Inorg. Chem.* (11) (2002), 2823–2828.
33. Paz FAA and Klinowski J, *J. Phys. Org. Chem.* 16(10) (2003), 772–782.
34. Paz FAA, Shi F, Klinowski J, Rocha J and Trindade T, *Eur. J. Inorg. Chem.* (13) (2004), 2759–2768.
35. Paz F and Klinowski J, *J. Solid State Chem.* 177(10) (2004), 3423–3432.
36. Paz FAA and Klinowski J, *Inorg. Chem.* 43(13) (2004), 3882–3893.
37. Paz FAA and Klinowski J, *Inorg. Chem.* 43(13) (2004), 3948–3954.
38. Shi FN, Paz FAA, Rocha J, Klinowski J and Trindade T, *Eur. J. Inorg. Chem.* (15) (2004), 3031–3037.
39. Paz FAA, Bond AD, Khimyak YZ and Klinowski J, *Acta Crystallogr., Sect. E: Struct. Rep. Online* 58(12) (2002), m608–m610.
40. Shi FN, Paz FAA, Rocha J, Klinowski J and Trindade T, *Inorg. Chim. Acta* 358(4) (2005), 927–932.
41. Girginova PI, Paz FAA, Nogueira HIS, Silva NJO, Amaral VS, Klinowski J and Trindade T, *Polyhedron* 24(4) (2005), 563–569.
42. Girginova PI, Paz FAA, Nogueira HIS, Silva NJO, Amaral VS, Klinowski J and Trindade T, *J. Mol. Struct.* 737(2-3) (2005), 221–229.
43. Poojary DM, Zhang B and Clearfield A, *Angew. Chem, Int. Ed. Engl.* 33(22) (1994), 2324–2326.
44. Crans DC, Jiang F, Anderson OP and Miller SM, *Inorg. Chem.* 37(26) (1998), 6645–6655.
45. Mao JG and Clearfield A, *Inorg. Chem.* 41(9) (2002), 2319–2324.
46. Clearfield A, Sharma CVK and Zhang BP, *Chem. Mater.* 13(10) (2001), 3099–3112.
47. Gutschke SOH, Price DJ, Powell AK and Wood PT, *Angew. Chem., Int. Ed.* 38(8) (1999), 1088–1090.
48. Mao JG, Wang Z and Clearfield A, *Inorg. Chem.* 41(23) (2002), 6106–6111.
49. Mahroof-Tahir M, Keramidas AD, Goldfarb RB, Anderson OP, Miller MM and Crans DC, *Inorg. Chem.* 36(8) (1997), 1657–1668.
50. Launay JP, Jeannin Y and Daoudi M, *Inorg. Chem.* 24(7) (1985), 1052–1059.

51. Choquesillo-Lazarte D, Covelo B, González-Pérez JM, Castiñeiras A and Niclós-Gutiérrez J, *Polyhedron* 21(14-15) (2002), 1485–1495.
52. Shi FN, Paz FAA, Girginova P, Rocha J, Amaral VS, Klinowski J and Trindade T, *J. Mol. Struct.* 789(1-3) (2006), 200–208.
53. Song JL, Prosvirin AV, Zhao HH and Mao JG, *Eur. J. Inorg. Chem.* (18) (2004), 3706–3711.
54. Pei H, Lu S, Ke Y, Li J, Qin S, Zhou S, Wu X and Du W, *Struct. Chem.* 15(3) (2004), 207–210.
55. Fan Y, Li G, Shi Z, Zhang D, Xu J, Song T and Feng S, *J. Solid State Chem.* 177(11) (2004), 4346–4350.
56. Paz FAA, Rocha J, Klinowski J, Trindade T, Shi FN and Mafra L, *Prog. Solid State Chem.* 33(2-4) (2005), 113–125.
57. Shi FN, Paz FAA, Girginova PI, Mafra L, Amaral VS, Rocha J, Makal A, Wozniak K, Klinowski J and Trindade T, *J. Mol. Struct.* 754(1-3) (2005), 51–60.
58. Shannon RD and Prewitt CT, *Acta Crystallogr., Sect. B: Struct. Sci.* 25 (1969), 925–946.
59. Shannon RD, *Acta Crystallogr., Sect. A: Found. Crystallogr.* 32 (1976), 751–767.
60. Griffith JS, The theory of transition - metal ions, 3rd ed., Cambridge University Press, 1971.
61. Figgis BN and Lewis J, The magnetic properties of transition metal complexes, vol. 6 of *Progress in inorganic chemistry*, John Wiley & Sons, Inc., 1964.
62. Figgis BN, Lewis J, Mabbs FE and Webb GA, *J. Chem. Soc. A* (3) (1967), 442–447.
63. Mabbs FE and Machin DJ, Magnetism and transition metal complexes, Chapman & Hall, London, 1973.
64. Kahn O, Molecular magnetism, Wiley–VCH, 1993.
65. Näther C, Greve J and Jeβ I, *Z. Naturforsch., B: Chem. Sci.* 58(1) (2003), 52–58.
66. Fetzer T, Jooss R, Lentz A, Debaerdemaeker T and Anorg Z, *Z. Anorg. Allg. Chem.* 620(10) (1994), 1750—1754.
67. Choudhury CR, Dey SK, Sen S, Bag B, Mitra S and Gramlich V, *Z. Naturforsch., B: Chem. Sci.* 57(11) (2002), 1191–1194.
68. Yaghi OM, Li G and Groy TL, *J. Solid State Chem.* 117(2) (1995), 256–260.
69. Orchard AF, Magnetochemistry, 1st ed., Oxford chemistry primers, Oxford: University Press, 2003.
70. Baca SG, Filippova IG, Gherco OA, Gdaniec M, Simonov YA, Gerbeleu NV, Franz P, Basler R and Decurtins S, *Inorg. Chim. Acta* 357(12) (2004), 3419–3429.
71. Zhang W, Bruda S, Landee CP, Parent JL and Turnbull MM, *Inorg. Chim. Acta* 342 (2003), 193–201.
72. Mrozinski J, Skorupa A, Pochaba A, Dromzee Y, Verdaguer M, Goovaerts E, Varcammen H and Korybut-Daszkiewicz B, *J. Mol. Struct.* 559(1-3) (2001), 107–118.
73. Wang YH, Feng L, Li Y, Hu C, Wang E, Hu N and Jia H, *Inorg. Chem.* 41(24) (2002), 6351–6357.

74. Sain S, Maji TK, Chaudhuri NR and Zangrando E, *Transition Met. Chem.* 27(7) (2002), 716–719.
75. Tong ML, Lee HK, Chen XM, Huang RB and Mak TCW, *J. Chem. Soc., Dalton Trans.* (21) (1999), 3657–3660.
76. Wu CD, Lu CZ, Yu YQ, Zhuang HH and Huang JS, *Acta Crystallogr., Sect. C: Cryst. Struct. Commun.* 58(3) (2002), m197–m198.
77. Lu JY, Norman C, Abboud KA and Ison A, *Inorg. Chem. Commun.* 4(9) (2001), 459–461.
78. Dong YB, Smith MD, Layland RC and Loye HCZ, *J. Chem. Soc., Dalton Trans.* (5) (2000), 775–780.
79. Tong ML, Cai JW, Yu XL, Chen XM, Ng SW and Mak TCW, *Aust. J. Chem.* 51(7) (1998), 637–641.
80. Zheng YQ, Kong ZP and Lin JL, *Z. Kristallogr. – New Cryst. Struct.* 217(2) (2002), 195–196.
81. Xiong RG, Liu CM, Zuo JL and You XZ, *Inorg. Chem. Commun.* 2(7) (1999), 292–297.
82. Wang QM, Wu XT, Zhang WJ, Sheng TL, Lin P and Li JM, *Inorg. Chem.* 38(9) (1999), 2223–2226.
83. Carlucci L, Ciani G, Proserpio D and Sironi A, *J. Chem. Soc., Dalton Trans.* (11) (1997), 1801–1803.
84. Sen S, Mitra S, Kundu P, Saha M, Krüger C and Bruckmann J, *Polyhedron* 16(14) (1997), 2475–2481.
85. Boudin S, Guesdon A, Leclaire A and Borel MM, *Int. J. Inorg. Mater.* 2(6) (2000), 561–579.
86. Bŏca R, Theoretical foundations of molecular magnetism, vol. 1 of *Current methods on inorganic chemistry*, 1st ed., Elsevier, 1999.
87. Barbara B, Gignoux D and Vettier C, Lectures on modern magnetism, Springer-Verlag, 1988.

MAGNETIC NANOPARTICLES FOR REMOVAL OF HEAVY METALS FROM WATER

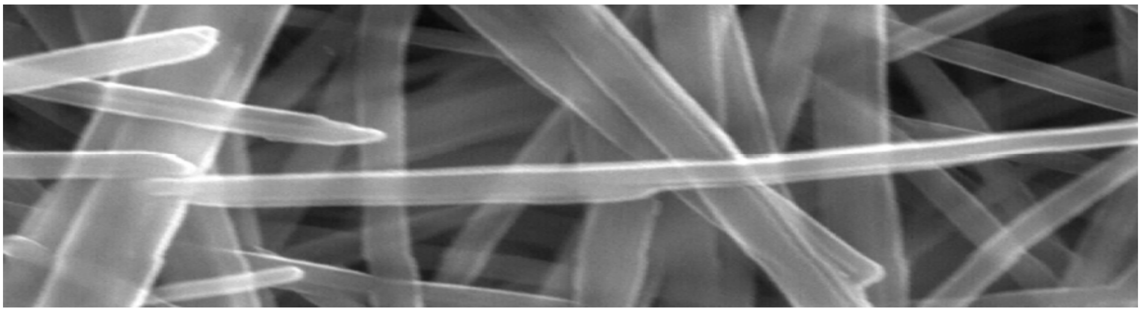

CHAPTER V

Chapter 5.

Magnetic nanoparticles for removal of heavy metals from water

5.1. Introduction

Nanoparticles exhibit distinct properties when are compared to their bulk analogues. They can enhance drastically the mechanical, photochemical, optical and magnetic properties. The particle size is expected to influence some characteristics such as structure (lattice symmetry and reduction of size parameters due to the higher importance of surface free energy with decreasing of particle size), electronic structure (quantum size effects) and chemical reactivity. For some semiconductors, when the particle size is reduced to a certain value, there is an increase of the energy gap and a "blue" shift of the optical band gap is observed in the optical spectrum. The new magnetic phenomena raised from the finite size and surface effects of very small magnetic particles are superparamagnetism, high field irreversibility, high saturation field, extra anisotropy or shifted loops after field cooling.[1]

Magnetic nanoparticles have innumerable applications including in the biomedical and environmental fields. Each potential application depends on the particle size, shape, interactions between particles, surface chemical stability, stability towards oxidation, ability of the switchable magnetic state to not be affected by temperature fluctuations. Among all the nano-sized materials, metal oxides play a major role in many areas of chemistry, physics and materials science. The magnetic properties of iron oxides have been studied more particularly for increasing of magnetic recording properties of nanostructured magnetite[2] (Fe_3O_4) and maghemite[3] ($\gamma-Fe_2O_3$) and for their use in composites due to their magneto-optical properties.[4,5] However, they also have been intensely investigated in bio- applications and environmental processes.[6]

The biomedical applications can be separated depending on whether the magnetic nanoparticles will be used *in vivo* or *in vitro*. In the group of *in vivo* applications can belong therapeutic[7–11] (as hyperthermia agents and in targeted drug delivery) and diagnostic applications[7–9] (as contrast agents for magnetic resonance imaging (MRI)), while mainly diagnostic use belong to the group of *in vitro* applications (separation/selection, magnetorelaxometry). The magnetic particles for these applications are generally "core-shell" type, thus stabilizing and isolating the magnetic core, turning possible the connection between the core and the biological or other species through organic or inorganic linkers (the shell). Some of the best results giving materials for bioseparation and purification of nucleic acids are core-shell nanoparticles of magnetite-silica.[12] Moreover the silica coating does not change the magnetic properties of these materials. The specific application of nanoparticles in biomedicine depend on their size.[13] Review of medical applications of magnetic nanoparticles (mainly Fe_3O_4) — for diagnosis, for MRI, as hyperthermia agents and for magnetic force-based tissue engineering was done by Ito *et al.*[14] Jun *et al.* have obtained 4, 6, 9 and 12 nm superparamagnetic Fe_3O_4 nanocrystals for MRI agents through thermal decomposition of iron(III) acetylacetonate for MRI agents.[15] Superparamagnetic silica coated magnetite (28 nm) functionalized with hydrophylic aminopropyl groups[16] (3–aminopropyltrimetoxysilane) and other, functionalized with 3–aminopropyltrimetoxysilane[17] (15 nm) were synthesized for transport/removal of biological molecules, drugs and metals in different medium by magnetic separation. The surface functional groups ($-OH$ and $-NH_2$ groups) realize the bond with the biological molecules or with biocompatible polymers. Superparamagnetic iron oxide nanoparticles are widely used for *in vivo* application in medicine.[18]

Environmental applications Nanotechnology in the environmental field can be divided in three main lines:

- pollution prevention — comprises different filters and membranes;
- detection — comprises the new sensors for detection of biological and chemical contaminants and monitoring devices;
- treatment and remediation — the purpose is to provide long term high quality of the water or enable the water reuse and recycling;

The removal of trace amounts of heavy metals from waste- and drinking water is of great importance, since they are highly toxic and can accumulate in the living organisms. The most common contaminants in the waste- and drinkable water are chlorinated organic compounds, cyanide and fluoride ions, and metallic ions, such as antimony, arsenic, barium, beryllium, cadmium, chromium, copper, lead, mercury and thallium which are very harmful for the health. Arsenic is carcinogen and when is in high concentration in water can provoke lung, skin or bladder cancer. Usually is met as three- or penta-valent ions (As(III) and As(V)). Lead(II) causes delays in physical or mental development of children and kidney problems, and high blood pressure of adults. The long exposure of copper in the water is responsible for liver or kidney damage; the same effects are provoked by the cadmium and mercury ions.[19]

Magnetic nanoparticles display great possibilities to selective removal of a wide range of target metal ions and compounds in wastewater. Their specific surface properties (density, large surface areas and high reactivity) influence the chemical behaviour of the particles and thus together with the size and shape dependent catalytic, optical and magnetic properties, influence their application for wastewater treatment. For these applications, the requirements for magnetic particles are to show high capacity for heavy metal uptake, a high magnetic susceptibility to facilitate quick sedimentation in a moderate magnetic field, to have size and a density which are low enough to prevent spontaneous sedimentation before reaction and before the application of magnetic field. Many separation methods have been used for metals removal: precipitation, chemical reduction, ion exchange, membrane separation, adsorption and biological treatment, among which the adsorption technique associated to magnetic separation is one of the most promising. This research trend has been focused in the development of low cost and high efficient magnetic materials. Such materials might be novel and modified nanometre sized adsorbents and ion exchangers such as zeolites, chitosan, fly ash, activated carbon, natural clays and magnetic oxides.[20] All these materials show high adsorption rates for metal ions in aqueous solutions. For example, 10 nm sized magnetite[21,22] and maghemite[23] display higher adsorption capacity for Cr(VI) than the commercially activated carbon.[23]

Iron oxides have been used mainly for the removal of As ions by adsorption together with clay minerals and other oxides.[24,25] The adsorption and desorption capacity of Fe_3O_4 towards As(III) and As(V) strongly depends on the particle size. As the particles size decreases from 300 to 12 nm, the adsorption capacity increases approximatively 200 times.[26] Hydrated Fe(III) oxides dispersed in commercial polymeric ion exchanger and Fe_3O_4 nanocrystals in polymeric beads, forming magnetically active polymer particles, are capable of removing high concentrations of As(III), As(V), Zn(II) and Cu(II) ions.[27] Magnetite nanoparticles have been largely used for removal of heavy metals from water. There are many examples of the use of nano-sized Fe_3O_4 in the composition of many perspective materials, due to its magnetic properties, high surface area, easy synthesis and low toxicity and price. Usually its surface is modified by attaching a very large range of inorganic or organic molecules thus stabilizing the particles, preventing their oxidation or providing them specific functionality. It is the most used material for the so-called magnetically assisted chemical separation (MACS) which combine the magnetic separation with surface adsorption, ion exchange and solvent extraction.[28] High selective hollow mesoporous aluminosilicate spheres with Fe_3O_4 cores of size 25.3 and 43 nm are suitable for adsorption of Hg^{2+}.[29] Chitosan can be covalently bound to the Fe_3O_4 surface after preliminary carboxymethylation. Such particles have diameters of 13.5 nm and can remove Cu(II) ions at $pH>2$.[30] Lately, chelating resins have also been used for this purpose due to their high adsorption capacity, selectivity and durability.[31] The presence of Fe_3O_4 particles in the resins enhances their granular strength, thermal stability and turns easy their separation. Magnetic resins have been used for removal of Pb(II),[31,32] Cd(II),[31] Zn(II),[31,32] Ca(II),[31] Mg(II),[31] Hg(II),[32,33] Cr(VI)[34] and Co(II),[35] and then removed from the water by applying an external magnetic field. Cr(VI) ions can be removed from water by 20 nm Fe_3O_4 particles coated with alginate and polyvinyl alcohol.[36] New materials of size 50 and 70 nm, consisting of silica coated Fe_3O_4, functionalized with $\gamma-$mercaptopropyltrimethoxysilane have been successfully applied for extraction of Cd(II), Cu(II), Hg(II) and Pb(II).[37] Potential reusable adsorbent material for magnetic separation of heavy metals is formed by Fe_3O_4 particles encapsulated in thiol containing polymer by acid-mediated seeded polymerization.[38] Its efficiency to remove Ag^+, Hg^{2+} and Pb^{2+} ions has been tested. This synthetic technique may be applied for the formation of similar core-polymer shell materials with applications in other domains too. The mercapto group ($-SH$) has a strong affinity towards coordination with soft metals and mercapto- ligands are thus excellent chelating agents for metals such as Ag^{2+} and Pb^{2+}. For example, Fe_3O_4 was functionalized with dimercaptosuccinic acid (DMSA) and tested for removal of Hg(II) and Pb(II) ions.[39] This is the first time that the use of such materials as magnetic sorbents for soft heavy metals has been reported. The interaction of the organic DMSA acid with the surface of the Fe_3O_4 is through the OH groups of the carboxylic group (under acidic condition) or direct

Fe-carboxylate linkage (under alkaline pH). The Hg^{2+} sorption capacities of the new DMSA-Fe_3O_4 nanoparticles and commercial product were compared; the novel materials showed high ability of metal removal.[39]

5.2. Preparation of functionalized magnetite nanoparticles

Magnetite Nanoparticles of magnetite can precipitate in bacteria and insects which is a natural phenomenon, called biomagnetism. Magnetostatic bacteria can live in dark and contain chains of 40–100 nm of Fe_3O_4 nanoparticles used for vertical orientation. Fe_3O_4 particles serving as field sensors for migration were also found in brains of bees, pigeons and tuna. Fe_3O_4 is also in the basis of the rock magnetism which can serve for monitoring the change of the Earth's magnetic field.

Magnetite is a common iron oxide whit a cubic inverse spinel structure. Its structure was revealed by X-ray diffraction in 1915 and is one of the first minerals to which this technique was applied.[40–42] It has face-centred cubic unit cell based on cubic closed-packed 32 O^{2-} ions along the axes [111]. There are eight formula units per unit cell. The tetrahedral and octahedral sites form the two magnetic sublattices, A and B respectively. The spins in the A sublattice are antiparallel to those in the B sublattice. The two sites are different and result in complex forms of exchange interactions of the iron ions between and within the two types of sites. Magnetite contains divalent and trivalent Fe ions and has the general formula $Fe^{III}[Fe^{II}Fe^{III}]O_4$*. The tetrahedral sites are occupied by the trivalent ions (surrounded by four oxygen atoms) while half of the octahedral sites are occupied by trivalent and half — of the divalent ions (surrounded by six oxygen atoms).[42] The structure consists of octahedral and mixed tetrahedral/octahedral layers stacked along [111] (see Fig. 1.9 (a) on p. 10). In Fig. 1.9 (b) is shown the sequence of Fe− and O− layers and Fig. 1.9 (c) shows the section of the structure with three octahedra and two tetrahedra. With negative AB exchange interactions, the net magnetic moment of magnetite is due to the B-site containing Fe^{2+}.

The most common methods and trends for synthesis of different magnetic nanoparticles with different sizes and morphologies are reviewed by many authors.[43–46] In particular, the basic synthetic methods and main properties of iron oxides, including of magnetite nanoparticles are described by Cornell and Schwertmann.[42] They all have the purpose of producing chemically stable particles with low rate of sedimentation and high magnetic susceptibility. The size, shape and composition of the nanoparticles depends on the type of salts used, the ratio $[Fe^{2+}]/[Fe^{3+}]$, the pH, the ionic strength of the medium and the reaction temperature. The synthesis is usually reproducible once the reactional conditions have been optimized.

For the synthesis of nanorod-like Fe_3O_4, the precipitation of Fe(II) and Fe(III) chloride solutions by hydrolysis of urea at 90 °C[47] and the hydrothermal synthesis[48] are often preferred. Other common synthetic methods are elevated temperature hydrolysis of chelate ion

---

[*] In brackets are ions which occupy octahedral sites.

alkoxide complexes in solution of corresponding alcohol, diethylene glycol or N-methyl diethanolamine[49] and microemulsion technique for synthesis of nanoscaled uniform and narrow sized Fe_3O_4 particles with water-in-oil reverse microemulsion systems.[50–53] Magnetite ferrofluid can be prepared by Massart's method[54] in acidic and alkaline medium from aqueous mixtures of ferric and ferrous chlorides. A method described by Sugimoto and Matijević[55] consists in ageing $Fe(OH)_2$ gels at 90 °C in the presence of KNO_3. Other authors have succeeded in the synthesis of monodispersed and size-controlled Fe_3O_4 by high temperature decomposition of iron(III) acetyleacetonate ($Fe(acac)_3$).[56,57] Synthetic methods under an applied external magnetic field might influence the magnetic parameters of the particles. Such materials display higher coercivity, saturation and remanent magnetization compared with randomly distributed magnetic particles prepared without magnetic field.[58,59]

Ligands known to form stable complexes with heavy metal ions are dithiocarbamates (DTC).[60] They present extraction properties which are very useful for purification of waste waters and determination of trace metals.[61–64] Co-precipitation is an old approach to concentrate and separate heavy metal ions to be analysed, but silica gel grafted with DTC has also been used for extraction of Co(II),[63,65] Hg(II),[65–68] Cu(II),[63,67] and Cd(II)[63,67] ions from aqueous solutions.

The main objective of the research presented in this chapter, is to show that silica coated nanoparticles can be used to purify water, by uptake of Hg^{2+} or other heavy metal ions. The materials efficiency will be promoted by the chemical functionalization of the silica surface consecutively with amino and dithiocarbamate groups.

5.2.1. Structural characterization and discussion

The synthesis of magnetite[†] by precipitation from an aqueous solution of iron(II) sulphate resulted in a crystalline black powder of Fe_3O_4 (compound **XXIV**), confirmed by powder XRD and Mössbauer spectroscopy. Further silica coating (compound **XXV**) was performed with hydrolysis of TEOS in alkaline conditions with ammonia acting as catalyst. The XRD pattern of pure magnetite (**XXIV**) is shown in Fig. 5.1. All the peaks match with those of magnetite reported in the database. The crystallinity of the obtained Fe_3O_4 was confirmed by electron diffraction performed with transmission electron microscope as well, shown in Fig. 5.5 (b). The only one unidentified peak at $2\Theta = 45$ (vertical red bar) belongs most probably to impurity on the sample holder. Further confirmation of the composition was done by Mössbauer spectroscopy. Mössbauer spectra are usually used to identify and characterize iron oxides, revealing information about charge and coordination of the ions. The iron oxides order magnetically over a wide range of temperatures and since the Mössbauer parameters of the various magnetically ordered Fe oxides differ a lot, the full identification or quantification in mixtures of such oxides is possible. Mössbauer spectroscopy was performed for two magnetite samples: with (compound **XXV**) and without SiO_2 coating (compound **XXIV**) (see Fig. 5.2 and Table 5.1). The spectrum of ferrimagnetic magnetite

---

[†] Detailed experimental procedure is described in Chapter 7 on p. 161.

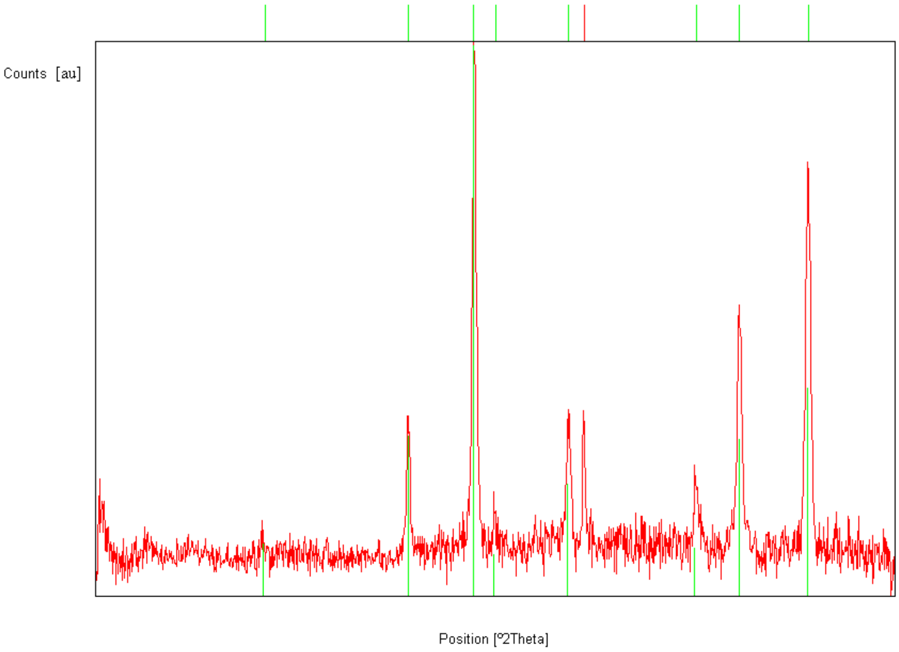

Figure 5.1.: Powder XRD pattern of magnetite, compound **XXIV** (with background correction). Vertical bars correspond to the XRD pattern of bulk magnetite (Ref. code 04–009–2285).

can be fitted with two sextets:[42] one, which corresponds to high spin Fe^{III} on the tetrahedral sites (hyperfine field B_{hf} = 49.2 T) and another, corresponding to $Fe^{2.5}$ on the octahedral sites. Electron dislocation causes the nucleus to sense one average valence (B_{hf} = 46.1 T). The results indicate that both materials are composed of magnetite and that the coating of silica does not induce any transformation.

FT–IR and ATR spectroscopies was applied for identification of the groups in the material functionalization with (3–aminopropyl)triethoxysilane and the further grafting of DTC groups. The data were compared with the existing values in the literature.[42,65,67,69,70] The

Table 5.1.: Mössbauer parameters of Fe_3O_4 and Fe_3O_4@SiO_2.

		Hyperfine field B_{hf} [T]	Quadrupole splitting ΔE_Q [mm/s]	Isomer shift [mm/s]	%
Fe_3O_4	Site 1	49.0	–0.093	0.25	53.3
Fe_3O_4	Site 2	46.7	0.10	0.72	46.7
Fe_3O_4@SiO_2	Site 1	49.5	–0.01	0.31	54.7
Fe_3O_4@SiO_2	Site 2	46.0	0.016	0.66	45.3
Fe_3O_4		49	$\leq \|0.02\|$	0.26	
at 295 K[42]		46	0.00	0.67	

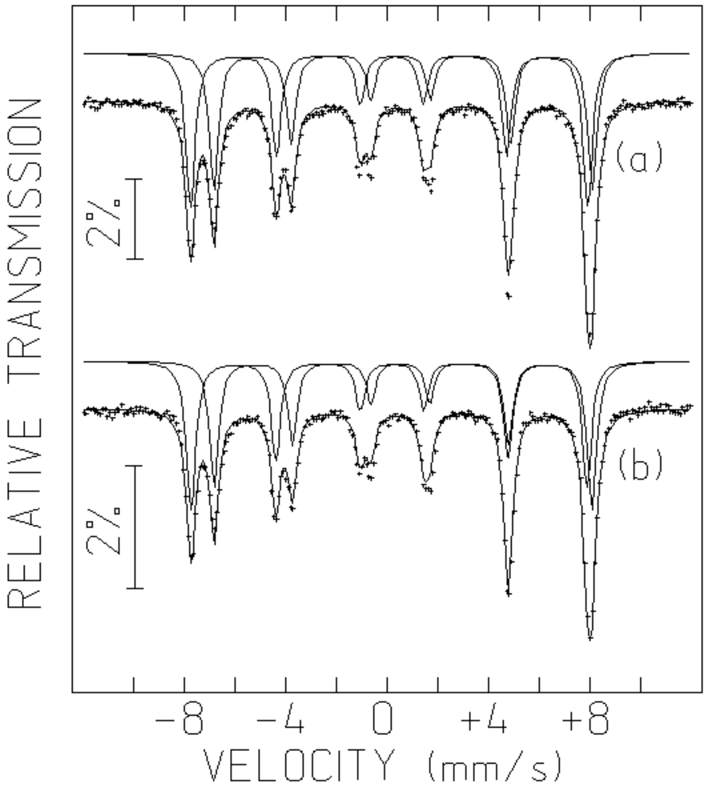

Figure 5.2.: Mössbauer spectra: (a) Fe_3O_4; (b) Fe_3O_4@SiO_2.

FT–IR (Fig. 5.3 (a)) of all compounds‡ show broad bands at about 3400 cm^{-1} (not shown) due to the ν(O−H) stretching of chemisorbed water. The FT–IR bands at around 570 cm^{-1} and 360 cm^{-1} (ATR (Fig. 5.3 (b)): around 523 and 311 cm^{-1}) (in the literature[42,70] 580 and 400 cm^{-1}) are characteristic for ν(Fe—O) stretching vibrations (in Fe_3O_4), due to the presence of magnetite (see Table 5.2).

The strong FT–IR band of compound **XXV** at 1096 and the weak bands at 802 and 953 cm^{-1} (ATR: 1055, 789 and 940 cm^{-1}) correspond to the SiO_2 stretching vibrations ν(Si—O—Si), ν(Si—OH), ν(Si—O—Fe). The peak at 798 cm^{-1} (FT–IR; shifted from 802 cm^{-1} and also assigned to ν(Si—O—Fe)) for compound **XXVI** can be assigned to the bending δ(—NH_2) and the stretching ν(C—N) vibrations (ATR: 791 cm^{-1}). The weak FT–IR bands at 1400–1600 (ATR: at about 1620 cm^{-1} for compound **XXVII**) might be assigned to the ν(C—N) stretching mode. The peaks are not strong enough to confirm the presence of these groups, moreover the very strong stretching band of ν(—Si—O—Si) around 1096 cm^{-1} (ATR: 1055) completely overlaps the strong bands of the ν(C—H), δ(N—H), ν(CS_2) and ν(C−N) groups.

---

‡compound **XXIV** — Fe_3O_4; compound **XXV** — Fe_3O_4@SiO_2; compound **XXVI** — Fe_3O_4@SiO_2@NH_2; compound **XXVII** — Fe_3O_4@SiO_2@NH@$CS_2^-$$Na^+$

Table 5.2.: Spectroscopic data (FT–IR and ATR (in italics)), surface area and elemental analysis: **XXIV** — Fe_3O_4, **XXV** — $Fe_3O_4@SiO_2$, **XXVI** — $Fe_3O_4@SiO_2@NH_2$, **XXVII** — $Fe_3O_4@SiO_2@NH@CS_2^-Na^+$.

Compound	Spectroscopic data							
	ν(Fe–O)	ν(Si–OH) (SiO_2)	ν(Si–O–Fe) (SiO_2)	ν(Si–O–Si)	ν(C–N) (APTES)	δ(NH_2) (APTES)	ν(N–C) (N–DTC)	ν(CS_2)
XXIV	572, 1634	—	—	—	—	—	—	—
	523, 311	—	—	—	—	—	—	—
XXV	575, 1634	802	953	1096	—	—	—	—
	553, 337	*789*	*940*	*1055*	—	—	—	—
XXVI	575, 1647	798	955	1096	overlapped	overlapped	—	—
	560, 341	*791*	*943*	*1064*			—	—
XXVII	576, 1647	802	965	1086	overlapped	overlapped	not visible	overlapped
	557, 338	*783*	*957*	*1031*			*1447*	
APTES (IR)	—	—	—	—	≈1100	≈800	—	—
	—	—	—	—	—	1460	—	—
	—	—	—	—	—	1525	—	—
CS_2	—	—	—	—	—	—	—	1558

	Elemental composition, %						Surface area, [m^2/g]
	C	H	N	S	Fe	Si	
XXIV	—	—	—		71.4	—	13
XXV	—	—	—		51.5	13.1	11
XXVI	0.464	0.0865	0.394	—	—	—	9
XXVII	0.77	0.40	0.07	0.11	—	—	9

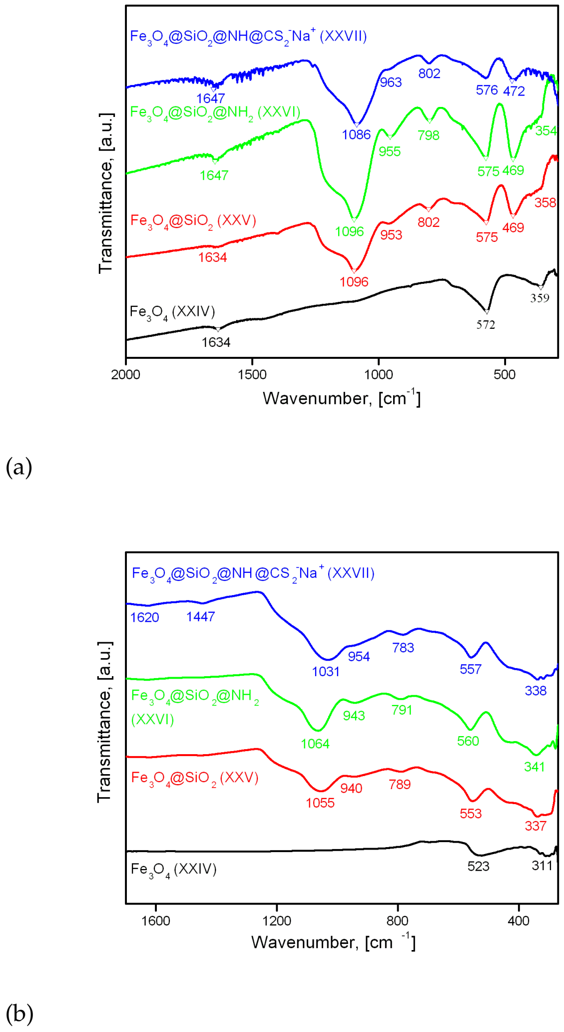

Figure 5.3.: FT–IR (a) and ATR (b) spectra of magnetite materials.

The presence of the amino groups and of the grafted CS_2 of the silica coated magnetite is suggested by the presence of a very weak ATR stretching band at 1447 cm^{-1} and confirmed by elemental analysis (see Table 5.2). In this table the results of ICP also confirme the quantiy of Fe and Si for compounds **XXIV** and **XXV**. For **XXIV** were found 71.4% of Fe (calculated 72%) and for sample **XXV** — 51.5% of Fe and 13.1% for Si (calculated 57% Fe and 10% of Si, respectively).

The morphology before and after surface modification was investigated by SEM (see Fig. 5.4) and TEM (Figs. 5.5 and 5.6). The starting magnetite particles have a cubic shape whose side is in average about 74 nm (± *ca.* 28 nm). The histogram in Fig. 5.7 (p. 150) shows the size distribution of these particles determined from the measurement of *ca.* 200 particles[§]. The TEM images (Fig. 5.6) show that every single particle become coated with a thin silica layer (with an average thickness of *ca.* 14 nm). Further surface modifications did not have any visible effects on the morphology (confirmed by TEM) and the crystalline phase

---

[§] The longer sides were measured for the particles which were not perfectly cubic.

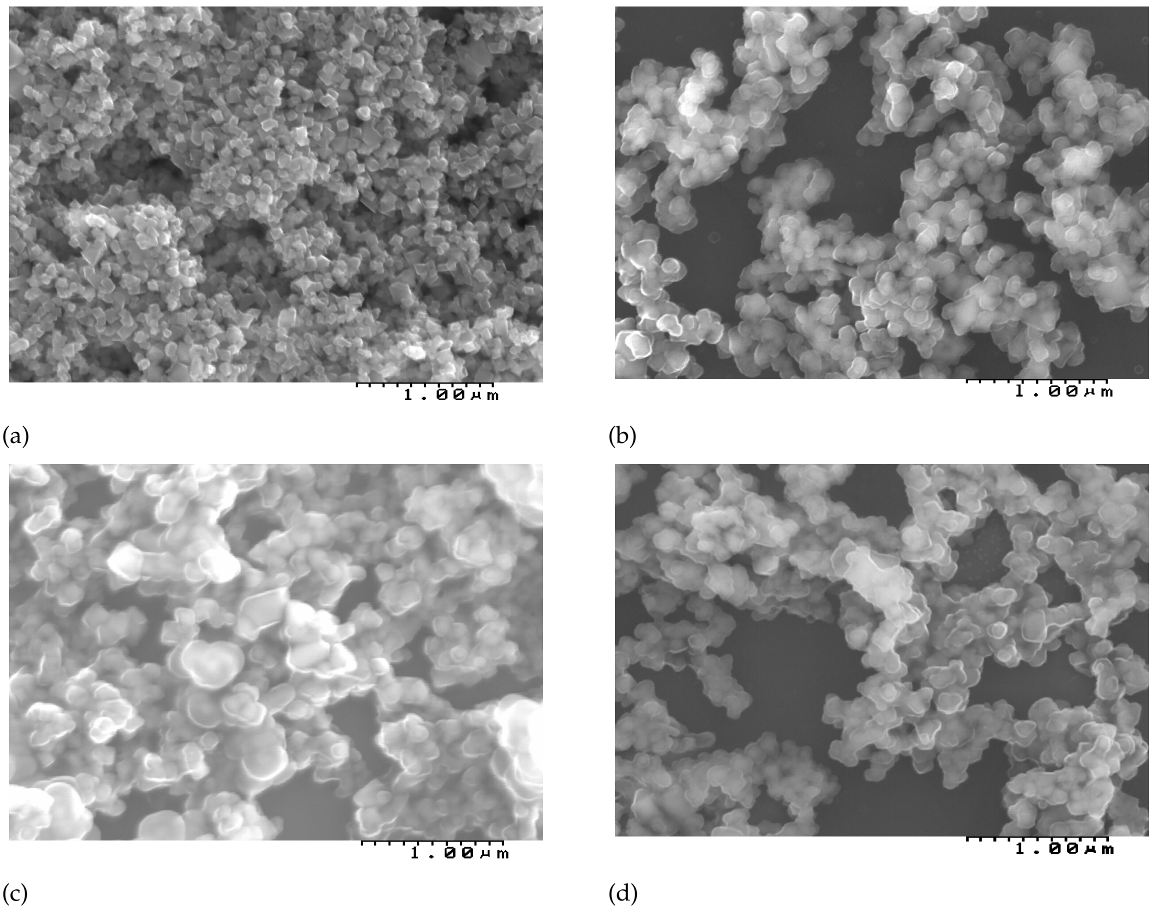

(a) (b) (c) (d)

Figure 5.4.: SEM images of: (a) Fe_3O_4; (b) $Fe_3O_4@SiO_2$; (c) $Fe_3O_4@SiO_2@NH_2$; (d) $Fe_3O_4@SiO_2@NH@CS_2^-Na^+$.

(confirmed by Mössbauer). According to this, with the silica coating the size of the particles has increased (Figs. 5.5 (a) and 5.6). The decrease in the surface area (Table 5.2) for the analysed samples can be due to the increase of the particle size together with the functionalization of the surface. In fact, the surface area of the materials decreased from 13 m^2/g (magnetite) to 11 m^2/g (silica coated sample) and to 9 for samples **XXVI** and **XXVII**. The surface area of the amine and DTC functionalized particles decreased slightly as compared to the non-organic functioinalized nanoparticles. This can be related to the "filling" or blocking of the porous silica surface after coating with APTES and CS_2.

5.2.2. Magnetic properties

Coercivity H_C and saturation magnetization M_S values were obtained from the hysteresis loops at room temperature (T = 293 K) with applied field range from –1.9 to 1.9 Tesla for pure magnetite and silica-magnetite composite (Fig. 5.8). The magnetization vales are presented per weight magnetite in composite material, considering the results from ICP (91 % Fe_3O_4 in silica composite). Details for the shape of the hysteresis loops and coercive fields are presented in the inset at Fig. 5.8. The data for the samples Fe_3O_4 and $Fe_3O_4@SiO_2$ are presented in Table 5.3. These values confirm the presence of large size magnetic particles.

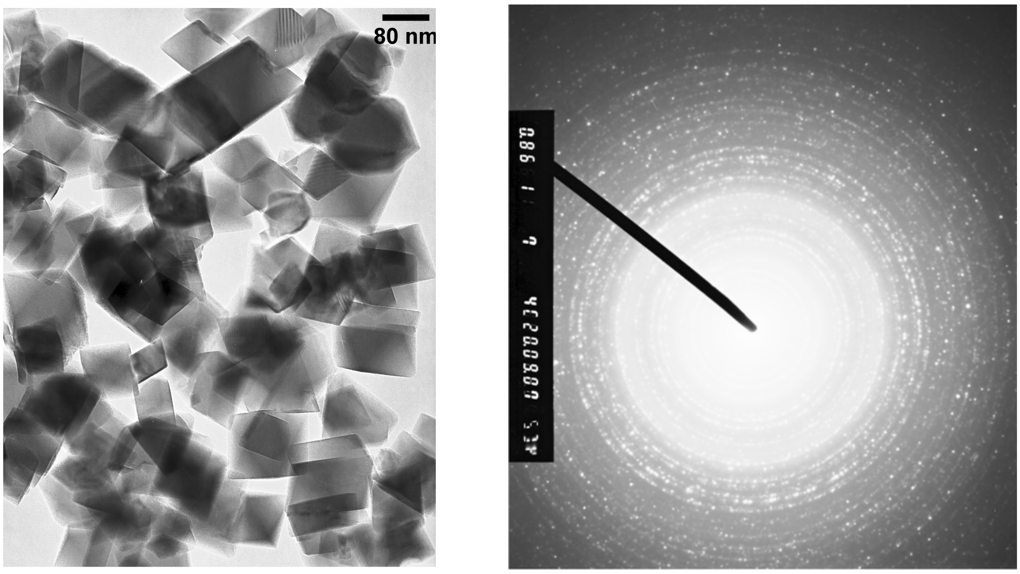

(a) (b)

Figure 5.5.: TEM images of: (a) Pure Fe_3O_4 (**XXIV**); (b) Electron diffraction pattern of Fe_3O_4.

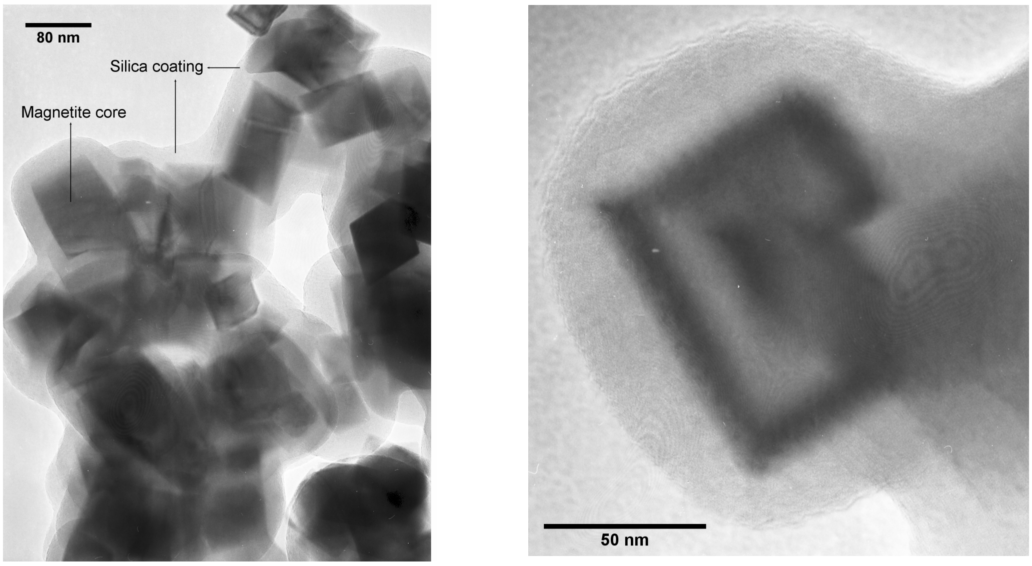

Figure 5.6.: TEM images of silica coated magnetite (**XXV**).

Table 5.3.: Measured and calculated magnetic parameters for samples **XXIV** and **XXV**.

	M_S [emu/g (Fe_3O_4)]	M_R [emu/g (Fe_3O_4)]	H_C [Oe]	M_R/M_S
Fe_3O_4	86	13	95	0.15
Fe_3O_4@SiO_2	62	11	153	0.18

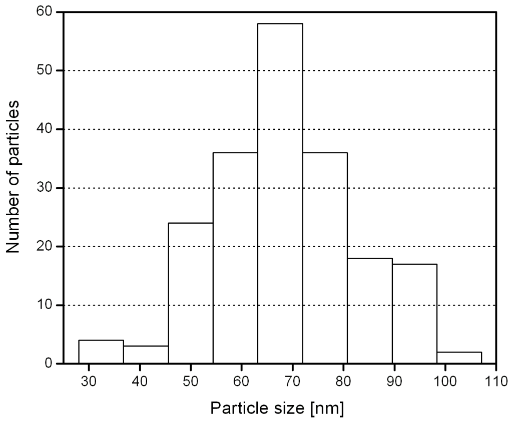

Figure 5.7.: Size distribution of pure magnetite particles.

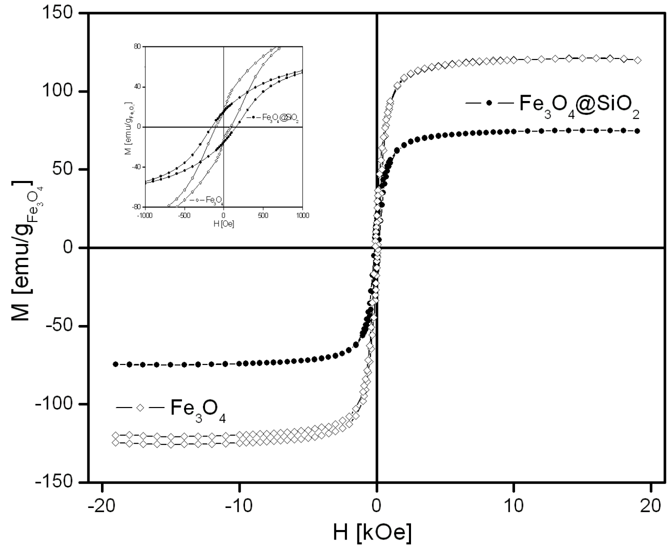

Figure 5.8.: Magnetic hysteresis loops of Fe_3O_4 and $Fe_3O_4@SiO_2$ at room temperature. The inset shows details of the hysteresis loops, showing the coercive fields (see also Table 5.3).

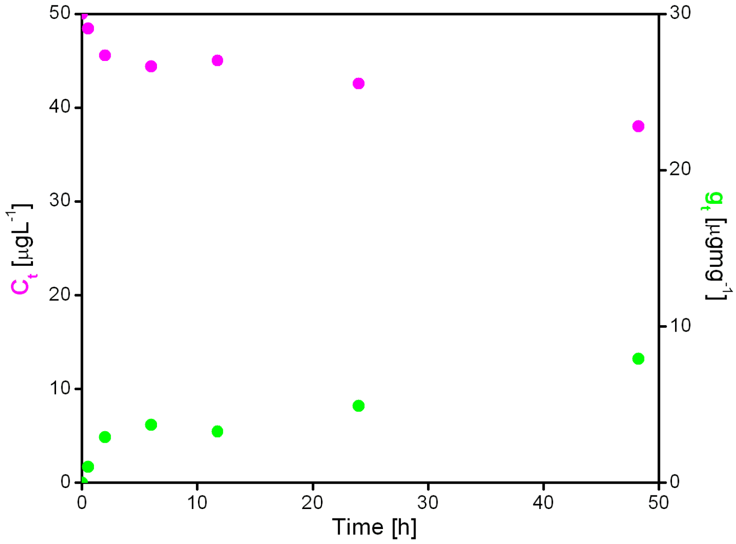

Figure 5.9.: Concentration of Hg^{2+} in aqueous solution (C_t; magenta) and/or sorbed onto the synthesized magnetite nanoparticles (q_t; green) as function of contact time. Compound $Fe_3O_4@SiO_2$.

The saturation magnetization has decreased with the modification of the pure magnetite while the coercivity has increased. The value of M_S for pure magnetite is very close to the value for bulk magnetite (90 emu/g,[42] 92 emu/g[71]), while the M_S, M_R and H_C of silica coated magnetite are close to the values to the values reported by Goya *et al.*[72] The uncoated particles perform higher magnetization. The silica shells surround the magnetite cores and prevents them from approaching each other so that the interaction between the magnetic cores decreases but nevertheless does not change crucially the magnetic properties.

5.2.3. Metal ions removal capacity of the nanomaterials

The next step was the evaluation of Hg^{2+} uptake from aqueous solutions using the above described nanomaterials. The whole experimental procedure described in Chapter 7 was repeated twice and confirmed the same trend of decreasing of the concentration of Hg^{2+} ions in the starting solution with the time. The residual Hg^{2+} concentration in solution of materials $Fe_3O_4@SiO_2$ and $Fe_3O_4@SiO_2@NH@CS_2^-$ was registered for different contact times (from 30 mins to 2 days) under mechanical stirring. In this way, the C = C_t curve along time was obtained for the residual Hg^{2+} concentration in solution (see Fig. 5.9 for compound $Fe_3O_4@SiO_2$ and Fig. 5.10 for compound $Fe_3O_4@SiO_2@NH@CS_2^-$ samples). A decrease of C_t along time approaching an equilibrium concentration was verified when the Hg^{2+} solutions were in contact with each of the synthesized nanoparticles, even when the initial Hg^{2+} concentration was very low (50 μgL^{-1}). This diminution is related to Hg^{2+} uptake by the nanomaterials.

The amount of metal sorbed by these materials at a given time, q_t (μgmg^{-1}), was

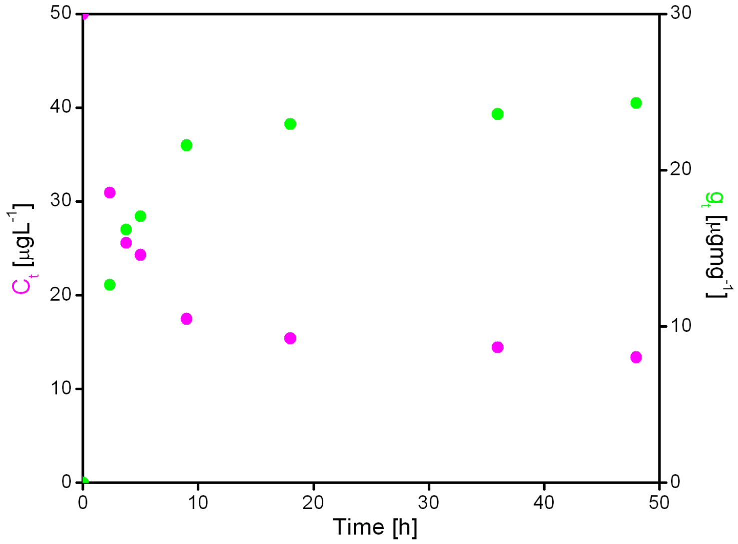

Figure 5.10.: Concentration of Hg^{2+} in aqueous solution (C_t; magenta) and/or sorbed onto the synthesized magnetite nanoparticles (q_t; green) as function of contact time. Compound $Fe_3O_4@SiO_2@NH@CS_2^-$.

calculated by the mass balance equation:

$$q_t = (C_0 - C_t)\frac{V}{W}, \tag{5.1}$$

where C_0 (μgL^{-1}) is the initial concentration of mercury in the liquid-phase and confirmed by control solution, C_t (μgL^{-1}) is the instantaneous liquid-phase concentration, V the volume of the solution (L) and W — the dry weight (in mg) of the material used.

In Figs. 5.9 and 5.10, the secondary Y axis represent the amount of Hg^{2+} in $Fe_3O_4@SiO_2$ and $Fe_3O_4@SiO_2@NH@CS_2^-$, respectively. As it is shown, the dithiocarbamato functionalized materials allowed a faster removal and a lower residual concentration of Hg^{2+} than $Fe_3O_4@SiO_2$ (higher removal capacity), thus being more efficient for its application in the purification of polluted waters from Hg^{2+}. Under the experimental conditions used in this work, 3 mg of $Fe_3O_4@SiO_2@NH@CS_2^-$ could reduce the concentration (C_0) of Hg^{2+} from 50 μgL^{-1} to an equilibrium concentration (C_e) of 13 μgL^{-1}, which correspond to a Hg^{2+} sorbed concentration at the equilibrium (q_e) of around 25 μg g^{-1}. In the case of $Fe_3O_4@SiO_2$, under identical conditions, C_e was 38 μgL^{-1} and q_e was around 8 μg g^{-1}.

The results for Hg^{2+} were compared to the removal capacity of these materials with Cd^{2+} and Pb^{2+}.[73] In brief, in preliminary tests it was found that the efficiency of the materials towards Pb^{2+} is higher than towards Cd^{2+}, but for both cases lower values were obtained as compared to the Hg^{2+} uptake. Fig. 5.11 shows the variations in the concentrations of the Cd^{2+} and Pb^{2+} ions in aqueous solutions of concentrations 250 μg/L as function of the time of contact between the metal ions and the materials. The results show that 32% of Cd^{2+} and

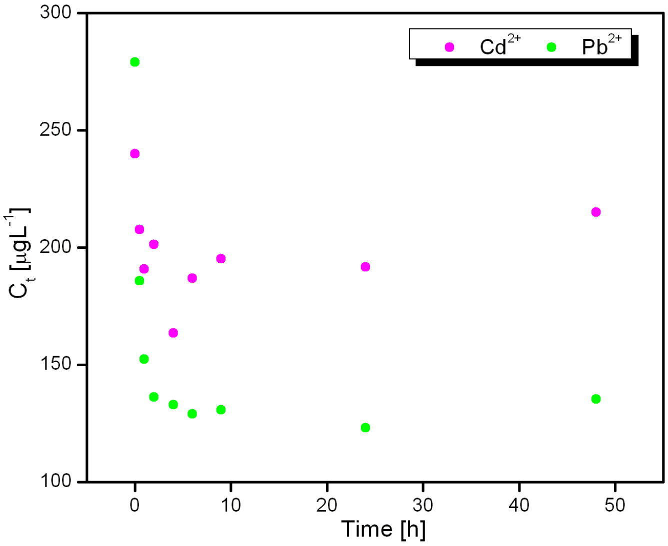

Figure 5.11.: The variation of concentration of the Cd^{2+} and Pb^{2+} ($\mu g/L$) as a function of time of contact in solutions with initial concentrations approximatively 250 $\mu g/L$ between the ions and the materials.

56% of Pb^{2+} were removed. In the beginning of the experiments, a significant quantity of metal ions was removed, followed by an increase of their concentration in solution. This increase is probably due to release of metal ions from the material due to adventitious factors.

The affinity of the dithiocarbamate ligands towards metal ions depends on the stability constant. Sulphur-containing ligands (thiols or sulphides) are capable of forming extremely strong complexes with Hg(II) with conditional stability constants of the order of 10^{30}.[64,74,75] The stability constant of the $Hg(DTC)_2$ complex according to the reaction

$Hg^{2+} + 2DTC^- \rightleftharpoons Hg(DTC)_2$

is ${}^cK_{HgL} = \frac{[HgL]}{[Hg^{2+}][L]^2}$. The log of the stability constant of the Hg−DTC complexes is about 38 while this for the complexes Cd−DTC and Pb−DTC were found to be 12.02 for Cd^{2+} and 13.71 for Pb^{2+} (determinated by spectroscopy in water at 20 °C).[76,77] The highest value for the complexes Hg−DTC predicts and confirms the highest affinity of the Hg^{2+} ions to the DTC ligand and turns these materials most effective for mercury uptake in aqueous solutions.

5.3. Final remark

The synthesis, surface modification and functionalization procedures of magnetite nanoparticles were reported in this chapter. Amino groups were attached to the surface of the silica-magnetite particles, and then functionalized with DTC groups. The particles were fully characterized and the sorption of Hg^{2+} from aqueous solution was investigated and compared to uptake of Pb^{2+} and Cd^{2+}. These ferrimagnetic magnetite particles have some advantages comparing to existing materials with similar applications. They can be synthesized easily and in large amounts with uniform morphology; the reactional superficial groups are expected to be more, since the surface area is higher, due to the small particle size; the magnetic particles can be readily separated from the water by moderate external magnetic field. The material have good chemical stability and high magnetic susceptibility too. The whole synthetic process together with the testing results of the materials are reproducible. The preliminary tests indicate high efficiency, especially towards Hg^{2+} ions, which is due to the presence of the DTC groups. As was mentioned above, mercury ions are a serious source of water contamination. The removal process described here requires low cost technology and offers high efficiency. In this context, these materials need further research, including their behaviour with solutions of different pH and chemical composition. Also kinetic studies involving these systems could be very helpful in understanding their behaviour.

References

1. Batlle X and Labarta A, *J. Phys. D: Appl. Phys.* 35(6) (2002), R15–R42.
2. Feltin N and Pileni MP, *Langmuir* 13(15) (1997), 3927–3933.
3. Morales MP, Pecharroman C, Carreño TG and Serna CJ, *J. Solid State Chem.* 108(1) (1994), 158–163.
4. Moreno EM, Zayat M, Morales MP, Serna CJ, Roig A and Levy D, *Langmuir* 18(12) (2002), 4972–4978.
5. Jolivet JP, Chaneac C and Tronc E, *Chem. Commun.* (5) (2004), 481–487.
6. Yang HH, Zhang SQ, Chen XL, Zhuang ZX, Xu JG and Wang XR, *Anal. Chem.* 76(5) (2004), 1316–1321.
7. Brigger I, Dubernet C and Couvreur P, *Adv. Drug Delivery Rev.* 54(5) (2002), 631–651.
8. Shinkai M, *J. Biosci. Bioeng.* 94(6) (2002), 606–613.
9. Mornet S, Vasseur S, Grasset F and Duguet E, *J. Mater. Chem.* 14(14) (2004), 2161–2175.
10. Arruebo M, Galán M, Navascués N, Téllez C, Marquina C, Ibarra MR and Santamaría J, *Chem. Mater.* 18(7) (2006), 1911–1919.
11. Arruebo M, Fernández-Pacheco R, Ibarra MR and Santamaría J, *Nano Today* 2(3) (2007), 22–32.
12. Bruce IJ, Taylor J, Todd M, Davies MJ, Borioni E, Sangregorio C and Sen T, *J. Magn. Magn. Mater.* 284 (2004), 145–160.
13. Fukumori Y and Ichikawa H, *Adv. Powder Technol.* 17(1) (2006), 1–28.
14. Ito A, Shinkai M, Honda H and Kobayashi T, *J. Biosci. Bioeng.* 100(1) (2005), 1–11.
15. Jun YW, Huh YM, Choi JS, Lee JH, Song HT, Kim S, Yoon S, Kim KS, Shin JS, Suh JS and Cheon J, *J. Am. Chem. Soc.* 127(16) (2005), 5732–5733.
16. Woo K, Hong J and Ahn JP, *J. Magn. Magn. Mater.* 293(1) (2005), 177–181.
17. Yamaura M, Camilo RL, Sampaio LC, Macedo MA, Nakamura M and Toma HE, *J. Magn. Magn. Mater.* 279(2-3) (2004), 210–217.
18. Gupta AK and Gupta M, *Biomaterials* 26(18) (2005), 3995–4021.
19. URL `http://www.epa.gov/safewater/contaminants/index.html`.
20. Hernandez-Ramirez O and Holmes SM, *J. Mater. Chem.* 18(24) (2008), 2751–2761.
21. Hu J, Lo IMC and Chen G, *Water Sci. Technol.* 50(12) (2004), 139–146.
22. Borai EH, El-Sofany EA and Morcos TN, *Adsorption* 13(2) (2007), 95–104.
23. Hu J, Chen GH and Lo IMC, *Water Res.* 39(18) (2005), 4528–4536.
24. Li L, Fan MH, Brown RC, Van Leeuwen JH, Wang JJ, Wang WH, Song YH and Zhang PY, *Crit. Rev. Environ. Sci. Technol.* 36(5) (2006), 405–431.
25. Mohan D and Pittman CU, *J. Hazard. Mater.* 142(1-2) (2007), 1–53.
26. Mayo JT, Yavuz C, Yean S, Cong L, Shipley H, Yu W, Falkner J, Kan A, Tomson M and Colvin VL, *Sci. Technol. Adv. Mater.* 8(1-2) (2007), 71–75.

27. Cumbal L, Greenleaf J, Leun D and SenGupta AK, *React. Funct. Polym.* 54(1-3) (2003), 167–180.
28. Ngomsik AF, Bee A, Draye M, Cote G and Cabuil V, *C. R. Chim.* 8(6-7) (2005), 963–970.
29. Guo LM, Li JT, Zhang LX, Li JB, Li YS, Yu CC, Shi JL, Ruan ML and Feng JW, *J. Mater. Chem.* 18(23) (2008), 2733–2738.
30. Chang YC and Chen DH, *J. Colloid Interface Sci.* 283(2) (2005), 446–451.
31. Atia AA, Donia AM and Yousif AM, *Sep. Purif. Technol.* 61(3) (2008), 348–357.
32. Zhang C, Li X and Pang J, *J. Appl. Polym. Sci.* 82(7) (2001), 1587–1592.
33. Atia AA, Donia AM, Abou-El-Enein SA and Yousif AM, *Sep. Sci. Technol.* 42 (2007), 1–18.
34. Sheha RR and El-Zahhar AA, *J. Hazard. Mater.* 150(3) (2008), 795–803.
35. Lee Y, Rho J and Jung B, *J. Appl. Polym. Sci.* 89(8) (2003), 2058–2067.
36. Li HD, Li Z, Liu T, Xiao X, Peng ZH and Deng L, *Bioresour. Technol.* 99(14) (2008), 6271–6279.
37. Huang CZ and Hu B, *Spectrochim. Acta, Part B* 63(3) (2008), 437–444.
38. Shin S and Jang J, *Chem. Commun.* (41) (2007), 4230–4232.
39. Yantasee W, Warner CL, Sangvanich T, Addleman RS, Carter TG, Wiacek RJ, Fryxell GE, Timchalk C and Warner MG, *Environ. Sci. Technol.* 41(14) (2007), 5114–5119.
40. Bragg WH, *Nature* 95 (1915), 561–561.
41. Nishikawa S, *Proc. Math. Phys. Soc. Tokyo* 8 (1915), 199–209.
42. Cornell RM and Schwertmann U, The iron oxides, 2nd ed., Wiley-VCH Verlag Berlin GmbH, 2003.
43. Tartaj P, Del Puerto Morales M, Veintemillas-Verdaguer S, González-Carre no T and Serna CJ, *J. Phys. D: Appl. Phys.* 36(13) (2003), R182–R197.
44. Tartaj P, Morales MP, Gonzalez-Carreno T, Veintemillas-Verdaguer S and Serna CJ, *J. Magn. Magn. Mater.* 290 (2005), 28–34.
45. Tang ZY and Kotov NA, *Adv. Mater.* 17(8) (2005), 951–962.
46. Osaka T, Matsunaga T, Nakanishi T, Arakaki A, Niwa D and Iida H, *Anal. Bioanal. Chem.* 384(3) (2006), 593–600.
47. Lian SY, Wang E, Kang ZH, Bai YP, Gao L, Jiang M, Hu CW and Xu L, *Solid State Commun.* 129(8) (2004), 485–490.
48. Wan J, Chen X, Wang Z, Yang X and Qian Y, *J. Cryst. Growth* 276(3-4) (2005), 571–576.
49. Caruntu D, Caruntu G, Chen Y, O'Connor CJ, Goloverda G and Kolesnichenko VL, *Chem. Mater.* 16(25) (2004), 5527–5534.
50. Lee KM, Sorensen CM, Klabunde KJ and Hadjipanayis GC, *IEEE T. Magn.* 28(5 pt 2) (1992), 3180–3182.
51. Zhou ZH, Wang J, Liu X and Chan HSO, *J. Mater. Chem.* 11(6) (2001), 1704–1709.
52. Tago T, Hatsuta T, Miyajima K, Kishida M, Tashiro S and Wakabayashi K, *J. Am. Ceram. Soc.* 85(9) (2002), 2188–2194.

53. Koutzarova T, Kolev S, Ghelev C, Paneva D and Nedkov I, *Phys. Status Solidi C* 3(5) (2006), 1302–1307.
54. Massart R, *IEEE T. Magn.* 17(2) (1981), 1247–1248.
55. Sugimoto T and Matijević E, *J. Colloid Interface Sci.* 74(1) (1980), 227–243.
56. Sun SH and Zeng H, *J. Am. Chem. Soc.* 124(28) (2002), 8204–8205.
57. Li Z, Chen H, Bao HB and Gao MY, *Chem. Mater.* 16(8) (2004), 1391–1393.
58. Wu MZ, Xiong Y, Jia YS, Niu HL, Qi HP, Ye J and Chen QW, *Chem. Phys. Lett.* 401(4-6) (2005), 374–379.
59. Wang J, Chen QW, Zeng C and Hou BY, *Adv. Mater.* 16(2) (2004), 137–140.
60. Wai C and Wang S, *J. Chromatogr., A* 785(1-2) (1997), 369–383.
61. Batterham GJ, Munksgaard NC and Parry DL, *J. Anal. At. Spectrom.* 12(11) (1997), 1277–1280.
62. Atanassova D, Stefanova V and Russeva E, *Talanta* 47(5) (1998), 1237–1243.
63. Gölcü A, *Transition Met. Chem.* 31(3) (2006), 405–412.
64. Black FJ, Bruland KW and Flegal AR, *Anal. Chim. Acta* 598 (2007), 318–333.
65. Venkatesan KA, Srinivasan TG and Rao PRV, *Colloids Surf., A* 180(3) (2001), 277–284.
66. Venkatesan KA, Srinivasan TG and Rao PRV, *Sep. Sci. Technol.* 37(6) (2002), 1417–1429.
67. Mahmoud ME, El-Essawi MM and Fathallah EMI, *J. Liq. Chromatogr. Relat. Technol.* 27(11) (2004), 1711–1727.
68. Goubert-Renaudin S, Schneider R and Walcarius A, *Tetrahedron Lett.* 48(12) (2007), 2113–2116.
69. Mahmoud ME, *Anal. Chim. Acta* 398 (1999), 297–304.
70. Bruce IJ and Sen T, *Langmuir* 21(15) (2005), 7029–7035.
71. Zaitsev V, Filimonov D, Presnyakov I, Gambino R and Chu B, *J. Colloid Interface Sci.* 212(1) (1999), 49–57.
72. Goya GF, Berquo TS, Fonseca FC and Morales MP, *J. Appl. Phys.* 94(5) (2003), 3520–3528.
73. Figueira P, Nanomagnetes para remoção de iões metálicos de águas naturais, Bachelor thesis, University of Aveiro, 2008.
74. Hsu H and Sedlak DL, *Environ. Sci. Technol.* 37(12) (2003), 2743–2749.
75. Larionov SV, Koroleva TI and Cheremisina IM, *Bulletin of the academy of science of the USSR, division of chemical science* 24(10) (1995), 2093–2096.
76. Starý J and Kratzer K, *Anal. Chim. Acta* 40(1) (1968), 93–100.
77. Pazukhina YE, Isakova NV, Nagy V and Petrukhin OM, *Solvent Extr. Ion Exch.* 15(5) (1997), 777–790.

CONCLUSIONS

CHAPTER VI

Chapter 6.

Conclusions

- **Coordination compounds of 1st row transition metals and ambidentate aromatic ligands**
  The magnetic properties of new coordination compounds of 1st row transition metals (Mn^{2+}, Co^{2+}, Ni^{2+} and Cu^{2+}) with 3–hydroxypicolinic, 2–hydroxynicotinic and 2–thionicotinic acid were investigated. These complexes were structurally characterized with single-crystal and powder X-ray diffraction, elemental analysis, infrared spectroscopy and thermo-analytical measurements. Some of the novel structures were successfully extended with the bridging ligand 1,2–bis(4–pyridyl)ethane, the tetramethylammonium counterion or with 1,10–phenanthroline. The compounds with HpicOH, HnicSH and these with Cu^{2+}, Ni^{2+} and HnicOH do not exhibit magnetic interactions, but showed paramagnetism with deviations from the Curie law at low temperatures. Their magnetic properties were analysed with physical models, which describe paramagnetic behaviours of transition metals systems where the electronic configurations and ligand environments differ. Metamagnetic behaviour was revealed by the coordination complex with Mn^{2+} and HnicOH. At low temperatures (< 6 K) the compound entirely changes the interactions from antiferro- to ferromagnetic. We cannot be certain about interaction paths since single-crystal were not obtained so that the structure was deduced from elemental analysis, infrared spectroscopy and thermo-analytical measurements. Another antiferromagnetic compound is with Co and HnicOH.
  We can speculate that the position of the hydroxyl group (of HpicOH and HnicOH) and the coordination mode of the ligand (mono- or polydentate) has a crucial influence on the magnetic properties. These results show that the materials containing 1st row transition metals and ligands, derivative of pyridine-carboxylic acids (in particular HnicOH) can show magnetic interactions and a future work in this direction can be of scientific interest.
- **Coordination compounds of lanthanides with picolinic acid and glutaric acid**
  Three new isostructural lanthanide-organic 1D coordination polymers with picolinic and glutaric acid, $[Ln(glu)(pic)(H_2O)_2]$ (where Ln = Sm^{3+}, Tb^{3+} and Eu^{3+}), were successfully isolated and characterised. These coordination polymers are composed of lanthanide dimers separated by long and flexible glutarato anions. All these compounds share common structural features and show efficient intramolecular aromatic ligand-to-lanthanide energy transfer. Magnetic interactions between the Tb^{3+} ions in its complex were not found. Nevertheless, the possibility to build such picolinic-containing lanthanide-organic polymers in which the length of the bridging ligand could be systematically varied open up some prospects for future work concerning the investigation of the photoluminescent and magnetic behaviour of other similar systems (which are also similar to these described in the previous chapter).

- **Magnetic behaviour of organic-inorganic hybrids of N–(phosphonomethyl) iminodiacetic acid and 1st row transition metals**

  The magnetic behaviour of organic-inorganic hybrids with the multidentate chelating ligand **pmida** and 1st row transition metals were investigated. There are no evidences for exchange interactions in the novel crystal structures of **pmida**. The paramagnetic behaviour observed in these compounds is due to the presence of the transition metals. Deviations from the Curie law at low temperatures due to the crystal field effects were observed. The values of magnetic parameters were calculated with fittings which are different depending on the metal electronic configurations and the ligand environments.
- **Magnetic nanoparticles for removal of heavy metals from water**

  The synthesis, surface modification and functionalization of ferrimagnetic Fe_3O_4 particles have been discussed. Amino groups (from 3–aminopropyltriethoxysilane) were attached to the surface of the silica-magnetite particles, and then functionalized with dithiocarbamate (DTC) groups. The particles were fully characterized and the sorption of Hg^{2+} from aqueous solution was investigated and preliminary compared to uptake of Pb^{2+} and Cd^{2+}. These ferrimagnetic magnetite particles have some advantages comparing to existing materials with similar applications. They can be synthesized easily and in large amounts with uniform morphology; the reactional superficial groups are expected to be available in a large amount, due to the small particle size; the magnetic particles can be readily separated from the water by moderate external magnetic field. The preliminary tests indicate high efficiency, especially towards Hg^{2+} ions, which is due to the presence of the DTC groups. The removal process described here requires low cost technology and offers high efficiency. In this context, these materials need further research, including their behaviour in solutions of different pH and chemical composition.

EXPERIMENTAL AND CHARACTERISATION TECHNIQUES

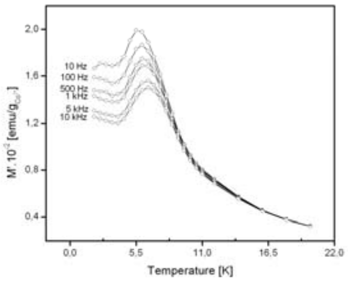

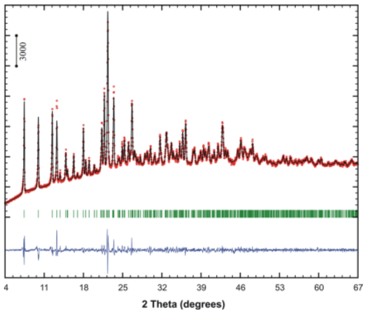

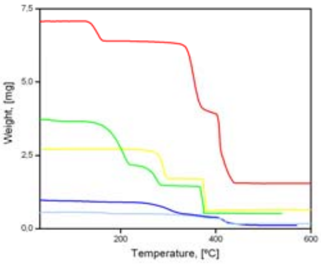

CHAPTER VII

Chapter 7.

Experimental and characterisation techniques

7.1. Experimental

7.1.1. Reagents

Chemicals (shown in Table 7.1) were readily available from commercial sources and were used as received without further purification from the main suppliers Aldrich, Panreac, Fluka and Riedel-de Haën with purity 97–99%. The reactions in aqueous medium from Chapters 2, 3 and 4 were performed in distilled water and these, described in Chapter 5, were performed in deionized water as described below.

Table 7.1.: List of reagents used in the work.

Name	Formula	Molecular weight [g/mol]
Ligands		
Acetic acid	CH_3COOH	60.05
(3–aminopropyl)triethoxysilane	$H_2N(CH_2)_3Si(OC_2H_5)_3$ $\rho = 0.946$ g/mL at 25 °C	221.37
1,2–Bis (4–pyridyl) ethane	$C_{12}H_{12}N_2$	184.24
4,4′–Bipyridine	$C_{10}H_8N_2$	156.18
Glutaric acid	$C_5H_8O_4$	132.11
3–Hydroxypicolinic acid	$C_6H_5NO_3$	139.11
2–Hydroxynicotinic acid	$C_6H_5NO_3$	139.11
2–Mercaptonicotinic acid	$C_6H_5NO_2S$	155.18
1,10–Phenanthroline	$C_{12}H_8N_2$	198.23
N–(Phosphonomethyl) iminodiacetic acid	$C_5H_{10}NO_7P$	227.11
Picolinic acid	$C_6H_5NO_2$	123.11
Pyrazine	$C_4H_4N_2$	80.09
Sodium metasilicate	$Na_2SiO_3 \cdot 5\,H_2O$	212.14
Tetraethyl orthosilicate	$Si(OC_2H_5)_4$ $\rho = 0.934$ g/mL at 25 °C	208.33
Metal compounds and counterions		
Ammonium iron(II) sulfate hexahydrate	$(NH_4)_2Fe(SO_4)_2 \cdot 6\,H_2O$	392.14
Carbon disulfide	CS_2 $\rho = 1.266$ g/mL at 25 °C	76.14

Continued on next page

Name	Formula	Molecular weight [g/mol]
Cobalt(II) chloride hexahydrate	$CoCl_2 \cdot 6\,H_2O$	273.93
Cobalt(II) acetate tetrahydrate	$Co(CH_3COO)_2 \cdot 4\,H_2O$	249.08
Copper(II) acetate 1–hydrate	$Cu(CH_3COO)_2 \cdot H_2O$	249.09
Copper(II) carbonate basic	$CuCO_3 \cdot Cu(OH)_2$	221.12
Europium(III) nitrate pentahydrate	$Eu(NO_3)_3 \cdot 5\,H_2O$	428.05
Iron(III) chloride hexahydrate	$FeCl \cdot 6\,H_2O$	270.30
Iron(II) sulphate heptahydrate	$FeSO_4 \cdot 7\,H_2O$	278.02
Manganese acetate tetrahydrate	$MnCl_2 \cdot 4\,H_2O$	245.09
Manganese(II) chloride tetrahydrate	$MnCl_2 \cdot 4\,H_2O$	197.91
Nickel(II) carbonate basic	$2\,NiCO_3 \cdot 3\,Ni(OH)_2 \cdot 4\,H_2O$	587.59
Nickel(II) chloride hexahydrate	$NiCl_2 \cdot 6\,H_2O$	237.71
Nickel(II) acetate tetrahydrate	$Ni(CH_3COO)_2 \cdot 4\,H_2O$	248.85
Samarium(III) acetate hydrate	$Sm(COO)_3 \cdot xH_2O$	327.48
Sodium hydroxide	NaOH	40.00
Terbium nitrate pentahydrate	$Tb(NO_3)_3 \cdot 5\,H_2O$	435.02
Potassium bromide	KBr	119.00
Potassium hydroxide	KOH	56.11
Potassium nitrate	KNO_3	101.10
Tetramethylammonium hydroxide pentahydrate	$(CH_3)_4NOH \cdot 5\,H_2O$	181.23
Tetramethylammonium hydroxide (25 wt. % in H_2O, $\approx$ 2.8M)	$(CH_3)_4NOH$ ρ = 1.016 g/mL at 25 °C	91.16
Vanadium(IV) oxide sulfate hydrate (anhydrous basis)	$VOSO_4 \cdot xH_2O$	163.00
Solvents		
Ammonia aqueous (28%)	NH_3OH ρ = 0.9 g/mL at 25 °C	35.05
Ethanol	C_2H_5OH ρ = 0.789 g/mL at 25 °C	46.07
2–Propanol	$(CH_3)_2CHOH$ ρ = 0.785 g/mL at 25 °C	60.10
2–Propanone	C_3H_6O ρ = 0.791 g/mL at 25 °C	58.08
Tetrahydrofuran	C_4H_8O ρ = 0.8892 g/mL at 20 °C	72.11

7.1.2. Syntheses

Chapter 2: Coordination compounds of 1^{st} row transition metals and ambidentate aromatic ligands

$[Co(picOH)_2(H_2O)_2]$ (I) and $mer-[N(CH_3)_4][Co(picOH)_3] \cdot H_2O$ (compound II) An aqueous solution of cobalt(II) chloride hexahydrate ($CoCl_2 \cdot 6\,H_2O$) (0.5 mmol) was added dropwise to an aqueous solution containing 3–hydroxypicolinic acid (HpicOH, 2 mmol) and tetramethylammonium hydroxide ($(CH_3)_4NOH$; 2 mmol) and then the final pH was adjusted to *ca.* 7 with 1M CH_3COOH. This mixture was stirred and treated under hydrothermal conditions at 150 °C over a period of 48 hours. After cooling, the solution was transferred to a semi-covered beaker for evaporation at room temperature. A pale orange powder of **I** was obtained (15.7 %) and orange single crystals of the same compound were grown after 10 days from the supernatant solution (m.p. 160 °C). Red crystals of **II** were obtained from the same mother solution in *ca.* 2 months (m.p. 228 °C).

$[Cu(picOH)_2]$ (compound III) An aqueous solution (*ca.* 3 mL) of copper(II) acetate 1-hydrate ($Cu(CH_3COO)_2 \cdot H_2O$) (0.5 mmol) was added dropwise to an aqueous solution (*ca.* 4 mL) containing HpicOH (2 mmol) and $(CH_3)_4NOH$ (2 mmol, 25 wt. % in water). The pH of the mixture was adjusted to *ca.* 7 using 1M CH_3COOH. The resulting mixture was transferred to the reaction vessel (autoclave). The reaction took place in a preheated oven at 150 °C over a period of 48 h after which the autoclave was cooled slowly to ambient temperature before opening. Green single-crystals of **III** were directly obtained from the autoclave contents.

$[Cu(picOH)_2(BPE)]_2 \cdot [Cu(picOH)_2(BPE)_2] \cdot 8\,H_2O$ (compound IV) 3 mL of aqueous solution of $Cu(CH_3COO)_2 \cdot H_2O$ (0.5 mmol) was added dropwise to an aqueous solution (*ca.* 4 mL) containing HpicOH (2 mmol), 3 mmol of 1,2–bis(4–pyridine)ethane (BPE) and $(CH_3)_4NOH$ (2 mmol). The pH of the mixture was adjusted to *ca.* 7 using 1M CH_3COOH. The resulting mixture was transferred to an autoclave. The reaction took place in a preheated oven at 150 °C over a period of 48 h after which the reaction vessel was cooled slowly to ambient temperature before opening. Green single-crystals of **IV** were obtained from the autoclave contents.

$Ni(picOH)_2(H_2O)_2$ (compound V) A solution with pH 7, containing 5 mL of 0.2 M HpicOH (0.1391 g) and 5 mL of 0.1 M sodium metasilicate (Na_2SiO_3) (0.1061 g) was stirred about 35 mins and left in covered test tubes, each containing 3.3 mL. In one week, 0.1184 g of nickel(II) chloride hexahydrate ($NiCl_2 \cdot 6\,H_2O$) in 6 mL H_2O was added dropwise to the gel (2 mL in each tube). It was possible to observe the crystal formation with the addition and diffusion of the first drops. In 3 days air- and light- stable needle-like crystals were grown.

$[Mn(H_2nicO)_2(H_2O)_2](H_2nicO)_2 \cdot 2\,H_2O$ (compound VI) Reactional mixture containing 0.25 mmol of manganese acetate tetrahydrate ($MnCl_2 \cdot 4\,H_2O$), 1 mmol of 2–hydroxynicotinic acid (HnicOH) and 1 mmol of potassium hydroxide (KOH) in 8 mL of distilled water (pH 9) was stirred through roughly at ambient temperature for 10 minutes and transferred into an autoclave. The hydrothermal reaction took place over a period of 5 days at 140 °C. After reacting, yellow single-crystals were collected from the colourless mother liquor.

$Ni[HnicO]_2[H_2O]_2$ (compound VII) Mixture containing 0.25 mmol of $NiCl_2 \cdot 6\,H_2O$, 1 mmol of HnicOH and 1 mmol of KOH in 8 mL of distilled water (pH 9) was stirred through roughly at ambient temperature for 10 minutes and transferred into an autoclave. The hydrothermal reaction took place over a period of 5 days at 140 °C. After reacting, green single-crystals were collected from the yellow mother liquor.

$Mn[HnicO]_2[H_2O]_2$ (compound VIII) These single crystals were obtained in a gel formed by Na_2SiO_3. A solution of $Na_2SiO_3 \cdot 5\,H_2O$ (0.1 M, 5 mL) was added dropwise to an aqueous solution (6 mL) containing 1 mmol HnicOH and 0.5 mmol KOH in 6 mL H_2O. The mixture was stirred and each test tube, with 5 mL of solution, was left for 24 hours. Afterwards, $MnCl_2 \cdot 4\,H_2O$ (0.25 mmol) was added to the gel. Yellow single crystals of **VIII** were grown over a period of 4 days.

$Co[HnicO]_2 \cdot 2\,H_2O$ (compound IX) A solution of 0.5 mmol $CoCl_2 \cdot 6\,H_2O$ in 10 mL H_2O was added dropwise to 2 mmol HnicOH in 20 mL H_2O under stirring. The pH of the acid solution was adjusted with KOH to 6 before the addition of the metal salt. With its addition, the colour of the reactional mixture changed from light to dark pink. Pink powder and transparent colourless liquor were collected after filtration.

$Mn[HnicO]_2 \cdot H_2O$ (compound X) 2 mmol HnicOH and 2 mmol $(CH_3)_4NOH$ in 10 mL H_2O were stirred. The pH of the solution was decreased to 6 with drops of 1M CH_3COOH. A solution of 0.5 mmol $MnCl_2 \cdot 4\,H_2O$ in 5 mL H_2O was added dropwise. While the solution of the metal salt was added, a yellowish precipitate was formed. Yellowish powder and dull colourless liquor were collected after filtration.

$Cu[HnicO]_2$ (compound XI) 2 mmol HnicOH and 2 mmol $(CH_3)_4NOH$ in 10 mL H_2O were stirred. The pH of the solution was decreased to 6 with drops of 1M CH_3COOH. A solution of 0.5 mmol $Cu(CH_3COO)_2 \cdot H_2O$ in 5 mL H_2O was added dropwise. After stirring about 5 mins, a precipitate was formed from the blue solution. Blue powder and transparent colourless liquor were collected after filtration.

$[Ni(phen)_3](H_2nic_2S_2)_2 \cdot 2\,H_2O$ (compound XII) A mixture with $NiCl_2 \cdot 6\,H_2O$ (0.1 mmol), 2–mercaptonicotinic acid (HnicSH 0.5 mmol) and 1,10–phenanthroline (phen, 0.5 mmol) in

H_2O (10 mL) was stirred and sealed in autoclaves. After 7 days hydrothermal reaction at 100 °C the light yellow crystals were collected by filtration and washed with water. The orange mother liquor was left for slow evaporation at room temperature.

[Co(phen)(HnicS)(nicS)] (compound XIII) A mixture containing cobalt(II) acetate tetrahydrate ($Co(CH_3COO)_2 \cdot 4\,H_2O$, 0.4 mmol), HnicSH (0.8 mmol), and phen (0.8 mmol) in H_2O (10 mL) was stirred and sealed in autoclaves. After 7 days reaction in oven at 100 °C the dark green crystals were collected by filtration and washed with water.

$[Mn(phen)_2(C_{12}H_7N_2O_5)](C_{12}H_8N_2O_4S_2) \cdot 2\,H_2O$ (compound XIV) A mixture of 0.1 mmol $MnCl_2 \cdot 4\,H_2O$, 0.5 mmol HnicSH, and 0.5 mmol phen in 10 mL H_2O was stirred and sealed in autoclaves. After 7 days reaction in oven at temperature 100 °C the yellow crystals were collected by filtration and washed with water.

Chapter 3: Coordination compounds of lanthanides with picolinic acid and glutaric acid

Synthesis of $[Ln(glu)(pic)(H_2O)_2]$, where Ln = Sm^{3+} (XV), Tb^{3+} (XVI) and Eu^{3+} (XVII) The three main synthesis methods have been used in order to design the lanthanide-containing extended networks: diffusion through gels, hydrothermal conditions, crystallization with slow evaporation at room temperature. Different approaches were used in order to obtain new compounds: by dissolving previously synthesized new lanthanide complexes and addition of the bridging ligands and also by new synthesis from the starting compounds. The first approach did not give rise to new extended structures, in all the cases the starting complexes were recrystallized. Preparation of single crystals of compound **XV** of an appropriate size and stability for single-crystal X-ray diffraction studies was carried out in a gel formed by sodium metasilicate. The solution of $Na_2SiO_3 \cdot 5\,H_2O$ (0.1 M, 5 mL) was added dropwise to an aqueous solution (10 mL, pH 4.3) containing glutaric and picolinic acids. The mixture was stirred and each test tube, with 5 mL of solution, was left for 24 hours. Afterwards, samarium(III) acetate hydrate ($Sm(COO)_3 \cdot xH_2O$) (0.25 mmol) was added to the gel. White single crystals of $[Sm(glu)(pic)(H_2O)_2]$ were grown over a period of 4 months.

Isostructural materials, mainly isolated as microcrystalline powders, of picolinic and glutaric acids with Tb^{3+} and Eu^{3+} (**XVI** and **XVII**) were synthesised by adding an aqueous solution of picolinic acid (1 mmol) to an aqueous solution containing glutaric acid (1 mmol) (pH 6.5, adjusted with KOH) and the corresponding lanthanide nitrate pentahydrate [$Ln(NO_3)_3 \cdot 5\,H_2O$, Ln = Tb and Eu] (0.25 mmol). For the compound $[Tb(glu)(pic)(H_2O)_2]$, small crystals could also be manually harvested which allowed unequivocally phase identification by means of the unit cell determination using single-crystal X-ray diffraction data.

Chapter 4: Magnetic behaviour of organic-inorganic hybrids containing N– (phosphonomethyl) iminodiacetic acid and transition metals

[Fe(H_2pmida)(H_2O)$_2$] (compound XVIII) A mixture of 2 mmol of ammonium iron(II) sulfate hexahydrate ($(NH_4)_2Fe(SO_4)_2 \cdot 6\,H_2O$) and 1.3 mmol of H_4pmida in 16 mL of distilled water was stirred through roughly at ambient temperature for 30 minutes and transferred to the reaction vessel, as was reported by Shi *et al.*[1] The reaction took place over a period of 4 days at 120 °C. After reacting, a large quantity of colourless crystals was isolated as a pure phase by vacuum filtering, washed with copious amounts of distilled water, and air-dried at room temperature.

[Co(pyr)(H_2O)$_4$][Co_2(Hpmida)$_2$(pyr)(H_2O)$_2$] $\cdot$ 2 (H_2O) (compound XIX) Mixture containing 1.2 mmol of H_4pmida, 1.4 mmol of $Co(CH_3COO)_2 \cdot 4\,H_2O$, 1.2 mmol of pyrazine ($C_4H_4N_2$) and 5 mmol of sodium hydroxide NaOH in 8 mL of distilled water was stirred through roughly at ambient temperature for 30 minutes and transferred to an autoclave, as was reported by Shi *et al.*[2] The reactions took place over a period of 4 days at 100 °C. After reacting, a large amount of orange single-crystals were readily obtained as a pure phase by vacuum filtration and washed with copious amounts of distilled water. This compound could also be isolated as large single-crystals from the slow evaporation of the autoclave mother liquor.

[Ni(pyr)(H_2O)$_4$][Ni_2(Hpmida)$_2$(pyr)(H_2O)$_2$] $\cdot$ 2 (H_2O) (compound XX) A mixture of 1.2 mmol H_4pmida, 1.2 mmol nickel(II) carbonate basic $2\,NiCO_3 \cdot 3\,Ni(OH)_2 \cdot 4\,H_2O$ and 1.2 mmol pyrazine ($C_4H_4N_2$) in 8 mL of distilled water was stirred through roughly at ambient temperature for 30 minutes and transferred into the autoclave, as was reported by Shi *et al.*[2] The reactions took place over a period of 4 days at 100 °C. After reacting, a large amount light-blue highly crystalline material was readily obtained as a pure phase by vacuum filtration and washed with copious amounts of distilled water.

($4,4'-$bpyH)$_2$[Mn($4,4'-$bpy)(H_2O)$_4$][V_2O_2(pmida)$_2$] $\cdot$ 2 H_2O (compound XXI) A mixture of 2.5 mmol of vanadium(IV) oxide sulfate hydrate $VOSO_4 \cdot xH_2O$, 1.2 mmol of manganese acetate tetrahydrate $Mn(CH_3COO)_2 \cdot 4\,H_2O$, 1.2 mmol of H_4pmida, 0.6 mmol of 4,4'-bpy and 5 mmol of NaOH in 10 mL of distilled water was stirred through roughly at ambient temperature for 30 minutes and transferred to the reaction vessel, as was reported by Shi *et al.*[3] The reaction took place over a period of 4 days at 100 °C. After reacting, a large amount of green single-crystals were readily obtained as a pure phase by vacuum filtration followed by washing with copious amounts of distilled water.

($4,4'-$bpyH)$_2$[Co($4,4'-$bpy)(H_2O)$_4$][V_2O_2(pmida)$_2$] $\cdot$ 2 H_2O (compound XXII) A mixture of 2.5 mmol of $VOSO_4 \cdot xH_2O$, 1.2 mmol of $Co(CH_3COO)_2 \cdot 4\,H_2O$, 1.2 mmol of H_4pmida, 0.6 mmol of 4,4'–bpy and 5 mmol of NaOH in 15 mL of distilled water was stirred through roughly at ambient temperature for 30 minutes and transferred to the reaction vessel, as was reported by Shi *et al.*[3] The reactions took place over a period of 4 days at 100 °C. After reacting, purple single-crystals were obtained from autoclave. The light-green mother liquor

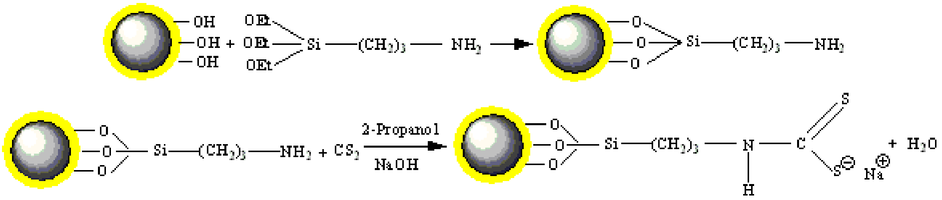

Figure 7.1.: Reactional scheme of synthesis and functionalization of magnetite. (the magnetite core is represented in black and the silica coating — in yellow)

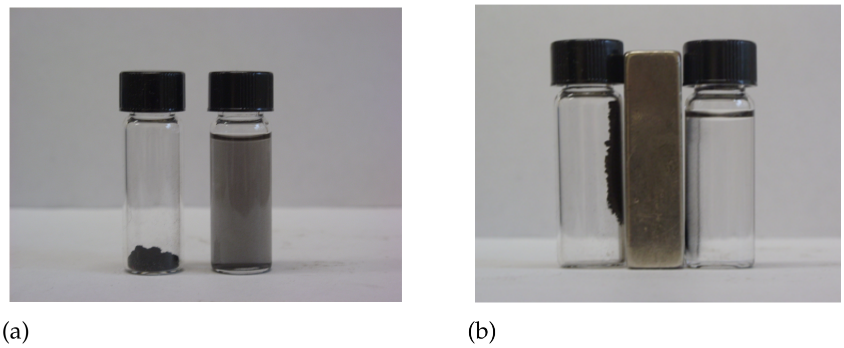
(a) (b)

Figure 7.2.: Magnetite nanoparticles without applied magnetic field and under the action of magnetic field: (a) Without applied magnetic field. Dried powder sample and particles dispersed in ethanol; (b) Under the action of a strong NdFeB magnet.

was allowed to stand still at ambient temperature, yielding after approximately one week large green single-crystals.

$[Cu_5(pmida)_2(4,4'-bpy)_3] \cdot 6.5H_2O$ (compound XXIII) A mixture containing 1 mmol of 4,4′–bpy, 1 mmol of H_4pmida and 1 mmol of copper(II) carbonate basic $CuCO_3 \cdot Cu(OH)_2$ in 20 mL of distilled water was stirred through roughly at ambient temperature for 30 minutes and transferred to an autoclave. The hydrothermal reaction took place over a period of 4 days at 100 °C. After reacting, a large amount of brownish single-crystals was collected.

Chapter 5: Magnetic nanoparticles for removal of heavy metals from water A scheme of the whole reactional process is shown in Fig. 7.1.

Synthesis of magnetite (Fe_3O_4 (XXIV)) and silica coated magnetite ($Fe_3O_4@SiO_2$ (XXV)) Magnetite particles were synthesized by precipitation from an aqueous solution of iron(II) sulfate heptahydrate ($FeSO_4 \cdot 7H_2O$) (20 g in 140 mL deionized water previously flushed with N_2), potassium nitrate (KNO_3) and potassium hydroxide (KOH).[4] At 90 °C, a solution of 1.62 g KNO_3 and 11.23 g KOH in 60 mL H_2O was added dropwise for 5 minutes under nitrogen bubbling. The black precipitate was stirred 1 hour at 90 °C and left overnight, and then washed with water by centrifugation or vacuum filtration. The powder is ferrimagnetic and a NdFeB magnet strongly attracts them, as can be seen in Fig. 7.2 (a) and (b).

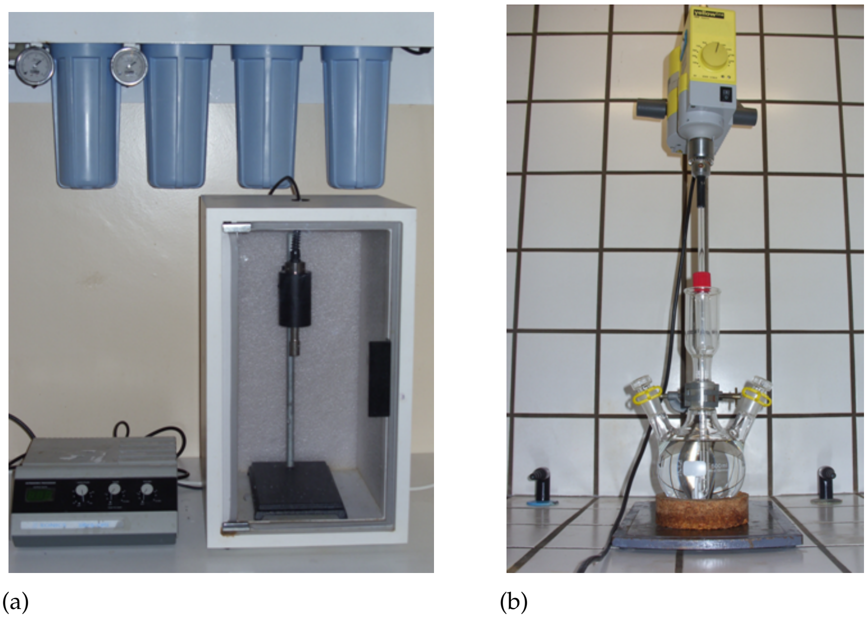

(a) (b)

Figure 7.3.: Experimental details about the magnetite silica coating procedure and the determination of the nanomaterials' efficiency: (a) Sonication horn (Sonic, Vibracell) where was performed the magnetite silica coating; (b) Experimental determination of Hg^{2+} uptake from a solution containing dispersed magnetite functionalized particles under mechanical stirring.

For performing silica coating, as a general rule, it is necessary to control the reaction conditions such as temperature, pH, the method of mixing the reactants, their concentration, and concentration of counterions (if added). The surface of the silica colloid is terminated with silanol groups ($-Si-OH$) which can ionize and generate a negatively charged interface at pH higher than 7. The chemical properties of silica are based on the silanol groups on the surface (they perform strong polar interactivity). These groups can be functionalized through various procedures, since the OH group can react with carboxyl, thiol, and amine groups.

In this case, the Fe_3O_4 nanoparticles were coated with SiO_2 using the alkaline hydrolysis of tetraethyl orthosilicate ($Si(OC_2H_5)_4$; TEOS) with ammonia solution acting as catalyst. Dispersions of Fe_3O_4 nanoparticles (7.5–200 mg) in ethanol (50–150 mL) were prepared and left for 15 min sonication with a sonication horn (Sonics, Vibracell; Fig. 7.3 (a)) in ice bath. Consecutively ammonia solution (28%) (3 to 12 mL) and TEOS (100 to 400 μl) were added and the dispersion was left in ice bath for 2 hours under sonication, as described previously by our group.[5] The quantity of Fe_3O_4 was varied until the reaction conditions were optimized, the ratio ammonia : TEOS being kept to be 30 : 1. Finally, the particles were washed with ethanol and collected. (b).

Synthesis of amine modified silica coated Fe_3O_4 ($Fe_3O_4@SiO_2@HN_2$ (compound XXVI))

The surface amino modification of the silica coated magnetite was performed with hydrolysis and condensation of APTES groups in ethanol at 40 °C. APTES has general formula $H_2N(CH_2)_3Si(OC_2H_5)_3$ and is a bifunctional organosilane molecule. From one side, there

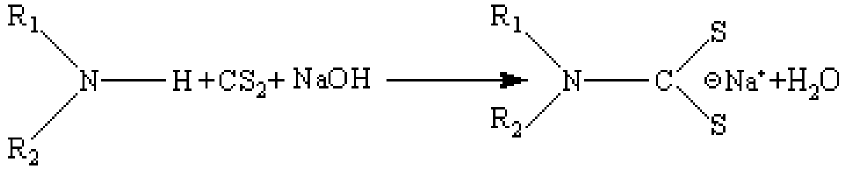

Figure 7.4.: Scheme of general synthesis of DTC's.

is amino group and from another, the $Si(OC_2H_5)$ group by which after hydrolysis of the alkoxy group it can attach to the Si−OH surface. During the reaction, two processes occur: hydrolysis of the three silane alkoxy groups to the silanol species and the condensation of these silanols with the free OH groups of the surface, which results in stable Si−O−Si bonds. Since as a competitive process can occur oligomerization, the products of the reaction depend on temperature, solvent, time, concentrations. Hydrophilic and protic solvents accelerate the hydrolysis and the condensation so that surface modification is promoted, although they can compete with the silane for the surface silanol groups by H− bonding. Study of the above enumerated reactional conditions was done by Bruce and Sen[6] and we have optimized our reactional conditions following the results of the reported work. There were not observed additional products from the two processes, neither from the silica coating. Catalyst was not used since the amino groups of APTES have basic character and could autocatalyze the reaction.

Silica coated magnetite particles were added to 50 mL of APTES, 0.2–2% (w/v), in ethanol. Experiments in tetrahydrofuran (THF) and water, and water/ethanol mixture 1:1 were performed too. The mixture was stirred over three hours with mechanical stirring at 40 °C. The particles were then washed with ethanol and magnetically collected.[6] After the attachment of the APTES molecules to the silica surface, the amino groups stay available for the further DTC grafting.

Grafting of dithiocarbamate (DTC) groups on the amine modified silica coated magnetite (Fe_3O_4@SiO_2@HN@CS_2^- (compound XXVII)) The dithiocarbamate group was grafted in alkaline conditions at room temperature following the procedure, described by Venkatesan *et al.*[7] As was mentioned in Chapter 5, the DTC bidentate ligand form strong complexes with noble metals and transition elements. The general scheme of synthesis of DTC's is shown in the Fig. 7.4. 6.3 mg amine modified silica coated magnetite was added to a reactional mixture containing 20 mL 0.1M NaOH, 4 mL 2–propanol and 0.3 mL CS_2. The dispersion was mechanically stirred for 6 hours. The powder was collected from the yellow-orange solution with centrifugation, and then washed with 2–propanol and dried at room temperature.

Tests for metal ions removal capacity of nanomaterials XXV and XXVII Silica coated magnetite and DTC functionalized particles were tested for their removal capacities of Hg^{2+}. For this purpose two experimental tests were performed, during which the particles were

Table 7.2.: Experimental details of tests for Hg^{2+} uptake capacities of nanomaterials: starting sample weights and time intervals of collections.

	Test 1		Test 2	
Compound	**XXV**	**XXVII**	**XXV**	**XXVII**
Initial quantity [mg]	3	3	3	3
Time intervals of sample collection	30 mins, 1h, 2h, 4h, 6h, 12h, 24h, 48h		48 mins, 1h, 2h, 4h, 6h, 12h, 24h, 48h	

allowed to be in contact with the metal cations for 48 hours in aqueous medium under continuous mechanical stirring (starting weights and time intervals of sample collections can be seen in Table 7.2). During the test of each material, a parallel experiment of stirring of reference blank solution was done, too.

From a standard solution of Hg^{2+} with concentration 1000 ppm were prepared two 500 mL solutions (A and B) of concentration 50 ppm in ultra-pure water. 250 μL of 0.1M NaOH were added to each of them, thus the pH being adjusted to *ca.* 7. 3 mg of silica coated material **XXV** were dispersed in solution A and after 2 mins of sonication the dispersion was left for 48 hours of continuous mechanical stirring, as shown in Fig. 7.3 (b). At the same time, the blank solution B was left under stirring too. After different intervals of time (Table 7.2), 20 mL of dispersion and blank solution were removed. The former was left for about 30 mins for magnetic separation with NdFeB magnet, while the latter was left still for the same time. Before each collection for analysis with atomic fluorescent spectrometer, the syringes for sample extraction, previously washed with 25% HNO_3 and ultra-pure water, were rinsed with 5 mL of dispersion (respectively blank solution). Before the analysis, 20 μL of concentrated HNO_3 were added to the collected solutions. The same procedure was applied for both materials. For each kind of material, the tests were repeated twice with structurally identical samples, synthesized by different reactions.

7.1.3. Synthetic approaches

A very important part of the synthesis of new coordination compounds with 1st row transition metals and lanthanides (Chapters 2 and 3) was the possibility to obtain high quality and air-stable single-crystals. For this purpose different synthetic techniques for single-crystal growth were applied:

- Slow evaporation at room temperature

  Aqueous solutions of the ligands were prepared by dissolving the free acids in slight excess of KOH in the same molar quantity as the ligand (2 parts). The pH was usually adjusted to 6–7 with addition of diluted solution of CH_3COOH, when needed. Eventually, of counter ions were added in equal molar quantity to the ligand. For some compounds $(CH_3)_4NOH$ was added instead KOH, which increases the pH value and acts as a counter ion at the same time. The solutions of the metal salts (0.5 parts) were added in dropwise to the ligands. This mixtures were stirred for 5 to 30 mins and then transferred into semi-covered beakers. If after stirring precipitation was formed, the powder was filtered off with vacuum filtration and then the mother liquor was left for slow evaporation at room temperature. The same procedure was applied in the reactions with bridging ligands, where the aqueous solutions with different quantities of bridging ligands (1, 2 or 3 parts) were added in the end.

- Hydrothermal syntheses

  In a typical synthesis, an aqueous solution of the metal salt (0.5 parts) was added dropwise to an aqueous solution containing 2 parts of ligands ans 2 parts of counterion, and then the final pH was adjusted to *ca.* 7 with 1M CH_3COOH. This mixture was treated under hydrothermal conditions. Syntheses were usually carried out in PTFE-lined stainless steel reaction vessels (*ca.* 40 cm^3) (Fig. 7.5), under autogeneous pressure and static conditions in a preheated oven at T = 100–150 °C for 2 to 5 days for the complexes of 1st row transition metals and for 5 to 7 days at 130–160 °C for the complexes of lanthanides. The vessels were cooled down slowly to ambient temperature before opening.

- Diffusion in gel

  Preparation of single crystals of an appropriate size and stability for single crystal X-ray diffraction studies was carried out also in a gel, formed from $Na_2SiO_3 \cdot H_2O$. A solution of $Na_2SiO_3 \cdot 5\,H_2O$ (0.1 M, 5 mL), was added dropwise to an aqueous solution (10 mL, pH with slight acid value) containing the ligand or mixture of the two ligands (with the bridging one). The mixture was stirred and each test tube, with 5 mL of solution, was left for 24 hours. Afterwards, a solution with 0.25 mmol of metal salt was added to the gel. Single crystals of new complexes were grown over different periods.

Diffusion with solvents, recrystallization or evaporation of solution to half volume were applied in some cases but these methods did not result in single-crystal growth.

The syntheses of same compound by different strategy were reproducible. They resulted in structurally identical microcrystalline powders and/or single crystals. The compounds are air- and light-stable, and usually insoluble in water and common organic solvents (DMSO, ethanol, methanol, acetone, dichloromethane, toluene, and chloroform).

7.2. Characterization techniques

Atomic fluorescent spectrometry Mercury analysis was performed by cold vapour atomic fluorescence spectroscopy (CV-AFS), on a PSA cold vapour generator, model 10.003, associated with a Merlin PSA detector, model 10.023, and using $SnCl_2$ as reducing agent. This analytical methodology is usually a hundred times more sensitive than atomic absorption, allowing the measurement of 1 $ng.L^{-1}$ of mercury.

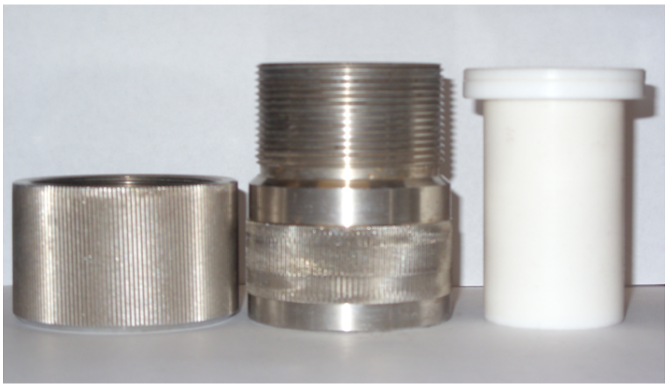

Figure 7.5.: PTFE-lined stainless steel reaction autoclave.

Elemental analysis Elemental analysis for C, H and N was performed in the Microanalysis Laboratory of the University of Aveiro using a CHNS-932 Elemental Analyser; in Chemistry department, University of Cambridge, UK using Exeter analytical CE 440 Elemental analyser with helium as purge gas and in Microanalysis Laboratory of the University of Santiago de Compostela, Spain.

Inducted coupled plasma (ICP) analysis Quantitative determination of Mn (compound **X**), Fe and Si (compounds **XXIV** and **XXV**) was carried out by Jobin Yvon JY 70 Plus ICP spectrometer. *Ca.* 10 mg of each sample were dissolved in 100 ml standard solution prepared with HNO_3 and HCl (HF was added to the solution for the analysis of the Si containing sample).

Infrared and Raman spectroscopy ATR and FT–IR spectra were measured on a Matson 7000 FT–IR spectrometer. FT-Raman spectra were measured on a Bruker RFS 100 with a Nd:YAG coherent laser (λ = 1064 nm). FT–IR spectra were detected from KBr disks (Aldrich, 99%+, FT–IR grade). For the ATR and FT–Raman spectra detection the samples were ground and other special preliminary treatment was not applied.

Magnetic measurements Fundamental importance for characterisation of magnetic properties and electron structure of new synthesized open-shell compounds of transition metals are magnetic measurements. There are various methods for measuring solid phase, such as neutron diffraction, Mössbauer spectroscopy, magnetic circular dichroism, superconducting quantum interference device (SQUID), quantum design physical properties measurement system (PPMS), vibrating sample magnetometer (VSM), electron paramagnetic resonance (EPR) spectroscopy. The SQUID is a mechanism used to measure extremely weak signals using a device called a Josephson junction. It is very powerful technique able to detect a huge change of energy. A Josephson junction is made up of two superconductors, separated by an insulating layer so thin that electrons can pass through. A SQUID consists of tiny loops of superconductors employing Josephson junctions to achieve superposition: each electron moves simultaneously in both directions. Because the current is moving in two opposite directions, the electrons have the ability to perform as qubits. SQUIDs have been used for a variety of testing purposes that demand extreme sensitivity.

In this work, the magnetic measurements were performed using:

Quantum Design SQUID magnetometer MPMS at the Faculty of Sciences, University of Lisbon (compounds **I–IV**);

Quantum Design SQUID magnetometer MPMS at the University of Porto (the compounds **V**, **XVIII**, **XIX–XXII**);

Quantum Design SQUID magnetometer MPMS, Quantum Design PPMS magnetometer and VSM at the Aragon Institute of Nanotechnolgy, University of Saragossa (Spain) (compounds **VII**, **IX–XIV**, **XVI**, **XXIII–XXV**);

VSM at Physics department, University of Aveiro (Portugal) (compound **XVI**);

Mössbauer spectroscopy at University of Coimbra (Portugal) (compounds **XXIV** and **XXV**).

The details about the measurement conditions are shown in Table 7.3.

Optical microscopy Crystal photographs (compounds **XV**; Chapter 3) were taken using a Stemi 2000 stereomicroscope equipped with Carl Zeiss lenses and a high-resolution AxioCam MRc5 digital camera connected to a personal computer.

Powder X-ray diffraction Powder X-ray diffraction patterns were recorded at room temperature using a Philips X'Pert diffractometer, operating with a monochromatic Cu-K_α radiation source at 40 kV and 50 mA. Simulated powder patterns were based on single-crystal data, and calculated using the STOE Win XPOW software package.

The collected powder X-ray diffraction pattern for compound **XVII**, Chapter 3 was indexed by means of the routines provided with the software program DICVOL04.[8] A Le Bail[9] whole-powder-diffraction-pattern profile fitting in the space group $P2_1/c$ (systematic absences unequivocally identified using CHECKCELL[10]) was performed with the FullProf.2k software package. The fit provided as in Fig. 3.2 in Chapter 3 was obtained by using a typical pseudo-Voigt peakshape function and, in the last stages of the fitting process the unit cell parameters and typical profile parameters, such as scale factor, zero shift, Caglioti function values and two asymmetry parameters were allowed to refine. Fixed background points were used. Refined unit cell parameters: a = 12.025(1) Å, b = 13.376(1) Å, c = 8.480(1) Å, β = 96.862(5)° (R_{Bragg} = 1.54% and χ^2 = 6.81).

Single-crystal X-ray Diffraction Data for compounds **I**, **III**, **IV** and **V** from Chapter 2; for compounds **XV** adn **XVI** from Chapter 3; for compounds **XVIII**, **XXI**, **XXII** and **XXIII** from Chapter 4 were collected at 180 K on a Nonius Kappa charge coupled device (CCD) area-detector diffractometer (Mo K_α graphite-monochromated radiation, λ = 0.7107 Å), equipped with an Oxford Cryosystems cryostream and controlled by the Collect software package.[11]

Table 7.3.: Details for the magnetic measurements.

Compound	Measurement	Temperature range, [K]	Applied magnetic field	Magnetometer
Chapter 2				
I	ZFC-FC	2–270	100 Oe	SQUID
II	ZFC-FC	2–270	100 Oe	SQUID
III	ZFC-FC	2–270	100 Oe	SQUID
IV	ZFC-FC	2–270	100 Oe	SQUID
V	ZFC-FC	4–300	100 Oe	SQUID
VII	ZFC-FC	1.8–200	1000 Oe	SQUID
IX	ZFC-FC	1.8–300	1000 Oe	SQUID
	MH	5	-9 to 9 Tesla	PPMS
X	ZFC-FC	1.9–300	1000 Oe	PPMS
	MH	1.9, 5, 15	–9 to 9 Tesla	PPMS
XI	ZFC-FC	1.8–300	1000 Oe	PPMS
XII	ZFC-FC	1.9–300	1000 Oe	PPMS
XIII	ZFC-FC	1.9–300	1000 Oe	PPMS
XIV	ZFC-FC	1.9–300	1000 Oe	PPMS
Chapter 3				
XVI	ZFC-FC	1.9–300	1000 Oe	PPMS
Chapter 4				
XVIII		4–300	100 Oe	SQUID
XIX		4.5–300	20 Oe	SQUID
XX		4.5–300	100 Oe	SQUID
XXI		4.5–300	20 Oe	SQUID
XXII		4.5–300	20 Oe	SQUID
XXIII		1.9–300	1000 Oe	SQUID, PPMS
Chapter 5				
XXIV		293	–1.9 to 1.9 Tesla	VSM
XXV		293	–1.9 to 1.9 Tesla	VSM

Images were processed using the software packages of Denzo and Scalepack,[12] and the data were corrected for absorption by using the empirical method employed in Sortav.[13,14]

Data for compounds **VI**, **VII**, **VIII**, **XII** and **XIV** from Chapter 2 were collected at 150 K (**VI**, **VIII**, **XII**), at 293 K (**VII**) and at 100 K (**XIV**) on a Bruker X8 Kappa CCD APEX II (2006; University of Aveiro, CICECO) diffractometer (Mo K_α graphite-monochromated radiation, λ = 0.7107 Å) (cell refinement: APEX2; data reduction: SAINT-Plus (Bruker, 2005); program(s) used to solve structure: SHELXTL (Bruker 2001); program(s) used to refine structure: SHELXTL; molecular graphics: DIAMOND (Brandenburg, 2006)).

Data for compounds **II** and **XIII** (Chapter 2) were collected at ambient temperature (at the Unidade de Raios-X, RIAIDT, University of Santiago de Compostela, Spain) on a Bruker SMART 1000 CCD area-detector diffractrometer (Mo K_α graphite-monochromated radiation, λ = 0.7107 Å), controlled by the SMART software package.[15] Images were processed using the SAINTPlus software package,[16] and data were corrected for absorption by using the semi-empirical method of SADABS.[17]

Data for compounds **XIX** and **XX** (Chapter 4) were collected at 293 K on a KUMA4CCD diffractrometer (Mo K_α graphite-monochromated radiation, λ = 0.7107 Å), in the scan mode, and controlled by the CrysAlis CCD software package.[18] 960 frames were measured at 1.25 intervals with a counting time of 50s or 36s per frame, for **XIX** and **XX** respectively. Data were corrected for absorption, the Lorentz and polarisation effects, and reduced using the CrysAlis RED software routines.[19] All the structures were solved by the direct methods of SHELXS-97,[20] and refined by full-matrix least squares on F2 using SHELXL-97.[21]

Cambridge structural database survey The Cambridge structural database (CSD) (Version 5.25, November 2003) contains structural data for 298097 organic and organometallic compounds, providing a valuable research tool to create electronic libraries of structural knowledge (e.g. geometrical aspects of coordination environments), and the ability to investigate the probability of occurrence of individual supramolecular motifs (e.g. hydrogen bonding and close contacts patterns).

Searches to collect the intended structural information (bond distances, number of hits, refcodes, bibliographic information and data collection details) were performed using the graphical interface ConQuest. It is important to note that the vast majority of the available crystal data in the database were collected at ambient temperature (72% of the structures were collected above 270 K). Thus, the statistical bond lengths forthcoming from the CSD searches are, in general, slightly longer than those obtained from diffraction data collected at lower temperatures. In this comparative work is assumed that these differences are very small.

Photoluminescence The luminescence spectra were recorded at room temperature with a modular double grating excitation spectrofluorimeter with TRIAX 320 emission monochromator (fluorolog-3, Jobin Yvon-Spex) coupled to a R928 Hamamatsu photomultiplier by means of the front face acquisition mode. The excitation source was a 450 W Xe arc lamp. Excitation spectra were corrected from λ = 240 to 600 nm for the spectral distribution of the lamp intensity using a photodiode reference detector. Emission spectra were also corrected for the spectral response of the monochromators and the detector by using typical correction spectra provided by the manufacturer. The lifetime measurements were acquired with the setup described for the luminescence spectra using a pulsed Xe−Hg lamp (6 μs pulse at half width and 20–30 μs tail).

Specific surface area The specific surface area of the particles was determined with nitrogen adsorption BET measurements performed with a Gemini Micromeritics instrument.

Scanning electron microscopy and Energy dispersive analysis of X-rays spectroscopy SEM and EDS (compounds **XV** and **XXI–XXVII**) were performed using a Hitachi S–4100 field emission gun tungsten filament instrument working at 25 kV. The samples reported in Chapters 3 and 4 were prepared by crystals' deposition on double-stick adhesive carbon tape mounted on aluminium sample holders and by carbon coating. The nanoparticles (dispersed in ethanol) were deposited over a glass plate (in case when EDS was not performed) and over carbon tape (when EDS was performed) and after drying were coated with carbon. EDS was performed for the confirmation of the presence of Fe and Si in the composition of the compounds **XXV**, **XXVI** and **XXVII**.

Transmission electron microscopy TEM, electron diffraction and EDS (compounds **XXIV**, **XXV**) were carried out using a Hitachi H-9000-NA microscope operating at 300 kV. The nanoparticles were dispersed in ethanol and a drop was deposited on carbon-coated copper grid. After the evaporation of the solvent, the microscopy was performed. EDS technique was used to confirm the presence of Fe and Si in the composition of materials **XXIV** and **XXV**.

Thermoanalytical measurements Thermogravimetric analyses (TGA) were carried out using a Shimadzu TGA-50, with different heating rates (10 or 20 °C/min) under continuous flow of air.

References

1. Shi FN, Paz FAA, Girginova P, Rocha J, Amaral VS, Klinowski J and Trindade T, *J. Mol. Struct.* 789(1-3) (2006), 200–208.
2. Shi FN, Paz FAA, Girginova PI, Mafra L, Amaral VS, Rocha J, Makal A, Wozniak K, Klinowski J and Trindade T, *J. Mol. Struct.* 754(1-3) (2005), 51–60.
3. Shi FN, Paz FAA, Girginova PI, Amaral VS, Rocha J, Klinowski J and Trindade T, *Inorg. Chim. Acta* 359(4) (2006), 1147–1158.
4. Schwertmann U and Cornell RM, Iron oxides in the laboratory. Preparation and characterization, VCH, 1991.
5. Neves MC, Liz-Marzan LM and Trindade T, *J. Colloid Interface Sci.* 264(2) (2003), 391–395.
6. Bruce IJ and Sen T, *Langmuir* 21(15) (2005), 7029–7035.
7. Venkatesan KA, Srinivasan TG and Rao PRV, *Colloids Surf., A* 180(3) (2001), 277–284.
8. Boultif A and Louër D, *J. Appl. Crystallogr.* 37 (2004), 724–731.
9. Lebail A, Duroy H and Fourquet JL, *Mater. Res. Bull.* 23(3) (1988), 447–452.
10. Laugier J and Bochu B, «CHECKCELL SOFTWARE P - A Software Performing Automatic Cell/Space Group Determination», Collaborative Computational Project Number 14 (CCP14), Laboratoire des Matériaux et du Génie Physique de l'Ecole Supérieure de Physique de Grenoble (INPG), France, 2000, matériaux et du Génie udareniata.
11. Hooft R, «Collect: Data Collection Software», Delft, The Netherlands, Nonius B. V., 1998.
12. Otwinowski Z and Minor W, Processing of X-ray diffraction data collected in oscillation mode, vol. 276 of *Methods in Enzymology*, 1st ed., Academic Press Inc, New York, 1997.
13. Blessing RH, *Acta Crystallogr., Sect. A: Found. Crystallogr.* 51 (1995), 33–38.
14. Blessing RH, *J. Appl. Crystallogr.* 30(4) (1997), 421–426.
15. «smart. Bruker Molecular Analysis Research Tool V. 5.054© Bruker AXS», Madison, WI, USA, 1997.
16. «saintPlus. Data Reduction and Correction Program V. 6.01© Bruker AXS», Madison, WI, USA, 1997.
17. Sheldrick GM, «SADABS, Bruker/Siemens Area Detector Empirical Absorption Correction Program Bruker AXS», Madison, WI, USA, 1998.
18. «KUMA CRYSTALIS CCD, Kuma Diffraction», Wroclaw, Poland, 1999.
19. «KUMA CRYSTALIS RED, Kuma Diffraction», Wroclaw, Poland, 1999.
20. Sheldrick GM, «SHELXS 97 PROGRAM CR, Program for Crystal Structure Solution», University of Göttingen, Germany, 1997.
21. Sheldrick GM, «SHELXS 97 PROGRAM CR, Program for Crystal Structure Refinement», University of Göttingen, Germany, 1997.

APPENDICES

Appendix A.

Physical constants, units and conversion

		SI system	*cgs emu* system
β	Bohr magneton	$9.27401549.10^{-24}$ J.T^{-1}	$9.27401549.10^{-21}$ erg.T^{-1}
k_B	Boltzman constant	$1.3806580.10^{-23}$ J.K^{-1}	$1.3806580.10^{-16}$ erg.K^{-1}
N	number of Avogadro	$6.022.10^{23}$ mol^{-1}	
g_e	factor for free electron	2.0023	

1 emu = 1 erg/Gauss = 10^{-3} JT^{-1}

1 Gauss = 10^{-4} Tesla

Oe = Gauss

1 K = 0.695038770 cm^{-1}

Appendix B.

Magnetic definitions and units

Basic definitions in the magnetism are magnetic field — H, magnetization — M, and magnetic induction, B. Standard practice is the use more often of the *cgs emu* (cgs: centimetre, gram, second) system than the international system (SI). However, many equations are different for the two systems. It means that some constants have units in one system but are equal to unity or are dimensionless in the other system. The units of the most important electromagnetic parameters are summarized in Table B.1 and some useful basic relations in magnetism are shown in Table B.2 .

Table B.1.: Electromagnetic parameters (A = Ampere, cm = centimetre, emu = electromagnetic unit, g = gram, m = meter, H = Henry).

Magnetic term	Symbol	SI unit	*cgs emu* units	Conversion factor
Magnetic induction	B	Tesla (T)	Gauss (G)	1 T = 10^4 G
Magnetic field	H	A/m	Oersted (Oe)	1 A/m = $\frac{4\pi}{10^3}$ Oe
Magnetization	M	A/m	emu/cm^3	1 A/m = 10^{-3} emu/cm^3
Mass magnetization	σ	Am^2/kg	emu/g	1 Am^2/kg = 1 emu/g
Molar magnetization	M_{mol}	Am^2/mol	emu/mol	1Am^2/mol = 10^3 emu/mol
Magnetic moment	μ	Am^2	emu, erg/G	1 Am^2, J/T = 10^3emu
Volume susceptibility	κ,χ	dimensionless	dimensionless, emu/cm^3	4π (SI) = 1 (cgs)
Mass susceptibility	χ_ρ	m^3/kg	emu/Oe.g	1 m^3/kg = $\frac{10^3}{4\pi}$ emu/Oe.g
Molar susceptibility	χ_{mol}	m^3/mol	cm^3/mol, emu/mol	1m^3/mol = $\frac{10^6}{4\pi}$ emu/mol

Continued on next page

Magnetic term	Symbol	SI unit	*cgs emu* units	Conversion factor
Permeability of free space	μ_0	H/m	dimensionless	$4\pi \times 10^{-7}$ H/m = 1 (cgs)
Volume energy density	W	J/m^3	erg/cm^3	1J/m^3 = 1×10 erg/cm^3

Explained in the frame of SI units, magnetism is due to the response of elementary current loops* of radius r and current i to the applied magnetic field, which tends to orientate their associated magnetic moments in its direction (Fig. B.1). A magnetic field with intensity H will be produced at the centre of the loop. It is proportional to the area A and the flowing current i:

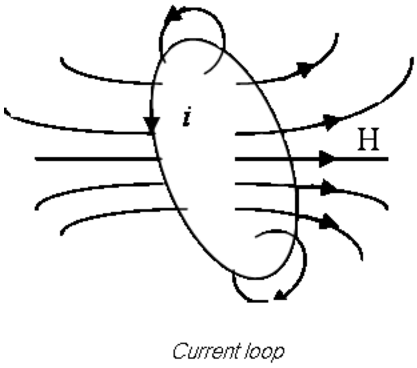

Figure B.1.: The magnetic dipole moment μ due to a current loop.

$$H = i/2r\,[A/m] \tag{B.1}$$

A magnetic moment $\mu^{\dagger}$ is associated with the current loop:

$$\mu = i \times Area\,\left[Am^2\right] \tag{B.2}$$

The intensity of magnetization M is magnetic moment per unit volume V:

$$M = \mu/V\,[A/m] \tag{B.3}$$

M and H have the same units. The magnetic moment per unit mass σ is:

$$\sigma = \mu/mass\,\left[Am^2/kg\right] \tag{B.4}$$

---

[*] In classical physics the model for the source of an atomic or molecular magnetic dipole is the current loop.

[†] In some literature is denote *m*; μ being preferred from chemists.

Table B.2.: Basic relationships in magnetism[1].

Quantity	SI units	CGS and EMU units
Magnetic induction	$\vec{B} = \mu_0 \left(\vec{H} + \vec{M}\right)$ $\vec{B} = \mu\vec{H}$	$\vec{B} = \vec{H} + 4\pi\vec{M}$ $\vec{B} = \mu\vec{H}$
Permeability	$\mu_r = \mu/\mu_0 = 1 + \chi$	$\mu = 1 + 4\pi\chi$
Volume magnetization	$\vec{M} = \vec{m}/V$	$\vec{M} = \vec{m}/V$
Volume susceptibility	$\chi = \partial\vec{M}/\partial\vec{H}$	$\chi = \partial\vec{M}/\partial\vec{H}$
Volume energy density	$W = \left(\vec{B}.\vec{H}\right)/2$	$W = \left(\vec{B}.\vec{H}\right)/8\pi$

[1] Ref. Kahn O, Molecular magnetism, Wiley—VCH, 1993.

The ratio of magnetization to magnetic field gives another quantity, called susceptibility.

$$\chi = M/H \tag{B.5}$$

It characterises the way in which an applied magnetic field H interacts with the angular momentum associated with the thermally populated state. In other words susceptibility is a measure of how magnetisable can become a substance in the presence of magnetic field and it can be used in a general way to describe various classes of magnetic materials. Mean susceptibility is expressed by:

$$\bar{\chi} = M/H = \mu_0 H/B \tag{B.6}$$

The quantity μ_0 relates the magnetic induction B to H and is called magnetic permeability. The mass susceptibility is expressed in Equation B.7 and the molar susceptibility — in Equation B.8, M_{mol} being the molar mass.

$$\chi_\rho = \chi/\rho \tag{B.7}$$

$$\chi_{mol} = \chi_\rho \times M_{mol} = \chi \times M_{mol}/\rho \tag{B.8}$$

In principle χ is the algebraic sum of two contributions associated with different phenomena, where χ^D and χ^P represent the diamagnetic and paramagnetic susceptibilities.

$$\chi = \chi^D + \chi^P \tag{B.9}$$

The former is negative and the latter — positive. When χ^D dominates, the sample is diamagnetic. When χ^P is the leading contribution, the sample is paramagnetic.

Appendix C.

Crystal and structure refinement data

Table C.1.: Crystal and structure refinement data for complexes of 3–hydroxypicolinic acid (**I–IV**).

	I	**II**	**III**	**IV**
Formula	$C_{12}H_{12}CoN_2O_8$	$C_{22}H_{24}CoN_4O_{10}$	$C_{12}H_8CuN_2O_6$	$C_{84}H_{88}Cu_3N_{14}O_{26}$
Formula weight	371.17	565.40	339.74	1900.30
Crystal system	Monoclinic	Monoclinic	Monoclinic	Triclinic
Space group	$P2_1/c$	$P2_1/n$	$P2_1/c$	P_i
a [Å]	11.491(2)	8.2794(20)	6.3355(13)	11.806(2)
b [Å]	9.1413(18)	12.8360(32)	11.405(2)	13.415(3)
c [Å]	6.8357(14)	23.5421(57)	8.0088(16)	15.060(3)
α (degrees (°))	90	90	90	115.16(3)
β (degrees (°))	91.84(3)	97.021(4)	92.64(3)	94.80(3)
γ (degrees (°))	90	90	90	97.33(3)
Volume (Å^3)	717.7(2)	2483.2(11)	578.1(2)	2115.7(7)
Z	2	4	2	1
D_c (g/cm^{-3})	1.718	1.512	1.952	1.491
F(0 0 0)	378	1172	342	985
Crystal size (mm)	0.35×0.23×0.18	0.36×0.20×0.15	0.18×0.12×0.10	0.32×0.14×0.05
Crystal type	brown blocks	orange prisms	brown blocks	brown blocks
Θ Range (°)	3.55 to 27.49	3.57 to 26.42	3.57 to 27.47	3.52 to 26.37
Index ranges	$-14 \leq h \leq 14$, $-11 \leq k \leq 11$, $-8 \leq l \leq 8$	$-10 \leq h \leq 10$ $-11 \leq k \leq 16$ $0 \leq l \leq 29$	$-8 \leq h \leq 8$, $-14 \leq k \leq 14$, $-8 \leq l \leq 10$	$-14 \leq h \leq 14$ $-16 \leq k \leq 16$ $-18 \leq l \leq 18$
Reflections collected	5621	21304	3443	18.847
Independent reflections	1638 ($R_{int} = 0.0407$)	5075 ($R_{int} = 0.0555$)	1315 ($R_{int} = 0.0284$)	8605 ($R_{int} = 0.0640$)
Final R indices $[I > 2\sigma(I)]$	$R_1 = 0.0277$, $wR_2 = 0.0711$	$R_1 = 0.00383$, $wR_2 = 0.0905$	$R_1 = 0.0280$ $wR_2 = 0.0731$	$R_1 = 0.0606$ $wR_2 = 0.1247$
Final R indices (all data)	$R_1 = 0.0347$, $wR_2 = 0.0736$	$R_1 = 0.0775$, $wR_2 = 0.1127$	$R_1 = 0.0373$ $wR_2 = 0.0778$	$R_1 = 0.1038$ $wR_2 = 0.1456$
Largest diff. peak and hole (eÅ^{-3})	0.354 and -0.614	0.389 and -0.490	0.283 and -0.436	1.003 and -0.488

Table C.2.: Crystal and structure refinement data for complexes of 3–hydroxypicolinic acid (V) and of 2–hydroxynicotinic acid (**VI–VIII**).

	V	**VI**	**VII**	**VIII**
Formula	$C_{12}H_{12}N_2NiO_8$	$C_{24}H_{26}MnN_4O_{16}$	$C_{12}H_{12}N_2NiO_8$	$C_{12}H_{12}MnN_2O_8$
Formula weight	370.95	681.43	370.95	367.17
Crystal system	Monoclinic	Monoclinic	Monoclinic	Monoclinic
Space group	$P2/n$	C 2/c	P 2_1/c	P 2_1/c
a [Å]	5.1212(10)	12.8238(5)	7.4248(4)	7.5735(8)
b [Å]	22.631(5)	7.4024(3)	12.2252(7)	12.5295(13)
c [Å]	6.6038(13)	28.3481(12)	7.5220(4)	7.6466(8)
α (degrees (°))	90	90	90	90
β (degrees (°))	110.52(3)	97.141(2)	100.27(0)	101.279(1)
γ (degrees (°))	90	90	90	90
Volume (Å^3)	716.8(3)	2670.12(19)	671.82(25)	711.588
Z	2	4	2	2
D_c (g/cm^{-3})	1.719	1.695	1.83364	1.714
F(0 0 0)	380	1404	380	
Crystal size (mm)	0.23×0.21×0.07	0.14×0.12×0.10	0.05×0.11×0.12	374
Crystal type	green needles	yellow needles	green needles	yellow needles
Θ Range (°)	3.75 to 27.50	3.58 to 27.48	3.92 to 27.48	3.84 to 27.48
Index ranges	$-6\leq h \leq 6$, $-26\leq k \leq 29$, $-8\leq l \leq 8$	$-16\leq h \leq 15$, $-9\leq k \leq 9$, $-34\leq l \leq$	$-8\leq h \leq 9$, $-15\leq k \leq 15$, $-9\leq l \leq 9$	$-9\leq h \leq 9$, $-16\leq k \leq 13$, $-9\leq l \leq 9$
Reflections collected	4043	23914	17206	9087
Independent reflections	1637 (R_{int} = 0.0365)	3072 (R_{int} =0.0384)	1525 (R_{int} =0.0329)	1557 (R_{int} =0.0244)
Final R indices $[I > 2\sigma(I)]$	R_1 = 0.0368, wR_2 = 0.0819	R_1 =0.0666, wR_2 =0.1392	R_1 =0.0287, wR_2 =0.0751	R_1 =0.0312, wR_2 =0.0859
Final R indices (all data)	R_1 = 0.0542, wR_2 = 0.0896	R_1 =0.0702, wR_2 =0.1403	R_1 =0.0347, wR_2 =0.0781	R_1 =0.0343 wR_2 =0.0876
Largest diff. peak and hole (eÅ^{-3})	0.299 and –0.360	1.027 and –0.592	1.067 and –0.340	0.886 and –0.282

Table C.3.: Crystal and structure refinement data for complexes of 2–mercaptonicotinic acid (**XII–XIV**).

	XII	**XIII**	**XIV**
Formula	$C_{60}H_{42}N_{10}NiO_{10}S_4$	$C_{24}H_{15}CoN_4O_4S_2$	$C_{48}H_{35}MnN_8O_{11}S_2$
Formula weight	1249.99	546.45	1018.9
Crystal system	Monoclinic	Monoclinic	Triclinic
Space group	$C2/c$	$P2_1/n$	$P\overline{1}$
a [Å]	27.0803(10)	10.262(2)	8.9637(2)
b [Å]	11.6951(4)	7.9900(16)	16.0986(4)
c [Å]	20.6337(8)	27.357(6)	16.3882(5)
α (degrees, °)	90	90	67.5
β (degrees, °)	123.5830(10)	94.77(3)	79.5
γ (degrees, °)	90	90	84.64(0)
Volume (Å^3)	5444.1(3)	2235.3(8)	2147.63(96)
Z	4	4	2
D_c (g/cm^3)	1.525	1.624	1.57552
F(0 0 0)	2576	1112	1048
Crystal size (mm)	0.32×0.16×0.12	0.20×0.16×0.06	0.26×0.24×0.16
Crystal type	light yellow needles	brown blocks	yellow needles
Θ Range (°)	3.52 to 27.48	3.63 to 24.78	3.52 to 27.48
Index ranges	$-34\leq h \leq 35$ $-15\leq k \leq 12$ $-26\leq l \leq 26$	$-12\leq h \leq 12$, $-9\leq k \leq 9$, $-32\leq l \leq 32$	$-11\leq h \leq 11$ $-20\leq k \leq 20$ $-20\leq l \leq 21$
Reflections collected	55128	15973	30175
Independent reflections	6176 (R_{int} =0.0308)	3817 (R_{int} =0.0672)	9705 (R_{int} =0.0319)
Final R indices $[I > 2\sigma(I)]$	R_1 =0.0287, wR_2 =0.0630	R_1 =0.0437 wR_2 =0.0914	R_1 =0.0408 wR_2 =0.1034
Final R indices (all data)	R_1 =0.0406, wR_2 =0.0675	R_1 =0.0980 wR_2 =0.1152	R_1 =0.0570 wR_2 =0.1156
Largest diff. peak and hole (eÅ^{-3})	0.300 and –0.351	0.347 and –0.332	0.588 and –0.581

Table C.4.: Crystal and structure refinement data for $[Sm(glu)(pic)(H_2O)_2]$ (**XV**).

	$[Sm(glu)(pic)(H_2O)_2]$
Formula	$C_{11}H_{14}NO_8Sm$
Formula weight	438.58
Crystal system	Monoclinic
Space group	$P2_1/c$
a[Å]	11.855(2)
b[Å]	13.477(3)
c[Å]	8.4804(17)
β (degrees (°))	92.42(3)
Volume [Å^3]	1346.4(5)
Z	4
D_c (g/cm^{-3})	2.164
F(0 0 0)	852
Crystal size (mm)	0.07×0.05×0.02
Crystal type	colourless blocks
Θ Range	3.78 to 27.51
Index ranges	$-15 \leq h \leq 15$, $-17 \leq k \leq 16$, $-10 \leq l \leq 10$
Reflections collected	13389
Independent reflections	3076 ($R_{int} = 0.0630$)
Final R indices $[I > 2\sigma(I)]^{a,b}$	$R_1 = 0.0307$ $wR_2 = 0.0660$
Final R indices (all data)^{a,b}	$R_1 = 0.0409$ $wR_2 = 0.0705$
Weighting scheme^c	m = 0.0247 n = 3.7121
Largest diff. peak and hole (eÅ^{-3})	0.892 and -0.949

[a] $R_1 = \sum \| F_0 | - | F_c \| / \sum |F_0|$. [b] $wR_2 = \sqrt{\sum \left[w \left(F_0^2 \right)^2 \right] / \sum \left[w \left(F_0^2 \right)^2 \right]}$. [c] $w = 1/ \left[\sigma^2 \left(F_0^2 \right) + (mP) + nP \right]$, where $P = \left(F_0^2 + 2F_c^2 \right) / 3$.

Table C.5.: Crystal and structure refinement data for for complexes of N–(phosphonomethyl) iminodiacetic acid (**XVIII–XX**).

	XVIII	**XIX**	**XX**
Formula	$C_5H_{12}FeNO_9P$	$C_{18}H_{38}Co_3N_6O_{22}P_2$	$C_{18}H_{38}Ni_3N_6O_{22}P_2$
Formula weight	316.98	929.27	928.61
Crystal system	Monoclinic	Triclinic	Triclinic
Space group	$P2_1/c$	$P-1$	$P-1$
a [Å]	6.4542(13)	7.0480(14)	6.9600(14)
b [Å]	26.148(5)	10.674(2)	10.680(2)
c [Å]	6.3246(13)	12.234(2)	12.140(2)
α (degrees (°))	90	71.18(3)	71.13(3)
β (degrees (°))	100.49(3)	79.85(3)	80.95(3)
γ (degrees (°))	90	72.86(3)	72.86(3)
Volume (Å^3)	1049.5(4)	829.1(3)	814.1(3)
Z	4	2	2
D_c (g/cm^{-3})	2.006	1.861	1.894
F(0 0 0)	648	475	478
Crystal size (mm)	0.07×0.05×0.05	0.25×0.07×0.04	0.26×0.09×0.09
Crystal type	brown blocks	orange needles	green needles
Θ Range	3.57 to 26.36	3.53 to 20.82	3.56 to 26.02
Index ranges	$-7 \leq h \leq 8$, $-32 \leq k \leq 32$, $-7 \leq l \leq 7$	$-7 \leq h \leq 7$, $-10 \leq k \leq 10$, $-12 \leq l \leq 12$	$-8 \leq h \leq 8$ $-13 \leq k \leq 13$ $-14 \leq l \leq 14$
Reflections collected	6059	8338	13123
Independent reflections	2123 ($R_{int} = 0.0626$)	1720 ($R_{int} = 0.0727$)	3199 ($R_{int} = 0.0438$)
Final R indices $[I > 2\sigma(I)]$	$R_1 = 0.0356$, $wR_2 = 0.0776$	$R_1 = 0.0410$, $wR_2 = 0.0752$	$R_1 = 0.0305$, $wR_2 = 0.0654$
Final R indices (all data)	$R_1 = 0.0583$, $wR_2 = 0.0838$	$R_1 = 0.0671$, $wR_2 = 0.0838$	$R_1 = 0.0447$, $wR_2 = 0.0695$
Largest diff. peak and hole (eÅ^{-3})	0.572 and –0.764	0.788 and –0.423	0.712 and –0.364

Table C.6.: Crystal and structure refinement data for complexes of N–(phosphonomethyl) iminodiacetic acid (**XXI–XXIII**).

	XXI	**XXII**	**XXIII**
Formula	$C_{40}H_{54}MnN_8O_{24}P_2V_2$	$C_{40}H_{54}CoN_8O_{24}P_2V_2$	$C_{40}H_{49}Cu_5N_8O_{20.5}P_2$
Formula weight	1249.67	1253.66	1353.90
Crystal system	Monoclinic	Monoclinic	Triclinic
Space group	$P2/c$	$P2/c$	$P-1$
a [Å]	10.821(2)	10.797(2)	10.286(2)
b [Å]	11.576(2)	11.371(2)	13.638(3)
c [Å]	20.641(4)	20.680(4)	19.051(4)
α (degrees (°))	90	90	79.87(3)
β (degrees (°))	101.96(3)	102.04(3)	76.03(3)
γ (degrees (°))	90	90	84.15(3)
Volume (Å^3)	2529.2(9)	2482.9(9)	2548.1(10)
Z	2	2	1
D_c (g/cm^{-3})	1.641	1.677	1.759
F(0 0 0)	1286	1290	1368
Crystal size (mm)	0.18×0.14×0.14	0.23×0.12×0.12	0.23×0.12×0.10
Crystal type	green blocks	green blocks	brown blocks
Θ Range	3.52 to 27.46	3.51 to 27.48	3.55 to 25.35
Index ranges	–14≤ h ≤ 14, –15≤ k ≤ 15, –26≤ l ≤ 26	–14≤ h ≤ 14 –14≤ k ≤ 14 –26≤ l ≤ 26	–12≤ h ≤ 12, –16≤ k ≤ 16, –22≤ l ≤ 22
Reflections collected	19352	24613	25963
Independent reflections	5770 (R_{int} = 0.0410)	5684 (R_{int} = 0.0472)	9277 (R_{int} = 0.0366)
Final R indices [$I > 2\sigma(I)$]	R_1 = 0.0404, wR_2 = 0.0920	R_1 = 0.0389, wR_2 = 0.0907	R_1 = 0.0652, wR_2 = 0.1553
Final R indices (all data)	R_1 = 0.0605, wR_2 = 0.1026	R_1 = 0.0578, wR_2 = 0.0995	R_1 = 0.0782, wR_2 = 0.1653
Largest diff. peak and hole (eÅ^{-3})	0.523 and –0.583	0.893 and –0.638	1.530 and –1.761

Appendix D.

Bond lengths and angles

Table D.1.: Bond lengths (in Å) and angles the complexes with ambidentate aromatic ligands (**I–XIV**).

Bond lengths[a]		***Bond angles***	
Compound [Co(picOH)$_2$(H$_2$O)$_2$] (**I**)			
Co(1)—O(1W)	2.0789(13)	O(1W)—Co(1)—O(1)	93.07(5)
Co(1)—O(1)	2.1105(12)	O(1W)—Co(1)—O(1)$^{\mathrm{i}}$	86.93(5)
Co(1)—N(1)	2.1245(15)	O(1W)—Co(1)—N(1)	89.15(6)
	Bond angles		
O(1W)—Co(1)—N(1)$^{\mathrm{i}}$	90.85(6)	O(1)—Co(1)—N(1)	78.23(5)
O(1)—Co(1)—N(1)$^{\mathrm{i}}$	101.77(5)		
Compound *mer*−[N(CH$_3$)$_4$][Co(picOH)$_3$] · H$_2$O (**II**)			
Co(1)—O(1)	2.077(2)	O(1)—Co(1)—O(7)	97.70(8)
Co(1)—O(4)	2.066(2)	O(4)—Co(1)—N(3)	98.16(9)
Co(1)—O(7)	2.078(2)	O(1)—Co(1)—N(1)	78.45(8)
Co(1)—N(1)	2.134(2)	O(7)—Co(1)—N(1)	87.93(8)
Co(1)—N(2)	2.149(2)	O(1)—Co(1)—N(2)	90.52(9)
Co(1)—N(3)	2.144(2)	O(7)—Co(1)—N(2)	171.45(9)
	Bond angles		
O(1)—Co(1)—N(3)	93.91(9)	O(7)—Co(1)—N(3)	78.93(8)
O(4)—Co(1)—O(1)	164.80(8)	N(1)—Co(1)—N(2)	96.08(9)
O(4)—Co(1)—O(7)	93.67(8)	N(1)—Co(1)—N(3)	163.84(9)
O(4)—Co(1)—N(1)	91.98(9)	N(3)—Co(1)—N(2)	98.22(9)
O(4)—Co(1)—N(2)	78.68(9)		
Compound [Cu(picOH)$_2$] (**III**)			
Cu(1)—O(1)	1.9541(15)	O(1)—Cu(1)—N(1)	83.96(6)
Cu(1)—N(1)	1.9680(16)	O(1)—Cu(1)—N(1)$^{\mathrm{i}}$	96.04(6)
Compound [Cu(picOH)$_2$(BPE)]$_2$ · [Cu(picOH)$_2$(BPE)$_2$] · 8 H$_2$O (**IV**)			

Continued on next page

---

[a] Symmetry transformations used to generate equivalent atoms: **I**: (i) $-x$, $2-y$, $-z$; **II**: —; **III**: (i) $-1+x$, $-1/2-y$, $1/2+z$; **IV**: (i) $1-x$, $2-y$, $1-z$; (ii) $-x$,$-y$, $-z$; (iii) $1-x$, $2-y$, $2-z$; **V**: (i) $1-x$, $-y$, $-z$; **VI**: (i) $-x$, y, $0.5-z$; **VII**: (i) $2-x$, $-y$, $-z$; **VIII**: (i) $-x$, $-y$, $-z$; **XII**: (i) $-x$, y, $0.5-z$.

Bond lengths[a]		*Bond angles*	
Polymer III			
Cu(1)—O(1)	2.298(3)	N(1)—Cu(1)—O(1)	77.98(12)
Cu(1)—N(1)	2.014(3)	N(1)—Cu(1)—O(1)^{i}	102.02(12)
Cu(1)—N(2)	2.046(3)	N(1)—Cu(1)—N(2)	89.20(13)
		N(1)—Cu(1)—N(2)^{i}	90.80(13)
		N(2)—Cu(1)—O(1)	90.38(11)
		N(2)—Cu(1)—O(1)^{i}	89.62(11)
Polymer IV			
Cu(2)—O(4)	2.280(3)	N(3)—Cu(2)—O(4)	78.04(13)
Cu(2)—N(3)	2.035(4)	N(3)—Cu(2)—O(4)^{ii}	101.96(13)
Cu(2)—N(4)	2.034(3)	N(4)—Cu(2)—O(4)	89.99(12)
		N(4)—Cu(2)—O(4)^{ii}	90.01(12)
		N(4)—Cu(2)—N(3)	90.43(13)
		N(4)—Cu(2)—N(3)^{ii}	89.57(13)
Complex			
Cu(3)—O(7)	2.254(3)	N(5)—Cu(3)—O(7)	79.58(12)
Cu(3)—N(5)	1.998(3)	N(5)—Cu(3)—O(7)^{iii}	100.42(12)
Cu(3)—N(6)	2.079(3)	N(5)—Cu(3)—O(6)	90.35(14)
		N(5)—Cu(3)—N(6)^{iii}	89.65(14)
		N(6)—Cu(3)—O(7)	88.38(12)
		N(6)—Cu(3)—O(7)^{iii}	91.62(12)

Compound Ni(picOH)$_2$(H$_2$O)$_2$ (**V**)

Ni(1)—N(1)^{i}	2.062(2)	N(1)^{i}—Ni(1)—N(1)	180.00(13)
Ni(1)—N(1)	2.062(2)	N(1)^{i}—Ni(1)—O(1)	99.42(7)
Ni(1)—O(1)	2.0654(18)	N(1)—Ni(1)—O(1)	80.58(7)
Ni(1)—O(1)^{i}	2.0654(18)	N(1)^{i}—Ni(1)—O(1)^{i}	80.58(7)
Ni(1)—O(1W)^{i}	2.073(2)	N(1)—Ni(1)—O(1)^{i}	99.42(7)
Ni(1)—O(1W)	2.073(2)	O(1)—Ni(1)—O(1)^{i}	180.00(12)
O(1W)—H(1A)	0.936(10)	N(1)^{i}—Ni(1)—O(1W)^{i}	87.70(8)
O(1W)—H(1B)	0.932(10)	N(1)—Ni(1)—O(1W)^{i}	92.30(8)
	Bond angles		
O(1)—Ni(1)—O(1W)^{i}	89.50(7)	O(1)^{i}—Ni(1)—O(1W)^{i}	90.50(7)
N(1)^{i}—Ni(1)—O(1W)	92.30(8)	N(1)—Ni(1)—O(1W)	87.70(8)
O(1)—Ni(1)—O(1W)	90.50(7)	O(1)^{i}—Ni(1)—O(1W)	89.50(7)
O(1)^{i}—Ni(1)—O(1W)	180.00(14)		

Continued on next page

---

[a] Symmetry transformations used to generate equivalent atoms: **I**: (i) $-x$, $2-y$, $-z$; **II**: —; **III**: (i) $-1+x$, $-1/2-y$, $1/2+z$; **IV**: (i) $1-x$, $2-y$, $1-z$; (ii) $-x$,$-y$, $-z$; (iii) $1-x$, $2-y$, $2-z$; **V**: (i) $1-x$, $-y$, $-z$; **VI**: (i) $-x$, y, $0.5-z$; **VII**: (i) $2-x$, $-y$, $-z$; **VIII**: (i) $-x$, $-y$, $-z$; **XII**: (i) $-x$, y, $0.5-z$.

Bond lengths[a]		*Bond angles*	

Compound $[Mn(H_2nicO)_2(H_2O)_2](H_2nicO)_2 \cdot 2\,H_2O$ (**VI**)

Mn(1)—O(2)^{i}	2.126(3)	O(2)^{i}—Mn(1)—O(2)	94.96(15)
Mn(1)—O(2)	2.126(3)	O(2)^{i}—Mn(1)—O(1)	95.76(10)
Mn(1)—O(1)	2.141(2)	O(2)—Mn(1)—O(1)	82.46(9)
Mn(1)—O(1)^{i}	2.141(2)	O(2)^{i}—Mn(1)—O(1)^{i}	82.46(9)
Mn(1)—O(1W)^{i}	2.215(3)	O(2)—Mn(1)—O(1)^{i}	95.76(10)
Mn(1)—O(1W)	2.215(3)	O(1)—Mn(1)—O(1)^{i}	177.39(15)
	Bond angles		
O(2)—Mn(1)—O(1W)^{i}	88.55(10)	O(2)^{i}—Mn(1)—O(1W)^{i}	168.40(9)
O(1)—Mn(1)—O(1W)^{i}	95.66(10)	O(1)^{i}—Mn(1)—O(1W)^{i}	86.19(10)
O(2)^{i}—Mn(1)—O(1W)	88.55(10)	O(2)—Mn(1)—O(1W)	168.40(9)
O(1)—Mn(1)—O(1W)	86.19(10)	O(1)^{i}—Mn(1)—O(1W)	95.66(10)
O(1W)^{i}—Mn(1)—O(1W)	90.18(15)	O(1)^{i}—Mn(1)—O(1W)	95.66(10)
Mn(1)—O(1W)—H(1W)	117.00(3)	Mn(1)—O(1W)—H(2W)	133.00(3)

Compound $Ni[HnicO]_2[H_2O]_2$ (**VII**)

Ni(1)—O(3)	2.0737(14)	O(3)—Ni(1)—O(3)^{i}	180.000
Ni(1)—O(1)	1.9868(14)	O(1)—Ni(1)—O(3)^{i}	89.05(6)
Ni(1)—O(1W)	2.0704(15)	O(1)—Ni(1)—O(3)	89.05(6)
	Bond angles		
O(1W)—Ni(1)—O(3)	92.90(6)	O(1)^{i}—Ni(1)—O(3)	90.95(6)
O(1)—Ni(1)—O(1W)	87.35(6)	O(1)—Ni(1)—O(1W)^{i}	92.65(6)
O(1W)—Ni(1)—O(3)^{i}	87.10(6)	O(1W)^{i}—Ni(1)—O(1W)	180.00(2)

Compound $Mn[HnicO]_2[H_2O]_2$ (**VIII**)

Mn(1)—O(2)	2.0787(13)	O(2)—Mn(1)—O(2)^{i}	180.000
Mn(1)—O(3)^{i}	2.1967(13)	O(2)—Mn(1)—O(3)^{i}	83.700(49)
Mn(1)—O(4W)	2.1951(15)	O(2)^{i}—Mn(1)—O(3)^{i}	96.300(49)
	Bond angles		
O(4W)—Mn(1)—O(3)^{i}	87.243(53)	O(4W)—Mn(1)—O(2)	92.130(55)
O(4W)—Mn(1)—O(4W)^{i}	180.000(55)	O(2)—Mn(1)—O(4W)^{i}	87.870(55)

Compound $[Ni(phen)_3](H_2nic_2S_2)_2 \cdot 2\,H_2O$ (**XII**)

Ni(1)—N(1)	2.1028(12)	N(2)—Ni(1)—N(2)^{i}	172.54(7)

Continued on next page

---

[a] Symmetry transformations used to generate equivalent atoms: **I**: (i) $-x$, $2-y$, $-z$; **II**: —; **III**: (i) $-1+x$, $-1/2-y$, $1/2+z$; **IV**: (i) $1-x$, $2-y$, $1-z$; (ii) $-x$,$-y$, $-z$; (iii) $1-x$, $2-y$, $2-z$; **V**: (i) $1-x$, $-y$, $-z$; **VI**: (i) $-x$, y, $0.5-z$; **VII**: (i) $2-x$, $-y$, $-z$; **VIII**: (i) $-x$, $-y$, $-z$; **XII**: (i) $-x$, y, $0.5-z$.

Bond lengths[a]		***Bond angles***	
Ni(1)—N(2)	2.0675(12)	N(2)—Ni(1)—N(3)	90.50(5)
Ni(1)—N(3)	2.0904(12)	N(2)—Ni(1)—N(3)$^{\mathrm{i}}$	95.24(5)
S(1)—S(2)	2.0537(5)	N(3)—Ni(1)—N(3)$^{\mathrm{i}}$	79.48(7)
	Bond angles		
N(2)—Ni(1)—N(1)	79.84(5)	N(3)—Ni(1)—N(1)	95.70(5)
N(2)—Ni(1)—N(1)$^{\mathrm{i}}$	94.83(5)	N(3)—Ni(1)—N(1)$^{\mathrm{i}}$	173.14(5)
C(21)—S(1)—S(2)	102.45(5)	C(27)—S(2)—S(1)	102.01(5)
N(1)—Ni(1)—N(1)$^{\mathrm{i}}$	89.51(7)		

Compound [Co(phen)(HnicS)(nicS)] (**XIII**)

Co(1)—N(2)	1.900(3)	N(2)—Co(1)—N(1)	92.07(14)
Co(1)—N(1)	1.908(4)	N(2)—Co(1)—N(3)	168.02(15)
Co(1)—N(3)	1.943(3)	N(1)—Co(1)—N(3)	94.16(15)
Co(1)—N(4)	1.950(4)	N(2)—Co(1)—N(4)	91.66(15)
Co(1)—S(1)	2.2844(13)	N(1)—Co(1)—N(4)	171.53(15)
Co(1)—S(2)	2.2939(13)	N(3)—Co(1)—N(4)	83.58(16)
	Bond angles		
N(2)—Co(1)—S(1)	98.06(10)	N(1)—Co(1)—S(1)	72.79(11)
N(3)—Co(1)—S(1)	93.56(11)	N(4)—Co(1)—S(1)	99.15(12)
N(2)—Co(1)—S(2)	72.65(10)	N(1)—Co(1)—S(2)	96.5(1)
N(3)—Co(1)—S(2)	96.45(11)	N(4)—Co(1)—S(2)	91.87(12)
S(1)—Co(1)—S(2)	165.87(5)		

Compound $[\mathrm{Mn(phen)_2(C_{12}H_7N_2O_5)](C_{12}H_8N_2O_4S_2)\cdot 2\,H_2O}$ (**XIV**)

Mn(1)—O(1)	2.1722(15)	O(2)—Mn(1)—O(1)	80.91(6)
Mn(1)—O(2)	2.0854(15)	O(2)—Mn(1)—N(3)	136.81(7)
Mn(1)—N(1)	2.3041(19)	O(1)—Mn(1)—N(3)	80.65(6)
Mn(1)—N(2)	2.2728(18)	O(2)—Mn(1)—N(2)	118.16(6)
Mn(1)—N(3)	2.2329(19)	O(1)—Mn(1)—N(2)	83.25(6)
Mn(1)—N(4)	2.2909(18)	N(3)—Mn(1)—N(2)	97.91(7)
S(1)—S(2)	2.0343(8)	O(2)—Mn(1)—N(4)	82.38(6)
N(5)—C(35)	1.446(3)	O(1)—Mn(1)—N(4)	118.76(6)
O(1)—C(28)	1.252(3)	N(3)—Mn(1)—N(4)	73.08(7)
	Bond angles		
N(2)—Mn(1)—N(4)	153.27(7)	O(2)—Mn(1)—N(1)	104.06(6)
O(1)—Mn(1)—N(1)	154.68(6)	N(3)—Mn(1)—N(1)	109.19(7)
N(2)—Mn(1)—N(1)	72.46(7)	N(4)—Mn(1)—N(1)	86.56(7)

Continued on next page

---

[a] Symmetry transformations used to generate equivalent atoms: **I**: (i) $-x$, $2-y$, $-z$; **II**: —; **III**: (i) $-1+x$, $-1/2-y$, $1/2+z$; **IV**: (i) $1-x$, $2-y$, $1-z$; (ii) $-x$,$-y$, $-z$; (iii) $1-x$, $2-y$, $2-z$; **V**: (i) $1-x$, $-y$, $-z$; **VI**: (i) $-x$, y, $0.5-z$; **VII**: (i) $2-x$, $-y$, $-z$; **VIII**: (i) $-x$, $-y$, $-z$; **XII**: (i) $-x$, y, $0.5-z$.

Bond lengths[a]		***Bond angles***	
N(6)—C(35)—N(5)	113.20(18)	C(41)—S(1)—S(2)	103.85(8)
C(47)—S(2)—S(1)	102.18(8)		

---

[a] Symmetry transformations used to generate equivalent atoms: **I**: (i) $-x$, $2-y$, $-z$; **II**: —; **III**: (i) $-1+x$, $-1/2-y$, $1/2+z$; **IV**: (i) $1-x$, $2-y$, $1-z$; (ii) $-x$,$-y$, $-z$; (iii) $1-x$, $2-y$, $2-z$; **V**: (i) $1-x$, $-y$, $-z$; **VI**: (i) $-x$, y, $0.5-z$; **VII**: (i) $2-x$, $-y$, $-z$; **VIII**: (i) $-x$, $-y$, $-z$; **XII**: (i) $-x$, y, $0.5-z$.

Table D.2.: Selected bond lengths (in Å) and angles (in °) for the Sm^{3+} coordination environment present in [Sm(glu)(pic)(H_2O)$_2$] (**XV**)[a].

[Sm(glu)(pic)(H_2O)$_2$]

Bond lengths		*Bond angles*	
Sm(1)—O(1)	2.355(3)	O(1)—Sm(1)—O(3)	141.54(10)
Sm(1)—O(6)^{ii}	2.508(3)	O(4)^{i}—Sm(1)—O(1W)	74.40(10)
Sm(1)—O(3)	2.452(3)	O(1)—Sm(1)—O(4)^{i}	90.50(10)
Sm(1)—O(1W)	2.407(3)	O(4)^{i}—Sm(1)—O(2W)	155.34(11)
Sm(1)—O(4)^{i}	2.358(3)	O(1)—Sm(1)—O(5)^{ii}	140.99(10)
Sm(1)—O(2W)	2.410(3)	O(5)^{ii}—Sm(1)—O(6)^{ii}	52.33(9)
Sm(1)—O(5)^{ii}	2.461(3)	O(1)—Sm(1)—O(6)^{ii}	120.16(10)
Sm(1)—N(1)	2.624(3)	O(5)^{ii}—Sm(1)—N(1)	76.10(10)
	Bond angles		
O(1)—Sm(1)—N(1)	64.97(10)	O(6)^{ii}—Sm(1)—N(1)	81.25(11)
O(1)—Sm(1)—O(1W)	77.48(10)	O(1W)—Sm(1)—O(3)	77.89(11)
O(1)—Sm(1)—O(2W)	72.55(10)	O(1W)—Sm(1)—O(5)^{ii}	131.92(10)
O(3)—Sm(1)—O(5)^{ii}	76.61(10)	O(1W)—Sm(1)—O(6)^{ii}	146.77(10)
O(3)—Sm(1)—O(6)^{ii}	71.56(10)	O(1W)—Sm(1)—O(2W)	84.31(11)
O(3)—Sm(1)—N(1)	149.60(11)	O(1W)—Sm(1)—-N(1)	131.30(11)
O(4)^{i}—Sm(1)—O(3)	110.58(10)	O(2W)—Sm(1)—O(3)	76.03(10)
O(4)^{i}—Sm(1)—O(5)^{ii}	77.47(10)	O(2W)—Sm(1)—O(5)^{ii}	126.89(10)
O(4)^{i}—Sm(1)—O(6)^{ii}	128.57(10)	O(2W)—Sm(1)—O(6)^{ii}	76.05(10)
O(4)—Sm(1)—N(1)	76.04(11)	O(2W)—Sm(1)—N(1)	110.80(11)

[a] Symmetry transformations used to generate equivalent atoms: (i) $2-x, 1-y, -z$; (ii) $2-x, 1-y, 1-z$.

Table D.3.: Bond lengths (in Å) and angles (in °) for compounds of H_4pmida (**XVIII–XXIII**).

Compound [Fe(H_2pmida)(H_2O)$_2$] (**XVIII**)

Bond lengths[a]		***Bond angles***	
Fe(1)—O(1W)	2.115(2)	O(1W)—Fe(1)—0(2W)	90.33(9)
Fe(1)—O(2W)	2.131(2)	O(1W)—Fe(1)—O(1)	89.84(9)
Fe(1)—O(1)	2.117(2)	O(1W)—Fe(1)—O(4)	95.46(9)
Fe(1)—O(2)$^{\mathrm{i}}$	2.051(2)	O(1W)—Fe(1)—N(1)	167.21(9)
Fe(1)—O(4)	2.182(2)	O(2W)—Fe(1)—O(4)	172.36(8)
Fe(1)—N(1)	1.311(2)	O(2W)—Fe(1)—N(1)	100.68(9)
P(1)—O(1)	1.519(2)	O(1)—Fe(1)—O(2W)	91.12(9)
P(1)—O(2)	1.493(2)	O(1)—Fe(1)—O(4)	93.86(9)
P(1)—O(3)	1.572(2)	O(1)—Fe(1)—N(1)	83.51(9)
C(3)—O(4)	1.257(4)	O(2)$^{\mathrm{i}}$—Fe(1)—O(1W)	96.36(1)
C(3)—O(5)	1.273(4)	O(2)$^{\mathrm{i}}$—Fe(1)—O(2W)	89.81(1)
C(5)—O(6)	1.211(4)	O(2)$^{\mathrm{i}}$—Fe(1)—O(1)	173.73(8)
C(5)—O(7)	1.334(4)	O(2)$^{\mathrm{i}}$—Fe(1)—O(4)	84.61(9)
	Bond angles		
O(2)$^{\mathrm{i}}$—Fe(1)—N(1)	90.23(9)	O(1)—P(1)—C(1)	105.43(2)
O(4)—Fe(1)—N(1)	74.19(8)	O(1)—P(1)—O(3)	106.10(2)
O(2)—P(1)—C(1)	108.13(2)	P(1)—O(1)—Fe(1)	115.95(2)
O(2)—P(1)—O(1)	116.43(2)	P(2)—O(2)—Fe(1)$^{\mathrm{ii}}$	152.81(2)
O(2)—P(1)—O(3)	112.15(2)	O(3)—P(1)—C(1)	108.15(2)

Compound [Co(pyr)(H_2O)$_4$][Co_2(Hpmida)$_2$(pyr)(H_2O)$_2$] · 2 (H_2O) (**XIX**)

Bond lengths[a]		***Bond angles***	
Co(1)—O(1)	2.076(4)	O(1)—Co(1)—N(1)	87.16(2)
Co(1)—O(4)	2.060(4)	O(1)—Co(1)—N(2)	95.0(2)
Co(1)—N(6)	2.052(4)	O(1)—Co(1)—O(1W)	86.23(2)
Co(1)—O(1W)	2.136(5)	O(4)—Co(1)—O(1)	93.57(2)
Co(1)—N(1)	2.159(5)	O(4)—Co(1)—O(1W)	178.64(2)
Co(1)—N(2)	2.087(5)	O(4)—Co(1)—N(1)	81.88(2)
Co(2)—O(2W)	2.074(5)	O(4)—Co(1)—N(2)	92.17(2)
Co(2)—O(3W)	2.049(4)	O(6)—Co(1)—O(1)	165.23(2)
Co(2)—N(3)	2.143(5)	O(6)—Co(1)—O(4)	93.13(2)
	Bond angles		
O(6)—Co(1)—O(1W)	87.38(2)	O(2W)—Co(2)—N(3)	93.6(2)
O(6)—Co(1)—N(1)	80.77(2)	O(2W)—Co(2)—N(3)$^{\mathrm{i}}$	86.4(2)
O(6)—Co(1)—N(2)	97.9(2)	O(3W)—Co(2)—O(2W)	90.49(2)

Continued on next page

---

[a] Symmetry transformations used to generate equivalent atoms: **XVIII**: (i) $x, y, 1+z$; (ii) $x, y, -1+z$; **XIX**: $1-x, -y, -z$; **XX**: $1-x, -y, 2-z$; **XXI** and **XXII**: (i) $x, -1+y, -z$; (ii) $2-x, 1-y, 2-z$; (iii) $1-x, y, 1/2-z$; **XXIII**: (i) $-1+x, y, z$.

Bond lengths[a]		***Bond angles***	
O(1W)—Co(1)—N(1)	99.45(2)	O(3W)—Co(2)—O(2W)$^{\mathrm{i}}$	89.51(2)
N(2)—Co(1)—N(1)	173.8(2)	O(3W)—Co(2)—N(3)	89.9(2)
N(2)—Co(1)—O(1W)	86.51(2)	O(3W)—Co(2)—N(3)$^{\mathrm{i}}$	90.1(2)

Compound $[\mathrm{Ni(pyr)(H_2O)_4}][\mathrm{Ni_2(Hpmida)_2(pyr)(H_2O)_2}]\cdot 2\,(\mathrm{H_2O})$ (**XX**)

Ni(1)—O(1)	2.065(2)	O(1)—Ni(1)—N(1)	88.39(8)
Ni(1)—O(4)	2.044(2)	O(1)—Ni(1)—O(1W)	87.11(9)
Ni(1)—N(6)	2.027(2)	O(4)—Ni(1)—O(1)	92.05(9)
Ni(1)—O(1W)	2.110(2)	O(4)—Ni(1)—O(1W)	177.82(8)
Ni(1)—N(1)	2.089(2)	O(4)—Ni(1)—N(1)	83.21(8)
Ni(1)—N(2)	2.033(2)	O(6)—Ni(1)—O(1)	168.66(7)
Ni(2)—O(2W)	2.039(2)	O(6)—Ni(1)—O(4)	92.34(9)
Ni(2)—O(3W)	2.038(2)	O(6)—Ni(1)—N(1)	81.76(8)
Ni(2)—N(3)	2.094(2)	O(6)—Ni(1)—N(2)	96.19(9)
Bond angles			
O(6)—Ni(1)—O(1W)	88.85(8)	O(2W)—Ni(2)—N(3)	92.94(10)
Ni(1)—Ni(1)—O(1W)	98.77(9)	O(2W)—Ni(2)—N(3)$^{\mathrm{i}}$	87.06(10)
N(2)—Ni(1)—O(1)	94.16(9)	O(3W)—Ni(2)—O(2W)	89.79(9)
N(2)—Ni(1)—O(4)	91.10(9)	O(3W)—Ni(2)—O(2W)$^{\mathrm{i}}$	90.21(9)
N(2)—Ni(1)—O(1W)	86.95(9)	O(3W)—Ni(2)—N(3)	89.23(9)
N(2)—Ni(1)—N(1)	173.85(8)	O(3W)—Ni(2)—N(3)$^{\mathrm{i}}$	90.77(9)

Compound $(4,4'\text{−bpyH})_2[\mathrm{Mn}(4,4'\text{−bpy})(\mathrm{H_2O})_4][\mathrm{V_2O_2(pmida)_2}]\cdot 2\,\mathrm{H_2O}$ (**XXI**)

M(1)—O(1W)	2.177(2)	O(1W)—M(1)—O(1W)$^{\mathrm{iii}}$	175.15(1)
M(1)—O(2W)	2.176(2)	O(1W)—M(1)—N(2)	92.43(5)
M(1)—N(2)	2.230(3)	O(1W)—M(1)—N(3)$^{\mathrm{i}}$	87.57(5)
M(1)—N(3)$^{\mathrm{i}}$	2.250(3)	O(2W)—M(1)—O(1W)	88.94(7)
V(1)—O(1)	1.598(2)	O(2W)—M(1)—O(1W)$^{\mathrm{iii}}$	91.14(7)
V(1)—O(2)	1.972(2)	O(2W)—M(1)—O(2W)$^{\mathrm{iii}}$	178.03(1)
V(1)—O(3)$^{\mathrm{ii}}$	1.996(2)	O(2W)—M(1)—N(2)	89.01(5)
V(1)—O(5)	2.028(2)	O(2W)—M(1)—N(3)$^{\mathrm{i}}$	90.99(5)
V(1)—O(7)	2.035(2)	N(2)—M(1)—N(3)$^{\mathrm{i}}$	180.0
V(1)—N(1)	2.391(2)	O(1)—V(1)—O(2)	104.72(9)
Bond angles			
O(1)—V(1)—O(3)$^{\mathrm{ii}}$	99.08(9)	O(1)—V(1)—O(5)	103.37(9)
O(1)—V(1)—O(7)	95.18(10)	O(1)—V(1)—N(1)	170.21(9)
O(2)—V(1)—O(3)$^{\mathrm{ii}}$	90.31(7)	O(2)—V(1)—O(5)	151.84(7)

Continued on next page

---

[a] Symmetry transformations used to generate equivalent atoms: **XVIII**: (i) $x, y, 1+z$; (ii) $x, y, -1+z$; **XIX**: $1-x, -y, -z$; **XX**: $1-x, -y, 2-z$; **XXI** and **XXII**: (i) $x, -1+y, -z$; (ii) $2-x, 1-y, 2-z$; (iii) $1-x, y, 1/2-z$; **XXIII**: (i) $-1+x, y, z$.

Bond lengths[a]		***Bond angles***	
O(2)—V(1)—O(7)	87.24(7)	O(2)—V(1)—N(1)	78.71(7)
O(3)$^{\text{ii}}$—V(1)—O(5)	87.19(7)	O(3)$^{\text{ii}}$—V(1)—O(7)	165.69(8)
O(3)$^{\text{ii}}$—V(1)—N(1)	90.00(8)	O(5)—V(1)—O(7)	88.33(8)
O(5)—V(1)—N(1)	73.25(7)	O(7)—V(1)—N(1)	75.69(8)

Compound $(4,4'\text{−bpyH})_2[\text{Co}(4,4'\text{−bpy})(\text{H}_2\text{O})_4][\text{V}_2\text{O}_2(\text{pmida})_2]\cdot 2\,\text{H}_2\text{O}$ (**XXII**)

M(1)—O(1W)	2.104(2)	O(1W)—M(1)—O(1W)$^{\text{iii}}$	176.07(1)
M(1)—O(2W)	2.094(2)	O(1W)—M(1)—N(2)	91.97(5)
M(1)—N(2)	2.127(3)	O(1W)—M(1)—N(3)$^{\text{i}}$	88.03(5)
M(1)—N(3)$^{\text{i}}$	2.141(3)	O(2W)—M(1)—O(1W)	89.31(7)
V(1)—O(1)	1.602(2)	O(2W)—M(1)—O(1W)$^{\text{iii}}$	90.79(7)
V(1)—O(2)	1.970(2)	O(2W)—M(1)—O(2W)$^{\text{iii}}$	177.21(9)
V(1)—O(3)$^{\text{ii}}$	1.998(2)	O(2W)—M(1)—N(2)	88.60(5)
V(1)—O(5)	2.026(2)	O(2W)—M(1)—N(3)$^{\text{i}}$	91.40(5)
V(1)—O(7)	2.036(2)	N(2)—M(1)—N(3)$^{\text{i}}$	180.0
V(1)—N(1)	2.393(2)	O(1)—V(1)—O(2)	104.65(8)
		Bond angles	
O(1)—V(1)—O(3)$^{\text{ii}}$	99.17(9)	O(1)—V(1)—O(5)	103.50(8)
O(1)—V(1)—O(7)	95.44(9)	O(1)—V(1)—N(1)	170.36(9)
O(2)—V(1)—O(3)$^{\text{ii}}$	90.35(7)	O(2)—V(1)—O(5)	151.81(7)
O(2)—V(1)—O(7)	87.26(7)	O(2)—V(1)—N(1)	78.75(7)
O(3)$^{\text{ii}}$—V(1)—O(5)	86.62(7)	O(3)$^{\text{ii}}$—V(1)—O(7)	165.32(7)
O(3)$^{\text{ii}}$—V(1)—N(1)	89.76(7)	O(5)—V(1)—O(7)	88.66(7)
O(5)—V(1)—N(1)	73.23(7)	O(7)—V(1)—N(1)	75.57(7)

Compound $[\text{Cu}_5(\text{pmida})_2(4,4'\text{−bpy})_3]\cdot 6.5\text{H}_2\text{O}$ (**XXIII**)

Cu(1)—N(1)	1.998(6)	N(1)—Cu(1)—O(1)	89.3(2)
Cu(1)—O(1)	2.098(4)	N(1)—Cu(1)—O(4)	81.7(3)
Cu(1)—O(4)	2.065(7)	N(1)—Cu(1)—O(6)	83.1(2)
Cu(1)—O(6)	2.003(6)	N(1)—Cu(1)—O(10)	173.0(3)
Cu(1)—O(10)	1.914(6)	O(1)—Cu(1)—O(4)	109.5(2)
Cu(2)—O(3)	1.879(4)	O(1)—Cu(1)—O(6)	120.1(2)
Cu(2)—N(2)	2.026(6)	O(1)—Cu(1)—O(10)	97.5(2)
Cu(2)—O(8)	2.280(6)	O(4)—Cu(1)—O(6)	127.6(2)
Cu(2)—O(11)	1.974(5)	O(4)—Cu(1)—O(10)	94.3(3)
Cu(2)—O(13)	1.981(4)	O(6)—Cu(1)—O(10)	95.0(3)
Cu(3)—O(2)	2.252(4)	O(3)—Cu(2)—N(2)	168.9(3)

Continued on next page

---

[a] Symmetry transformations used to generate equivalent atoms: **XVIII**: (i) $x, y, 1+z$; (ii) $x, y, -1+z$; **XIX**: $1-x, -y, -z$; **XX**: $1-x, -y, 2-z$; **XXI** and **XXII**: (i) $x, -1+y, -z$; (ii) $2-x, 1-y, 2-z$; (iii) $1-x, y, 1/2-z$; **XXIII**: (i) $-1+x, y, z$.

Bond lengths[a]		***Bond angles***	
Cu(3)—O(13)	2.319(4)	O(3)—Cu(2)—O(8)	105.9(2)
Cu(3)—N(3)	1.939(6)	O(3)—Cu(2)—O(11)	92.8(2)
Cu(3)—N(5)	1.941(5)	O(3)—Cu(2)—O(13)	95.6(2)
Cu(4)—O(2)	2.152(4)	N(2)—Cu(2)—O(8)	85.1(3)
Cu(4)—N(7)	1.921(5)	N(2)—Cu(2)—O(11)	84.3(3)
Cu(4)—N(4)	1.922(5)	N(2)—Cu(2)—O(13)	82.4(3)
Cu(5)—O(12)	2.280(4)	O(8)—Cu(2)—O(11)	97.6(2)
Cu(5)—N(6)	1.917(6)	O(8)—Cu(2)—O(13)	105.5(2)
Cu(5)—O(12)	2.584(4)	O(11)—Cu(2)—O(13)	152.2(2)
Cu(5)—N(8)	1.923(6)	O(3)—Cu(2)—N(2)	168.9(3)
Cu(1)—Cu(1)$^{\mathrm{i}}$	12.723	O(2)—Cu(3)—O(13)	90.5(1)
Cu(2)—Cu(2)$^{\mathrm{i}}$	11.933	O(2)—Cu(3)—N(3)	104.6(2)
Cu(3)—Cu(3)$^{\mathrm{i}}$	12.593	O(2)—Cu(3)—N(5)	100.9(2)
Cu(4)—Cu(4)$^{\mathrm{i}}$	14.363	O(13)—Cu(3)—N(3)	100.1(2)
Cu(5)—Cu(5)$^{\mathrm{i}}$	17.936	O(13)—Cu(3)—N(5)	100.5(2)
Cu(1)—Cu(2)	5.502	N(3)—Cu(3)—N(5)	146.8(2)
Cu(1)—Cu(3)	6.437	O(2)—Cu(4)—N(7)	107.2(2)
Cu(1)—Cu(4)	5.372	O(2)—Cu(4)—N(4)	103.9(2)
Cu(1)—Cu(5)	6.500	N(7)—Cu(4)—N(4)	148.9(2)
Cu(2)—Cu(3)	3.846	O(12)—Cu(5)—N(6)	101.3(2)
Cu(2)—Cu(4)	5.702	O(12)—Cu(5)—O(12)	83.1(1)
Cu(2)—Cu(5)	4.997	O(12)—Cu(5)—N(8)	92.1(2)
Cu(3)—Cu(4)	3.014	N(6)—Cu(5)—O(12)	96.4(2)
Cu(3)—Cu(5)	8.698	N(6)—Cu(5)—N(8)	165.4(2)
Cu(4)—Cu(5)	9.838	O(12)—Cu(5)—N(8)	91.0(2)
		Bond angles	
Cu5 O12 Cu5	96.9(1)	Cu2 O13 Cu3	126.7(2)
Cu3 O2 Cu4	86.4(1)		

---

[a] Symmetry transformations used to generate equivalent atoms: **XVIII**: (i) $x, y, 1+z$; (ii) $x, y, -1+z$; **XIX**: $1-x, -y, -z$; **XX**: $1-x, -y, 2-z$; **XXI** and **XXII**: (i) $x, -1+y, -z$; (ii) $2-x, 1-y, 2-z$; (iii) $1-x, y, 1/2-z$; **XXIII**: (i) $-1+x, y, z$.

Appendix E.

Hydrogen-bonding geometry and angles

Table E.1.: Hydrogen-bonding geometry (distances in Å and angles in °) for compounds of ambidentate aromatic ligands (**I–XIV**).

D—H···A[a]	***d*(D···A)**	**<(DHA)**
Compound **I**		
O(1W)—H(1A)···O(2)$^{\mathrm{i}}$	1.799(19)	167(2)
O(1W)—H(1B)···O(1)$^{\mathrm{ii}}$	1.841(10)	168(2)
O(3)—H(3)···O(2)	1.83	146
Compound **II**		
O(3)—H(4A)···O(2)	2.577(3)	145.3
O(6)—H(6A)···O(5)	2.540(3)	147.2
O(9)—H(9)···O(8)	2.547(3)	145.5
O(1W)—H(1A)···O(1)	2.822(3)	172(3)
O(1W)—H(1B)···O(8)$^{\mathrm{i}}$	2.766(3)	169(4)
Compound **III**		
O(3)—H(3)···O(2)	2.602(2)	146.2
C(4)—H(4)···O(1)$^{\mathrm{i}}$	3.288(2)	148.7
O(5)—H(5)···O(2)$^{\mathrm{i}}$	3.311(3)	144.0
Compound **IV**		
O(3)—H(3A)···O(2)	2.530(3)	147
O(6)—H(6A)···O(5)	2.508(3)	146
O(9)—H(9A)···O(8)	2.532(3)	147
O(1W)···O(2)	2.754(3)	—
C(1W)···O(2W)$^{\mathrm{i}}$	2.775(3)	—
O(2W)···O(5)	2.794(3)	—

Continued on next page

---

[a] Symmetry transformations used to generate equivalent atoms: **I**: (i) $x, 1.5-y, 1/2+z$; (ii) $-x, 1/2+y, 1/2-z$; **II**: (i) x, 1.5–y, 1/2+z; **III**: (i) -1+x, -(1/2)-y, (1/2)+z; **IV**: (i) $1+x, 1+y, z$; (ii) $-1+x, y, -1+z$; (iii) $x, -1+y, z$; (iv) $1-x, 1-y, -z$; (v) $x, y, 1+z$; **V**: (i) $-x+1, -y, -z$; (ii) $-x, -y, -z$; **VI**: (i) $-x+0.5, y-0.5, -z+0.5$; (ii) $-x+0.5, y+0.5, -z+0.5$; (iii) $x+0.5, y-0.5, z$; **VII**: (i) $-x+1, -y, -z$; (ii) $-x+2, y-1/2, -z+1/2$, (iii) $x, -y+1/2, z+1/2$; **VIII**: (i) $x, -y+3/2, z+1/2$; (ii) $-x, y-1/2, -z+1/2$; (iii) $-x+1, -y+1, -z$; **XII**: (i) $x, y-1, z$; (ii) $x, y+1, z$; **XIII**: (i) $x-1, y-1, z$; **XIV**: (i) $-x+1, -y, -z+1$; (ii) $-x+1, -y+1, z+1$; (iii) $x+1, y-1, z+1$.

D—H$\cdots$A^{a}	***d*(D$\cdots$A)**	**<(DHA)**
O(2W)$\cdots$O(4W)$^{\mathrm{ii}}$	2.776(3)	—
O(3W)$\cdots$O(1W)$^{\mathrm{iii}}$	2.860(3)	—
O(3W)$\cdots$O(1W)$^{\mathrm{iv}}$	2.697(3)	—
C(4W)$\cdots$O(8)	2.938(3)	—
O(4W)$\cdots$O(3W)$^{\mathrm{v}}$	2.756(3)	—

Compound **V**

O(1W)—H(1A)$\cdots$O(1)$^{\mathrm{i}}$	2.718(3)	158(3)
O(1W)—H(1B)$\cdots$O(2)$^{\mathrm{ii}}$	2.707(3)	161(3)
O(3)—H(3)$\cdots$O(2)	2.570(3)	146(1)

Compound **VI**

O(1W)—H(2W)$\cdots$O(2W)$^{\mathrm{i}}$	2.794(4)	176.(4)
O(1W)—H(1W)$\cdots$O(4)$^{\mathrm{ii}}$	2.745(4)	173.(4)
O(2W)—H(3W)$\cdots$O(1)	2.787(4)	164.(4)
O(2W)—H(4W)$\cdots$O(2)$^{\mathrm{iii}}$	2.764(4)	162.(4)
O(5)—H(6)$\cdots$O(4)	2.572(4)	155.(5)
N(1)—H(1)$\cdots$O(3)$^{\mathrm{iii}}$	2.694(4)	154.(4)
N(2)—H(2)$\cdots$O(2W)$^{\mathrm{iii}}$	2.793(4)	153.(4)

Compound **VII**

N(1)—H(1)$\cdots$O(3)$^{\mathrm{i}}$	2.891(2)	171(3)
O(1W)—H(2W)$\cdots$O(2)$^{\mathrm{ii}}$	2.697(2)	170(2)
O(1W)—H(1W)$\cdots$O(2)$^{\mathrm{iii}}$	2.776(2)	165(2)

Compound **VIII**

O(1W)—H(1W)$\cdots$O(2)$^{\mathrm{i}}$	2.687(2)	173(2)
O(1W)—H(2W)$\cdots$O(2)$^{\mathrm{ii}}$	2.762(2)	166(2)
N(1)—H(1)$\cdots$O(3)$^{\mathrm{iii}}$	2.886(2)	168(2)

Compound **XII**

Continued on next page

---

[a] Symmetry transformations used to generate equivalent atoms: **I**: (i) $x, 1.5 - y, 1/2 + z$; (ii) $-x, 1/2 + y, 1/2 - z$; **II**: (i) x, 1.5–y, 1/2+z; **III**: (i) -1+x, -(1/2)-y, (1/2)+z; **IV**: (i) $1 + x, 1 + y, z$; (ii) $-1 + x, y, -1 + z$; (iii) $x, -1 + y, z$; (iv) $1 - x, 1 - y, -z$; (v) $x, y, 1 + z$; **V**: (i) $-x + 1, -y, -z$; (ii) $-x, -y, -z$; **VI**: (i) $-x + 0.5, y - 0.5, -z + 0.5$; (ii) $-x + 0.5, y + 0.5, -z + 0.5$; (iii) $x + 0.5, y - 0.5, z$; **VII**: (i) $-x + 1, -y, -z$; (ii) $-x + 2, y - 1/2, -z + 1/2$, (iii) $x, -y + 1/2, z + 1/2$; **VIII**: (i) $x, -y + 3/2, z + 1/2$; (ii) $-x, y - 1/2, -z + 1/2$; (iii) $-x + 1, -y + 1, -z$; **XII**: (i) $x, y - 1, z$; (ii) $x, y + 1, z$; **XIII**: (i) $x - 1, y - 1, z$; **XIV**: (i) $-x + 1, -y, -z + 1$; (ii) $-x + 1, -y + 1, z + 1$; (iii) $x + 1, y - 1, z + 1$.

D—H$\cdots$A^a	***d*(D$\cdots$A)**	**<(DHA)**
O(1W)—H(1W)$\cdots$O(3)	2.8032(17)	177(2)
O(1W)—H(2W)$\cdots$O(2)$^{\mathrm{i}}$	2.9242(17)	151.3(19)
O(1)—H(4)$\cdots$O(4)$^{\mathrm{ii}}$	2.4524(16)	167.5(19)
O(2W)—H(2D)$\cdots$O(1)$^{\mathrm{i}}$	2.732(3)	171(3)

Compound **XIII**

O(2)—H(1A)$\cdots$O(4)$^{\mathrm{i}}$	2.430(5)	168(6)

Compound **XIV**

O(1W)—H(1W)$\cdots$O(2W)	2.762(3)	159(3)
O(2W)—H(3W)$\cdots$O(8)$^{\mathrm{i}}$	2.722(3)	167(3)
O(1W)—H(2W)$\cdots$O(4)$^{\mathrm{ii}}$	2.820(3)	166(3)
O(6)—H(6)$\cdots$O(2)	3.115(2)	121(2)
O(6)—H(6)$\cdots$O(3)	2.500(2)	174(3)
O(9)—H(4)$\cdots$O(5)$^{\mathrm{iii}}$	2.514(2)	160(3)

---

[a] Symmetry transformations used to generate equivalent atoms: **I**: (i) $x, 1.5-y, 1/2+z$; (ii) $-x, 1/2+y, 1/2-z$; **II**: (i) x, 1.5–y, 1/2+z; **III**: (i) -1+x, -(1/2)-y, (1/2)+z; **IV**: (i) $1+x, 1+y, z$; (ii) $-1+x, y, -1+z$; (iii) $x, -1+y, z$; (iv) $1-x, 1-y, -z$; (v) $x, y, 1+z$; **V**: (i) $-x+1, -y, -z$; (ii) $-x, -y, -z$; **VI**: (i) $-x+0.5, y-0.5, -z+0.5$; (ii) $-x+0.5, y+0.5, -z+0.5$; (iii) $x+0.5, y-0.5, z$; **VII**: (i) $-x+1, -y, -z$; (ii) $-x+2, y-1/2, -z+1/2$, (iii) $x, -y+1/2, z+1/2$; **VIII**: (i) $x, -y+3/2, z+1/2$; (ii) $-x, y-1/2, -z+1/2$; (iii) $-x+1, -y+1, -z$; **XII**: (i) $x, y-1, z$; (ii) $x, y+1, z$; **XIII**: (i) $x-1, y-1, z$; **XIV**: (i) $-x+1, -y, -z+1$; (ii) $-x+1, -y+1, z+1$; (iii) $x+1, y-1, z+1$.

Table E.2.: Hydrogen-bonding geometry (distances in Å and angles in °) for [Sm(glu)(pic)(H_2O)$_2$] [a] (**XV**).

[Sm(glu)(pic)(H_2O)$_2$]

D—H···A	d(D···A)	<(DHA)
O(1W)—H(1A)···O(5)^{i}	2.753(4)	175(4)
O(1W)—H(1B)···O(3)^{ii}	2.687(4)	174(4)
O(2W)—H(2A)···O(6)^{iii}	2.842(4)	159(5)
O(2W)—H(2B)···O(1)^{iv}	2.764(4)	172(4)

[a] Symmetry transformations used to generate equivalent atoms: (i) $x, y, -1+z$; (ii) $x, 1/2-y, -1/2+z$; (iii) $2-x, -1/2+y, 1/2-z$; (iv) $x, 1/2-y, 1/2+z$.

Table E.3.: Hydrogen-bonding geometry (distances in Å and angles in °) for compounds with H$_4$pmida (XVIII–XXII).

D—H···A[a]	***d*(D···A)**	**<(DHA)**
Compound **XVIII**		
O(1W)—H(1C)···O(3)^{i}	2.880(3)	180(3)
O(1W)—H(1D)···O(1)^{ii}	3.107(3)	164(4)
O(2W)—H(2C)···O(4)^{iii}	2.809(3)	167(3)
O(2W)—H(2D)···O(1)^{i}	2.732(3)	171(3)
O(3)—H(3)···O(5)^{iv}	2.556(3)	170(3)
O(7)—H(7)···O(5)^{v}	2.681(3)	169(3)
Compound **XIX**		
O(1W)—H(1C)···O(7)^{i}	2.770(6)	168(6)
O(1W)—H(1D)···O(2)^{ii}	2.713(6)	171(6)
O(2W)—H(2C)···O(5)^{i}	2.752(7)	152(6)
O(2W)—H(2D)···O(4W)^{iii}	2.692(9)	171(6)
O(3W)—H(3A)···O(4)^{iv}	2.776(6)	156(5)
O(3W)—H(3B)···O(7)^{v}	2.737(6)	174(6)
O(4W)—H(4D)···O(3)^{vi}	3.057(8)	140(9)
O(3)—H(3C)···O(5)^{vii}	2.717(7)	172(7)
Compound **XX**		
O(1W)—H(1C)···O(7)^{i}	2.708(3)	178(3)
O(1W)—H(1D)···O(2)^{ii}	2.764(3)	163(3)
O(2W)—H(2C)···O(5)^{iii}	2.721(3)	161(3)
O(2W)—H(2D)···O(4W)^{iv}	2.648(5)	169(3)
O(3W)—H(3A)···O(4)	2.715(3)	164(3)
O(3W)—H(3B)···O(7)^{iii}	2.775(3)	170(3)
O(4W)—H(4D)···O(3)^{v}	3.065(4)	142(6)
O(3)—H(3C)···O(5)^{v}	2.644(3)	173(3)
Compound **XXI**		
N(4)—H(4C)···O(4)^{i}	2.571(3)	171(3)

Continued on next page

---

[a] Symmetry transformations used to generate equivalent atoms: **XVIII**: (i) $-x, 1-y, -z$; (ii) $1-x, 1-y, -z$; (iii) $-1+x, y, z$; (iv) $-1+x, y, -1+z$; (v) $-1+x, 1.5-y, -1/2+z$; **XIX**: (i) $-1+x, -y, z$; (ii) $2-x, 1-y, 1-z$; (iii) $x, 1-y, z$; (iv) $2-x, -y, -z$; (v) $-1+x, -1+y, z$; (vi) $-1+x, 1+y, z$; **XX**: (i) $2-x, 1-y, 1-z$; (ii) $1+x, y, z$; (iii) $1-x, 1-y, 2-z$; (iv) $x, 1-y, 1+z$; (v) $1-x, 2-y, 1-z$; **XXI** and **XXII**: (i) $2-x, y, 1.5-z$; (ii) $x, -1+y, z$; (iii) $1-x, 1-y, 1-z$; (iv) $x, -1+y, -1+z$; (v) $1-x, -y, -z$; (vi) $-1+x, y, -1+z$; (vii) $1-x, y, 1.5-z$; (viii) $2-x, y, 1/2-z$; (ix) $2-x, 1-y, 1-z$.

D—H$\cdots$A^{a}	***d*(D$\cdots$A)**	**<(DHA)**
O(1W)—H(1C)$\cdots$O(3W)^{ii}	2.682(3)	173(3)
O(1W)—H(1D)$\cdots$O(6)^{iii}	2.683(3)	167(3)
O(2W)—H(2C)$\cdots$O(8)^{iv}	2.802(3)	172(3)
O(2W)—H(2D)$\cdots$N(5)^{v}	2.753(3)	165(3)
O(3W)—H(3A)$\cdots$O(4)^{vi}	2.769(3)	169(3)
O(3W)—H(4B)$\cdots$O(8)^{vii}	2.778(3)	153(3)
O(4W)$\cdots$O(4W)^{viii}	2.602(8)	
O(4W)$\cdots$O(6)^{ix}	2.768(5)	

Compound **XXII**

N(4)—H(4C)$\cdots$O(4)^{i}	2.574(3)	172(3)
O(1W)—H(1C)$\cdots$O(3W)^{ii}	2.684(3)	176(3)
O(1W)—H(1D)$\cdots$O(6)^{iii}	2.683(3)	170(2)
O(2W)—H(2C)$\cdots$O(8)^{iv}	2.812(3)	173(3)
O(2W)—H(2D)$\cdots$N(5)^{v}	2.750(3)	168(2)
O(3W)—H(3A)$\cdots$O(4)^{vi}	2.766(3)	169(3)
O(3W)—H(4B)$\cdots$O(8)^{vii}	2.766(3)	153(3)
O(4W)$\cdots$O(4W)^{viii}	2.394(12)	
O(4W)$\cdots$O(6)^{ix}	2.764(6)	

---

[a] Symmetry transformations used to generate equivalent atoms: **XVIII**: (i) $-x, 1-y, -z$; (ii) $1-x, 1-y, -z$; (iii) $-1+x, y, z$; (iv) $-1+x, y, -1+z$; (v) $-1+x, 1.5-y, -1/2+z$; **XIX**: (i) $-1+x, -y, z$; (ii) $2-x, 1-y, 1-z$; (iii) $x, 1-y, z$; (iv) $2-x, -y, -z$; (v) $-1+x, -1+y, z$; (vi) $-1+x, 1+y, z$; **XX**: (i) $2-x, 1-y, 1-z$; (ii) $1+x, y, z$; (iii) $1-x, 1-y, 2-z$; (iv) $x, 1-y, 1+z$; (v) $1-x, 2-y, 1-z$; **XXI** and **XXII**: (i) $2-x, y, 1.5-z$; (ii) $x, -1+y, z$; (iii) $1-x, 1-y, 1-z$; (iv) $x, -1+y, -1+z$; (v) $1-x, -y, -z$; (vi) $-1+x, y, -1+z$; (vii) $1-x, y, 1.5-z$; (viii) $2-x, y, 1/2-z$; (ix) $2-x, 1-y, 1-z$.